Erkan Demirci

Reactions on modified and bimetallic surfaces: H_2, CO and methanol on Pd(111), Cu(110)+O and Ni/Cu(110)

PhD THESIS

For obtaining the academic degree

„Doktor der Technischen Wissenschaften“

Graz University of Technology

Supervisor:

Ao. Univ.-Prof. Dipl.-Ing. Dr. techn. Adolf Winkler

Institute of Solid State Physics

Graz, May 2010

EIDESSTATTLICHE ERKLÄRUNG

Ich erkläre an Eides statt, dass ich die vorliegende Arbeit selbständig verfasst, andere als die angegebenen Quellen/Hilfsmittel nicht benutzt, und die den benutzten Quellen wörtlich und inhaltlich entnommene Stellen als solche kenntlich gemacht habe.

Graz, am …… ……..
(Unterschrift)

Englische Fassung:

STATUTORY DECLARATION

I declare that I have authored this thesis independently, that I have not used other than the declared sources / resources, and that I have explicitly marked all material which has been quoted either literally or by content from the used sources.

…… ……..
date (signature)

Acknowledgement

First of all I would like to express my deep appreciation to my supervisor, Prof. Dr. Adolf Winkler, who has given me the opportunity of working in his group and introduced me to the field of surface science. He has encouraged me to strive for independence and excellence in my scientific research, as well as providing his personal support in my endeavors. In addition, I am grateful to him for having had the opportunity to collaborate with the other surface science groups who have been associated with my supervisor.

A great contribution to what I learned about density functional theory (DFT) using Vienna ab-initio simulation package (VASP) goes to Prof. Dr. Axel Gross from the Institute for Theoretical Chemistry, Ulm University in Germany who supervised and introduced me theory world. I owe special thanks to Dr. Christian Carbogno for providing valuable suggestions that improved my DFT knowledge in first period.

I owe special thanks to Dr. Lidong Sun, Dr. Michael Hohage and Prof. Dr. Peter Zeppenfeld from the University of Linz for taking optical measurements of reactions as a real time characterization.

Prof. Dr. Robert Schennach supported me in my research group. He introduced me into surface chemistry. Furthermore, we have crowned with a nice collaboration in part of my thesis.

I would like to acknowledge all members of the surface science group, past and present, Dr. Stefan Mülleger, Dr. Markus Kratzer, Dr. Hans Peter Koch, Dr. Paul Frank, DI Jörg Killmann and DI Johanna Stettner for many pleasant hours of working in a climate of friendship. I am also indebted to Martin Kornschober, without his help it would not have been possible to work with the reliable instruments of stainless steel and copper.

I am very grateful to the FWF (*Fonds zur Förderung der wissenschaftlichen Forschung, Austria*) for supporting my studies.

Last but not least I would like to express my gratitude to my parents who helped me to concentrate on completing this thesis and supported me continuously and unconditionally during the course of my studies.

Abstract

The study of adsorption is of significant importance for industrially relevant processes in which surfaces play a crucial role. The most explicit example is heterogeneous catalysis since usually the reactants have to adsorb on the catalyst surface before they can react. In this context physical and chemical aspects of the adsorption process both on single-crystal model catalysts as well as on real catalyst systems are important. This doctoral thesis is concerned with the interaction of oxygen, carbon monoxide, molecular and atomic hydrogen/deuterium and methanol on Cu(110), Pd(111) and Ni/Cu(110) surfaces using several experimental tools and density functional theory (DFT) calculations. The first part is about Cu(110) and Cu(110)-(2×1)O stripe phase and its interaction with methanol. The results, obtained by temperature desorption spectroscopy (TDS), low energy electron diffraction (LEED), Auger electron spectroscopy (AES), reflection absorption infrared spectroscopy (RAIRS) and reflection difference spectroscopy (RDS) measurements have been compared with previous studies in order to obtain a better understanding of the adsorption/desorption features of methanol. Adsorption of methanol on clean and oxygen pre-covered Cu(110) at 200 K and 270 K yielded different reaction intermediates and products. Actually, for both surfaces the sticking coefficient of methanol exhibits even opposing behaviors at these temperatures. Additional angular resolved thermal desorption experiments revealed further interesting features of methanol adsorption: from the oxygen covered stripe phase Cu(110) surface a bimodal desorption behavior was observed, indicating different desorption from the clean and oxygen covered part of the surface.

To perform a quantitative determination of the reaction products, the methanol/Pd(111) system has been chosen. With in-line TDS we could exactly determine the ratio between associatively desorbing methanol and pure hydrogen and carbon monoxide desorption, as a result of dehydrogenation. Preadsorption and postadsorption of atomic/molecular deuterium on a methanol covered Pd(111) surface has also been studied to obtain a better understanding of the C-H bond breaking.

The interaction of nickel tetra-carbonyl ($Ni(CO)_4$) with the Cu(110) surface has been probed to obtain a bimetallic nickel-copper surface. Adsorption at surface temperatures lower than 160 K this organometallic molecule exhibits an interesting adsorption/desorption feature. It condenses in

two discrete states and shows an unusual frequency factor for desorption compared to small molecules. At elevated temperatures $Ni(CO)_4$ decomposes into carbon monoxide and nickel on Cu(110), which yields a bimetallic surface formation. While a thick nickel film can be epitaxially grown on Cu(110), a (1×2) LEED pattern existing for a coverage lower than 1 ML, indicate the formation of a Cu-Ni surface alloy. As typical example of the combination of a transition and a non-transition metal, the Ni/Cu(110) surface alloys have been studied particularly for carbon monoxide adsorption/desorption. Combining a number of experimental techniques and theoretical calculations, the adsorption behavior of CO on Cu(110), Ni/Cu(110) and Ni(110) has been studied in detail. In TDS three new adsorption states have been observed for CO on a 0.25 ML Ni/Cu(110) surface. In this case, the best configuration of nickel can be explained by nickel dimers which consist of both in-surface and adjacent subsurface atom. These new states also indicate that the geometric effects for CO adsorption are dominant instead of electronic effects on the Ni/Cu(110) bimetallic surface. In addition to that the interaction between atomic hydrogen and carbon monoxide with the Ni/Cu(110) surface has been studied by a series of experiments. The most important result of these studies was that even with atomic hydrogen no methanation of CO could be obtained.

Kurzfassung

Die Untersuchung des Adsorptionsverhalten ist in industriellen, oberflächensensitiven Prozessen von großer Bedeutung. Ein wichtiges Beispiel bietet die heterogene Katalyse, bei welcher der Reaktand normalerweise zuerst auf der Katalysatoroberfläche adsorbieren muss bevor die Reaktion stattfinden kann. In diesem Zusamenhang sind beide, physikalische sowie chemische Aspekte des Adsorptionsprozesses, von großer Wichtigkeit, und zwar sowohl bei einkristallinen Modellsystemen als auch bei industriell gefertigten Katalysatoren. Diese Dissertation beschäftigt sich mit der Interaktion von Sauerstoff, Kohlenmonoxid, molekularem und atomarem Wasserstoff/Deuterium und Methanol auf Cu(110), Pd(111) und Ni/Cu(110) Oberflächen. Dafür wurden verschiedene experimentelle Untersuchungsmethoden and Dichtefunktionaltheorie (DFT) Berechnungen durchgeführt. Der erste Teil handelt von den gestreiften Phasen der Cu(110) und Cu(110)-(2x1)O Oberflächen und deren Interaktion mit Methanol. Die Ergebnisse aus thermischer Desorptionsspektroskopie (TDS), Low Energy Electron Diffraction (LEED), Auger-Elektronen-Spektroskopie (AES), reflection absorption infrared spectroscopy (RAIRS) und reflection difference spectroscopy (RDS) Messungen wurden mit bereits publizierten Untersuchungen verglichen, um ein besseres Verständnis der Adsorptions- und Desorptionseigenschaften von Methanol zu erlangen. Adsorption von Methanol auf sauberem und sauerstoffbedecktem Cu(110) bei 200 K und 270 K führte zu unterschiedlichen Reaktionsintermediaten und Reaktionsprodukten. Tatsächlich zeigt sich bei beiden Oberflächen sogar ein jeweils entgegengesetztes Verhalten des Haftkoeffizienten von Methanol bei diesen Temperaturen. Winkelaufgelöste thermische Desorptionsspektroskopie ermöglichte die Identifizierung eines zusätzlichen interessanten Effekts der Methanoladsorption: Von den sauerstoffbedeckten gestreiften Phasen der Cu(110) Oberfläche wurde ein bimodales Desorptionsverhalten beobachtet, welches auf eine unterschiedliche Desorption von den reinen- und sauerstoffbedeckten Teilen der Oberfläche hindeutet.

Um eine quantitative Bestimmung der Reaktionsprodukte durchzuführen wurde das Methanol/Pd(111) System gewählt. Mithilfe von „in-line“ TDS konnte das Verhältnis zwischen assoziativ desorbierendem Methanol und purer Wasserstoff- und Kohlenmonoxiddesorption, welches eine Resultat von Dehydrierung ist, exakt gemessen werden. Die Präadsorption und Postadsorption von atomarem/molekularem Deuterium auf einer Methanol bedeckten Pd(111)

Oberfläche wurde ebenfalls untersucht, um ein besseres Verständniss von der Aufspaltung der C-H Bindung zu erlangen.

Die Interaktion von Nickel Tetracarbonyl ($Ni(CO)_4$) mit der Cu(110) Oberfläche wurde studiert um eine bimetallische Nickel-Kupfer Oberfläche zu erzeugen. Bei Präparationstemperaturen unter 160 K weist dieses organometallische Molekül interessante Adsorptions- und Desorptionseigenschaften auf. Es kondensiert in zwei diskreten Zuständen und zeigt außerdem einen, im Vergleich zu kleinen Molekülen, ungewöhnlich hohen Frequenzfaktor. Bei erhöhten Temperaturen zersetzt sich $Ni(CO)_4$ in Kohlenstoffmonoxid und Nickel auf Cu(110), welches eine bimetallische Oberflächenformation ausbildet. Während eine dicke Nickelschicht epitaktisch auf Cu(110) aufwächst, existiert bei Bedeckungen unter 1 ML eine (1x2) LEED Struktur, welche die Formation einer geordneten Cu-Ni Oberflächenlegierung anzeigt. Als typisches Beispiel für die Kombination eines Übergangs und Nichtübergangsmetalls wurde speziell die Kohlenstoffmonoxid Adsorption/Desorption auf Ni/Cu(110) Oberflächenlegierungen untersucht. Durch Kombination einiger experimenteller Methoden und theoretischer Berechnungen wurde das Adsorptionsverhalten von CO auf Cu(110), Ni/Cu(110) und Ni(110) im Detail studiert. Im TDS wurden drei neue Adsorptionszustände für CO auf 0.25 ML Ni/Cu(110) beobachtet. In diesem Fall kann die beste Konfiguration durch Nickel Dimere beschrieben werden, welche aus Oberflächenatomen und aus nahen Subsurface-Atomen bestehen. Diese neuen, diskreten Desorptionszustände zeigen auch, dass für die CO Adsorption die geometrischen Effekte gegenüber den elektronischen Effekten auf einer Ni/Cu(110) bimetallischen Oberfläche dominant sind. Zusätzlich dazu wurde die Interaktion zwischen atomarem Wasserstoff und Kohlenmonoxid mit der Ni/Cu(110) Oberfläche in einer Serie von Experimenten untersucht. Das hierbei wichtigste Ergebnis war, dass selbst mit atomarem Wasserstoff keine Methanisierung von CO erreicht werden konnte.

Contents

List of symbols and abbreviations

AES	Auger electron spectroscopy
amu	Atomic mass unit
DFT	Density functional theory
E_{act}	Activation energy
E_{ads}	Adsorption energy
E_{des}	Desorption energy
ER	Eley-Rideal reaction mechanism
L	Langmuir (1×10^{-6} Torr·s)
LEED	Low energy electron diffraction
ML	Monolayer
QMS	Quadrupole mass spectrometer
RAIRS	Reflection absorption infrared spectroscopy
RDS	Reflectance difference spectroscopy
RT	Room temperature
STM	Scanning tunneling microscopy
TDS	Thermal desorption spectroscopy
Θ	Coverage
UHV	Ultra-high vacuum
XPS	X-ray photoelectron spectroscopy
VASP	Vienna ab-initio simulation package

Chapter I

1. Introduction

This dissertation is the result of a project (supported by the Förderung der wissenschaftlichen Forschung, *FWF*) that was mainly performed at the Graz University of Technology (*TU Graz*)-Surface Science Group of Institute of Solid State Physics. As complementary experimental and theoretical studies in some part of the thesis, we carried out the collaboration with the Institute of Experimental Physics-Johannes Kepler University (*JKU*) Linz and the Institute of Theoretical Chemistry-Ulm University. The aim of this work was to investigate adsorption/desorption mechanisms of atoms and molecules (atomic/molecular hydrogen and deuterium, carbon monoxide, water, methanol) on single crystal surfaces and bimetallic surfaces; Cu(110), Pd(111) and Ni/Cu(110), respectively.

The field that deals with the processes taking place on a surface of a solid is called "surface science". The structure and the electronic properties of the surface of a solid are inherently different from the rest of the solid (the bulk). Related to this also the binding energy for many atoms and molecules at surfaces is different from the equivalent energies in the bulk and hence, the chemical properties of the surface are special. The surface atoms cannot interact symmetrically with neighboring atoms and their effect is unbalanced. Therefore, they frequently cannot satisfy their bonding requirements in the same way as bulk atoms, this generally yields to the formation of bonds with foreign atoms or molecules on the surface. This process is of considerable interest for both fundamental and applied research.

The last few decades have witnessed enormous progress in the description of surfaces, both experimentally and theoretically. A great number of surface sensitive analytical tools have been developed to get detailed pictures of surface structures and reactions. In addition, density functional theory (DFT) calculations as a means of ´determining' surface structures and energies has been developed. Actually, modern surface physics finds applications in many technologies, for example, in heterogeneous catalysis (methanol synthesis, ammonia synthesis, oil

synthesis…), microelectronics, novel organic materials, electrochemistry, adhesion, astrophysics, biology, etc.

Heterogeneous catalytic reactions of gaseous molecules on metal surfaces are one of the great motivations for studying chemical reactions because of their industrial importance. In worldwide, heterogeneous catalysis is involved in literally billions of pounds´ worth of economic activity. Since the beginning of the twentieth century, many patents have been deposited claiming to use either new catalyst or new processes. The Haber-Bosch process or the Fischer-Tropsch synthesis are famous frontier examples for such heterogeneous catalytic processes [1,2]. The inexpensive production of ammonia from N_2 and H_2 gas mixtures over an alkali metal promoted iron catalysts is possible using the Haber-Bosch process. The Fischer-Tropsch chemistry transforms synthesis gas, H_2/CO (also called syngas) into more useful complex hydrocarbons and intermediate chemicals over iron or cobalt catalysts.

The most important properties of a catalyst can be characterized as reactivity and selectivity. A heterogeneous catalyst increases the reactivity by supplying reaction paths with a lower energetic cost. The control of the reaction path can also maximize the amount of target products by improving the selectivity. An efficient catalyst has apparently economic advantages, lowering the costs and enlarging the gain. Recently, moreover, catalysts extend its usage to reduce pollution by converting hazardous waste to less harmful materials.

The innate complexity of practical catalytic systems has lead to “trial and error” procedures as the common approach for the design of new and more proficient catalyst. Unfortunately, this approach is far from being efficient and does not permit to reach deep insight into the nature of the catalytic process. The consequence of this difficulty is a rather limited knowledge about the molecular mechanisms of heterogeneous catalysis. In order to get more insight about catalysis on a molecular scale, surface science experiments on extremely well controlled conditions have to be performed. This can just be accomplished by studying each single process separately where a maximum of idealization can be provided by using single crystal surfaces under ultra high vacuum conditions. However, even under these extremely idealized conditions it is still very difficult, almost impossible, to gain precise information about the molecular mechanisms without an unbiased theoretical guide.

One of the important issues in surface science is the interaction between molecules and surfaces which is defined by the specific properties of the substrates and adsorbates and determine the adsorption site, the orientation and symmetry of the adsorption complex, as well as the geometric and electronic structure. Usual surface science experiments deal with the study of either the kinetics of adsorption/desorption (e.g. in TDS) or with the characterization of adsorbates or products of reactions by in-situ tools (e.g in AES, XPS, UPS, LEED, STM etc…).

In the present work the partial and total oxidation of methanol on clean Cu(110) and on (2×1) oxygen stripe phase of Cu(110) was studied by thermal desorption spectroscopy, angle-resolved thermal desorption spectroscopy, reflectance absorption infrared spectroscopy and reflectance difference spectroscopy methods (in chapter 4). More investigations were performed on a Cu(110)- (2×1)O stripe phase surface since the sticking coefficient and reactivity of methanol is much more pronounced on such a surface than on a clean or totally oxygen covered of Cu(110) surface. However, an increase of the oxygen coverage yields a reduction of the C-H bond breaking barrier of adsorbed methoxy and to the formation of formaldehyde [3,4,5].

In addition to the adsorption of methanol on a Cu(110) single crystal surface a Pd(111) surface was used to investigate both the reactivity of methanol and the determination of the reaction products by mainly thermal desorption spectroscopy (in chapter 5). The interaction of methanol with transition metal surfaces has been investigated by several workers because of its relevance to environmental pollution and industrial processes. In other words, the importance of this reaction is that it is a model for the production of methanol from hydrogen and carbon monoxide. The main interest has been focused recently whether the C−O bond of adsorbed methanol on Pd (111) can be opened or not. In this study, there is no indication for C-O bond scission when methanol was adsorbed on the clean Pd(111). In order to better understand the reaction mechanism of methanol, the pre-adsorption and post-adsorption of atomic and molecular deuterium was applied on the methanol/Pd(111) system. In case of post-adsorption of atomic H we have found significant amounts of partially and fully deuterated methanol due to the C-H bond activation [6,7].

An interesting condensation and desorption behavior of nickel tetra-carbonyl ($Ni(CO_4)$) which is one of the organo-metallic molecules, was observed on Cu(110) (in chapter 6). It clearly showed a double desorption peak due to the formation of both a monolayer and the nucleation and growth

of multilayer islands. Compared to small molecules its frequency factor for desorption was unusually high, which is about $\nu=1.6\times10^{19}s^{-1}$ [8]. At elevated temperatures, this molecule decomposes into nickel and carbon monoxide. Thus, it can be used to deposit nickel films on surfaces, in particular for the preparation of bimetallic and alloy surfaces.

In chapter 7, Ni/Cu(110) bimetallic surfaces prepared both by dissociation of $Ni(CO)_4$ and by evaporation of nickel were used to investigate carbon monoxide adsorption/desorption dynamics and kinetics in detail. Three new adsorption states of CO with desorption peaks between that of CO on clean Cu(110) and clean Ni(110) were found. Besides the experimental methods, DFT calculations, using the Vienna ab-initio simulation package code, were performed to identify these new states. An optimum configuration of nickel for CO adsorption on Cu(110) were nickel dimers consisting of in-surface and adjacent subsurface atom. Thus, the adsorption of CO can be explained by local (geometric) effects rather than by long-range (electronic) effects [9].

Since for the proper activity and selectivity of a particular catalyst often very distinct adsorption energies are required, bimetallic systems can be used to tailor the catalytic properties. Thus, as a final work, the adsorption and desorption behavior of hydrogen and the mutual interaction between adsorbed hydrogen and CO on the Ni/Cu(110) is presented in chapter 8. While these bimetallic surfaces have a strong influence on CO adsorption, yielding to three new desorption peaks, they have only little influence on hydrogen adsorption/desorption and nearly show the individual desorption behavior from the pure Cu and Ni sites. Co-adsorption of hydrogen and CO leads to a lot of interesting results, but no reaction between the two species can be observed to obtain methanation products [10].

Chapter II

2. Fundamentals

2.1. Adsorption terminology and definitions

When the interaction between a surface (adsorbent) and an approaching particle (adsorptive) leads to a situation where the particle is kept in close distance to the surface (adsorbate) this process is called adsorption. The involved bonding mechanisms are distinguished with respect to their physical origin [11,12]. Adsorption is subdivided depending on the strength of the interaction between the adsorbate and the adsorbent: physisorption (weak interaction) and chemisorption (strong interaction).

2.1.1. Physisorption

In the case of weak adsorbate-substrate interactions due to van der Waals forces one speaks of physical adsorption or physisorption. In this case, no exchange of electrons is observed. Physisorption is characterized by interaction energies comparable to heats of vaporization (condensation). The typical binding energies of physisorption are at most a few kcal/mole [13]. Therefore, physisorption can only be seen at temperatures below 150 K. A common example of this type of adsorption is noble-gas adsorption on metal surfaces.

For a physisorption system interaction between the adsorbate and the surface atoms can be written by the Lennard-Jones potential:

$$V(r) = V_0 \left\{ \left(\frac{r_0}{r}\right)^{12} - 2\left(\frac{r_0}{r}\right)^{6} \right\} = V_{rep.}(r) + V_{attr.}(r) \qquad (2.1)$$

where the r^{-6} term indicates the attractive dipole interaction between the atoms (or molecule) an the surface at distance r. The Pauli repulsion potential between these species is typically approximated by r^{-12}, while $-V_0$ is the potential at the equilibrium distance, r_0. The interaction potential in Eq.2.1 indicates the sum over all two-body potentials with both a repulsive

interaction and an attractive interaction. Fig.2.1 shows the potential energy curve in one-dimension for an adsorbate approaching a surface along the perpendicular distance, r.

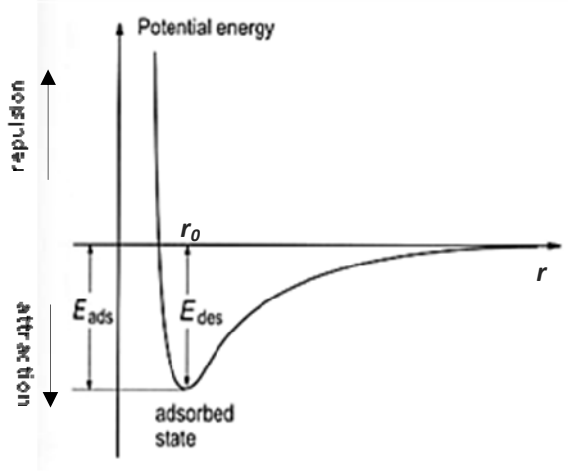

Figure 2.1: Potential energy for the physisorption of a particle on the surface of a solid: *r*, distance between molecule and surface; r_0 equilibrium separation.

The zero energy for the system has been chosen for the situation in which the adsorbate is infinitely far away (V(r) = 0 for r = ∞). The adsorption energy, E_{ads} is obtained at the equilibrium distance r_0, where the potential energy curve shows a minimum. The surface-adsorbate bond strength decreases with increasing position of *r*.

2.1.1. Chemisorption

The chemisorption indicates a chemical bond formation between the adsorbate and substrate which corresponds to large binding energies or adsorption energies. This bond can be either covalent (sharing of electrons) or ionic (electronic transfer) [14]. Unlike in physisorption a short equilibrium distance between the adsorbate and the substrate takes place. Therefore, the van der Waals forces are not dominant in such surface systems.

When a molecule adsorbs on a solid surface, the redistribution of electrons in the molecule to form a bond with the surface is often accompanied by emptying bonding orbitals or causing antibonding orbitals to become occupied which leads to dissociative adsorption [11,14,15]. The formation of new chemical bonds during adsorption is exothermic by 1-5 eV. Due to the presence

of energetically unfavorable transition states along the reaction coordinate, activation barriers often prevent direct chemisorption at low impingement energies and surface temperatures.

At lower surface temperatures these activation barriers can alternatively be overcome by increased residence time of the molecule on the surface. While in a physisorbed bound state, the molecule has the opportunity to make repeated attempts to overcome the activation barrier. With an appropriate choice of surface temperature, the rate of desorption from the physisorbed state can be minimized while providing adequate thermal energy to promote chemisorption. Since the rate of chemisorption from the physisorbed state is related to the population of adsorbates and the residence time, the rate of precursor-mediated chemisorption will be seen to decrease when the surface temperature is increased.

Adsorption with dissociation into two or more fragments is called *dissociative adsorption*. The potential energy curve in Fig.2.2 represents to this process. The process may be homolytic, as in the chemisorption of hydrogen or heterolytic for e.g. carbon monoxide. The process can be formulated:

$$AB + 2^{*} \rightarrow A + B \tag{2.2}$$

where * represents a surface site, *AB* is molecule, *A* and *B* are separated individual atoms.

The curve denoted by *AB* in Fig.2.2 represents the potential energy of molecule *AB* approaching the surface. There is a shallow minimum (physisorption minimum) before the curve rises steeply. The other curve *A+B* corresponds to the interaction of the widely separated atoms *A* and *B* with the surface. At infinite distance from the surface the energetic difference E_{diss} between the two potential curves is equal to the dissociation energy of the free molecule *AB*. Close to the surface it is energetically more favorable to have two separate atoms interacting with the surface than the intact molecule. This corresponds to the dissociative adsorption scenario.

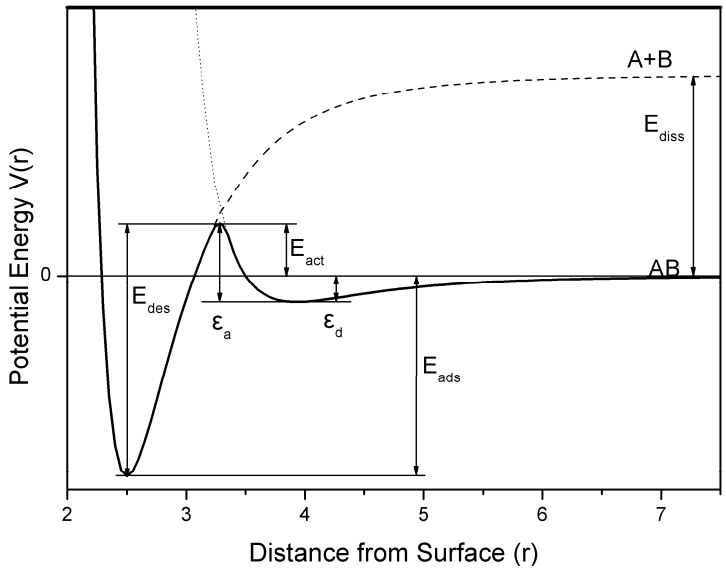

Figure 2.2: A potential energy plot for dissociative chemisorption of an adsorbate on an adsorbent according to Lennard-Jones. E_{act} is the activation barrier for activated chemisorption. E_{ads} is the binding energy in the chemisorbed state. E_{diss} is the dissociation energy for the *AB* molecule. E_{des} is an energy for desorption.

The exact location of the crossing point between the curves *AB* and *A+B* determines whether there is a barrier for dissociative adsorption or not. In Fig.2.2, the activated dissociative adsorption with the adiabatic dissociation barrier given by, E_{act} is shown. The adiabatic barrier will be somewhat lower due to the avoided crossing between the adiabatic potential curves. If the crossing of the two curves is closer to the surface and thus at a potential energy < 0 eV, the molecule can dissociate spontaneously at the surface and we have non-activated dissociative adsorption.

2.2. The adsorption process

Often the amount adsorbed is measured as a function of the partial pressure or gas concentration at a given temperature and the result is expressed as an *adsorption isotherm*. There are many empirical adsorption models, but the most common is the *Langmuir adsorption isotherm model*. This model assumes that the adsorbent has *S* sites per unit mass, of which S_0 are unoccupied and S_1 are occupied by adsorbate molecules [16].

$$S = S_0 + S_1 \tag{2.3}$$

The assumption of having S number of sites implies that there is a limit to the amount that can be adsorbed, i.e. saturation value of adsorption.

2.2.1. The condensation coefficient

As mentioned in the above section as the initial step the collision of the gaseous molecule with the surface takes place. The rate *I* of impingement, usually expressed as molecule $s^{-1}cm^{-2}$, is given by [17]:

$$I = \frac{dN_i}{dt} = \frac{P}{\sqrt{2\pi mkT}} \tag{2.4}$$

where *P* is the gas pressure, *m* the molecular weight of the gaseous molecule, *T* the temperature of the gas and k_B the Boltzmann´s constant.

As an assumption the rate of adsorption or condensation of a gas onto the sites is proportional to the product of the number of unoccupied sites and the gas pressure.

$$r_{cond.} = k_2 P S_0 \tag{2.5}$$

The rate of desorption or evaporation is assumed to be proportional to the number of occupied sites.

$$r_{des} = k_1 S_1 \tag{2.6}$$

At equilibrium, the rate of adsorption is equal to the rate of desorption.

$$r_{cond.} = r_{des} \Rightarrow k_2 P S_0 = k_1 S_1 \Rightarrow k_2 P(S - S_1) = k_1 S_1 \tag{2.7}$$

The amount adsorbed, Θ, can be expressed as a fraction of the sites that are occupied:

$$\Theta = \frac{S_1}{S} \Rightarrow k_2 P(1 - \Theta) = k_1 \Theta \Rightarrow \Theta = \frac{k_2 P}{k_1 - k_2 P} = \frac{KP}{1 - KP} \tag{2.8}$$

where the equilibrium constant, K ($K=k_2/k_1$), is the ratio of the adsorption rate constant and the desorption rate constant. It has the units of the reciprocal of pressure. In the limit of low pressures: $\Theta \approx KP;\ P \to 0$.

2.2.2. Sticking probability

The sticking coefficient is the probability of particles to adsorb on a surface which is defined by the ratio of the number of adsorbing particles N_{ads} and the number of impinging particles N_{imp}:

$$S(\Theta) = \frac{dN_{ads}(\Theta)}{dN_{imp}} \tag{2.9}$$

Sticking is not only determined by the energy transfer of the impinging particle but also by the ability of the surface to form bonds. The rate of adsorption is also expressed by the sticking probability $S(\Theta)$ and the impingement rate I:

$$r_{ads} = S(\Theta).I \tag{2.10}$$

In principle to calculate a coverage dependent sticking probability, $S(\Theta)$, in Eq.2.11, one can use uptake curves which are plots of the coverage Θ as a function of the exposure of the gas [11]. In a typical experiment one exposes a surface to various amounts of adsorbate and measures that amount of gas that sticks in *molecules/cm*^{2}. Note that the uptake of gas is initially rapid, but it quickly saturates. However, no saturation is seen in systems where multilayers form.

There exist numbers of papers describing sticking probability measurement in the literature which allow a determination with higher accuracy. Typically, the initial sticking probability in the limit of zero coverage $S(0)$ is measured and the variation of the sticking probability with coverage $S(\Theta)$ is expressed as the ratio $\frac{S(\Theta)}{S(0)}$. Usually the sticking coefficient drops from its initial value at zero coverage to zero at saturation coverage. This behaviour can be described by the adsorption model introduced by Langmuir [18]. The Langmuir Adsorption Model is based on the following assumptions:

i) adsorption is limited by the monolayer coverage
ii) all adsorption sites are equivalent
iii) only one molecule can reside in an adsorption site

Thus an incident molecule can now stick with some probability at a free site and is scattered at an occupied site. If a molecule dissociates into *n* species there are *n* free adsorption sites needed. In the simple case the fact that a molecule might need adjacent free adsorption sites to dissociate is neglected. The probability for a molecule to find an adsorption site at a coverage Θ can then generally be expressed as $(1-\Theta)^n$where *n* is called the kinetic order. Eq. 2.10 can then be rewritten into:

$$r_{ads} = s(0) \cdot (1-\Theta)^n \cdot I \tag{2.11}$$

Where *n* is the number of sites that are needed to hold the adsorbate, *S(0)* is the initial sticking coefficient at zero coverage. For molecular adsorption *n=1* holds and for dissociative adsorption *n=2* holds if the dissociative products are mobile.

2.2.3. Eley-Rideal (ER) mechanism

The Eley-Rideal (ER) process is one of the mechanisms to describe surface reactions. The ER type of mechanism is associated with a direct process, and a typical example would be the interaction [19,20];

$$A(s) + AB(g) \rightarrow A_2B(g) \tag{2.12}$$

where *(s)* and *(g)* stand for species adsorbed at the surface and in the gas phase, respectively. This direct mechanism involves only a gas phase collision, so that there is insufficient time to accommodate the incoming reactant *AB*. A good example for a process described by the ER mechanism is the abstraction of hydrogen on a *Cu* surface. This particular reaction can be written;

$$H(gas) + H(ads) + Cu \rightarrow H_2(g) + Cu \tag{2.13}$$

2.3. Thermal desorption

The process in which adsorbate species gain enough energy from the thermal vibrations on the surface atoms to escape from the adsorption well and leave the surface is called thermal desorption.

2.3.1. Desorption kinetics

An ideal desorption system comprises: a uniform surface with all adsorption sites identical, negligible interaction between adsorbed molecules on the surface, the molecular form of the adspecies is the same as that of the gaseous adsorbate [17]. The kinetic approach to the thermal desorption spectra is described in terms of the desorption rate, r_{des}. Based on the Polanyi-Wigner equation in 2.14 an evaluation of TDS is possible [21]:

$$r_{des} = -\frac{d\Theta}{dt} N_0 = \nu_n(\Theta)(N_0\Theta)^n \exp\left(-\frac{E_{des}(\Theta)}{RT}\right) \qquad (2.14)$$

$$T = T_0 + \beta t$$

where the r is the number of desorbing species per time and surface area; Θ is the coverage in monolayers; t is the time; n is the order of desorption; v is the pre-exponential factor of desorption; E_{des} is the activation energy of desorption; R is the gas constant; T is the temperature; T_0 is the temperature at which the experiment starts; β is the heating rate, equal to dT/dt. In Eq. 2.14, the correlation between the desorption rate, the coverage and the kinetic parameters are described. One has to mention that this approach to thermal desorption spectroscopy only holds if the pumping speed is constant and sufficiently high in order to prohibit significant re-adsorption of desorbed particles on the sample.

Attractive or repulsive interactions between the adsorbate molecules make the desorption parameters E_{des} and v dependent on coverage. The TD spectra of three different adsorbate systems, corresponding to zeroth-, first- and second order kinetics, are shown in Fig.2.3.
In the case of zero-order desorption ($n = 0$), the desorption rate does not depend on the coverage. The peak maximum is shifted to higher temperatures with increasing coverage, Θ. Furthermore

the TD spectra of different coverage have a common leading edge (in Fig.2.3a). In other words, characteristic of the TDS is the exponential increase with *T* and the rapid drop after all molecules have desorbed. Zero-order desorption is characteristic for desorption of a homogeneous multilayer film.

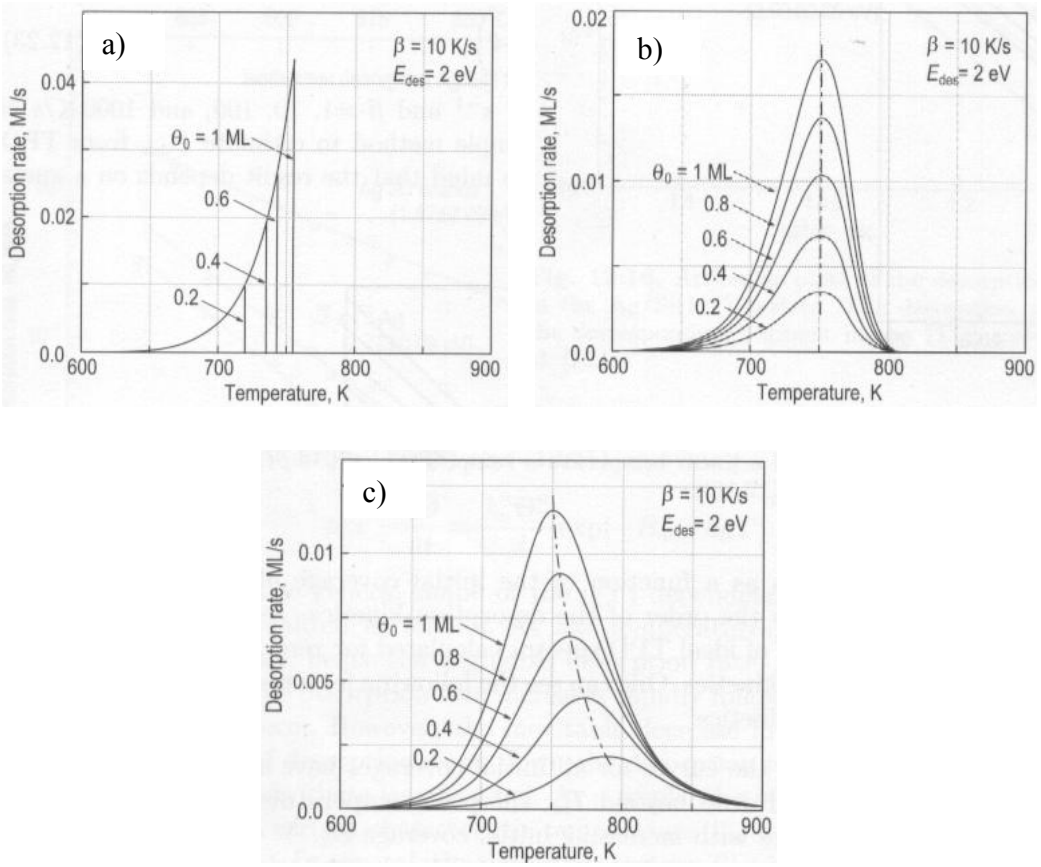

Figure 2.3: Calculated thermal desorption spectra with increasing coverage (a) zero-order desorption, (b) first-order desorption and (c) second-order desorption [18].

For a first-order desorption (*n = 1*), the desorption rate is proportional to the coverage. The TD spectra show a characteristic asymmetric shape and the peak maximum stays at the same temperature with increasing coverage (in Fig.2.3b). First-order desorption occurs when the single atoms (molecules) desorb from their adsorption sites without interacting with each other.

Finally, for a second-order desorption (*n = 2*), the symmetric shape of the TD spectra is characteristic (in Fig.2.3c). The rate of desorption depends on the coverage squared (Θ^2), this

leads to TDS peak maxima which shift to lower temperatures with increasing coverage. Second-order desorption corresponds to the recombinative desorption of molecules.

2.3.2. Interpretation of thermal desorption spectra

Because TDS offers interesting opportunities to interpret desorption in terms of reaction kinetic theories (such as the transition state formalism) we will discuss TDS in some more detail. A simple method to determine the desorption order is the logarithm of $\frac{d\Theta}{dt}$, as a function of the coverage when neglecting a coverage dependence of the desorption energy, E_{des} and pre-exponential factor, v:

$$\ln(\mathrm{r_{des}}) = \mathrm{n} \cdot \ln\Theta + \ln\nu_{\mathrm{n}} - \frac{\mathrm{E_{des}}}{\mathrm{RT}} \tag{2.15}$$

The isotherm $ln\,(r_{des}) = f(ln\Theta)$ yields the desorption order as the slope of the function.

For further evaluation of TD spectra, in case of the zero order desorption ($n=0$), the Polanyi-Wigner equation has the following form:

$$\mathrm{r_{des}} = -\mathrm{N_0}\frac{\mathrm{d\Theta}}{\mathrm{dT}} \cdot \frac{\mathrm{dT}}{\mathrm{dt}} = -\mathrm{N_0}\frac{\mathrm{d\Theta}}{\mathrm{dT}} \cdot \beta = \nu_0 \cdot \mathrm{N_0} \cdot \exp\left(-\frac{\mathrm{E_{des}}}{\mathrm{RT}}\right) \tag{2.16}$$

where β is the heating rate [$K \cdot s^{-1}$]. Taking the logarithm of equation (2.16) we obtain:

$$\ln(\mathrm{r_{des}}) = -\frac{\mathrm{E_{des}}}{\mathrm{RT}} + \ln\left(\frac{\nu_0}{\beta}\right) + \ln\mathrm{N_0} \tag{2.17}$$

If one plots the logarithm of the rate versus $1/T$, E_{des} corresponds to the slope of a straight line. From the intercept at the axis of the ordinate one can calculate the pre-exponential factor only if the desorption rate was calibrated correctly and the surface density N_0 is known.

For first order desorption it is possible to determine the desorption energy, E_{des} with experimentally obtained TD spectra according to the concept which was introduced by P. A. Redhead [21]. As a starting point, we again take the assumption that the desorption parameters in the Polanyi-Wigner (Eq. in 2.14) are independent of coverage.

For the temperature at which the peak exhibits its maximum, $T=T_m$, the derivative of the desorption rate has to hold $\frac{dr_{des}}{dT}\big|_{T_m} = 0$. Then according to $r_{des} = -\frac{d\Theta}{dt} = -\beta\frac{d\Theta}{dT}$, $r_{des} = -\frac{d^2\Theta}{dT^2}\big|_{T_m} = 0$ has to be fulfilled. Thus one can obtain:

$$\frac{d^2\Theta}{dT^2} = \frac{\nu}{\beta}\cdot\frac{d\Theta}{dT}\cdot exp\left(-\frac{E_{des}}{RT}\right) + \frac{\nu}{\beta}\cdot\Theta\cdot\frac{E_{des}}{RT^2}\cdot exp\left(-\frac{E_{des}}{RT}\right)$$

Evaluation of that expression at $T=T_m$ yields:

$$\frac{d\Theta}{dT}\big|T_m = \Theta\cdot\frac{E_{des}}{RT_m^2}$$

If the expression $\frac{d\Theta}{dT}$ can be substituted by the Eq. 2.14 for first order desorption, one can get:

$$\frac{E_{des}}{k_B T^2} = \frac{\nu}{\beta}\cdot exp\left(-\frac{E_{des}}{k_B T_m}\right)$$

The logarithm of this equation yields

$$\mathrm{E_{des}} = \mathrm{RT_m}\left[\ln\left(\frac{\nu\cdot\mathrm{T_m}}{\beta}\right) - \ln\left(\frac{\mathrm{E_{des}}}{\mathrm{k_B T_m}}\right)\right] \qquad (2.18)$$

The second part in the brackets is small relative to the first and is estimated as $ln\left(\frac{E_{des}}{RT_{max}}\right) = 3.64$ [21]. T_m is the temperature at the peak maximum and ν is the frequency factor for first order desorption, which has to be known. For many first order systems the frequency factor is unknown. However customary approaches for ν are to take the commonly chosen value of $\nu = 10^{13}s^{-1}$ without being too inaccurate. But this is not recommendable for large molecules, or to assume $\nu_0 \approx \nu$ and insert the value of the frequency factor for zero order desorption. In systems where the multilayer growth is significantly different from the monolayer growth, this assumption does not have to be correct: In the case of $Ni(CO)_4$ on Cu(110) it turned out that the frequency factors of the first monolayer and of the multilayer differ by six orders of magnitude (see in chapter 6).

2.3.3. Angular-resolved thermal desorption spectroscopy (AR-TDS)

More information on the interaction between a gas molecule and a metal surface can be obtained by using angle-resolved thermal desorption spectroscopy (AR-TDS). In this method one measures the angular distribution of the gas molecules that leave from the surface via desorption. The angular distribution of the desorbed molecules depends strongly on the activation energy, E_A for dissociative adsorption [22].

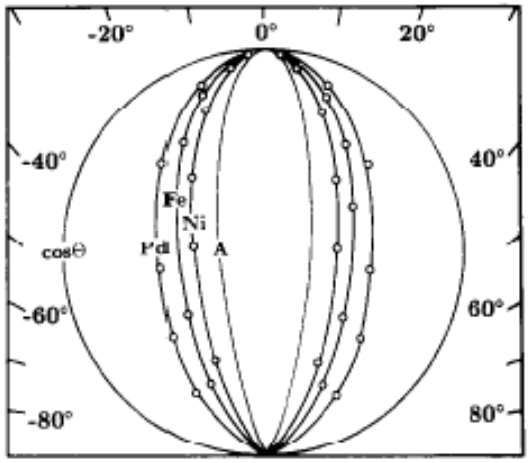

Figure 2.4: Experimental angular distribution of hydrogen from Pd, Ni and Fe at 900 K. An activation barrier of 1 eV height at 900 K would end up in a distribution depicted in curve A [22,23].

In the early days of surface science one assumed that the particles desorbing from a surface obey a cosine distribution. Later, one recognized that only the sum of all particles leaving a surface has to be a cosine. This includes not only desorbing particles but also elastically and inelastically scattered particles.

In one of the most famous experiments in surface physics van Willigen showed that hydrogen desorbing from metal surfaces (Fe, Pd and Ni) exhibited strongly forward focused angular distributions, shown in Fig.2.4 [22].

Due to his basic interpretation of data in terms of a one-dimensional barrier model: a Maxwellian hitting a one-dimensional barrier will be attenuated in the low energy end of the spectrum. This can easily be explained: In order to pass over the activation barrier, the normal component of the translational energy, $E \cdot Cos^2\varphi$ has to be larger than the activation energy E_A. With increasing angles fewer and fewer particles are able to overcome the barrier. An approach to describe the angular dependence of the desorption flux has been approximated by the expression:

$$D(\varphi) = D_0 \cdot \mathrm{Cos}^n\varphi \tag{2.19}$$

Usually angular distributions are measured by tilting of samples in front of a directional detector. Since in our case this was not possible, we used a different approach. Based on the latter assumption one can determine that angular distribution by a simple experiment described in section 3.5.2 and a comparison with a MC simulation is presented in Chapter 4. The obtained dataset consisted of ion-current signals which were assigned to the lateral displacement of the sample in front of a QMS aperture.

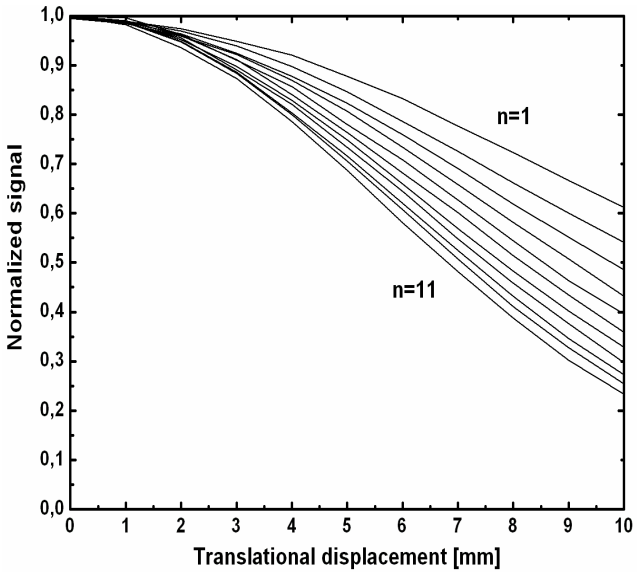

Figure 2.5: Normalised signal intensities as a function of sample displacement with respect to the QMS aperture-sample axis, as obtained by Monte Carlo simulations. Parameter: Exponent *n* in the angular distribution in form of $\cos^n\varphi$, in increments of $\Delta n = 1$. Sample diameter: 10 mm, QMS-aperture diameter: 7 mm, sample-aperture distance: 17 mm.

To obtain this distribution we modelled the experiment by Monte Carlo simulations for the similar geometric arrangement and assuming Eq.2.19. This is a frequently adopted angular distribution function for desorption processes [23]. In Fig. 2.5 we present the results of our MC calculations (QMS signal vs. lateral sample displacement) for our geometrical arrangement using different exponents of *n* (from n=1 to n=11*)*. These data show that the QMS signal dependence of the lateral sample displacement is pronounced enough to be used for proper angular distribution measurements. This aspect is important from the experimental point of view because many sample holders do not allow for sample tilting, but lateral displacements can usually be done on any sample holder. An additional advantage of this procedure is that in this case the angular distribution can be measured for two different azimuthal directions (X and Y) quasi-simultaneously, which is usually not possible in case of sample tilting around one axis.

Chapter III

3. Surface analytical methods: Experimental and theoretical

In order to get useful information with surface science techniques the experiments have to be performed under well-defined conditions, which require ultrahigh vacuum equipment. Therefore, this chapter starts with a brief description of the ultrahigh vacuum (UHV) chamber. Then the cleaning procedure of the samples by ion sputtering and thermal treatment is described. Afterwards all the analytical tools which are used in this thesis will be presented: Auger electron spectroscopy (AES), low energy electron diffraction (LEED), thermal desorption spectroscopy (TDS), preparation of bimetallic surfaces (by electron beam evaporation, and dissociation of nickel tetra carbonyl), infrared spectroscopy (IR), reflectance difference/anisotropic spectroscopy (RDS/RAS). Besides that a short description of all other instruments used and their theoretical background is given. The chapter ends with a description of density functional theory (DFT), which is based on the Hohenberg-Kohn theorem.

3.1. Ultra-high vacuum system (UHV)

All the experimental results presented in this work have been performed in an ultra-high vacuum (UHV) system. UHV conditions are required for two principal reasons in surface science experiments: *i)* to allow the use of low energy electron and ion-based experimental techniques without undesirable interference from gas phase scattering *ii)* to enable atomically clean surfaces to be prepared and to be maintained in contamination free state for the duration of the experiment. At these low pressures (in our case 1×10^{-10} Torr) the mean free path of a gas molecule is approximately over 500 km, so gas molecules will collide with the chamber walls many times before colliding with each other [18]. In other words with this base pressure a contaminant with a sticking coefficient of 1 and mass 28 needs ~ 30 hours to cover a Cu(110)

surface with a saturation. This is a pre-condition for reliable studies, especially for a technique which is very sensitive to specific contaminants.

(a)

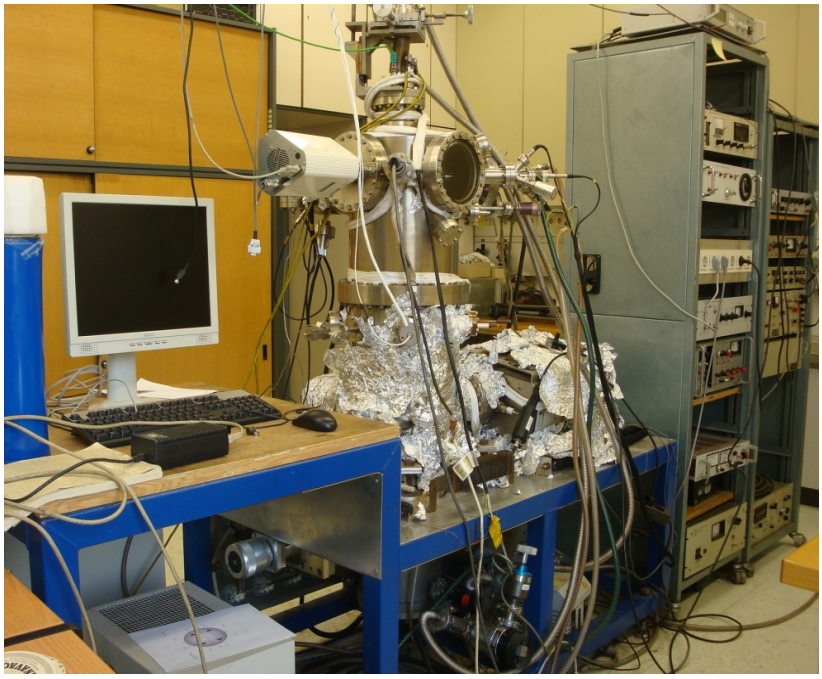

(b)

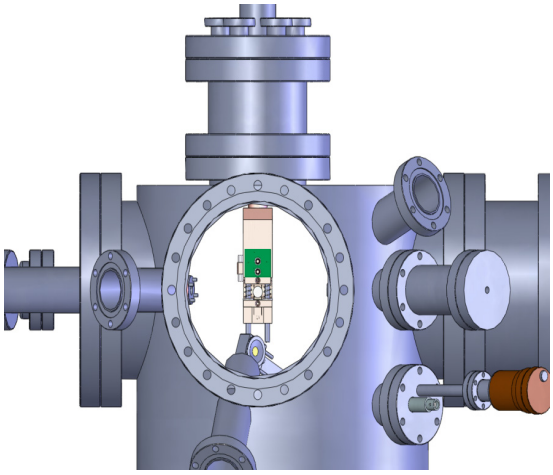

Figure 3.1: (a) A picture of the complete UHV system with the electronic control panel. (b) A drawing of the UHV system with the sample holder.

In order to achieve UHV conditions, some of the following conditions are required: use of low-outgassing materials such as special stainless steels, use of low vapor pressure materials

(ceramics, glass, metals, etc), high pumping speed, baking the system to get rid of water or some hydrocarbons adsorbed on the chamber walls etc.

In this study the UHV system consists of a main chamber for sample preparation and characterization with various spectroscopic tools (Fig.3.1a). The system is pumped by a rotary vane pump, a turbo molecular pump, an ion getter pump and a Ti-sublimation pump.

The preparation chamber is equipped with a sample manipulator (Fig.3.1b and Fig.3.2), in which the sample can be cooled down to 100 K via liquid nitrogen and heated up to 1000 K via resistive heating. The sample holder is also fixed onto a differentially pumped rotary stage in the main chamber. This set-up allows an almost 360º rotation of the sample and additionally a linear shifting in x, y and -z direction of ± 10 mm.

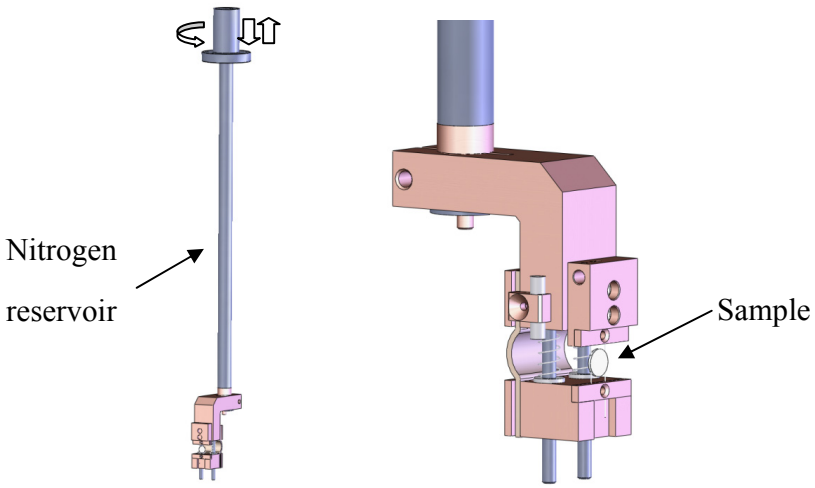

Figure 3.2: Drawing of the sample holder: whole body **(left)** and close view **(right).**

3.2. Preparation of clean sample surfaces

In the present study we have used a Cu(110) sample and a Pd (111) sample. Both samples have a disc shape (10 mm in diameter, 2 mm in thick) and grooves which are milled into its rim. Two tantalum wires (Ø 0.25 mm) are engaged in the groove forming two intricate loops which hold the disc at its diameter (Fig.3.3). The ends of the wires are clamped between two electrical contacts which are mounted onto the copper block. The contacts are isolated from the copper

block by ceramic inlays which provide good thermal conductivity but are electrical insulators. A side view of the installed sample in the sample holder can be seen in figure (3.2). The sample temperature was measured by means of a NiCr/Ni-thermocouple which was spot-welded close to the sample rim at the backside. By concurrent resistive heating of the tantalum wires and liquid nitrogen cooling the sample temperature could be controlled in a range of 100 K to 1000 K. A LAB-View based computer program provided a comfortable regulation of the sample temperature.

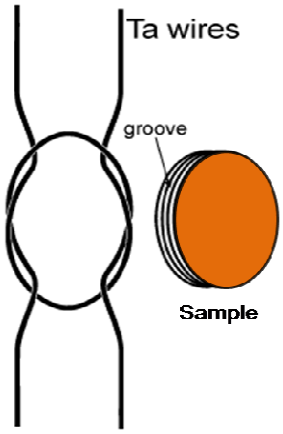

Figure 3.3: Mounting of the sample via tantalum wires

The samples before inserting them into the vacuum were dipped in alcohol and ultra-sonic cleaned and then rinsed in deionized water. Afterwards, the surface was dried with high purity pressurized nitrogen. Then the samples were inserted into the vacuum system. In order to remove surface contaminants (like carbon, oxygen, sulfur) from the surface, the samples were sputtered with Ar^+ ions at room temperature. The ion energy was 1 keV and the sputtering time was 15-20 minutes at an argon pressure of 5×10^{-5} Torr.

In this study we have used both a Cu(110) sample and a Pd(111) sample. After the same sputtering process for the samples they were flashed to ~ 800 K (for Cu(110)) and 1000 K (for Pd(111)) for a few minutes in order to remove the shallow implanted argon and to reconstruct the crystal structure of the clean surface. During flashing the system pressure was always in the 1×10^{-10} Torr range. After flashing the cleanliness of the surface was checked with AES and/or

LEED. No carbon, oxygen and sulfur were detected on the surface by AES. In case of LEED, a (1x1) structures were observed for the Cu(110) and the Pd(111) samples.

3.3. Auger electron spectroscopy (AES)

The chemical composition of a surface in the 5 Å to 20 Å region near the surface can be analyzed by Auger electron spectroscopy (AES) under high or ultrahigh vacuum conditions [24]. The method is based on the Auger effect which generates secondary electrons of the elements with a special kinetic energy which in turn can be detected by an energy dispersive analyzer. In this study a so called cylindrical mirror analyzer (CMA) is used.

The primary electrons, typically having an energy in the range of 2-5 keV, creates a core hole and both electrons leave the atom. In this state the ionized atom is highly excited and tends to minimize its energy by filling the hole in the core shell by an electron of an outer shell. The refilling electron changes from a state of lower binding energy to a state of higher binding energy. Due to the energy conservation law the excess energy has to be transferred. This can either happen by emitting a photon (fluorescence) or by energy transfer to another electron, which in turn is ejected out of the atom leaving a double ionized atom behind. The leaving electron is then called the Auger electron and carries an energy which depends on the energetic location of the initially removed electron and the final two electron holes. The de-excitation processes are illustrated in Fig.3.4.

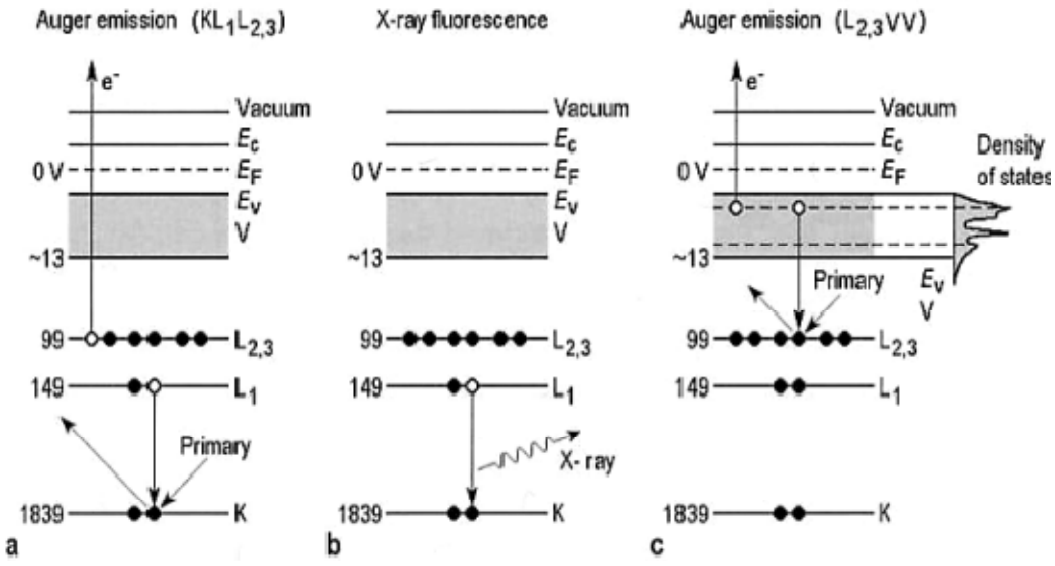

Figure 3.4: a) and b) are illustrations of two competing de-excitation processes as response to a core level ionisation. c) Auger emission process involving valance band states [18].

According to the example illustrated in Fig.3.4 the energy of the Auger electron can be estimated by

$$\mathrm{E}_{\mathrm{KL_1L_{2,3}}} = \mathrm{E_K} - \mathrm{E}_{\mathrm{L_1}} - \mathrm{E}_{\mathrm{L_{2,3}}} - \phi \qquad (3.1)$$

where the subscripts define the initial energy levels of the electrons. ϕ is the work function of the material, which can be expressed as: $\phi = E_{vacuum} - E_{Fermi}$. Considering the whole measurement procedure it turns out that the work function of the sample has no influence on the final electron energy but the work function of the detector has to be taken into account. Thus one has to insert the detector work function into the latter expression. Note that Eq. 3.1 is a rough estimation which does not take into account the final emission because in the latter relation the specific energy levels of the neutral atom are used and not those from the ion. For a more detailed description of the method the reader may be referred to the corresponding literature [18,25].

3.4. Low energy electron diffraction (LEED)

The low energy electron diffraction (LEED) technique is used to determine surface structures in surface science. The LEED apparatus consists of an electron gun, which emits electrons perpendicular onto the surface, a grid system and a screen (Fig.3.5) [18]. The electrons coming from the gun are diffracted due to their wave character at the surface, only elastically diffracted electrons contribute to the pattern on the screen. The inelastically scattered ones cannot pass a grid in front of the screen, which is at a potential slightly smaller than the kinetic energy of the primary electron beam. Hence, the electron energy and the modulus of the wave vector $\vec{k}$ are conserved:

$$|\overrightarrow{k_0}| = |\vec{k}| = \frac{2\pi}{\lambda} \tag{3.2}$$

where k_0 is the wave vector of the incoming and k of the diffracted electron, whereas the length of the k-vektor is determined by the wavelength which is a function of the beam energy E, which is typically varied between 20 and 200 eV.

$$|k| = \frac{2\pi}{\lambda};\ \lambda[\text{Å}] \approx \sqrt{\frac{150.1}{E[\text{eV}]}} \tag{3.3}$$

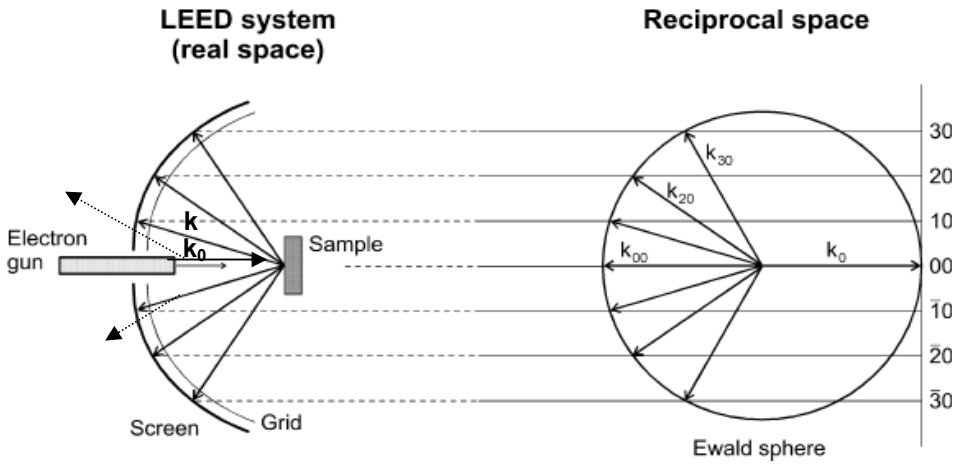

Figure 3.5: A relation between the LEED system in real space and the Ewald sphere, and the accomplishment of the diffraction pattern in reciprocal space.

The electron wavelength is in the range of the interatomic distances (1-2Å) on the surface and the electrons are therefore diffracted at the periodic surface structure. In other words, electron scattering is surface sensitive if electrons have the right energy which is illustrated in Fig.3.6. It can be clearly seen that in the range of LEED electrons the penetration depths of the electrons is very small, namely a few atomic layers. Thus, the LEED electrons penetrate only a very short distance into the solid, so that the diffraction is determined almost entirely by the surface atoms.

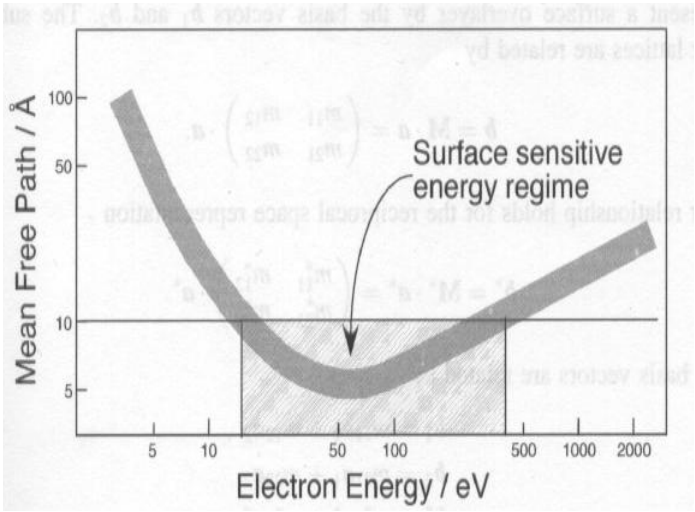

Figure 3.6: A compilation of experimental data of the dependence of the mean free path λ on the electron energy [26].

The diffraction pattern of LEED is determined by the two dimensional surface periodicity since electrons do not penetrate into the crystal bulk. The lattice vectors can be described a_1 and a_2, which are both parallel to the surface plane [26]. A general lattice point within the surface is an integer multiple of these lattice vectors:

$$R = ha_1 + ka_2 \tag{3.4}$$

The Bragg condition in two- dimension yields to the definition of the reciprocal lattice vectors a_1^* and a_2^* which fulfill the set of equations:

$$a_1 a_1^* = a_2 a_2^* = 2\pi \tag{3.5a}$$

$$a_1 a_2^* = a_2 a_1^* = 0 \tag{3.5b}$$

These reciprocal lattice vectors are also parallel to the surface plane and define the LEED pattern in *k*-space. Each diffraction spot corresponds to the sum of integer multiples of a_1^* and a_2^*.

$$G = \sum_{i=1}^{2} (h + k)a_i^* \tag{3.6}$$

The reciprocal space of the surface therefore consists of rods perpendicular to the surface (in Fig.3.5 numbered with 00, 10,...), which satisfy the Laue diffraction condition. In three dimensions a grid (depending on the crystal structure) of rods emerges perpendicularly from the surface. The Ewald sphere in Fig.3.5 determines exactly the directions of the diffracted electrons according to the Laue condition and the energy conservation: The directions from the centre of the Ewald sphere (with has a radius of k_0, i.e. the wave vector of the incoming electrons) to any point where the Ewald sphere intersects the rods are the wave vectors k_{00}, k_{10},... of the diffracted electrons. This is due to the fact that the connecting line between the point of the arrow representing k_0 in the figure and any cross point of the rods with the Ewald sphere is also a reciprocal lattice vector, *G*. Thus, the resulting pattern on the screen caused by electrons diffracted in characteristic directions is indeed an intersection between the Ewald sphere and the reciprocal surface lattice. The curvature of the screen and the Ewald sphere tend to cancel each other and a direct image of the reciprocal surface lattice is obtained. There will always be a solution of the diffraction conditions unless the incident wave vector is too small (i.e. smaller than the shortest reciprocal lattice vector on the surface). Due to the dependence of the Ewald sphere on the electron energy, the spots on the screen move closer to the center if the energy is increased (the wavelength decreases and k_0 and the radius of the Ewald sphere increase) and vice versa. A more detailed description of the LEED technique can be found in the corresponding literature [26,27,28].

3.5. Quadrupole mass spectrometry (QMS)

The QMS is used to analyze the particles of the gas inside an UHV chamber according to their mass and to determine the partial pressure. As any other mass spectrometer the QMS consists of three components: the ion source with electron impact ioniser, the actual quadrupole analyser consisting of four cylindrical rods, and the ion detector (electron multiplier) (Fig.3.7). The quadrupole analyser consists of four cylindrical rods, arranged symmetrically at a distance $r_0(x,y)$

around the optical axis *z* of the system. Opposite rods are electrically connected. A voltage of $U(t) = \pm U + V\cos(\omega t)$ is applied to the two pairs of opposite rods. By changing the voltages *U* and V, but holding the ratio $\frac{U}{V}$ constant for each voltage, only particles with a certain mass to charge ratio move along a stable track and reach the detector where they are subsequently detected by a secondary electron multiplier.

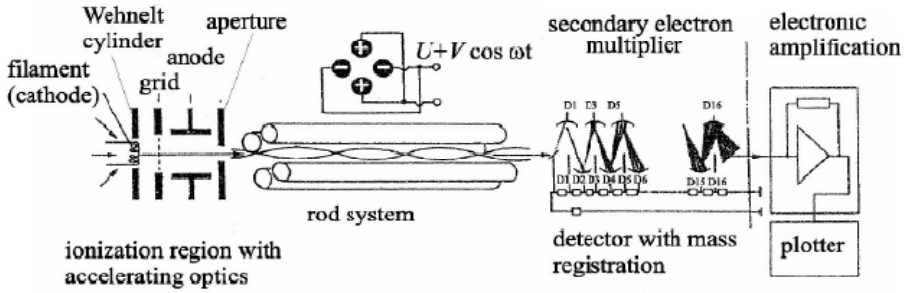

Figure 3.7: Illustration of a quadrupole mass spectrometer with the main parts: ionization region, rod system and detector region [29].

Only ions of a certain mass/charge ratio (*m*/*Ze)* will reach the detector for a given ratio of voltages. The double ionized particles appear in the spectrum at half of their molecular mass, triply charged ions at one third, etc. due to their *m*/*Ze* ratio [29]. By this method, molecules with molecular masses of over 1000 can be detected even if the mass spectrometer has a maximum range of, e.g., 300 amu. Apart from the isotope pattern of the molecular ions one can also observe products of ion fragmentation processes. The simplest way of detecting ions or electrons is *via* the detection of their charges. In simple quadrupole mass spectrometers the ions hit a metallic collector cone (Faraday cup) and the charge transferred is recorded using an electrometer preamplifier, which can detect currents down to a pA-range. For even lower ion currents one uses secondary electron multipliers or channeltron multipliers.

3.5.1 Thermal desorption spectroscopy (TDS)

Thermal desorption spectroscopy (TDS) which is also referred to as temperature programmed desorption (TPD), is one of the most frequently employed techniques for the determination of kinetic parameters of desorption processes or decomposition reactions. First a surface is exposed to a gas. After exposure, the sample surface is rotated to face the mass spectrometer detector and heated with a temperature program $\beta(t) = dT/dt$ (with the temperature T usually being a linear function of the time t). As the substrate temperature is increased, however, there will be a point at which the thermal energy of the adsorbed species is such that one of several things may occur: *i)* a molecular species may decompose to yield either gas phase products or other surface species, *ii)* an atomic adsorbate may react with the substrate to yield a specific surface compound, or diffuse into the bulk of the underlying solid, *iii)* certain adsorbed species may have enough energy to escape. The third options is called the desorption process, where the desorption products will be detected as a rise in pressure for a certain mass, e.g. by mass spectrometry. The TDS experiments are often performed using a quadrupole mass spectrometer (Fig.3.8a,b) and well-defined surfaces of single-crystalline samples in a continuously pumped ultra-high vacuum (UHV) chamber.

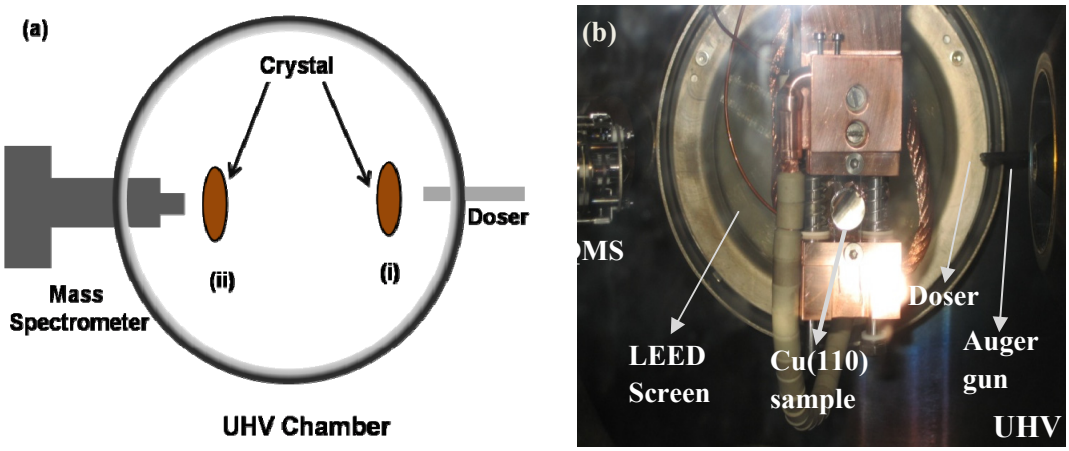

Figure 3.8: (a) The illustration of TDS set-up, (i)The experiment starts by dosing the clean sample crystal at position. (ii) The sample is then moved to face quadrupole mass spectrometer. (b) The picture of the Cu(110) sample in the UHV chamber is shown with various surface science tool.

3.5.2. Measurement of angular distribution of desorption

For angle resolved desorption measurements, the sample is usually tilted in front of a directional detector. Since our sample holder did not allow for tilting we proceeded in the following way: A number of desorption experiments were performed with different sample positions with respect to the sample-aperture axis by shifting the sample laterally up to ± 10 mm in X and Y direction. This also yields a QMS signal (after proper subtraction of the background signal) which depends on the actual angular distribution of the desorbing species. Sample position and QMS aperture in UHV chamber are shown in Figure 3.9.

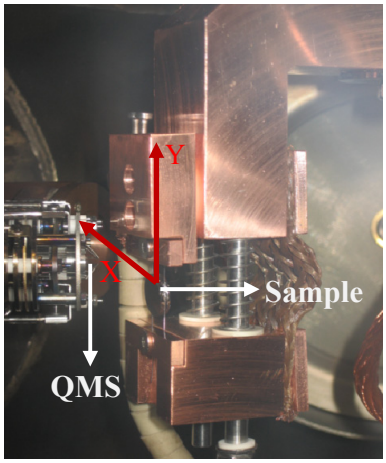

Figure 3.9: The mass spectrometer aperture, the Cu (110) sample with sample holder and the shift directions for angular distribution measurements.

3.6. The Ni/Cu(110) bimetallic surface preparation

To obtain a nickel-copper bimetallic surface we used two different techniques. In the first case at the appropriate surface temperature the dissociation of nickel tetra-carbonyl, $Ni(CO)_4$ on Cu(110) was used in order to prepare a bimetallic surface. As a second method, the nickel was evaporated onto the Cu(110) surface by a commercial electron beam evaporator. In this case the amount of evaporated nickel was measured with a quartz microbalance which could be positioned instead of the sample.

3.6.1. Electron beam evaporation (EBE)

A commercial electron beam evaporator (OMICRON EFM 3 UHV Evaporator) was used to obtain a bimetallic Ni/Cu(110) surface. A photograph and scheme of the evaporation assembly with installed nickel evaporator is seen in Fig.3.10. A Ni rod was heated by electron beam bombardment from a tungsten wire filament, causing evaporation. The evaporation cell was contained in a water cooled copper shield. By this, the background pressure during evaporation could be kept below 5×10^{-10} Torr .

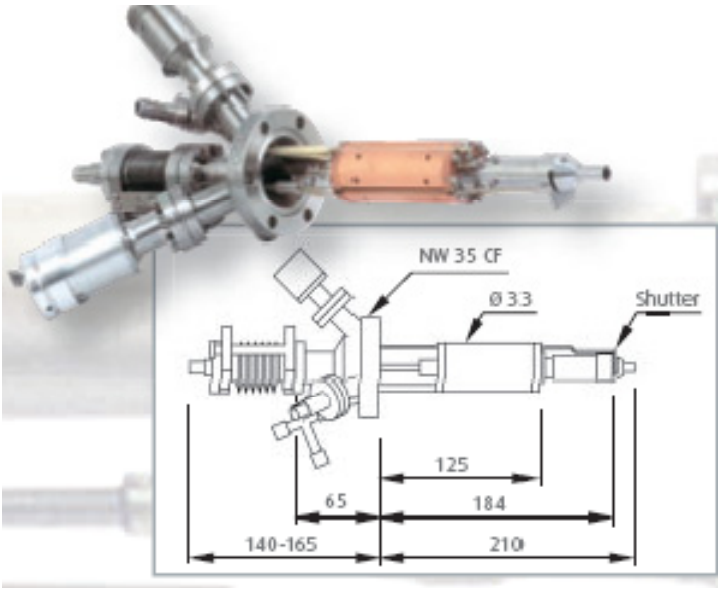

Figure 3.10: A photograph and a schematic drawing of the electron beam evaporator (OMICRON EFM 3 UHV Evaporator) unit with installed Ni evaporator. The distance between sample and the front of the evaporator was 18 mm [30].

The film thickness is monitored by a quartz microbalance (INFICON Compact Crystal Sensor) which can be positioned exactly at the sample location, where subsequently thin film deposition is carried out. The basic idea of a quartz microbalance is the piezoelectric effect. When we apply a voltage in some certain crystal surface direction, the crystal will be distorted and changed its shape, which is proportional to the applied voltage. When an AC voltage is applied the crystal will vibrate. The resonance frequency is sensitive to the mass of the crystal. This characteristic

can be used to obtain the amount of deposited material on the substrate. Using the resonance frequency difference, the deposition rate can be calculated.

3.6.2. Nickel tetra-carbonyl ($Ni(CO)_4$) dissociation

Nickel tetra-carbonyl is an organonickel compound with the chemical formula $Ni(CO)_4$. It has a tetrahedral form with Ni-C=1.817 Å and C-O=1.127 (Fig.3.11) where four carbon monoxide (carbonyl) molecules are connected to the center atom nickel. It is very volatile at room temperature and highly toxic.

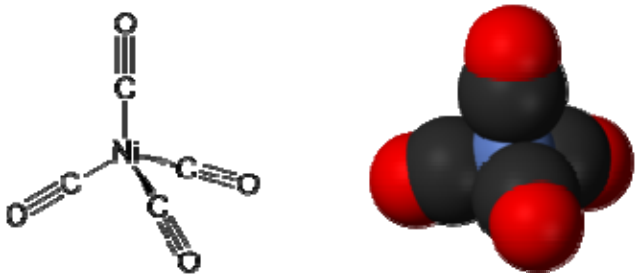

Figure 3.11: The illustration of the $Ni(CO)_4$ molecule. Carbon and oxygen are connected by triple bonds and are covalently bonded to the nickel atom via the carbon ends [31].

At the temperature above 180 K, $Ni(CO)_4$ starts to decompose to carbon monoxide, and nickel sub-carbonyls form ($Ni(CO)_3$, $Ni(CO)_2$, Ni(CO)) as well as nickel metal. They are shown in the mass spectrum between mass number 50 amu and 200 amu (Fig 3.12). In addition to that it decomposes on the chamber walls. This property of organometallic molecules can be used to form a bimetallic surface. More details will be given in chapter 7. In addition to that some interesting features of $Ni(CO)_4$ condensation on Cu(110) are presented in chapter 6.

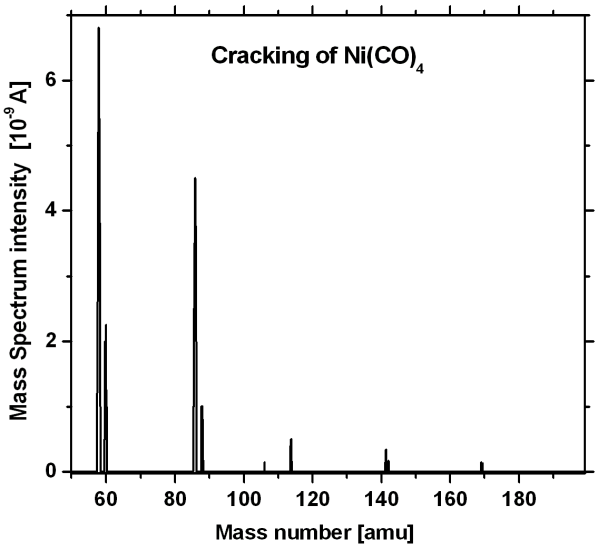

Figure 3.12: Mass spectrum (cracking pattern) of a $Ni(CO)_4$ gas as obtained in our particular case at a total pressure of $4x10^{-8}$ Torr where the mass numbers are represented with Ni: 58 amu, NiCO: 86 amu, $Ni(CO)_2$: 114 amu, $Ni(CO)_3$: 142 amu, $Ni(CO)_4$: 170 amu; the signals at 60 amu and 88 amu stem from the Ni^{60} isotope.

3.7. Infrared spectroscopy (IR)

Infrared spectroscopy was among the first methods to be applied to the direct characterization of adsorbates, with the earliest investigations of adsorption of finely divided materials being published in 1940s [32]. These earliest studies used transmission infrared spectroscopy, in which the infrared beam passes through a prepared sample and the change in its absorption spectrum following adsorption is monitored. Subsequent instrumental developments, notably including the increasing availability of Fourier transform infrared (FT-IR) spectrometers, progressed the methods during the 1970s and 1980s. Reflection-absorption infrared spectroscopy is one of the latest applications of FT-IR.

In this study, to get more information on the surface process during the reaction and desorption of particles which is not possible with thermal desorption spectroscopy (TDS), we have used the reflection absorption infrared spectroscopy (RAIRS-with a grazing incidence angle of 83º) technique. This method is proper to understand how the preferred adsorption sites are changed during the adsorption/desorption process. Furthermore one can follow adsorption or desorption kinetics by measuring IR spectra as function of time or temperature.

The RAIRS investigations have been performed using a Brucker ifs 66 v/S Fourier transform infrared (FTIR) spectrometer. This FT-IR is attached to the UHV chamber in a RAIRS set-up. This set-up is described in more detail in [33]. The FT-IR has two different detectors which are a pyroelectric detector and a liquid nitrogen cooled mercury cadmium telluride (MCT) semiconductor detector. In this study the MCT type detector is used due to its higher sensitivity and faster scan property than the pyroelectric detector. One has to mention that the MCT detector can not be operated at room temperature. The LN_2 cooled detector is hold behind the potassium bromide (KBr) window. In order to isolate it thermally the device is mounted in a Dewar which has to be evacuated to high vacuum. As an infrared source, we have used a silicon carbide (SiC, Globar) source.

A schematic representation of an FT-IR spectrometer is given by Fig. 3.13. The Michelson interferometer consists of a fixed and a movable mirror (M1 and M2, respectively) and a beam splitter. Additionally there are two light sources: an infrared source and a laser.

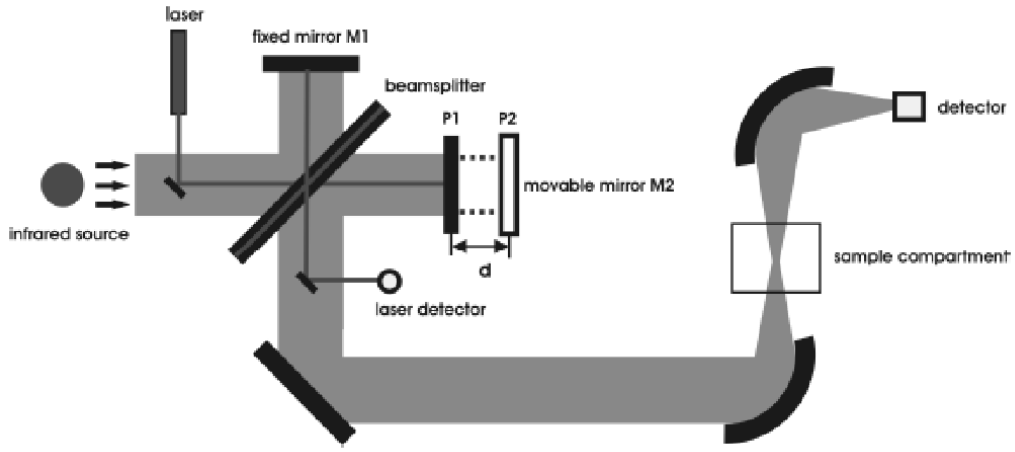

Figure 3.13: The optical path of a Fourier transformation spectrometer. The main parts are the infrared source, the Michelson interferometer and a MCT detector [34].

The laser is used to determine the position of the movable mirror, the infrared source to interact with the adsorbates on the sample. Because of the two light sources there are also two detectors. The signal is passed to the sample which is located in the UHV chamber and finally it is detected by the detector (external MCT detector).

The spectrometer is managed by the OPUS software. It allows managing different adjusting parameters for various measurements. For a grazing incidence angle of about 83° a scan time of 15 min was chosen with a resolution of 4 cm^{-1} and a modulation frequency (or mirror velocity) of 10 kHz (Modulation frequency, is $f_{\tilde{\nu}}^{mod} = \frac{1}{T_{\tilde{\nu}}^{mod}} = \frac{V}{S_{\tilde{\nu}}} = \frac{V}{\lambda/_2} = 2V\tilde{\nu}$ where $T_{\tilde{\nu}}^{mod}$ is the time between two zero crossings of the interferogram of the laser, V is the mirror velocity, cms^{-1} and $S_{\tilde{\nu}}$ is the way that has to be passed by the mirror that the optical path difference is λ, which is the wave length of the laser. $\tilde{\nu}$ is the infrared frequency in wavenumbers, cm^{-1}). In case of temperature-resolved measurements, a scan time of 1 minute and a modulation frequency of 60 kHz was used for each cycle. The time gap between two cycles was 10 s, hence every 70 s one spectrum is taken for the measurement.

3.8. Reflectance difference/anisotropic spectroscopy (RDS/RAS)

Reflectance difference spectroscopy (RDS, also called RAS—reflectance anisotropy spectroscopy) is a normal incidence reflectance technique that utilizes the anisotropy of reconstructed semiconductor and metal surfaces and is capable of sensing the stoichiometry and symmetry of the uppermost atomic monolayers of cubic semiconductors and metals. It is a new and extremely sensitive method to investigate the anisotropy of metal surfaces, the adsorption kinetics of inorganic atoms and molecules [5,35,36,37]. Furthermore, being a purely optical method, RDS can be applied to samples in any transparent environment, which would allow bridging the pressure gap between ultra-high vacuum and the high pressure reaction regime. A picture of an RDS system which is attached to an UHV chamber is shown in Fig 3.14a. RDS measures the difference of the reflectivity for light linearly polarized along two orthogonal surface directions $[1\bar{1}0]$ and $[001]$, normalized to the average reflectivity.

$$\frac{\Delta r}{r} = 2\frac{r_{[1\bar{1}0]} - r_{[001]}}{r_{[1\bar{1}0]} + r_{[001]}} \qquad (3.12)$$

The experimental setup of the system is illustrated in Fig.3.14b. The RDS system used in this study is the Aspnes type [38] which uses light generated by a 75 W xenon-lamp with energies ranging from 1.5 to 5.5 eV. After the light is linearly polarized by a prism polarizer, it passes a

strain-free window (in case of in situ UHV experiments) and enters the UHV chamber, where it is reflected at the sample.

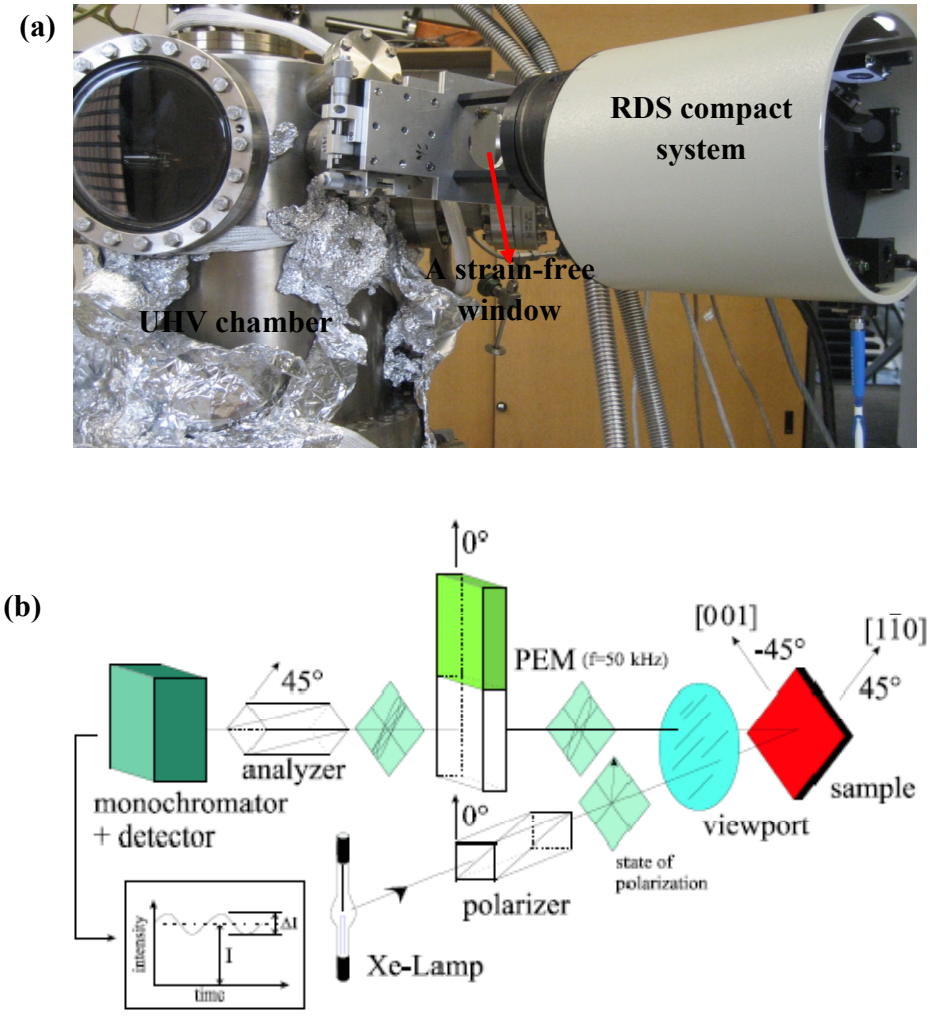

Figure 3.14: a) A picture of the RDS system which is attached to a UHV chamber b) a schematic drawing of the reflectance difference spectroscopy (RDS) set-up [39].

The polarization direction is chosen in a way to maximize the anisotropy signal: for samples with two-fold symmetry the polarization direction is adjusted to be 45° off the primary axes of the surface, resulting in an equal projection of the polarization vector on these primary axes. After reflection from the surface, the difference of the reflectivity of both polarization directions leads to a rotation of the polarization vector and to a relative phase shift (ellipticity) in the reflected

beam. This change in the polarization state is analyzed spectroscopically with a lock-in technique using a photoelastic modulator (PEM), analyser, diffraction grating and photomultiplier for detection.

This procedure allows one to simultaneously determine the amplitude $|\Delta r/r|$ and the phase shift $\Delta\Theta$ and, hence, the real and imaginary part of the complex reflectance difference $\Delta r/r$. All optical components are placed outside the vacuum. The light is transmitted through a strain-free window into the UHV chamber, where the experiments discussed in this paper have been performed.

RDS has been initially applied to semiconductor surfaces, metal-semiconductor interfaces and metal surfaces and recently used to investigate organic layers on various surfaces. In this thesis, we present a real time reflectance RDS study of the adsorption and reaction of methanol on the bare Cu(110) surface and the Cu-CuO stripe phase. For a partially reconstructed surface like the Cu-CuO stripe phase, the reconstructed fraction of the surface and, hence, the oxygen coverage in the range $0\ \mathrm{ML} \leq \Theta_o \leq 0.5\ \mathrm{ML}$ can be determined quantitatively by RDS [40]. Besides, surface processes like adsorption or desorption as well as reactions can be monitored in real time by recording the changes of the RD signal at a selected wavelength which is called reflectance difference kinetic (RDK).

3.9. Density functional theory (DFT)

The basic lemma of density functional theory (DFT) was proposed by Hohenberg and Kohn in 1965 which is also known as the famous Hohenberg-Kohn theorem [41]. *"The ground-state density n(r) of a system of interacting electrons in an external potential uniquely determines this potential"*. In recent years this theory has been improved in order to understand extremely complex molecular and catalytic systems together with the improvement in computer power. DFT can be regarded as a revised successor of the Thomas-Fermi theory [42,43,44]. The main idea of DFT is the substitution of the multi-dimensional wave function $\psi(r_1, r_2, \cdots\cdots, r_N)$ of N interacting electrons by the simple electron density n(r) which is a function of three-dimensional coordinates. The implementation of this idea via effective one-particle Schrödinger-equations has been developed by Kohn and Sham [45]. The big success of DFT and its contribution to the scientific progress resulted in the Nobel prize for chemistry in 1998 for Walter Kohn.

3.9.1. Kohn-Sham equations

We will start with the time-independent, non-relativistic Schrödinger equation for the wave function ψ of N interacting electrons:

$$E\psi = \hat{H}\psi = \left(\hat{T} + \hat{V} + \hat{V}_{ext}\right)\psi \qquad (3.13)$$

where the Hamilton operator of the system consist of the following terms: the kinetic energy $\hat{T}$ operator, the electron-electron interaction potential $\hat{V}$ and an external applied potential $\hat{V}_{ext}$ which includes also the electron-nuclei Coulomb interaction [46,47,48,49]. Eq.3.13 is taken into account the decoupling of the electronic and ionic movements (the Born-Oppenheimer approximation). However, the electron-phonon excitations are excluded and nuclei coordinates are considered as only a parameter in this equation. The Hohenberg-Kohn theorem was the first to proof the following two objectives: there is a one-to-one correspondence between the electron ground-state density and the many body wave function of interacting electrons, which means that the ground-state electron density is uniquely determined by the external potential.

$$N(r) \rightarrow |\psi[n]\rangle \text{ and } n(r) \rightarrow V_{ext}(r) \qquad (3.14)$$

The ground state solution of the Schrödinger equation is deduced by minimizing the expectation value of the total energy by the use of the Raleigh-Ritz variation principle [50,51,52]. The iterative cycle of minimization will be continued until self-consistency is accomplished with respect to a trial wave function. The minimization using the electron-density reaches the ground state energy via the relations in Equation 3.15,

$$\mathrm{E_o} = \min_{\psi} \langle\psi|\mathrm{T+V+V_{ext}}|\psi\rangle = \min_{\mathrm{n(r)}} \mathrm{E\,[n(r)]} \tag{3.15}$$

where

$$\mathrm{E[n] = T[n] + V_H[n] + E_{xc}[n] + V_{ext}[n]} \tag{3.16}$$

$T[n]$ is the kinetic energy functional for non-interacting electrons and $\mathrm{V_{ext}[n]}$ is the functional of the external potential. The Hartree energy $V_H[n]$ which describes the classical Coulomb energy of electrons is given by

$$\mathrm{V_{H[n]}} = \frac{1}{2}\int \mathrm{drdr'}\frac{\mathrm{e^2}}{4\pi\epsilon_0}\frac{\mathrm{n(r)n(r')}}{|\mathrm{r-r'}|} \tag{3.17}$$

where e is the elementary charge and ϵ_0 is the dielectric constant. The exchange-correlation energy$E_{xc}[n]$ is included in the total energy as a purely quantum mechanical interaction. The accuracy of DFT strongly depends on the proper determination of this exchange-correlation energy and functional, respectively. Generally this exchange correlation functional is unknown and approximations are needed. The advantage of the functional approach is that $E_{xc}[n]$ only depends on the three dimensional charge density. The electron-density of *N* independent electrons is expressed as

$$\mathrm{N(r)} = \sum_{\mathrm{i=1}}^{\mathrm{N}} |\varphi_\mathrm{i}(\mathrm{r})|^2 \tag{3.18}$$

The $\varphi_i(r)$ are selected to be orthonormal to each other: $\langle\varphi_i|\varphi_j\rangle = \delta_{ij}$. Furthermore, the variation of the energy functional $E(n)$ leads to a set of Kohn-Sham equations [45], which are equivalent to the many-electron problem:

$$\left[-\frac{\hbar^2}{2m}\nabla^2 + V_{eff}(r)\right]\varphi_i(r) = \varepsilon_i(r)\varphi_i(r) \tag{3.19}$$

where m is the mass of an electron and ε_i are the eigenvalues of the Kohn-Sham equations. Furthermore the effective potential, V_{eff}, is given by:

$$V_{eff}(r) = V_H(r) + V_{xc}(r) + V_{ext}(r) \tag{3.20}$$

The exchange-correlation potential $V_{xc}(r)$ is given by the functional derivative of the exchange-correlation energy with respect to the electron density,

$$V_{xc}(r) = \frac{\delta E_{xc}[n(r)]}{\delta_n(r)} \tag{3.21}$$

By solving the Kohn-Sham equations self-consistently one gets a set of wave functions φ_i and Kohn-Sham eigenvalues ϵ_i. Self-consistency means that from an initially guessed electron density, the eigenfunctions φ_i are calculated as solutions of the Kohn-Sham equations and in the following iterations the newly calculated charge density is inserted in the Kohn-Sham equations. This procedure is repeated until the converged charge density is obtained which then leads to the ground state energy. Mixing new and old charge density can accelerate the convergence significantly. Advanced mixing techniques, like the modified Broyden's method [53], can speed up the convergence by utilizing more than the charge density of the electronic step and damping spurious Fourier components of the intermediate charge density.

The Kohn-Sham equations yield a double counting of the electron-electron interactions, when one considers the sum of single-particle Kohn-Sham eigenvalues as total energy. By removing the over-counted energies one gets the exact ground state energy of the system:

$$E[n] = \sum_{i=1}^{N} \epsilon_i - \frac{1}{2}\int dr V_H(r)n(r) - \int dr V_{xc}(r)n(r) + E_{xc}(n) \tag{3.22}$$

Therefore the eigenvalues of the Kohn-Sham equation are not the energies of single electron states but the derivatives of the total energy with respect to the occupation numbers of these states [54].

3.9.2. Exchange-correlation functionals

The major problem with DFT is that the exact functionals for exchange and correlation E_{xc} are not known except for the free electron gas. A simple approximation of this functional is the local density approximation (LDA) [45]. LDA hypothesis could be applied to the limiting cases of a slowly varying density and very high densities.

$$\mathrm{E_{xc}(n)} = \int \mathrm{dr\, n(r)\varepsilon_{xc}[n(r)]} \tag{3.23}$$

Here $\varepsilon_{xc}(n)$is the exchange and correlation energy per particle of a homogeneous electron gas with density *n*. Thus the LDA exchange-correlation potential is fully localized which means that it depends only on the density at position *r*:

$$\mathrm{V_{xc}^{LDA}} = \frac{\partial}{\partial \mathrm{n}} \mathrm{n\varepsilon_{xc}(n)}\Big|_{\mathrm{n=n(r)}} \tag{3.24}$$

The LDA exchange-correlation itself can be obtained using an interpolation scheme between analytic asymptotic behaviors and intermediate results based on quantum Monte Carlo calculations of the homogeneous electron gas [55]. Furthermore, the LDA satisfies important sum rules for the electron-hole pairing. Surprisingly, in spite of the inexact representation of the inhomogeneous electron gas, LDA has been successful for various bulk and surface problems [56]. LDA yields relatively reliable lattice constants and ionic configurations, but in fact the reasons for this good accuracy are not fully understood.

The attempts to improve DFT by using a Taylor expansion of the exchange-correlation energy $\varepsilon_{xc}(n)$ in the density has not been successfull since it violates the sum rule for the exchange-correlation hole [46,57,58]. The GGA exchange-correlation energy [59,60,61], expressed as:

$$\mathrm{E_{XC}[n]} = \int \mathrm{drn(r)\varepsilon_{xc}(n(r), |\nabla n(r)|)} \tag{3.25}$$

which includes the gradient of the density $|\nabla(n(r))|$ overcomes this problem. Calculations, using GGA, achieve chemical accuracy [61] for many chemical problems. There are still a number of failures in GGA in spite of the success of the functional of Perdew and Wang (PW91) [60,62] and Perdew-Burke-Ernzerhof (PBE) [61]. These are [61]: (a) wrong description of van der Waals forces, (b) insufficient electron affinities of negative ions, (c) underestimation of cohesive

energies, (d) underestimation of band gaps, (e) wrong long-range of the effective one-particle potential at large distances, (f) erroneous representation of anti-ferromagnetic insulators as metals. All results reported in this thesis have been calculated using the PW91 [60] and PBE [61] functional where the PBE is a simplification of PW91, which yields almost identical numerical results with a simpler formula from a simpler derivation.

3.9.3. Plane wave basis sets with special k-points

In the previous sections we have shown that a many-body problem can be transformed into a quasi-single problem (Eq.3.19). However, for solid systems this means that the solutions of the Kohn-Sham equations need to handle the dynamics of an infinite number of non-interacting electrons in a static high-dimensional potential. By using Bloch's theorem one can simplify the system from an infinite number to a finite number of electrons within a single primitive unit cell [61]. In the case of a periodic system the obvious choice is to expand the wave function in a discrete plane wave basis set:

$$\varphi_{k,j}(r) = \sum_{G} c_{j,k+G} \exp\left[i(k+G)\cdot r\right] \tag{3.26}$$

where G is the reciprocal lattice vector, k is restricted to the first Brillouin zone and j is the band index. Because the computational power is restricted and it is impossible to handle an infinite number of plane waves one needs a truncation at each k point, set by an energy-cutoff:

$$E_{cutoff} = \frac{\hbar^2}{2m} |k+G|^2 \tag{3.27}$$

By enlarging E_{cutoff} one can control the quality of the calculations. The cutoff-energy is not the only parameter which influences the convergence. Also the size of the supercell is an important factor. The reason is that the values were calculated with VASP (Vienna ab-initio simulation package) and its plane wave basis set is periodic in all three space directions. If the super cell is too small, neighboring molecules interact strongly with each other. In the case of a cutoff energy of 400 eV a side length of 20 Å is enough that the system is converged. For comparison in the case of a cutoff energy of 600 eV a side length 15 Å is already enough.

The electronic wave functions will be almost identical when the k points are very close together. Hence the electronic wave function over a region of k space can be represented by the wave function at a single k point. Hence the calculation of the electrostatic potential requires only a finite number of electronic states at a finite number of k points, and this electrostatic potential together with the external potential then determines the total energy of the system. Thus the total energy of solid systems per unit cell is represented by:

$$\mathrm{E} = \langle \mathrm{H} \rangle = \frac{1}{\mathrm{V}} \sum_{\mathrm{i}} \int_{\mathrm{v}} \mathrm{dk} \mathrm{H_i(k)} \mathrm{f}\big(\epsilon_{\mathrm{i}}(\mathrm{r})\big) \approx \frac{1}{\mathrm{V}} \sum_{\mathrm{k}} \mathrm{H_i(k)} \mathrm{f}\big(\epsilon_{\mathrm{i}}(\mathrm{r})\big) \tag{3.28}$$

where $\langle H \rangle$ is the expectation value of the Hamiltonian, V the volume of the reciprocal unit cell, $f_i\big(\epsilon_i(r)\big)$ a weight factor and i is the band index. One can improve the accuracy of the discrete approximation to the Brillouin zone integration by the usage of broadening methods (Methfessel-Paxton smearing [63]) or an improved interpolation scheme (the linear tetrahedron method [64]). Interpolation methods require more than one k point to be used in each direction. If one handles surface science problems one k point in the direction of the surface normal is enough due to the fact that there is no periodicity and therefore no band dispersion in this direction.

By employing Bloch's theorem and a plane wave basis set, the Kohn-Sham equations Eq. (3.19) are transformed to,

$$\sum_{\mathrm{G'}} \left[\frac{\hbar^2}{2\mathrm{m}} |\mathrm{k} + \mathrm{G}|^2 \delta_{\mathrm{G,G'}} + \mathrm{V_{eff}(G - G')} \right] \mathrm{C_{i,k+G'}} = \varepsilon_{\mathrm{i}} \mathrm{c_{i,k+G}} \tag{3.29}$$

where the kinetic energy $\frac{\hbar^2}{2m}|k+G|^2$ is diagonal and $V_{eff}(G-G')$ is the Fourier transform of the effective potential. By a diagonalization of the Hamiltonian matrix of Eq.3.29 the eigenvalues ε_i can be obtained. The chosen energy cutoff determines the size of this matrix. Modern iterative methods avoid the direct diagonalization when trying to find the electron state minimum [65,66].

In the Vienna ab initio simulation package (VASP) [67,68] the Kohn-Sham equations are implemented as follows: the wave function is developed in plane waves on a finite k point mesh, and the resulting Hamiltonian is iteratively solved either by a sequential conjugate gradient (CG) minimization [69,70] or by a residual minimization method (RMM) [66,71] using a direct

inversion in the iterative subspace. By the Hellman-Feynman theorem [72] the force F_I on an ion at position R_I can be computed,

$$F_I = -\frac{dE}{dR_I} = -\frac{\partial E}{\partial R_I} \tag{3.30}$$

as derivatives of the basis set with respect to the position of the ion, the so-called Pulay-forces, happen to cancel each other for a plane wave basis set [56]. This allows for an efficient and accurate geometry optimization.

3.9.4. Pseudopotential approximation

In order to obtain smoothly varying wavefunctions and potentials so called pseudo-potentials are introduced. The concept of pseudopotentials is based on the observation that the chemical properties of most atoms are determined by their valence electrons [58]. Therefore, it is desirable to replace the core electrons together with the strong ionic potential (pseudowaves are shown in Fig.3.15). The starting point for the generation of pseudopotentials is an all-electron calculation for the isolated atom.

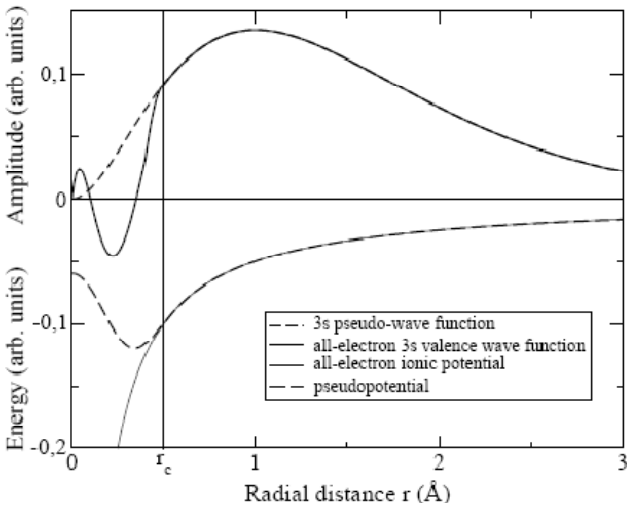

Figure 3.15: A schematic illustration of the difference between the all-electron and pseudo *3s* wave function and their corresponding potentials [58].

The pseudopotential and pseudo wave function are identical to the true potential and wave function outside the core radius, r_c. One can see that the nodes of the true wave function are removed inside the core radius but at the same time the norm of the wave function and with it all scattering properties of the full system are preserved. The general form of norm-conserving pseudopotentials is given by

$$V_{pseudo}(r) = \sum_{l,m} |Y_{lm}\rangle\, V_l(r) \langle Y_{lm}| \tag{3.31}$$

where $|Y_{lm}\rangle$ denotes spherical harmonics. It is called semi-local since it is local in the radial part and non-local in the angular part. The implementation of a plane wave basis in the pseudopotential approach was first done by Troullier and Martins [73] and Rappe et al. [74]. The accuracy of the pseudopotential calculations is only determined by the energy convergence of the valence electrons, since core electrons are not directly considered.

One can achieve a significant reduction of the computational effort by maintaining an accurate description of most systems by the use of norm-conserving pseudopotentials. In the case of palladium, the number of electrons is reduced from 46 to the 10 d electrons [48]. Furthermore, by giving up the norm conservation one can reduce the computational effort. The first approach was suggested by D. Vanderbilt [75,76] and is implemented in VASP [77]. But this ansatz violates charge conservation. To overcome this problem the full, norm-conserving charge density has to be reconstructed by the introduction of an overlap matrix derived augmentation charge in the core region.

It has to be mentioned that the pseudopotential is constructed from an exact all electron calculation of the free atom [48]. The chosen core radius influences the transferability of the pseudopotential to molecular or bulk systems and has to be verified. Further, the exchange-correlation functional has to be the same when constructing and applying the pseudopotential approximation to avoid significant errors [78].

3.9.5. The supercell approach

Due to Bloch's theorem and the usage of a plane wave basis set the considered problem becomes periodic in all three spatial dimensions. For bulk metal calculations, this is naturally satisfied. By introducing a surface, however, periodicity in one direction is removed. Assuming the surface is normal to the *z* direction, one would have to deal with a semi-infinite bulk region and a semi-infinite vacuum region along the *z* axis with periodicity only preserved in the *x*-*y* plane [48,58,79].

In the so-called slab approach, however, one replaces the semi-infinite metal by a slab with two surfaces and a finite number of layers. By doing so, one obtains a two-dimensional lattice where the periodicity is given by the surface unit cell. To recover three-dimensional periodicity, the slab is now repeated in the *z* direction by adding a sufficiently large vacuum region in between them as illustrated in Fig. 3.16. This allows the computationally efficient expansion of the wave function in a plane wave basis set even for a non-periodic surface problem.

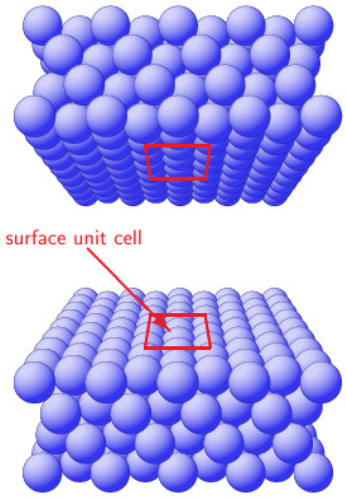

Figure 3.16: Illustration of the supercell approach, in which surfaces are represented through an infinite array of slabs [58].

However, one has to check that this artificial supercell is still close enough to the physical reality: The vacuum region must be large enough (≥10 Å) to separate both surfaces of the slab and to

avoid any interactions of opposing surfaces or adsorbates. For example, the convergence of the work function for Cu(110) requires a five layer Cu slab with 12 Å of vacuum layer.

Moreover, the slab has to be thick enough to accurately model bulk states and any surface relaxations. For low-index metal surfaces, four or more layers are already sufficient to achieve convergence. Finally, the size of the surface unit cell has to be chosen such that it either corresponds to known experimental coverages or is large enough to exclude any lateral interactions between adsorbates.

3.9.6. Geometry relaxations

A substrate is constructed by stacking atomic layers with the bulk lattice constant. For close packed (111) and (100) surfaces of face centered cubic (fcc) crystals, 4 or 5 layers are already sufficient for converged results. The rather open surface (110) requires also only 5 atomic layers. Since the slabs are separated in z-direction so that there is no interaction, only one *k*-point along this direction is required. However, the ideal bulk positions are no longer stable at a surface. At the surface of a solid the electronic structure and charge density are strongly modified. Considering the charge density of metal surfaces, the surface electron distribution is much smoother than in the bulk. This Smoluchowski smoothing [80] leads to a rather uniform distribution of the charge density thus lowering the kinetic energy of the surface electrons. As a result of the surface charge density redistribution, the ion cores experience inward forces to the bulk. For a realistic slab model, the surface ion relaxation is included by computing the ionic forces by the Hellmann-Feynman theorem. In Cu substrates, the relaxation of the upper-most ions affects the ion positions by only a few hundredth of an Angstrom. The shift of the second layer atoms is generally smaller than in the first layer.

3.9.7. Surface energies of clean surfaces

Surfaces can be assumed to be created by cleaving an infinite solid. This requires energies, otherwise a crystal would cleave spontaneously. Surface energies γ of a monoatomic solid at 0 K can be calculated according to [81]:

$$\gamma = \frac{1}{2A}(E_{slab} - N \cdot E_{bulk}) \quad (3.32)$$

Where E_{slab} is the total energy of the slab per supercell with N atoms, E_{bulk} is the bulk cohesive energy per atom, A is the surface area in the supercell. Typically 4 layers for a (111) and five layer for a (100) surface are sufficient in slab calculations.

3.9.8. Adsorption energies

The DFT total energy *E[n]* is used to determine the adsorption energy E_{ads} which is defined as the total energy difference between the adsorbate system and the sum of the clean substrate and the gas-phase atom or molecule. In molecular non-dissociative adsorption, the adsorption energy is defined as

$$E_{ads} = E_{adsorbate} - (E_{slab} + E_{mol}) \quad (3.33)$$

For many closed-shell molecules, it corresponds simply to the physisorption energy, and in most case this will be underestimated in GGA. In the case of open-shell molecules, e.g. CO, Eq.3.33 gives the chemisorption energy of the molecule. However, for dissociative adsorption, e.g. of hydrogen, the adsorption energy per atom includes the bond breaking of the gas-phase molecule:

$$E_{ads} = E_{slab+H} - \left(E_{slab} + \frac{1}{2}E_{H_2}\right) \quad (3.34)$$

Chapter IV

4. Methanol adsorption on Cu(110) and on Cu(110)-(2×1)O stripe phase

Copper, one of the most extensively used metals in the history of civilization, is an important material in modern industry. Copper used as a catalyst is frequently applied in reactions, such as methanol synthesis gas shift reaction and alcohol dehydration/dehydrogenation. Methanol is of particular interest as a means of hydrogen storage in the context of fuel cell technology. In this chapter, I present integral and angle resolved thermal desorption spectroscopy data using methanol adsorption and oxidation on clean and oxygen covered Cu(110 surfaces. In addition to that the interaction of methanol on the same surfaces has been investigated using reflection absorption infra red spectroscopy (RAIRS). As a new surface science tool, reflectance difference spectroscopy (RDS) has been used to perform a real time measurement on the adsorption and reaction of methanol.

4.1. Introduction

The interaction of methanol with low-index copper surfaces has been a model system for the study of alcohol adsorption on metal surfaces, These studies were also motivated by the significant role copper plays in the catalytic synthesis and oxidation of methanol [82,83]. Especially, the influence of oxygen on a Cu(110) surface on the methanol adsorption and reaction rate has attained considerable interest [5,84,85,86,87]. The sticking coefficient for methanol can be increased by more than an order of magnitude due to oxygen [5,84]. Oxygen on Cu(110) forms a special surface oxide by nucleation and aggregation of Cu–O added rows, resulting in a (2×1) superstructure [88,89]. At 0.25 ML of oxygen the so called Cu-CuO stripe phase forms, which consists of well ordered stripes of equidistant copper oxide and clean copper areas,

separated by about 6 nm [90]. This self-assembled surface has attained considerable interest recently as a template for nanostructured thin films [91].

Here we present a detailed and systematic study of the influence of oxygen on Cu(110) on the methanol adsorption and the subsequent reaction products by using integrated/angle resolved thermal desorption spectroscopy, reflection absorption infra red spectroscopy and reflectance difference spectroscopy. In particular, we concentrate on the specific Cu-CuO stripe phase which forms after adsorption of 0.25 ML of oxygen. The results were published in reference [3].

4.2. The (2×1) Cu-O stripe phase

For the preparation of the Cu-CuO stripe phase, the clean Cu(110) sample surface (with a (1x1) LEED pattern in Fig.4.1a) was dosed with oxygen at 550 K to yield a coverage of 0.25 ML. This is half of the saturation layer as determined by Auger electron spectroscopy, which is correlated to 0.5 ML of oxygen, according to the literature [90]. The formation of a (2x1) superstructure for the 0.25 ML and 0.50 ML (oxygen saturated) oxygen covered surfaces was observed by LEED (in Fig.4.1b,c). A schematic drawing of the Cu(110)-(2x1) stripe phase is depicted in Fig. 4.2.

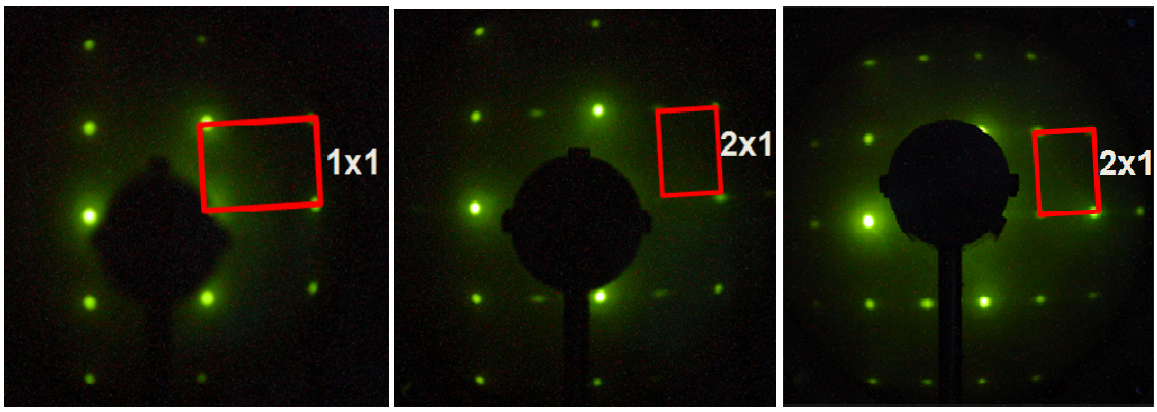

Fig.4.1: LEED pattern of a) a (1x1) clean Cu(110), b) a (2x1) Cu(110)-0.25 ML oxygen stripe, c) a (2x1) Cu(110)-0.50 ML oxygen surfaces. U_B=135 eV.

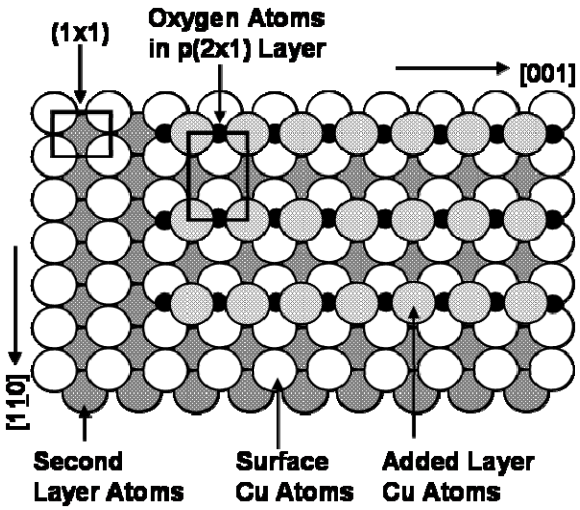

Fig.4.2: A model drawing of the added row (2x1) oxygen structure on Cu(110), leading to the Cu-CuO stripe.

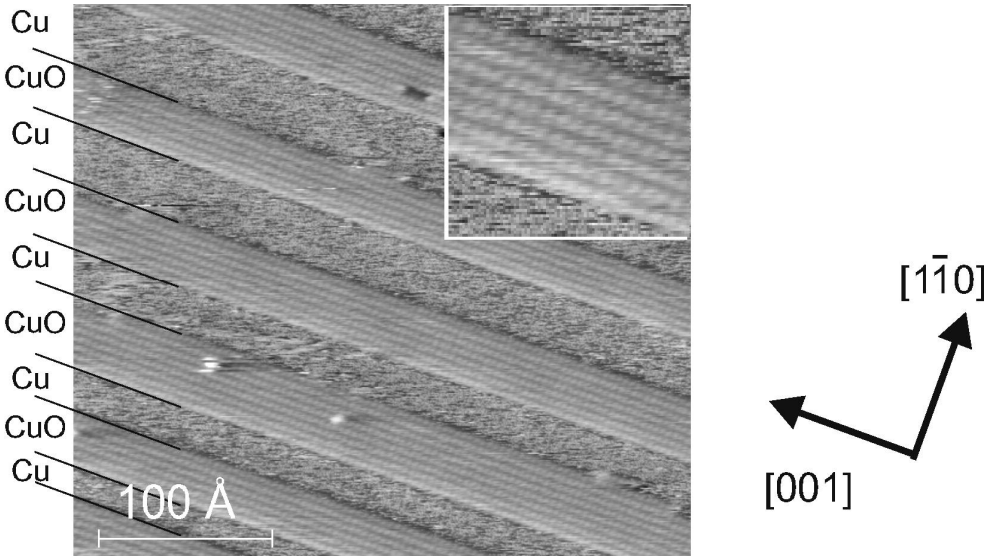

Fig. 4.3: STM image of a Cu(110)-(2×1)O striped surface after adsorption of about Θ_o=0.25 ML oxygen at 500 K. The insert shows a more close view of CuO. The [001] substrate azimuth and the Cu and the Cu(110)-(2×1)O stripes are indicated in both images [91].

The Cu-O stripe phase provides an almost ideal template to study the adsorption properties of molecules. Its structure is quasi one-dimensional and extremely well ordered. It is composed of structurally and chemically distinct Cu and Cu-O domains. The STM image, in Fig. 4.3, shows a long-range ordered nanostructured surface with the Cu(110)-(2×1)O stripe phase. The stripe phase consists of elongated Cu(110)-(2×1)O islands (stripes) separated by clean Cu(110) areas. By varying the oxygen coverage Θ_0 between 0 ML and 0.5 ML (the (2×1) saturation value) the width of the Cu-O stripes can be tuned from 2.2 nm up to >10 nm [91].

4.3. Influence of oxygen on methanol adsorption

Multiplexed thermal desorption spectra for the reaction products after methanol dosing of 12 Langmuir (L) at 190 K on a clean, a 0.25 ML (stripe phase) and a 0.5 ML oxygen covered Cu(110) surface are shown in Fig. 4.4a,b,c. The mass spectrometer has been tuned to the masses m = 2 (hydrogen), m = 18 (water), m = 30 (formaldehyde), m = 32 (methanol) and m = 44 (carbon dioxide). More masses, in particular of cracking products, have been measured but will not be displayed since they do not yield additional information. As already outlined in the literature, the sticking coefficient for methanol is quite small on the clean and the fully oxygen covered Cu(110) surface, but rather high on a partially oxygen covered Cu(110) surface. On the clean surface (Fig. 4.4a), methanol shows two desorption peaks at about 270 K and 320 K. At 320 K formaldehyde also desorbs, which is clearly not a cracking product of methanol but a true reaction product. (In the gas phase spectrum of methanol the mass m = 30 is only about 10% of mass m = 32). A small hydrogen desorption peak at about 340 K is also observed, whereas the small m = 2 peak at 270 K is the cracking product of methanol. No significant water and carbon dioxide desorption can be observed.

The desorption spectra after exposing a 0.25 ML oxygen covered Cu(110) surface (stripe phase) to methanol are depicted in Fig. 4.4b. In this case three methanol peaks can be observed, at 240 K, at 270 K and at 340 K. The largest signal in the multiplexed mass spectrum is formaldehyde at 340 K. The broad m = 30 peak around 250 K is partially the cracking product of methanol. In addition to hydrogen at 345 K, in the case of the oxygen covered copper surface also desorption of water around 250 K and of carbon dioxide at 440 K can be observed.

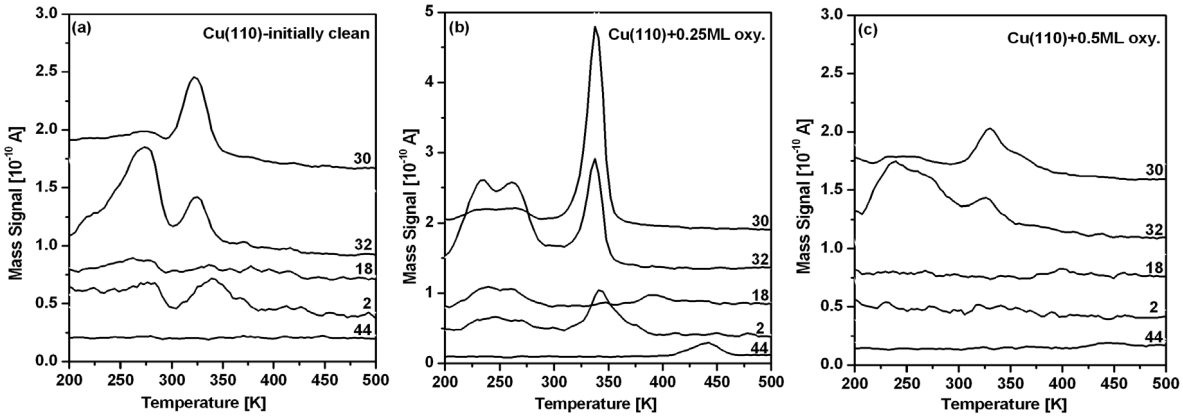

Fig. 4.4a, b, c: Thermal desorption spectra for different reaction products after dosing (a) clean Cu(110), (b) Cu(110)+ 0.25 ML oxygen and (c) Cu (110)+ 0.5 ML oxygen covered surface with 12 L methanol at 190 K.

On the oxygen saturated Cu(110) surface (0.5 ML) the amount of adsorbed methanol is decreased again. Most of the methanol desorbs around 250 K, whereas the desorption peak at 330 K is quite small. The amount of desorbed formaldehyde is also quite small and the desorption peak shows a tail up to 370 K. No significant quantities of hydrogen, water and carbon dioxide can be seen in the spectra.

In addition we have performed equivalent measurements for larger methanol exposures to differentiate between the kinetics (sticking coefficient) and the energetics (saturation coverage). The data for 50 L methanol exposure are shown in Fig. 4.5a,b,c. The most interesting finding is that the desorption spectra after methanol exposure on the clean copper surface (Fig. 4.5a) are quite similar to that obtained from the 0.25 ML oxygen covered surface (Fig. 4.5b). This tells us that after this extended methanol exposure apparently oxygen has accumulated on the surface. We will address this point in more detail in the discussion section. A comparison between the 12 L and 50 L exposure on the 0.25 ML oxygen covered surface shows that all corresponding spectra are already qualitatively similar, but in the latter case all signals are larger by about a factor of 1.5. This is most probably an experimental artefact, caused by the decreased pumping speed for all the species after this high methanol exposure of 50 L. A similar argumentation can be made by comparing the desorption spectra after 12 L and 50 L methanol exposure on the 0.5

ML oxygen covered surface. In other words, on the 0.25 ML and 0.5 ML oxygen covered surface saturation of methanol exists already at or below 12 L exposure.

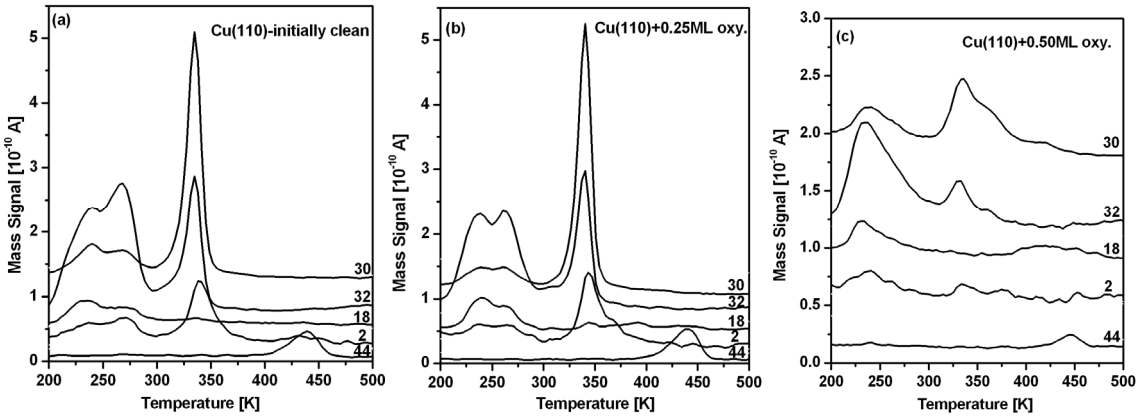

Fig. 4.5a,b,c: Thermal desorption spectra for different reaction products after dosing (a) clean Cu(110), (b) Cu(110)+ 0.25 ML oxygen and (c) Cu (110)+ 0.5 ML oxygen covered surface with 50 L methanol at 190 K.

For the special case of the Cu-CuO stripe phase we have also performed systematic desorption studies as a function of exposure in the low coverage regime, to obtain further information on the adsorption and desorption kinetics. In Fig. 4.6a,b,c sets of desorption spectra for methanol, formaldehyde and hydrogen are shown. In this particular case the adsorption temperature of 220 K was slightly higher than in the previous case due to experimental reasons, therefore the intensity of the low temperature part of the methanol spectra in Fig. 4.6a is somewhat reduced. However, this does not influence the main features in the spectra. The low temperature peak maxima for methanol decrease with increasing coverage and the FWHM is quite broad (30 K). On the other hand the methanol desorption peak around 350 K shifts to higher temperature with increasing coverage and the FWHM is extremely small (10 K). A similar feature is observed for the desorption spectra of hydrogen and formaldehyde: Peaks shifting to higher temperature with increasing coverage and a FWHM of less than 10 K.

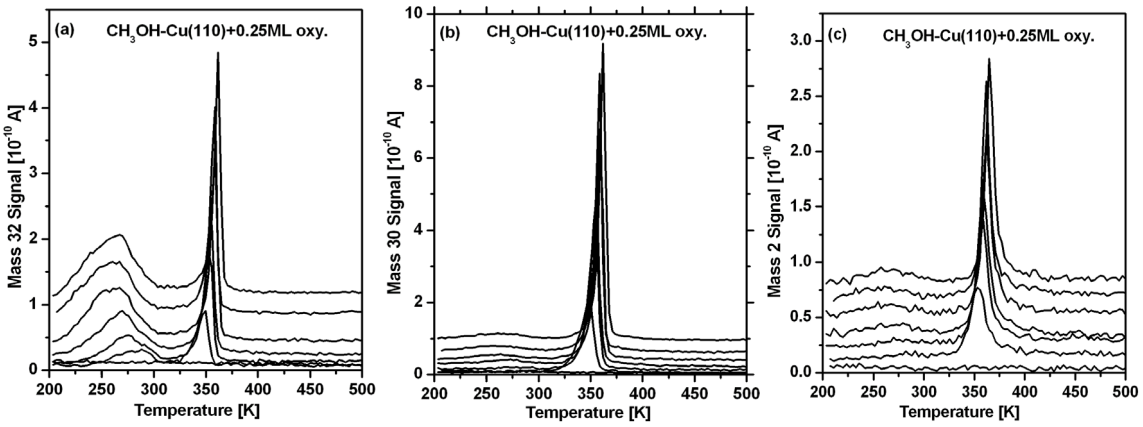

Fig. 4.6a,b,c: Thermal desorption spectra for (a) methanol, (b) formaldehyde and (c) hydrogen as a function of methanol exposure on Cu(110)+0.25 ML oxygen (stripe phase) at 220 K. The methanol exposures are 0.0, 0.15, 0.3, 0.45, 0.9, 1.5 and 3.0 L, respectively.

Comparing the methanol desorption peaks in the low temperature regime (200 K -300 K) for the three different oxygen pre-covered Cu(110) surfaces (Fig. 4.4a,b,c) one can observe some clear differences. There are actually two desorption peaks in this temperature regime, at 230 K and 270 K, which are well resolved and of similar height for the stripe phase surface. On the clean surface only the high temperature peak (270 K) is pronounced, whereas on the oxygen saturated surface the low temperature peak (T = 230 K) is dominant. Therefore we can correlate the desorption peak at 270 K to desorption from the clean parts of the Cu(110) surface, whereas desorption around 230 K originates from the Cu(110)(2x1) oxygen covered parts of the surface. Additional information can be obtained from the accompanied water desorption peaks in this temperature regime (Fig. 4.5). While in the temperature range of 270 K only little water desorbs, in the range of 230 K relatively more water desorption accompanies the methanol desorption. Although there exist conflicting statements in the literature concerning the state of methanol on the copper surface at 200 K, the majority of investigations indicate that methanol is already dissociated into methoxy and hydrogen at this temperature. In the case of adsorbed oxygen part of the separated hydrogen will form stable hydroxyl species on the surface. Therefore, the methanol peak at 230 K can be assigned to recombination of methoxy and hydrogen and at the same time recombination of hydrogen and hydroxyl to water takes place. The fact that both species desorb in a parallel fashion indicates that the rate limiting step for these processes is the diffusion of hydrogen to the

reactants. If no (or only little) oxygen is on the surface the recombinative desorption of methanol takes place at higher temperature (270 K) and no (or very little) water desorption can be observed. The higher desorption temperature for methanol may be either due to a lower diffusion probability for hydrogen or to a higher binding energy of methoxy on the clean surface.

Comparing the methanol and water desorption spectra in the same temperature regime after high methanol exposure of 50 L reveals further interesting results (Fig. 4.5). For the initially clean surface the methanol desorption peak at 270 K is still the most prominent, but in this case also a significant peak around 230 K shows up, which we have attributed to desorption from oxygen covered regions. Indeed, also water desorbs in this region. We therefore have to assume that during extended methanol exposure also some C-O bond breaking, in addition to the O-H bond breaking already takes place. This bond breaking might take place at steps or other defects on the surface. One could speculate that coadsorbed oxygen or water is responsible for this result. But as already mentioned in the experimental section our methanol gas phase is very clean. The strongest evidence for some C-O bond breaking, however, comes from Auger electron spectroscopy which showed some carbon remaining on the surface after the desorption process.

One interesting additional feature can be observed in the desorption trace for mass 30. We have so far assumed that the traces for m = 30 in the temperature range of 200 K – 300 K are qualitatively due to methanol cracking in the QMS. However, from the different height ratios for the double peaks of m = 30 and m = 32 in Fig. 4.6a we have to conclude that at least some of the m = 30 signal at around 240 K is actually due to desorbing formaldehyde. Indeed, formaldehyde adsorption/desorption studies on clean and oxygen covered Cu(110) by Sexton at al. [92] have shown that formaldehyde desorbs around 230 K. High resolution XPS studies by Steinrück et al. [87] also indicated the existence of some amount of formaldehyde after methanol adsorption on a clean copper surface at 100 K and subsequent heating to 220 K.

The common feature for the desorption peaks appearing in the temperature range of 340 K is their extremely narrow shape. The full width at half maximum (FWHM) for the methanol, formaldehyde and hydrogen peaks is about 10 K. “Normal” FWMH´s for recombinative desorption peaks in this temperature range are between 50 K and 70 K. Formally, the desorption peaks become narrower in case of attractive lateral interactions in the adsorbed layer. In this case the peak maxima should also shift to higher temperature with increasing coverage. This is exactly

the case for these species as one can see in Fig. 4.6a,b,c. Both, the methanol and formaldehyde, desorb exactly at the same temperature. The hydrogen spectra are slightly but clearly shifted to higher temperature with respect to the former species by about 10 K. Desorption of these three species therefore proceed in a concerted manner: For the more strongly adsorbed methoxy species, which remained on the surface after the reaction processes in the low temperature regime, the C-H bonds start to break. This leads to the reaction limited immediate desorption of formaldehyde around 340 K, since adsorbed formaldehyde on Cu(110) would already desorb at 220 K [92]. Some of the separated hydrogen can recombine with the methoxy species which also leads to immediate methanol desorption since adsorbed intact methanol also would already desorb far below 300 K. The remaining hydrogen on the surface can finally recombine to molecular hydrogen. This process is to some extent desorption limited since the desorption temperature for pure hydrogen recombination on clean Cu(110) is also in the same temperature range around 325 K [93]. However, comparing the shifted peaks in Fig. 4.6c with the non shifting desorption peaks for pure hydrogen recombination from Cu(110) [93], reveals again that hydrogen desorption is also mainly reaction limited in this case. The narrow shape of the desorption spectra can also be caused by an unusual pre-exponential factor for the desorption process, as sometimes observed when desorption goes along with a phase transition [94,95]. However, it is far beyond the scope of this work to analyse in detail the desorption kinetics in terms of desorption energy and prefactor for this complicated reaction process.

4.4. Methanol adsorption at around room temperature

As we have shown before the CO_2 desorption stems from a formate species on the surface. However, in this case also hydrogen desorption should be seen in the temperature region where CO_2 desorbs. In order to enhance this formate formation, methanol was dosed at 270 K on Cu(110)+0.25 ML oxygen stripe surface and a TDS experiment was done from 270 K to 500 K.

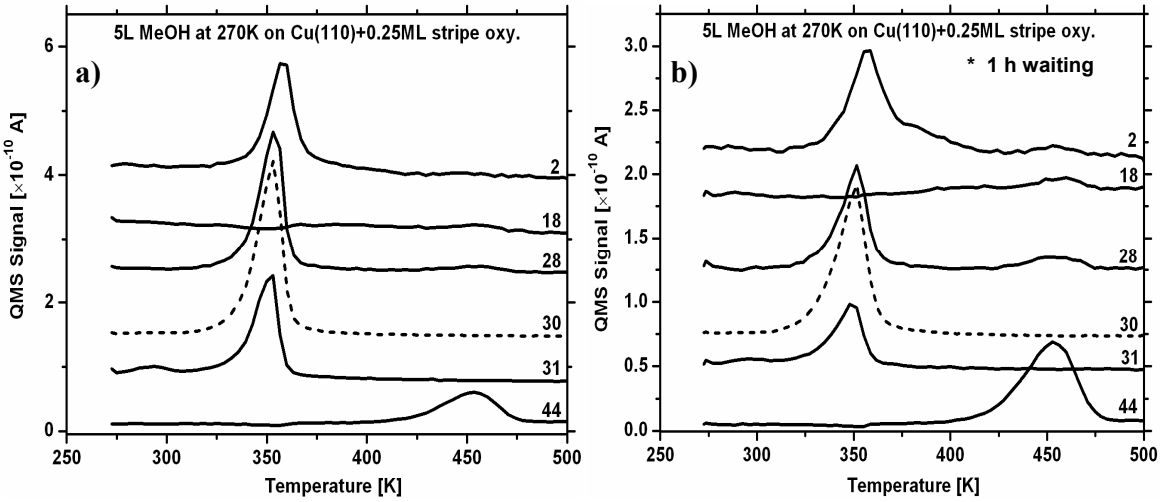

Fig. 4.7: (a) TDS obtained after adsorption of 5 L methanol at 270 K on oxygen precovered (0.25 ML) Cu(110). (b)TDS obtained after adsorption of 5 L methanol at 270 K on oxygen precovered (0.25 ML) Cu(110). In the latter case after the adsorption a waiting period of 1 hour at 270 K was used before desorption. The heating rate was 2 Ks^{-1}.

Fig. 4.7a shows that the subsequent TDS experiment reduces the amount of formaldehyde desorbing, while the amount of CO_2 desorption hardly changes. This indicates that the intermediate leading to CO_2 formation is stabilized by this experiment. In Fig. 4.7b the same experiment was done, but there was a waiting period of 1 hour at 270 K in UHV between methanol adsorption at 270 K and the TDS experiment. In this case the formaldehyde desorption is further suppressed and the amount of CO_2 formed increased slightly. In addition, one could detect a small hydrogen peak and some water desorption in the temperature range of the CO_2 desorption peak. These points will be discussed in more detail by using reflection absorption infra red spectroscopy (RAIRS) tool in section 4.6.

4.5. Angular distribution of the reaction products

As outlined in the experimental paragraph we have carried out angular distribution measurements of desorption species by shifting the sample in front of the QMS. In Fig. 4.8a,b the integrated and background subtracted peak areas for the relevant reaction products after adsorption of 50 L methanol on the initially clean Cu(110) surface are plotted for different sample displacements. In

addition, curves obtained from Monte Carlo simulations for the same geometrical arrangement by assuming angular distributions in the form of a $\cos^n\Theta$ function are inserted [3].

The low temperature methanol peak and the water peak, which are both observed around 250 K, exhibit a nearly cosine distribution (n = 1). The narrow desorption peaks which appear at 350 K show a much more forward focused angular distribution (formaldehyde: n = 3, methanol: n = 5, hydrogen: n = 7). The angular distribution for carbon dioxide, which takes place around 450 K, can be described by an exponent n = 2. However, from the experimental error bars and according to Fig. 2.5, the exponents n are only accurate within about Δn ±1. Furthermore, I would like to emphasize that the description of the angular distribution in form of a $\cos^n\Theta$ function is just a fit which is frequently used in the literature [23].

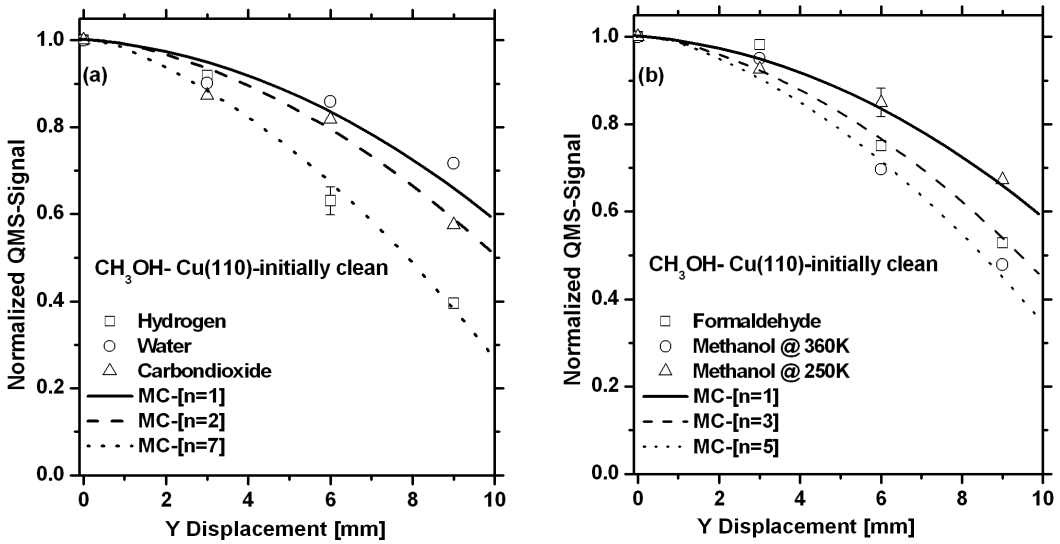

Fig.4.8a,b: Angular desorption distribution of different reaction products after exposing a Cu(110) surface to 50 L methanol at 190 K, as measured by sample displacement in Y direction (parallel to the Cu[001] direction). The lines are obtained from Monte Carlo simulations using different exponents n in the distribution function in form of $\cos^n\Theta$.

Comparable angular distribution measurements (Fig. 4.9a,b,c) were performed on the Cu-CuO stripe phase. The stripe direction is along the [001] direction of Cu(110), i.e. the vertical (Y) direction. The data points have been obtained in the same manner as described above. An oxygen

exposure of 3 L was used in this case, which already yields a quite high desorption signal. The sample was now displaced both in Y and X direction, in order to observe a possible anisotropy of the angular distribution.

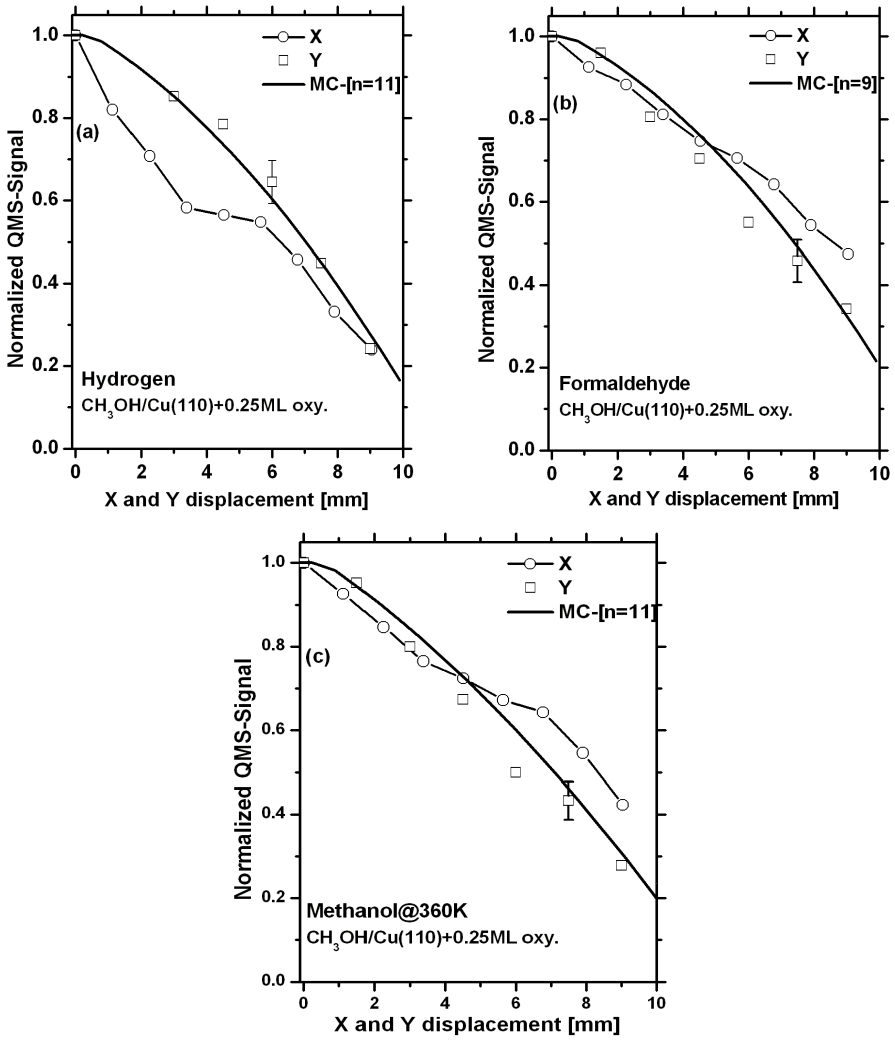

Figure 4.9.a,b,c: Angular desorption distribution of different reaction products after exposing the Cu-CuO stripe phase surface to 3 L methanol at 190 K, as measured by sample displacement in X direction (parallel to the [1$\underline{1}$0] direction) and Y direction (parallel to the Cu[001] direction). The smooth lines for the Y direction are obtained from Monte Carlo simulations using different exponents *n* in the distribution function in form of $\cos^n\Theta$. The data points for the X direction are connected to guide the eye.

We will just focus on the angular distribution for the species showing the narrow desorption peak around 350 K. Whereas for the Y direction the change of the signal with sample displacement corresponds roughly to a $\cos^{9\text{-}11}\Theta$ distribution, for the X direction a bimodal distribution seems to exist. In this case we have just connected the measured data points by lines to guide the eye. In this context we note that the data points are averages from several experimental sets. There exist still quite large error bars mainly due to the difficulties in preparing exactly the same oxygen coverage for the stripe phase. Please have in mind that for each data point the sample had to be cleaned and a fresh stripe phase with 0.25 ML oxygen had to be prepared always prior to methanol adsorption.

The angular distribution measurements on the reaction products (Fig. 4.8a,b) corroborate the peculiar features of the individual desorption peaks. Desorption of methanol and water in the low temperature regime (200 K – 300 K) from the initially clean surface exhibit a close to cosine distribution. The coverage dependence of the corresponding desorption peaks (shift to lower temperature with increasing coverage) and the FWHM of about 30 K show a quite "normal" behaviour for simple recombinative desorption. The three species which desorb around 350 K with the very small FWHM of 10 K and which exhibit peaks shifting to higher temperature with increasing coverage, show a much stronger forward focused angular desorption distribution. Formaldehyde desorbs with $\cos^3\Theta$, methanol with $\cos^5\Theta$ and hydrogen even with $\cos^7\Theta$. Such behaviour could be interpreted as being due to recombinative desorption via an activation barrier which involves an activation barrier for adsorption. That means, the energy level for the transition state of recombination is above the zero energy level for the free reaction product [96]. Such scenarios have been investigated experimentally and theoretically in detail for simple systems, like hydrogen on copper, etc. [93,97].

However, in our particular case this scenario seems to be too simple because several processes take place nearly simultaneously: At a surface temperature of about 300 K, after the first desorption peak of methanol and water has occurred, still some methoxy species are on the surface. Further temperature increase finally leads to C-H bond breaking at around 350 K. This leads to immediate desorption of formaldehyde and by recombination of the separated hydrogen with methoxy to methanol and/or to recombinative hydrogen desorption. Recent DFT calculations by Gross et al. [106] have shown that a high activation barrier of 1.6 eV exists in order to break the C-H bond of the methoxy species next to an adsorbed hydrogen atom, which

then leads to a desorbing formaldehyde molecule, leaving two hydrogen atoms on the surface. The energy of the produced formaldehyde molecule is still 1.2 eV above the zero energy level. This excessive energy leads inherently to a hyperthermal desorption flux and to a forward focused angular desorption distribution. We assume that part of this excess energy is also channelled into the other reaction products, namely methanol and hydrogen, which therefore also leads to a forward focused angular desorption distribution.

On the 0.25 ML oxygen covered Cu(110) surface the angular distributions of the reaction products show some distinct features (Fig. 4.9a,b,c). In this case the well defined stripe phase was prepared and a methanol exposure of 3 L was sufficient to obtain a high coverage. There is a clear difference in the angular distribution in X and Y direction. Whereas along the stripes (Y direction) the angular distribution shows a smooth change, equivalent to a distribution function of about $\cos^{9\text{-}11}\Theta$, in X direction a good fit with a $\cos^{n}\Theta$ function is not possible. The signal change with sample displacement in X direction shows rather a bimodal function, with a second signal maximum around 6-7 mm sample shift. This can be correlated with an additional angular distribution peaked around 20° off normal. This is a strong indication that some of the reaction/desorption proceeds at the border line between the CuO and Cu stripes, where the reaction products desorb inclined with respect to the sample surface normal. This result is not in contradiction with the observed shrinking of the (2x1) stripes in the [001] direction according to STM studies by Bowker et al. [82]. The removal of the oxygen from the stripe phase during thermal desorption takes place mainly in form of CO_2 desorption at 440 K, which shows a rather broad desorption distribution (n = 2). This has been checked by AES and LEED as a function of temperature.

4.6. RAIRS studies of methanol on clean Cu(110) and on Cu(110)- oxygen stripe phase

The interaction of methanol on Cu(110) and on the oxygen stripe phase on Cu(110) has also been investigated using reflection absorption infra red spectroscopy (RAIRS), in addition to thermal desorption spectroscopy (TDS). These systems have been investigated with several surface analytical tool in the past, as we have mentioned in Section 4.1. However, to the best of our knowledge only reference [92] performed vibrational spectroscopy on this surface. On the

Cu(100) surface more studies using reflection absorption infra red spectroscopy (RAIRS) have been published [98, 99, 100]. While most of the assigned frequencies are similar on Cu(110) and on Cu(100), there is a rather large difference in the ν-CO frequency of methoxy between the two surfaces (980 cm^{-1} on Cu(100) [98] and 1020 cm^{-1} on Cu(110) [92]).

RAIRS measurements were done using a Bruker IFS66v/S FTIR spectrometer and an external liquid N_2 cooled MCT detector attached to the same UHV system, as described earlier [101]. A grazing incidence angle of about 83° and a scan time of 15 min were used with a resolution of 4 cm^{-1}.

4.6.1. Adsorption of methanol on clean Cu(110) surface

As presented in Fig 4.5.a, methanol can adsorb on an initially clean Cu(110) surface using large exposure (about higher than 50 L) where TDS shows similar results with preadsorbed oxygen. In Fig. 4.10, RAIRS spectra are taken after methanol is exposed on the clean Cu(110) surface at two different temperatures 100 K and 200 K.

For the exposure of 10 L methanol at 100 K (lower curve in Fig 4.10), from TDS experiments it is known that a multilayer peak of methanol appears. The vibrational feature at 1050 cm^{-1} stems from the ν-CO stretching vibration of the methanol molecule and the two peaks at 2948 and 2832 cm^{-1} are the symmetric and asymmetric stretching vibrations of the CH_3 group, which was also assigned in the past [92].

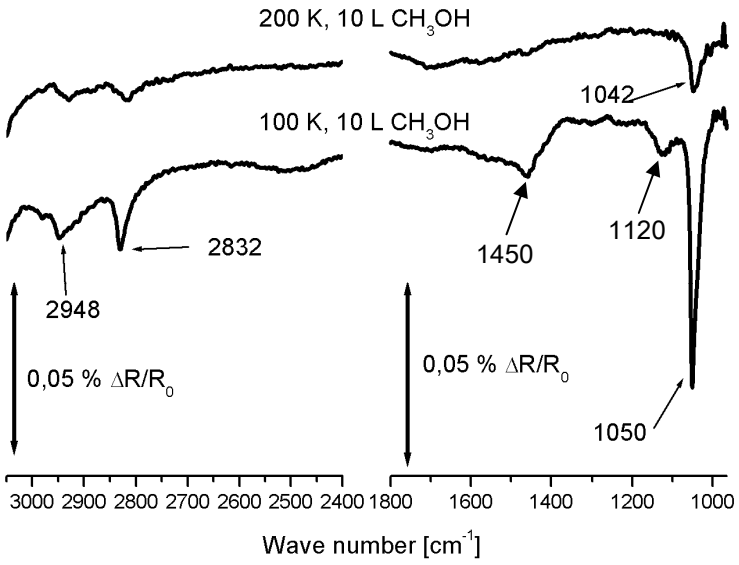

Fig.4.10. IR spectra of methanol after adsorption of 10 L methanol at 100 K and 200 K on Cu(110).

The peaks at 1120 and 1450 cm^{-1} have been reported to belong to the methyl rocking and methyl bending vibrations, respectively. The upper curve was obtained after 10 L methanol adsorption at 200 K. This leads to a submonolayer of methanol on the Cu(110) surface, since the sticking coefficient at this temperature is very small. One can again see the ν-CO frequency, which is shifted down to 1042 cm^{-1} and the ν-CH_3 frequencies are at the same positions as in the multilayer. The ν-CO vibration of methanol is in the same frequency range on Cu(110) as on Rh(111) and Pd(111) [102].

According to detailed DFT calculations, carried out by I. Bako [4], an adsorbed methoxy on a Cu(110) surface is energetically more favorable when it sits on a short bridge site (A and B), compared to the long bridge site (A_1 and B_1) of clean Cu(110) surface (Fig.4.11). Another observation in this calculation is that the C-H bonds of the CH_3 group are rather parallel to the surface in case of methoxy. More details about the calculation are given in reference [4].

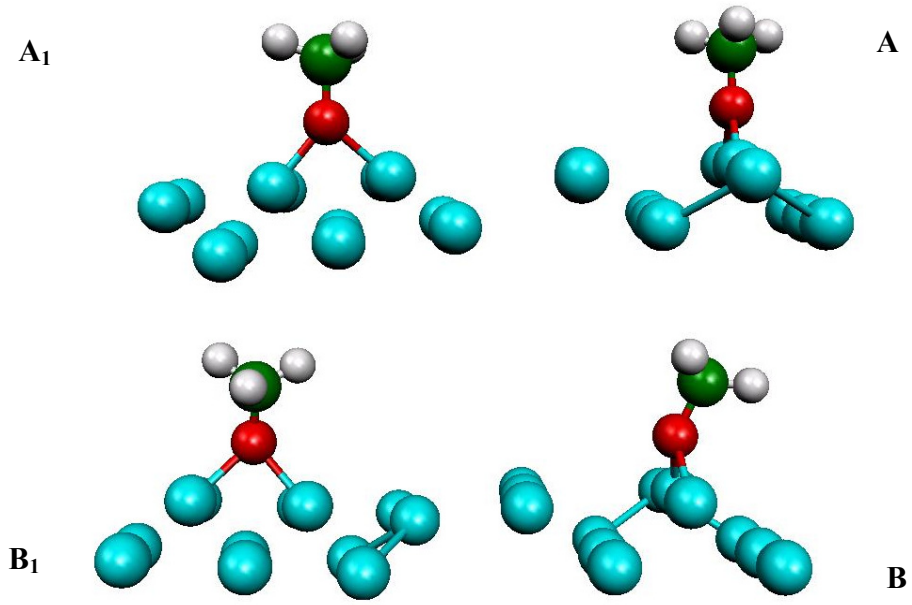

Fig.4.11. The four stable geometries of the methoxy species on Cu(110). A1 is methoxy on the long bridge site perpendicular to the surface, A is methoxy on the short bridge site perpendicular to the surface, B1 is methoxy on the long bridge site tilted to the surface and B is methoxy on the short bridge site tilted to the surface. Cu atoms are blue, carbon is green, oxygen red and hydrogen light grey [4].

4.6.2. Adsorption of methanol on Cu(110)-0.25 ML oxygen stripe phase

When oxygen is preadsorbed on the Cu(110) surface before methanol adsorption a much higher sticking coefficient for methanol is found [3,5]. This has been interpreted in terms of a much faster methoxy formation by a proton transfer from methanol to coadsorbed oxygen. However, when one compares the RAIRS spectra of methanol on Cu(110) in Fig. 4.10 to methanol on oxygen precovered Cu(110) in Fig. 4.12 one can clearly see that the ν-CO vibrations are the same in both cases, suggesting that the methanol on the oxygen covered Cu(110) surface does not react immediately to methoxy at the adsorption temperature. After adsorption at 100 K, which leads to a methanol multilayer, the RAIR spectra are the same on both surfaces. However, at an adsorption temperature of 200 K (meaning in the monolayer regime) there is a slight difference, as the CH_3 frequencies at 2830 cm^{-1} and 2948 cm^{-1} are much less intense on the oxygen precovered surface compared to the clean Cu(110) surface.

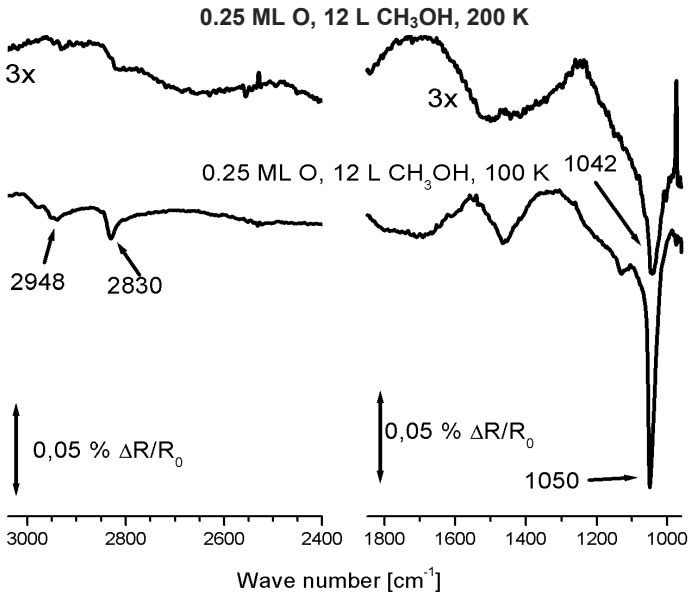

Fig. 4.12. IR spectra of methanol after adsorption of 12 L methanol at 100 K and 200 K on 0.25 monolayer oxygen on Cu(110). The positions of the CO and CH vibrations are given in the spectra.

In order to get more insight into the reactions going on the oxygen precovered copper surface experiments were designed to measure IR spectra as a function of surface temperature. After the adsorption of methanol on the 0.25 ML oxygen precovered Cu(110) surface at a temperature of 100 K, IR spectra were recorded in situ during the following thermal desorption experiment with a heating rate of 0.1 Ks^{-1} up to a temperature of 600 K. The measuring time for one spectrum was 70 seconds corresponding to 390 scan. Hence, every 7 K a new spectrum was recorded. The results are shown in Fig.4.13. Due to the adsorption temperature of 100 K one finds a quite large ν-CO peak, which stays constant up to about 125 K, when it starts to decrease rapidly up to about 175 K. This is due to the desorption of the methanol multilayer (see figure 4.13). With desorption of the multilayer the ν-CO signal shifts from about 1050 cm^{-1} to 1040 cm^{-1} (compare to figure 4.10). The ν-CO signal of the methanol monolayer seems to be constant from 175 K up to about 275 K (see figure 4.13). However, one has to keep in mind that methoxy on the short bridge site has the same ν-CO as methanol. This fact together with the decrease of the CH_3 frequencies shown in figure 4.13, suggests that in this temperature region the reaction starts by methoxy formation from methanol. In addition, at about 210 K a shoulder appears in the IR at

approximately 1020 cm^{-1} (see figure 4.13). This vibrational feature can be attributed to methoxy bound on the long bridge site according to the DFT results in [4].

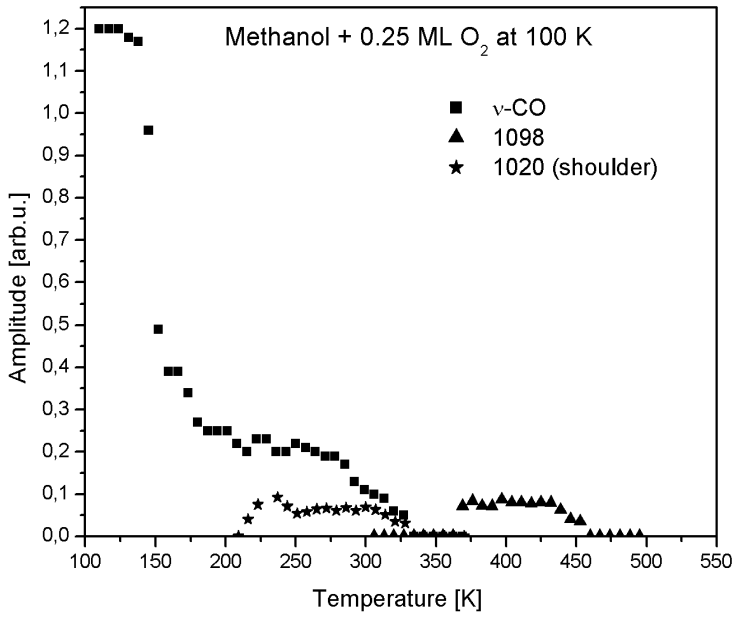

Fig.4.13. IR-peak intensities as a function of temperature from temperature programmed RAIRS experiments obtained with a heating rate of 0.1 Ks^{-1} after the adsorption of 12 L methanol at 100 K on oxygen precovered Cu(110). The intensities of the ν-CO frequency of methanol and methoxy (squares) and the vibrational features at 1020 (stars) and 1098 cm^{-1} (triangles) are shown as a function of the surface temperature.

The ν-CO signal of both methoxy species in the IR decreases and it disappears around 330 K with increasing surface temperature (Fig.4.13). At temperatures above 350 K a new vibrational feature at about 1098 cm^{-1} is found, which shows a constant small intensity up to about 430 K and then decreases again till it also disappears at about 450 K. The end of the methoxy signal in the RAIRS experiments (330 K) is at lower temperatures than the end of the thermal desorption of methanol and formaldehyde presented in Fig.4.4b (360 K). This difference is due to the two different heating rates (2 Ks^{-1} in TDS and 0.1 Ks^{-1} in the temperature programmed RAIRS experiments). One can see that the vibration at 1098 cm^{-1} seen in figure 4.13 is found in the temperature region after the formaldehyde desorption is finished (compare with Fig.4.4b). Therefore, it is unlikely that this vibration is due to formaldehyde. According to DFT calculations

the CO stretching vibration of formaldehyde would be around 1311 cm^{-1} [4], but we do not see a vibrational feature in this wavenumber range in our experiments. From comparison with the TPD data and the literature it would be more likely that the vibration at 1098 cm^{-1} is associated with a formate group as CO_2 desorption has been attributed to come from formate on the surface.

4.7 Adsorption of methanol on Cu(110) and Cu(110)-(2×1) O stripe phase studied by RDS

In this section, we present a real time reflectance difference spectroscopy (RDS) study of the adsorption and reaction of methanol on the clean Cu(110) surface and the Cu-CuO stripe phase composed of alternating Cu(110) and Cu(110)-(2×1)O stripes.

4.7.1. The Cu-CuO stripe phase investigated by RDS

A highly periodic arrangement of alternating Cu and CuO stripes has been shown in Fig.4.3. The STM image in Fig.4.3 corresponds to the case of half monolayer saturation θ_0=0.25. In the well ordered stripe phase the Cu and CuO stripes are separated by straight monatomic step edges running along the [0 0 1] direction.

Fig.4.14a shows the RDS spectrum recorded from the Cu(110)–(2×1) O surface, obtained after oxygen adsorption at room temperature followed by annealing to 500 K. In this case, all the oxygen adsorbates are dissociated and chemisorbed, additionally, the Cu(110) surface is reconstructed. Reflectance difference spectra recorded at 200 K from the well ordered Cu–CuO stripe phase with oxygen coverages θ_0 between 0 ML and 0.5 ML are plotted in Fig.4.14a. A pronounced peak at 2.1 eV can be clearly seen in the spectrum of the bare Cu(1 1 0) surface. This peak is attributed to three different contributions, namely optical transitions between surface states, surface modified bulk interband transitions and intraband transitions [103,104]. Among these, the surface state contribution is the dominant one and is extremely sensitive to the presence of surface defects and adsorbates [36]. Indeed, when the Cu–CuO stripe phase is formed after adsorption of oxygen, the RD signal at 2.1 eV decreases monotonously with increasing oxygen coverage θ_0. Plotting the RD intensity at 2.1 eV as a function of θ_0 determined by Auger electron spectroscopy (AES), one can see from Fig.4.14b that the RD signal decreases linearly with θ_0.

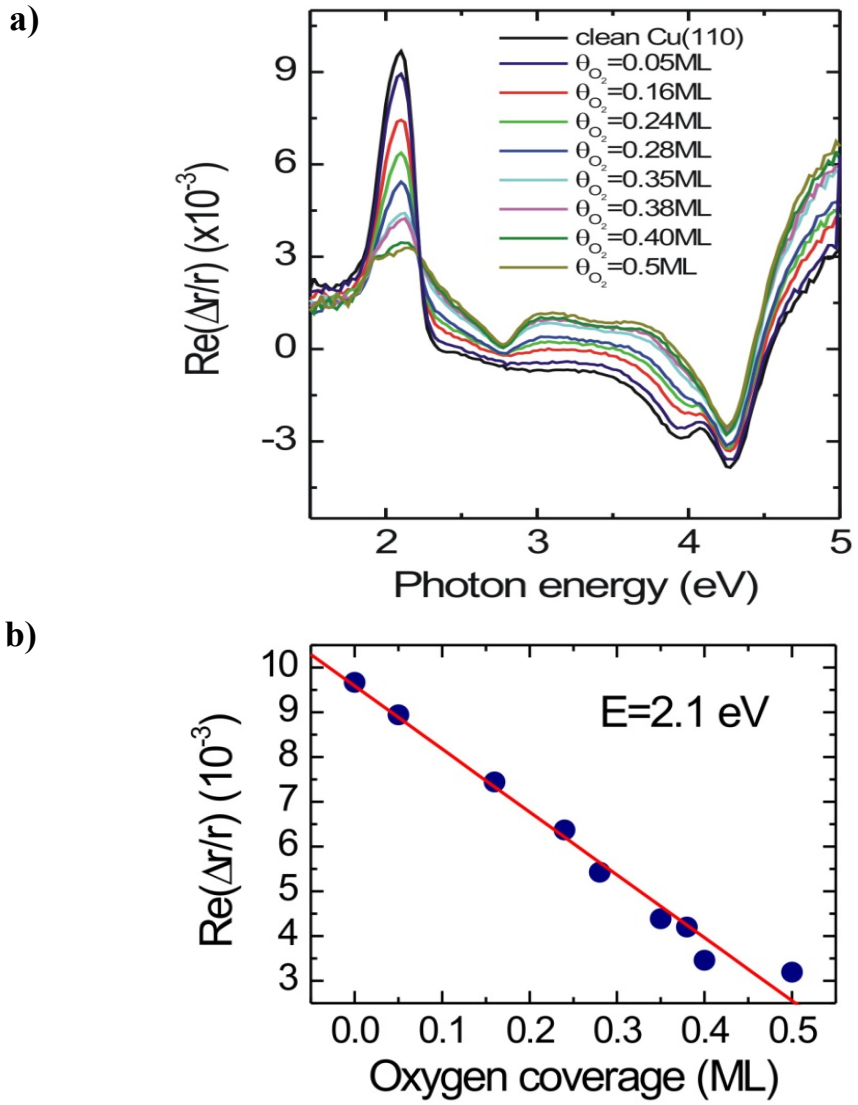

Fig.4.14. (a) Real part of RD spectra recorded from the Cu–CuO stripe phase for different oxygen coverages θ_O. (b) RD signal at 2.1 eV (filled circles) as a function of θ_O with a linear fit to the data (solid line). All measurements were performed at 200 K. The oxygen coverage θ_O was determined by Auger electron spectroscopy.

4.7.2. A real-time measurement of methanol adsorption

It is known from previous RDS measurements on Cu(110) that the optical anisotropy feature at 2.1 eV, which stems from the anisotropy of the surface state transition at the Y point of the Brillouin zone, is very sensitive to gas adsorption [5,105]. A real time measurement has been

performed to methanol adsorption on the Cu(110)–(2×1) O surface which is shown in Fig.4.15. The RD signal at 2.1 eV is recorded with a sampling time of 1 s during methanol exposure. The sample temperature was kept at 200 K during methanol exposure. For a clean sample surface, the RD signal at 2.1 eV decreases only very slowly and saturates at a total methanol dose of 50 L (inset in Fig. 4.15). This can be attributed to a very small sticking coefficient for methanol on the clean Cu(110) surface. However, it is evident from Fig. 4.15 that the sticking coefficient of methanol on the Cu-CuO stripe phase is about two orders of magnitude larger than on the bare Cu(110) surface.

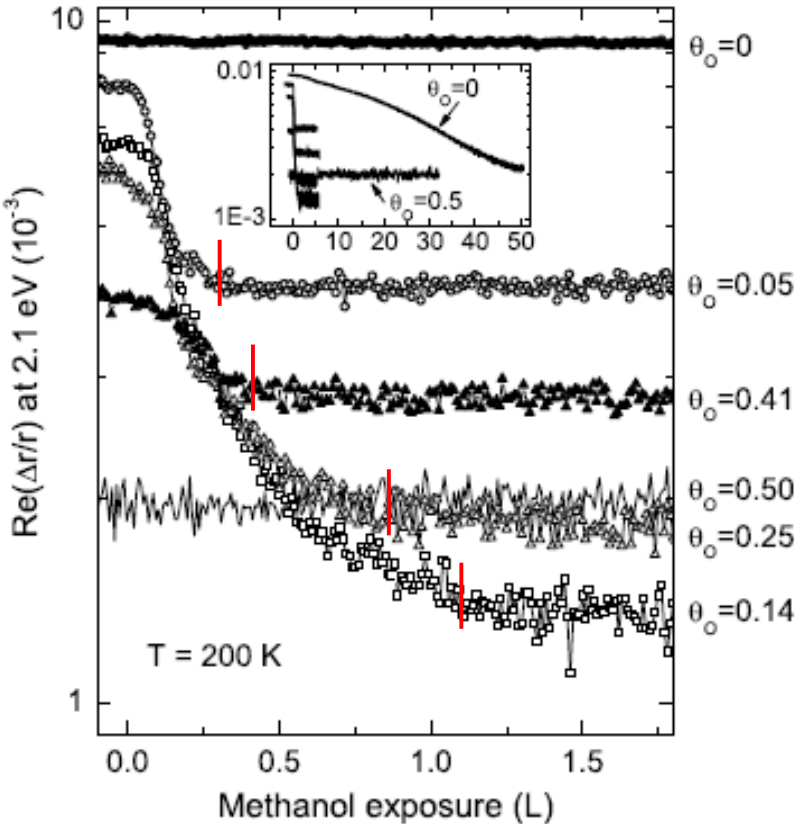

Fig.4.15. RD signal at 2.1 eV recorded during methanol adsorption at 200 K on the clean Cu(110) surface ($\theta_O = 0$) and on the Cu-CuO stripe phase with different oxygen precoverages of θ_O. The saturation of methanol exposure for each measurement is marked by the vertical lines. The inset shows the same curves displayed over a larger exposure range.

This result clearly evidences the promotor effect of oxygen on the Cu(110) surface reported previously [106]. Besides, the saturation exposure of methanol (M_{sat}), which is determined by the exposure where the RD signal of 2.1 eV becomes saturated, depends strongly but not monotonically on the initial oxygen coverage of the Cu-CuO stripe phase. Furthermore, the maximum coverage of adsorbed methanol is estimated to occur for an oxygen precoverage around θ_O=0.14.

Finally, on an oxygen precoverage of θ_O =0.5 corresponding to the fully oxygen covered Cu(110)-(2×1)O surface, the surface becomes fully inert and no change of the RD signal can be detected even after a methanol exposure of 30 L at 200K (inset in Fig. 4.15). This observation fully agrees with the previous methanol adsorption study [86] where the authors have demonstrated that below 330 K the fully saturated Cu(110)-(2×1)O surface is completely unreactive.

4.7.3. Consumption of oxygen upon adsorption/desorption of methanol

The reaction process of methanol at different stages was studied by RDS as shown in Fig. 4.16. The intensity around 2.1 eV for the initial Cu-CuO stripe phase decreases linearly with oxygen coverage, θ_O. After an exposure of 5 L of methanol on the stripe phase at 200 K, the RD signal drops further or is completely quenched, depending on the oxygen precoverage. The decrease of the RD signal at 2.1 eV upon methanol adsorption indicates a further reduction of the area fraction of the bare Cu surface. In fact, it is well known that at 300K upon adsorption on the Cu-CuO stripe phase, methanol molecules will react with the oxygen atoms, producing methoxy molecules which form a (5×2) superstructure on the initially uncovered Cu(110) areas [86,107,108]. The reaction can be expressed as:

$$2CH_3OH^{gas} + O^{ads} \rightarrow 2CH_3O^{ads} + H_2O^{gas} \qquad (4.1)$$

In this study, a weak (5×2) LEED pattern was also observed after 5 L methanol exposure on Cu-CuO at 200 K which was very unstable and quickly disappeared due to irradiation of the electron beam. The model proposed for the (5×2) methoxy formation involves a coverage of 0.4 of the methoxy molecules, i.e., each methoxy covers 2.5 unit cells of Cu(110) [107,108]. Therefore,

following the reaction stoichiometry in Eq. (4.1), it is clear that two methanol molecules will remove one oxygen atom from the (2×1)O stripes on the surface and increase the bare Cu(110) area by 2 unit cells. On the other hand, the formed two methoxy molecules are then incorporated in the (5×2) phase and decrease the bare Cu(110) area by 5 unit cells. As a result, the total amount of the bare Cu(110) surface area should decrease by $\frac{1}{2}(5-2) = 1.5$ Cu unit cells per adsorbed molecule.

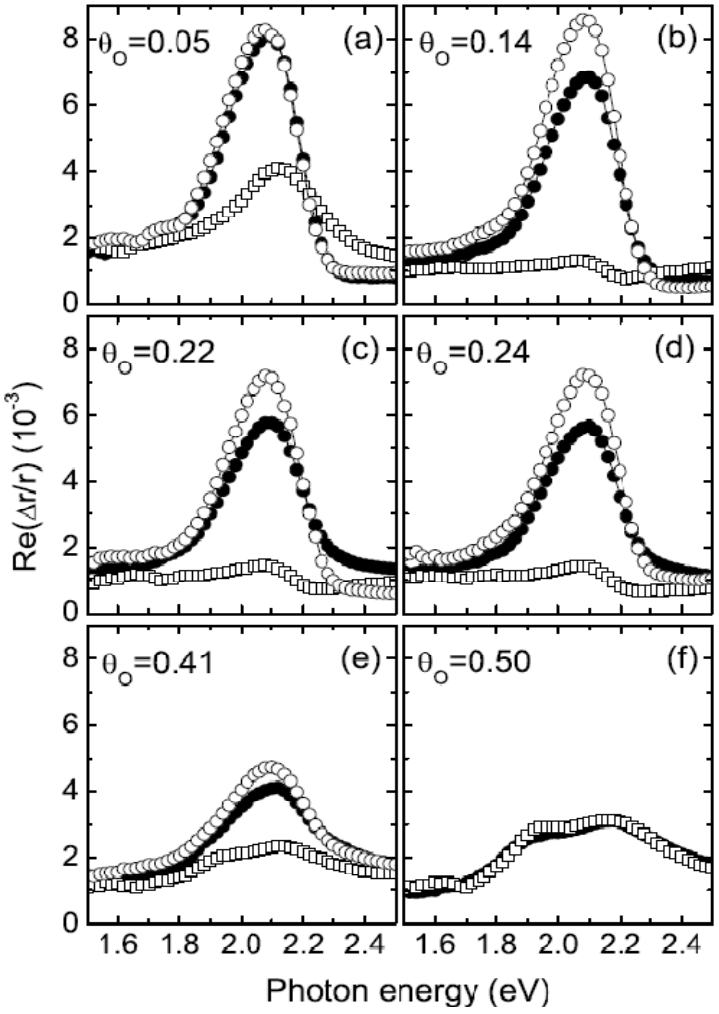

Fig.4.16. Different stages of methanol reaction on the Cu-CuO stripe phase with initial oxygen coverages, θ_O of 0.05, 0.14, 0.22, 0.24, 0.41, and 0.5 ML as shown by the RD spectra around 2.1 eV. Filled circles: before methanol adsorption; open squares: after 5 L methanol exposure; open circles: after heating to 400 K. All spectra were taken at 200 K.

However, the decrease of the RD signal at 2.1 eV due to methanol adsorption is more than what one would expect from this simple estimate. This is most evident for the stripe phase with θ_O=0.14 (Fig. 4.16b), where the maximum coverage of methoxy that can be formed according to Eq. (4.1) is $2\theta_O$ = 0.28, which is only about 2/3 of the saturation coverage 0.4 of the (5×2) methoxy phase. Nevertheless, the RD signal at 2.1 eV in Fig. 4.15 is completely quenched upon methanol adsorption. The lower RD signal can be explained by additional disorder on the Cu(110) surface, in particular due to the formation of atomic vacancies. Indeed, as reported in [86], adding two methoxy molecules not only use one oxygen atom but also require two Cu atoms to be integrated into the reconstructed (5×2) methoxy phase. On the other hand, the atomic ratio of oxygen and Cu within the Cu(110)-(2×1)O stripes is 1:1. Therefore, the Cu atom released from the CuO stripes alone will not be sufficient and an additional Cu atom must be supplied. In fact, on the Cu(110) surface, there are two possible ways for Cu adatom generation; an evaporation from step edges and an expulsion from flat terraces. Since our experiments were carried out at 200 K where the surface diffusivity of Cu adatoms and vacancies is quite small [109], the first source can be excluded. Hence, the only possibility is to expel Cu atoms from terrace sites during the formation of the methoxy induced (5×2) reconstruction leaving behind atomic vacancies on the Cu(110) terraces which do not readily anneal at this low temperature.

In Fig. 4.16, also the RD spectra are presented after heating the sample up to 400 K. In this case, the RD signal is not just recovered but reaches a level which is higher than before methanol adsorption. This result clearly shows that the total fraction of the bare Cu areas has increased as compared to the situation before methanol adsorption. Indeed, it is well known from studies using other surface sensitive methods like temperature-programmed desorption (TPD) [92], photoemission (PE), and high resolution X-ray photoelectron spectroscopy (HRXPS), that the dominating methanol reaction products desorb at temperatures below 400 K, thus leaving behind bare Cu areas. In fact, the total surface fraction of the bare Cu areas should be even larger than before adsorption because part of the oxygen initially incorporated in the CuO stripes has been removed by the reaction with methanol according to Eq. (4.1). In this case, after desorption of the methanol products, the remaining oxygen reorganizes into a well ordered CuO stripe phase but with reduced oxygen coverage. The total amount of oxygen that has been consumed in the reaction process can be precisely determined by taking the differences between before methanol adsorption and after desorption.

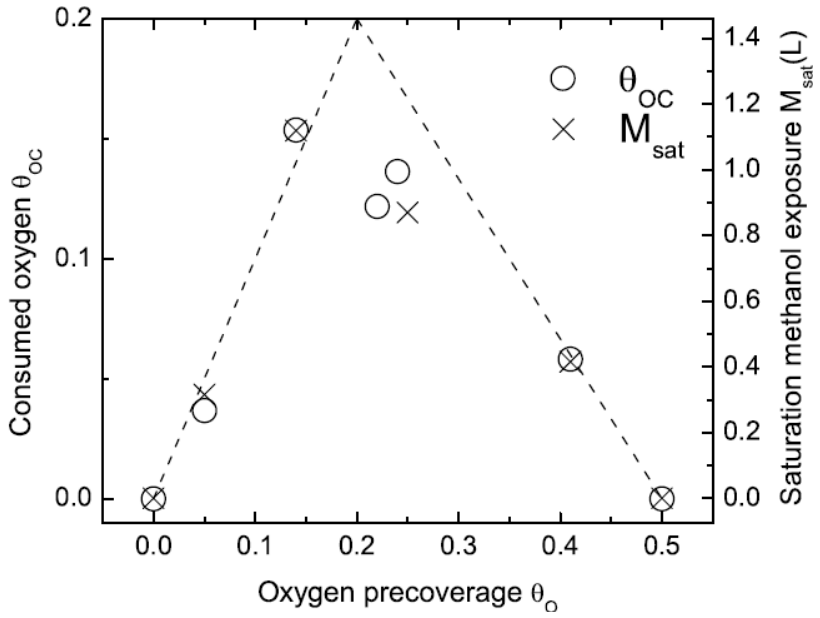

Fig. 4.17 Amount of oxygen consumed during adsorption, reaction and desorption of methanol θ_{OC} (open circles) as a function of the initial oxygen coverage θ_O and saturation of methanol exposure, M_{sat} (crosses). The dashed line indicates the dependence assuming that all methanol is transformed into methoxy and water according to Eq. 4.1.

The M_{sat} (the saturation of methanol exposure; determined from Fig. 4.15) and the θ_{OC} (the consumption of oxygen during methanol oxidation as deduced from Fig. 4.16) are compiled in Fig.4.17. Both M_{sat} and θ_{OC} show the same dependence on the precoverage of oxygen θ_O: first M_{sat} and θ_{OC} increase linearly with the initial oxygen coverage of the stripe phase reaching a maximum around θ_O = 0.2 ML and then decrease for large values of θ_O. Furthermore, the oxygen consumed during methanol oxidation is directly proportional to the saturation exposure of methanol M_{sat}. This observation indicates that the rate of methanol oxidation is constant under the current experimental conditions. According to Fig. 4.17, it can be calculated that in order to react away one oxygen atom from the surface, roughly 2.70 methanol molecules are required. This number is rather close to the value of 2 expected from Eq.4.1. Together with the fact that the reaction rate is independent on the surface morphology, this suggests that the sticking coefficient of methanol on the Cu(110)-(2×1)O stripe phase at 200 K is close to unity. Being aware that the sticking coefficient of methanol on both bare Cu(110) and Cu(110)-(2×1)O under the same condition is almost zero, we can speculate that the diffusion barriers for methanol on both bare

Cu(110) and (2×1)O stripes should be very low so that the molecules can reach the reaction sites during their limited lifetime on the surface, The product of the reaction, i.e., the methoxy species should also be very mobile on Cu(110) at this temperature to leave the reaction site active for the upcoming methanol. This high mobility of the methoxy molecules also ensures the formation of a well ordered (5×2) methoxy structure at this temperature. The dashed lines in Fig. 4.17 correspond to the theoretical prediction based on the following three assumptions: (a) the adsorption process exactly follows the reaction stoichiometry described by Eq. (4.1) and (b) methoxy forms a (5×2) superstructure with a local coverage of 0.4 and (c) completely desorbs at temperatures below 400 K. Assumption (c) is rationalized by the fact that upon heating, the majority of the adsorbed methoxy is known to decompose to formaldehyde and atomic hydrogen according to:

$$CH_3OH^{ads} \rightarrow CH_2O^{gas} + H^{ads} \tag{4.2}$$

In Eq.4.2, adsorbed hydrogen may either react with the adsorbed methoxy to form methanol or combine to molecular hydrogen where the formaldehyde, methanol and molecular hydrogen readily desorb upon their formation at around 350K [3,86]. As can be seen from Fig. 4.17, for this idealized situation, the maximum of the oxygen consumption should occur at θ_O = 0.2. Below this coverage, the reaction is limited by the supply of oxygen atoms, whereas above this coverage it is limited by the availability of adsorption sites (clean Cu areas) for the methoxy molecules [86]. The measured oxygen consumption is smaller than expected from this model. The deviation of the experimental data points from the model prediction could be explained by: (a) residual disorder on the Cu(110) areas after heating to 400 K and a correspondingly lower RD signal; (b) the fact that the (5×2) methoxy structure is not perfectly ordered and has a lower density than the nominal value of 0.4; (c) the oxygen removal according to Eq. 4.1 is not complete at 200 K, i.e., instead of forming H_2O which desorbs immediately, some of the H atoms created upon dissociation of methanol to methoxy may attach to the oxygen atoms on the CuO stripes forming OH groups which remain on the surface. The formation of stable hydroxyl groups at the [001] ends of CuO islands was also suggested in Ref. [86]. On the other hand, one should be aware that the reaction is more complicated than assumed in the simple model above. Besides the formation of methoxy and formaldehyde another reaction may occur, namely, from methanol to formate according to:

$$CH_3O^{ad} + O^{ads} \rightarrow HCOO^{ads} + 2H^{ads} \quad (4.3)$$

A formate intermediate formation (HCOO) has been formulated in HRXPS and other studies [108]. This reaction obviously does not show the removal of oxygen from the surface via the water formation and desorption. Furthermore, as a consequence of formate formation and further dissociation, CO_2 desorption at around 450 K is reported (3,87). Noting that the thermal annealing in the current study was always terminated at 400 K, i.e., below the CO_2 desorption temperature, the oxygen consumption determined in this study and reported in Fig. 4.17 may indeed be underestimated.

4.7.4. Methanol adsorption at 270 K studied by reflectance difference kinetics (RDK)

The change of the RDS signal at 2.1 eV upon methanol adsorption at 270 K is shown in Fig. 4.18 for various oxygen pre-coverages on Cu(110. The methanol dosing pressure was 2.6×10^{-9} Torr. As can be seen in Fig. 4.18, pre-adsorbed oxygen can influence the methanol uptake considerably. The strongest change of the adsorption kinetics takes place already at an oxygen coverage of less than 0.08 ML.

Although it is known that the change of the RDS signal is not necessarily proportional to the adsorbate coverage [36], the initial slope should still be proportional to the initial sticking coefficient. In Fig. 4.19 relative initial sticking coefficients for methanol as a function of the oxygen pre-coverage on Cu(110) are shown. One can clearly see the steep increase at very low oxygen coverage and subsequently a nearly linear decrease of the sticking coefficient. At saturation oxygen coverage the initial sticking coefficient is virtually zero.

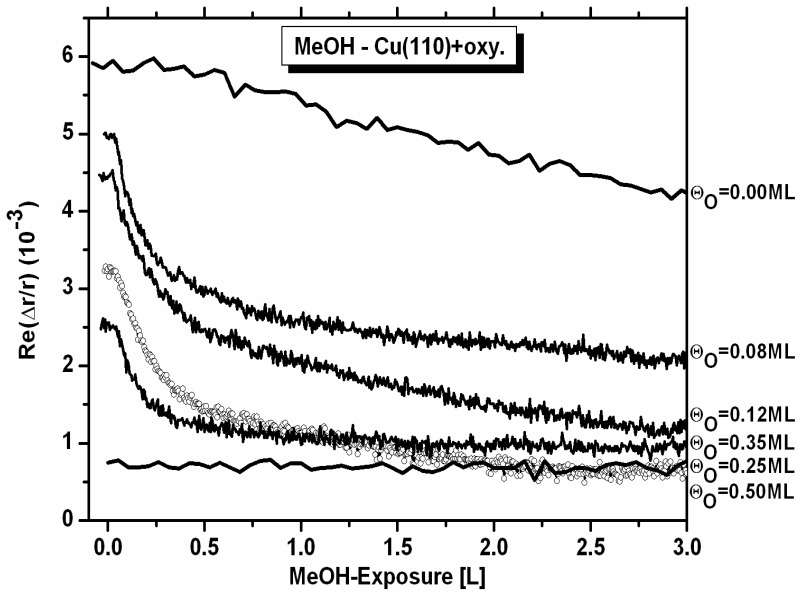

Fig. 4.18: Change of the RD signal at 2.1 eV as a function of the methanol exposure on Cu(110), pre-covered with different amounts of oxygen. Adsorption temperature: 270 K, Dosing pressure: 2.6×10^{-9} Torr. The oxygen coverage was prepared at 550 K to form the stripe phase.

This sticking behaviour can easily be described by making the following assumptions: i) Methanol adsorption proceeds via a strong precursor above the clean copper areas, ii) the sticking coefficient at some "active" sites is very high, iii) on the CuO islands the sticking coefficient is close to zero, and iv) no precursor state exists on the CuO island surface. The fact that the sticking coefficient is so high already at an oxygen coverage of less than 0.08 monolayers is indicative of a long precursor lifetime. In the ideal case of a long lived precursor above the clean copper areas with a large root mean square (RMS) displacement, the sticking coefficient should abruptly increase at the very beginning of oxygen coverage and then linearly decrease as a function of oxygen coverage. This linear dependence is quite well fulfilled in Fig. 4.19.

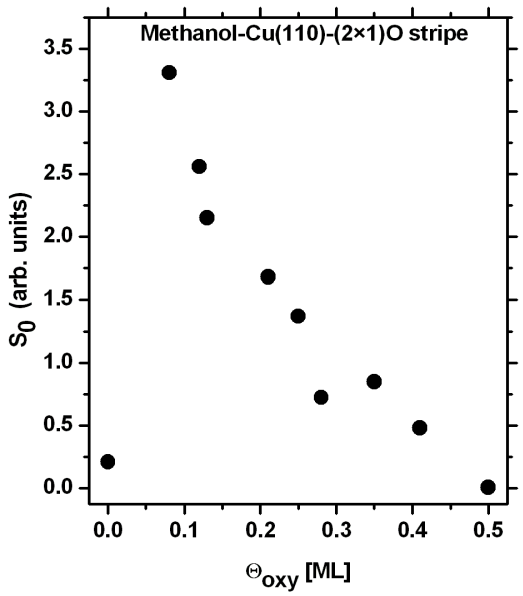

Fig. 4.19: Initial sticking coefficient of methanol on Cu(110) as a function of the oxygen pre-coverage, as obtained from the initial slopes in Fig 4.18.

A comparison of the RDS signal at 2.1 eV change caused by the methanol uptake curve at 200 K and 270 K on a clean and a Cu(110)-0.25 ML oxygen stripe phase is shown in Fig. 4.20a,b. On the stripe phase surface (Fig. 4.20b) the initial sticking coefficient (initial slope) for MeOH at 200 K is larger than that at 270 K. On the other hand, on the clean copper surface (Fig. 4.18), where the sticking coefficient is of course much smaller than on the stripe phase copper surface (see Fig. 4.18) this behaviour is reversed. This can be explained quite well with the model of a precursor assisted adsorption kinetics. The RMS displacement of methanol in the precursor state, which depends on the activation barrier for diffusion, increases with increasing surface temperature, whereas the life time in the precursor, which depends on the desorption energy, decreases. On the clean surface, where it is difficult to find an active site for adsorption, the RMS displacement plays the dominant role, which is larger at higher surface temperature. On the 0.25 ML stripe phase surface, where a high number of preferable adsorption sites exist, the lifetime is the important parameter, which is longer at lower surface temperature.

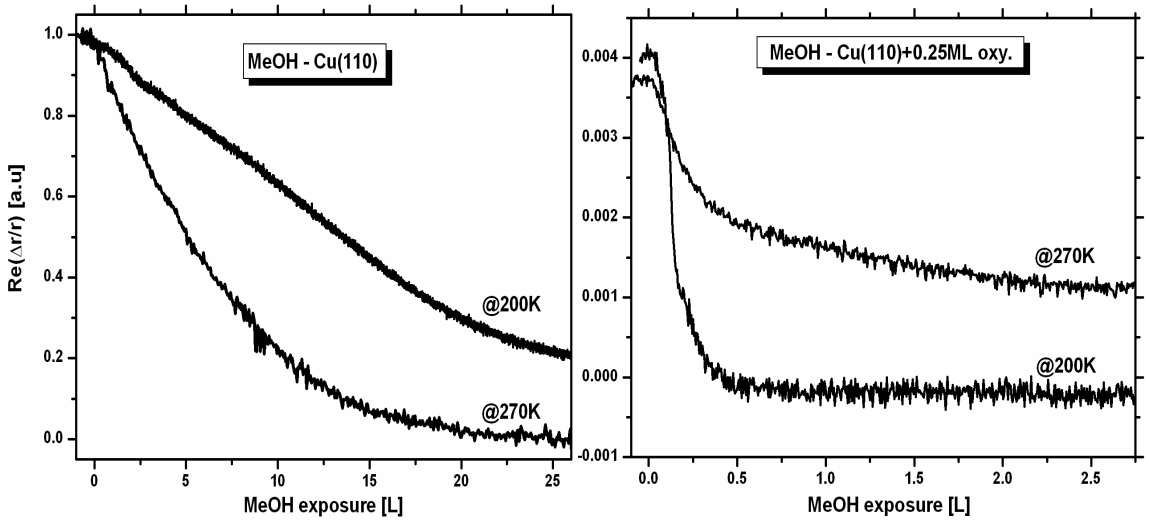

Fig. 4.20: Change of the RDS signal at 2.1 eV as a function of methanol exposure, (a) on the clean Cu(110) surface and (b) on the Cu(110)-0.25 ML oxygen covered stripe phase surface for adsorption temperatures of 200 K and 270 K, respectively.

In Fig. 4.21 we show a typical 2.1 eV RDS signal change as a function of the methanol exposure for various amounts of oxygen in the stripe phase covered surface at 270 K. In addition to Fig.4.18, in this figure the change of the RDS signal as a function of the waiting time (1 hour) after methanol exposure is also shown. Note that such an experimental situation was also measured by TDS as presented in Fig.4.7b.

After stopping the methanol exposure, the RD signal at 2.1 eV starts to recover indicating an increase of the bare Cu area on substrate. This observation suggests that the adsorbates gradually desorb from the surface leaving behind a growing fraction of uncovered Cu(110). While the decrease of the 2.1 eV peak is understood for the methanol adsorption, its slow increase with time is not clear yet after stopping the methanol exposure. To investigate the composition of the desorbing species, a mass analysis with the QMS was performed. To solve this problem the sample was switched several times between directly in front of the QMS and moved away from QMS during waiting time. When the sample was in front of the QMS, the methanol signal increased but the hydrogen signal decreased.

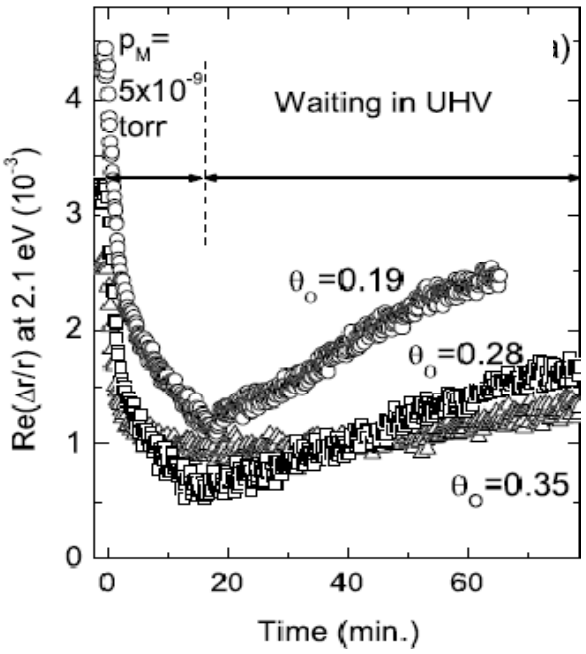

Fig.4.21: RDS at 2.1 eV recorded during methanol adsorption and waiting 1 h in UHV at 270K on the Cu-CuO stripe phase with different oxygen precoverages Θ_O.

This observation clearly indicates that methanol molecules desorb from the surface, hydrogen from the residual gas is consumed during waiting. That means methoxy can take the adsorbed H to transform into methanol and does not need the (strongly bound) hydrogen from the OH. Furthermore it would mean that due to the relatively large H coverage the branching of methoxy into formaldehyde is suppressed. This is in good agreement with our TDS results which were previously discussed.

4.8 Summary and conclusion

We have investigated the reaction products after methanol dosing of a Cu(110) surface at 190 K and 270 K, covered with different amounts of oxygen, by thermal desorption, angle resolved thermal desorption spectroscopy, reflection absorption infra red spectroscopy and reflectance difference spectroscopy. In particular, we have focused on the Cu-CuO stripe phase with 0.25 ML of oxygen on Cu(110). A recombinative desorption of methanol and water takes place at temperature between 200 K and 300 K, which exhibits a nearly cosine angular desorption

distribution. The corresponding thermal desorption spectra posses a FWHM of about 30 K and show a peak shift to lower temperature with increasing coverage, as expected for normal recombinative desorption. The species methanol, formaldehyde and hydrogen which desorb nearly simultaneously at around 350 K, exhibit a very narrow desorption peak (FWHM = 10) and the peaks shift to higher temperature with increasing coverage. The corresponding angular distributions show a strongly forward focused function. This indicates a more complicated desorption process, involving high activation barriers for the C-H bond breaking, as suggested by recent theoretical calculations. For the Cu-CuO stripe phase the angular distribution of the reaction products at 350 K is clearly anisotropic. The desorption distribution along the stripes shows a forward focused distribution, whereas the distribution normal to the stripes shows a bimodal shape, indicating inclined desorption at the border lines between the Cu and CuO stripes. In addition, in the TDS results one can see that adsorbing 50 L of methanol on oxygen free Cu(110) leads to coadsorption of water, which can be incorporated in the methanol rows formed on the surface. This coadsorbed water leads to a very similar TPD of this adsorbed layer as methanol adsorbed on the oxygen stripe phase.

RAIRS measurements also show very similar spectra for a monolayer of methanol with and without preadsorbed oxygen due to the fact that one cannot distinguish adsorbed methanol and methoxy adsorbed on the more stable short bridge site by looking at the ν-CO frequency. However, methoxy adsorbed in the long bridge site shows the ν-CO vibration at lower wavenumbers and it is found with increasing surface temperature. The formation of carbon dioxide during thermal desorption seems to take place via a previously unknown η-formaldehyde and OH intermediate on the surface that was detected in temperature programmed RAIRS experiments. Complementary TDS experiments indicate that this species can be populated by methanol adsorption at elevated temperatures.

At 200 K, the RDS, as a versatile tool for in-situ monitoring of surface reactions, showed that on the clean surface as well as on the fully oxygen saturated surface, the initial sticking coefficient of methanol is very low. In contrast the sticking coefficient on the Cu-CuO stripe phase is close to unity. Most probably the high mobility of the methanol on the stripe phase and of methoxy on clean Cu(110) play a role for the high sticking coefficient. The methanol uptake has a maximum at the oxygen precoverage of θ_o=0.2 ML. At 270 K the sticking coefficient of methanol on the well ordered Cu-CuO stripe phase is rather low as compared to 200 K but on the clean surface

this behavior is reversed. A precursor assisted adsorption kinetics can best explain this situation. The RMS displacement of methanol in the precursor state, which depends on the activation barrier for diffusion, increases with increasing surface temperature, whereas the life time in the precursor, which depends on the desorption energy, decreases. On the clean surface, where it is difficult to find an active site for adsorption, the RMS displacement plays the dominant role, which is larger at higher surface temperature. On the 0.25 ML stripe phase surface, where a high number of preferable adsorption sites exist, the lifetime is the important parameter, which is longer at lower surface temperature.

Chapter V

5. Interaction of molecular and atomic deuterium with methanol on Pd(111)

Palladium is one of the transition metals which may be used as a catalyst material for methanol synthesis/decomposition. Palladium and palladium alloys show interesting features in catalyzing methanol decomposition. Methanol plays an important role as an intermediate product in chemical industry, but also as a potential future energy carrier. The advent of methanol powered fuel cells brought new life into the research of the reaction of methanol with metal surfaces. The most important step for the fuel cell application is the dehydrogenation of methanol. The dehydrogenation reaction of methanol on Pd(111) has been studied in several papers with many different methods Nevertheless, it has not been clear whether an opening of the C – O bond in methanol is possible. In this chapter we have focused on the interaction of deuterium with methanol on the Pd(111)surface. In addition to that we present a detailed description on the quantitative determination of the reaction products.

5.1. Introduction

The adsorption/desorption of methanol on transition metal surfaces has been the subject of numerous investigations, since many modern technologies are based on the dissociation (e.g., fuel cells) or the synthesis of methanol (e.g., petrochemical industry) within the last decades [6,7,23,111,117,113,115,116]. Palladium is one of the transition metals which may be used as a catalyst material for methanol synthesis/decomposition. Palladium is an essential component in the field of heterogeneous catalysis due to its special attributes concerning hydrogenation and dehydrogenation reactions as relevant for fuel cells.

In particular, for the system CH_3OH–Pd(111) a comprehensive data set is available. Both a number of experimental techniques and a number of theoretical studies have been applied to elucidate this adsorption system. One major issue concerns the branching of the adsorbed methanol into the individual reaction products. Interestingly, only little quantitative information is available on this subject. One of the purpose in this study is to provide a detailed description on the quantitative determination of the reaction products based on TDS.

The mutual interaction between adsorbed methanol and produced hydrogen is of great importance. Palladium and palladium alloys show interesting features in catalyzing methanol decomposition. Interestingly, however, no systematic study on the fundamental processes of the methanol/hydrogen interaction on palladium can be found in the literature, to the best of our knowledge. Yet, another reason for our studies is the fact that even under UHV conditions, due to the high sticking coefficient of hydrogen, some coadsorption of hydrogen will always exist in methanol adsorption studies on palladium. Therefore, we have also focused in this work on the interaction of hydrogen (deuterium) with methanol on the Pd(111) surface and its effect on the reaction products by using thermal desorption spectroscopy. The influence of both preadsorption and postadsorption of molecular deuterium on the adsorption and reaction kinetics of methanol has been studied. The main part of this work, however, deals with the interaction of *impinging deuterium atoms* with the methanol adsorbate.

5.2. Quantitative determination of reaction products for the methanol/Pd(111) system

In order to obtain quantitative data one has to calibrate the desorption spectra, either by comparing with a known desorption spectrum [118] or by using other reference points, e.g. LEED patterns for the saturation coverage, a quartz microbalance, etc. In principle, the desorbed amount can be obtained from TDS if an absolute pressure measurement is available and if the effective pumping speed S_p [cm^3/s] and the surface area A [cm^2] are known:

$$N = K \cdot S_p \cdot \int p dt / A \left[\frac{\text{molecules}}{\text{cm}^2} \right] \tag{5.1}$$

with $K = 3.3\text{x}10^{16}$ [molecules/Torr cm^3] for a gas at 300 K. In many cases the pumping speed is not known with sufficient accuracy. In addition, if the effective pumping speed is very high the pressure integral may become too small to be determined with sufficient accuracy. To circumvent this problem desorption can be performed with a mass spectrometer in line-of-sight. In this case the pumping speed does not play a role, but on the other hand a number of new (and often unknown) parameters determine the measured mass spectrometer signal. Nevertheless, we will demonstrate in this paper that in-line mass spectrometry can be successfully used to determine quantitatively the amount of desorbed particles. The procedure will be applied to evaluate the reaction products in TDS after the adsorption of methanol on a clean Pd(111) surface.

5.2.1 Data evaluation method

A description of the procedure to quantitatively determine the reaction products (methanol, carbon monoxide, hydrogen and water), which desorb after dosing the Pd(111) sample with a saturation of the chemisorption layer of methanol will be presented. First the sensitivity of the mass spectrometer for CH_3OH, H_2, CO and H_2O has to be determined. Our mass spectrometer yielded the following ion currents I_{QMS} for the individual gases at measured partial pressures p_m of $4\text{x}10^{-8}$ Torr: H_2: $2.8\text{x}10^{-8}$ A at m=2, CO: $8.2\text{x}10^{-9}$ A at m=28, methanol: $2.7\text{x}10^{-9}$ A at m=32, water: $9\text{x}10^{-9}$ A at m=18.

The sensitivity c_p of the quadrupole mass spectrometer (QMS) is defined as

$$c_p = \frac{I_{QMS}}{p} \quad \left[\frac{\text{A}}{\text{Torr}}\right] \tag{5.2}$$

The pressure p_m as measured by an ion gauge has to be corrected by the relative sensitivity factor S for the individual gases (with respect to the nitrogen sensitivity S=1) to obtain the true pressure p:

$$p = \frac{p_m}{S} \quad [\text{Torr}] \tag{5.3}$$

These factors have been determined to 0.42 for hydrogen, 1.1 for carbon monoxide, 1.9 for methanol and 0.9 for water in the literature [119]. We would like to emphasise that the ion gauge

in principle has to be calibrated additionally with an absolute pressure gauge, e.g. a spinning rotor gauge, to obtain the absolute sensitivity for nitrogen [118]. This is, however, not a prerequisite for these calculations. For our purpose we require the factor c_n which correlates the mass spectrometer signal with the gas density.

$$c_n = \frac{I_{QMS}}{n} = \frac{I_{QMS} S}{K p_m} \quad \left[\frac{\mathrm{A \cdot cm^3}}{\mathrm{molecule}} \right] \tag{5.4}$$

($n=Kp$, with $K = 3.3\text{x}10^{16}$ molecules/Torr cm^3 for a gas at 300 K)

The following sensitivity factors were obtained:

$c_n(H_2) = 8.9\text{x}10^{-18}$ Acm^3/H_2-molecule

$c_n(CO) = 6.8\text{x}10^{-18}$ Acm^3/CO-molecule

$c_n(H_2O) = 6.1\text{x}10^{-18}$ Acm^3/H_2O-molecule

c_n(MeOH) = $3.9\text{x}10^{-18}$ Acm^3/methanol molecule

As already mentioned before the TDS was performed with the sample in line-of-sight to the mass spectrometer, but off-line spectra are additionally needed for the calibration. In case of an in-line spectrum, both, molecules entering the ionisation region directly from sample as well as molecules having randomised in the vacuum chamber will contribute to the mass spectrometer signal. After subtracting the corresponding off-line spectrum we obtain a TDS signal which exclusively stems from the directly desorbed molecules. Thus we obtain a signal which is proportional to the desorption flux F [molecules/cm^2 s] normal to the surface. We have to take into account that the mass spectrometer is a gas density detector. The density n [cm^{-3}] depends on the flux F and the molecule velocity v [cm/s]:

$$n = \frac{F}{v} \left[\frac{\mathrm{molecules}}{\mathrm{cm^3}} \right] \tag{5.5}$$

The QMS signal I during a TDS can be expressed by n and c_n according to Eq. 5.4. However, the actual number of molecules n′ contributing to the QMS signal depends on the flux F_A through the aperture area A_A (0.385 cm^2) and the effective volume for ionisation, which is not known. One can give a dimensionless geometry factor $g = n/n'$. Then the QMS signal can be written as:

$$I = c_n \cdot n = c_n \cdot n' \cdot g = c_n \cdot \frac{F_A}{v} \cdot g \tag{5.6}$$

Then we determine the flux F_A though the aperture. It depends on the geometric arrangement and on the angular distribution of the desorbing molecules. The solid angle Ω defined by the aperture area and the distance between aperture and sample is $\Omega = A_A/d^2$. If the angular desorption distribution $D(\Theta)$ can be described by a function $\cos^n\Theta$, as usually done in the literature [23], then the flux normal to the surface F_0 is given by:

$$F_0 = \frac{n+1}{2\pi} F_{total} \tag{5.7}$$

The flux through the aperture with 50% transparency and for small Ω then is approximately:

$$F_A \approx \frac{F_0 \cdot \Omega}{2} = \frac{(n+1) \cdot A_A \cdot F_{total}}{4\pi \cdot d^2} \tag{5.8}$$

Finally, the QMS signal can be described by inserting Eq. 5.8 into Eq. 5.6:

$$I = \frac{c_n \cdot g \cdot (n+1) \cdot A_A \cdot F_{total}}{4\pi \cdot d^2 \cdot v} \tag{5.9}$$

Time integration of Eq. 5.9 yields the area of the desorption spectrum A_{TDS} [As]:

$$A_{TDS} = \int I \cdot dt = \frac{c_n \cdot g \cdot (n+1) \cdot A_A \cdot \int F_{total} dt}{4\pi \cdot d^2 \cdot v} \tag{5.10}$$

The integral of the total flux vs. time is equal to the total amount of adsorbed particles

($N_{total} = \int F_{total} dt$). From a reference spectrum for a specific gas, for which the coverage is known (typically the saturation coverage), and the corresponding area of the thermal desorption spectrum A_{TDS} one can deduce the unknown geometry factor g:

$$g = \frac{A_{TDS} \cdot 4\pi \cdot d^2 \cdot v}{c_n \cdot (n+1) \cdot A_A \cdot N_{total}} \tag{5.11}$$

The velocity of the particles needs further consideration in Equ. 5. 11. The mean energy $\langle E \rangle$ of a Maxwellian flux is $2kT$ [120]. This is true when desorption proceeds without an activation barrier for adsorption. In this case the angular distribution can be described by a $\cos^n\Theta$ function with n=1. In case of a non-thermal desorption, e.g for desorption over an activation barrier, where $n \neq 1$, and if furthermore normal energy scaling (NES) can be assumed to hold [121], then the mean energy of the desorption flux can be given by [93]:

$$\langle E \rangle = \frac{n+3}{2} kT = \frac{mv^2}{2} \tag{5.12}$$

Using this formula we deduce the v_{rms}, which we use as the representative velocity v at the desorption temperature T for molecules with mass m of the corresponding thermal desorption peak:

$$v = \sqrt{\frac{(n+3)kT}{m}} \tag{5.13}$$

The saturation thermal desorption spectrum of CO on Pd(111) has been used for the determination of the geometry factor. The in-line and off-line spectra after dosing the Pd(111) surface at 140 K with 5.5 L CO are shown in Fig. 5.1a. This exposure was shown to be sufficient to saturate the surface. According to the literature the saturation coverage is 0.75 monolayers [122,123]. The surface density of the Pd(111) surface is 1.54×10^{15} atoms/cm^2, therefore the total number N_{total} of CO molecules contributing to the TDS is 1.16×10^{15} molecules/cm^2.

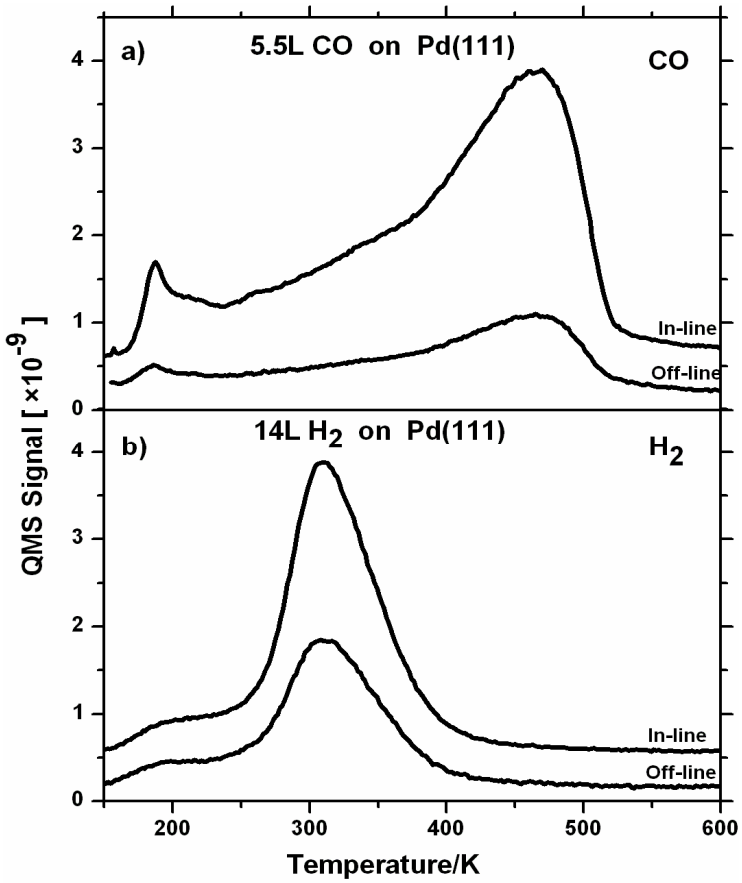

Fig. 5.1a,b: In-line and off-line saturation desorption spectra for (a) CO and (b) H_2 after dosing a Pd(111) surface to 5.5 L CO and 14 L H_2, respectively. Adsorption temperature: 140 K, heating rate: 2K/s

The areas of the in-line and off-line TD spectra are 2.67×10^{-7} A·s and 7.63×10^{-8} A·s, respectively. The net signal A_{TDS} therefore is 1.91×10^{-7} A·s. The exponent n of the angular distribution is taken to be 1, according to the literature [124]. The peak maximum of the CO desorption peak is at 470 K, which we insert into Eq.5.13 for the determination of the velocity. This yields the velocity v = 7.45×10^{4} cm/s. Inserting all these quantities into Eq. 5.11 results in a geometry factor g = 85.

In Fig.5.1b, the same procedure with the saturation of hydrogen on Pd(111) has been applied to get more confidence into the evaluation procedure. The areas of the in-line and off-line spectra are 1.49×10^{-7} A·s and 8.48×10^{-8} A·s, respectively. The saturation coverage is 1 ML [H-atoms/Pd-atoms] [125], the exponent n of the angular distribution is 1.3 [126], the peak temperature is 310 K, leading to a mean velocity of 2.35×10^{5} cm/s. From these data we obtain a geometry factor g =

90. This is in quite good agreement with the value obtained for CO and we take for the further calculations a mean value of g = 87. It is difficult to specify the total error for this value but we estimate it to be less than 15%.

Now the different reaction products after dosing the Pd(111) surface to methanol can be calculated by the experimentally obtained geometry factor g.

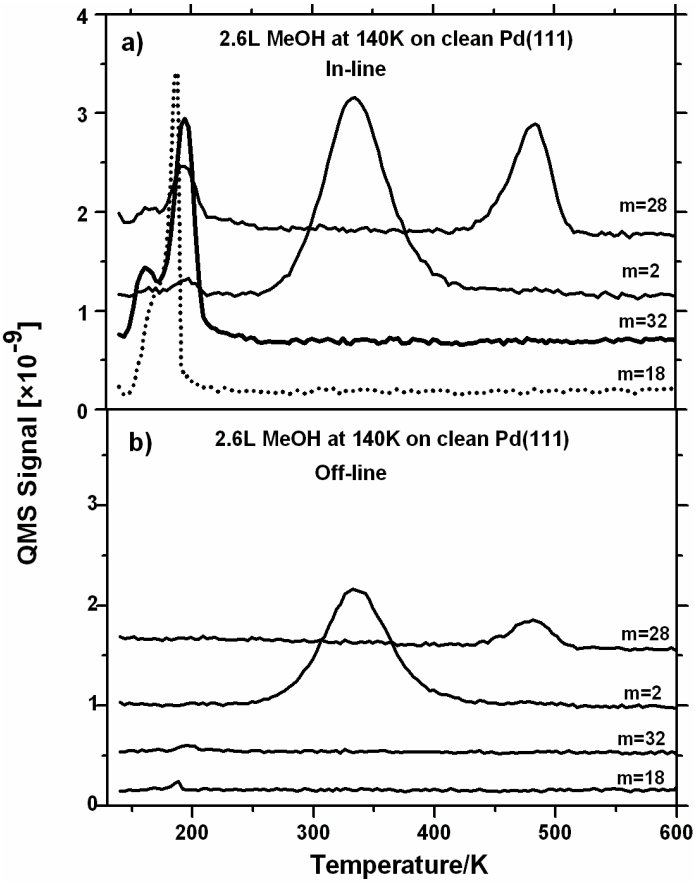

Fig. 5.2a,b: (a) In-line and (b) off-line desorption spectra for the reaction products methanol, CO, H_2 and H_2O after dosing a Pd(111) surface to 2.6 L methanol. Adsorption temperature: 140 K, heating rate: 2K/s.

The in-line and off-line multiplexed thermal desorption spectra after dosing 2.6 L methanol at 140 K are shown in Fig. 5.2a,b, respectively. This is sufficient to saturate the chemisorbed layer, as can be seen by the already existing onset of the multilayer desorption peak at 160 K. The calculated areas for the in-line spectra are 2.7×10^{-8} A·s for methanol (chemisorbed peak at 190 K only), 6.9×10^{-8} A·s for hydrogen at around 340 K, 2.25×10^{-8} A·s for CO at 480 K and 2.7×10^{-8} A·s for water at around 180 K. The corresponding off-line signals are 1×10^{-9} A·s (methanol), 4.3×10^{-8} A·s (hydrogen), 6.0×10^{-9} A·s (carbon monoxide) and 8×10^{-10} A·s (water), respectively. From these data we can calculate the total amount of desorbing species from the equation:

$$N = \frac{A_{TDS} \cdot 4\pi \cdot d^2 \cdot v}{c_n \cdot g \cdot (n+1) \cdot A_A} \tag{5.14}$$

and obtain the following result: $N_{MeOH} = 1.6 \times 10^{14}$ MeOH/cm^2, $N_{H2} = 3.5 \times 10^{14}$ H_2/cm^2, $N_{CO} = 1 \times 10^{14}$ CO/cm^2 and $N_{H2O} = 1.3 \times 10^{14}$ H_2O/cm^2. (For the determination of the water and methanol content we used an exponent n=1. To the best of our knowledge no literature data are available for these quantities).

These data need some interpretation: Obviously, there is a considerable amount of pre-adsorption of water and hydrogen during cooling down the sample to the base temperature of 140 K. But also during methanol exposure a slight increase of the water and hydrogen signal in the gas phase is observed, due to displacement effects on the chamber walls. It is of course a matter of the experimental conditions (pumping speed, history of the vacuum chamber, gas purity) to which extent the co-adsorbates influence the methanol coverage, but they can most probably never be totally avoided. The possibility that the water desorption signal stems from C-O bond scission can be ruled out for the clean Pd(111) surface. No carbon residuals have been observed on the surface after desorption. The CO signal can exclusively be attributed to the dehydrogenation of methanol. The co-adsorption of CO from the gas phase plays only a negligible role, as checked experimentally. Then, as a result of the dehydrogenation of methanol ($CH_3OH \rightarrow CO + 2H_2$), the amount of 1×10^{14} CO/cm^2 has to be accompanied by 2×10^{14} H_2/cm^2. This means that the difference to the experimentally obtained amount of hydrogen (1.5×10^{14} H_2/cm^2) has to originate from pre-adsorbed hydrogen. We have recently studied the influence of pre-desorbed deuterium on Pd(111) on the methanol adsorption and have observed that chemisorption of methanol is strongly suppressed by pre-adsorbed deuterium [7]. It is safe to assume that both, the preadsorbed

hydrogen as well as the predsorbed water will block available surface sites for methanol adsorption. Therefore, the quantitatively observed amount of initially adsorbed methanol of $2.6x10^{14}$ MeOH/cm^2 is a lower limit. With respect to the branching of the adsorbed methanol into associative methanol desorption and dehydrogenation we obtain a ratio of 62% to 38%, respectively. This is close to the branching ratio of 55%:45%, as determined by Davis and Barteau [127].

5.3. Reaction of molecular and atomic deuterium with methanol on Pd(111)

One of the important issues in this context concerns the activation of the O-H, C-O and C-H bonds involved, which basically determines the intermediate and final products of methanol decomposition. The individual reaction routes depend strongly on the type of the metal surface (noble metal, transition metal), the geometric surface structure (flat or rough surfaces, surface defects), the chemical composition of the surface (impurities, co-adsorbates, surface alloys), as well as on the surface temperature and the methanol partial pressure. It is therefore not surprising that the specific routes of methanol decomposition on individual metal surfaces are sometimes still a matter of controversy.

Palladium is frequently used as model catalyst material for methanol synthesis/decomposition. It is also an essential component in the field of heterogeneous catalysis due to its special attributes concerning hydrogenation and dehydrogenation reactions as relevant for fuel cells. Many surface science studies have dealt with the methanol/palladium system to provide a detailed understanding of the single reaction steps in the methanol decomposition. In particular, for the system CH_3OH-Pd(111) a comprehensive data set is available. In one of the earliest investigations, Gates and Kesmodel [128] used high-resolution electron energy loss spectroscopy (HREELS) to elucidate the interaction of methanol with Pd(111). They observed the basic features of this system, namely that at 140 K methanol forms a chemisorbed and a physisorbed phase. They concluded that chemisorbed methanol is molecularly adsorbed and bonds with the oxygen lone pair to palladium and that no methoxy is formed. During sample heating some dehydrogenation takes place which finally leads to the desorption of hydrogen and carbon monoxide. The influence of oxygen on methanol adsorption was subsequently studied in some

detail by Davis and Barteau [129] by applying thermal desorption spectroscopy (TDS). In that case additional reaction products of formaldehyde, formate and carbon dioxide showed up.

The question as to the possibility of breaking the C-O bond of methanol on clean Pd(111) is a matter of controversy ever since Winograd et al. [115,113] found the first evidence for this process by applying x-ray photoelectron spectroscopy (XPS) and secondary ion mass spectrometry (SIMS). However, according to their experiments the C-O dissociation should only take place in a very narrow coverage range around 1 monolayer of methanol. Whereas this observation has been confirmed by some other groups (Rebholz and Kruse [114], Schennach et al. [111]), Guo at al. could not verify this finding by isotopic mixing experiments [116]. Theoretical calculations by Zhang and Hu [130] also showed that the activation barrier for the C-O bond scission is much larger than for the O-H bond scission on the clean surface. One could therefore speculate that surface impurities and/or surface defects might be responsible for the C-O bond activation. In this context XPS and polarization modulated infrared reflection absorption spectroscopy (PM-IRAS) experiments in the group of Freund [110] did not reveal a significant influence of the surface roughness on the C-O activation, but an influence of the surface temperature. With respect to the chemisorbed methanol state it is still not unambiguously clear if it is a molecular state or a methoxy state [113,131].

In this work we will focus on the interaction of hydrogen (deuterium) with methanol on the Pd(111) surface and its effect on the reaction products by using thermal desorption spectroscopy. Both, the influence of pre-adsorption and post-adsorption of molecular deuterium on the adsorption and reaction kinetics of methanol has been studied. The main part of this work, however, deals with the interaction of impinging *deuterium atoms* with the methanol adsorbate. In this case the O-H as well as the C-H bonds can be broken. However, no evidence for significant C-O bond activation could be found. For most of the reaction products we could obtain quantitative data, by using a calibration method for the thermal desorption spectra as described in a previously published paper [6].

Atomic deuterium was supplied to the sample via a doser of the Bertel type [132]. This doser consists of an electron beam heated tungsten tube which yields nearly 100% of deuterium in atomic form at a temperature of about 1900 K. We have previously characterized this device with respect to the degree of dissociation and the angular variation of the effusion flux [133].

Molecular deuterium was dosed with the same doser without heating the device. In case of gas exposure via the dosers the enhancement factors for the effective exposure were experimentally determined. These factors are taken into account for all exposures given in Langmuir (1 L (Langmuir) = $1x10^{-6}$ Torr s). In the case of atomic dosing the exposure is again given in Langmuir, as obtained from the pressure increase in the chamber, the dosing time and the enhancement factor. Actually, the angular distribution of the effusing deuterium is similar for both, molecular and atomic deuterium. Therefore the impingement rate is the same for deuterium in both forms (1 D_2 = 2 D). See a more detailed discussion of atomic hydrogen dosing in ref. [133].

5.3.1 Adsorption of methanol on clean and deuterium pre-covered Pd(111)

In Fig. 5.3 multiplexed TDS spectra are shown after dosing the the clean Pd(111) surface with 1.6 L of methanol at 140 K.

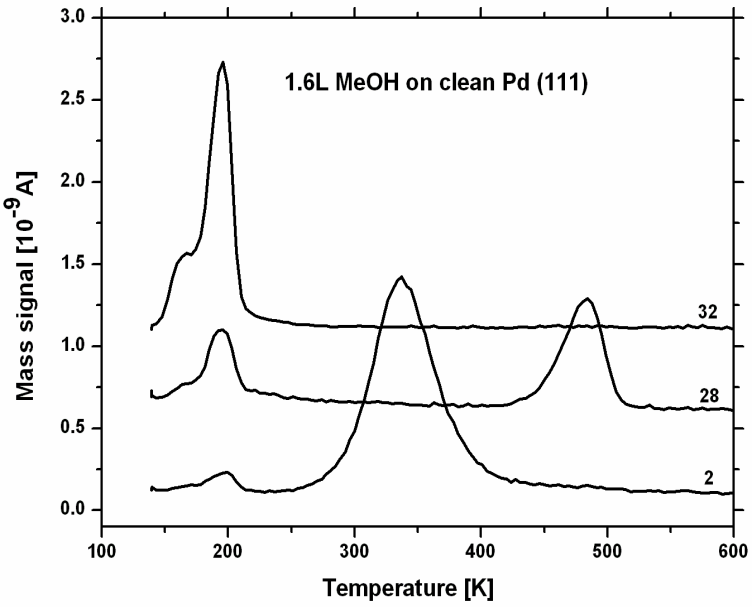

Fig.5.3. Thermal desorption spectra after dosing a clean Pd(111) surface with 1.6 L methanol at 140 K. Heating rate: 2 K/s.

For clarity the desorption curves have been offset in this figure and in all the following figures which show desorption traces. The exposure of 1.6 L is sufficient to nearly saturate the

chemisorbed monolayer (desorption peak at 195 K) and to populate the multilayer to some extent (desorption peak at 160 K). This is in good agreement with the data by Chen et al. [113]. Some chemisorbed methanol fully dehydrogenates during sample heating, leading to hydrogen desorption around 340 K and carbon monoxide desorption around 480 K.

In addition, as it is already shown in Fig 5.2a, some water desorbs at about 180 K, which stems from residual gas adsorption. However, contrary to the work by Chen et al. no methane desorption was observed. We could demonstrate that some amount of methane desorption arises only when the palladium surface is contaminated with oxygen. Concerning the H_2/CO ratio of the desorption spectra we would like to note that it cannot be directly associated with the stoichiometric ratio of 1 CO to 2 H_2 molecules, as expected from dissociated methanol. The reason is that some of the hydrogen also stems from pre-adsorption of hydrogen from the residual gas during sample cooling prior to methanol dosing, which adsorbs with a quite high initial sticking probability of about 0.5 [134]. Even at a base pressure of only $2x10^{-10}$ Torr the residual hydrogen partial pressure is large enough to contribute to this undesired pre-adsorption. We have recently described a procedure for the quantitative determination of the reaction products upon methanol adsorption on Pd(111) and the branching of chemisorbed methanol into molecular desorption and dissociation of methanol into CO and hydrogen [6]. From these quantitative measurements we determined the amount of about 0.1 ML of pre-adsorbed hydrogen and 0.1 ML water. On the other hand the CO signal can be assumed to stem almost exclusively from dissociated methanol, as checked experimentally. According to these calculations the saturation coverage of methanol on a clean Pd(111) surface would amount to 0.45 monolayers ($6.9x10^{14}$ MeOH/cm^2), from which 62±5 % desorb associatively at around 195 K and 38±5 % dissociate to hydrogen and CO [6].

Since we have shown that pre-adsorption of hydrogen cannot be fully excluded, due to its rather high sticking probability, we first investigated the influence of the pre-adsorbed hydrogen isotope deuterium on the methanol adsorption on Pd(111). Multiplexed desorption spectra after dosing the surface with 5 L of D_2 at 130 K and then dosing with 1.6 L methanol are shown in Fig. 5.4.

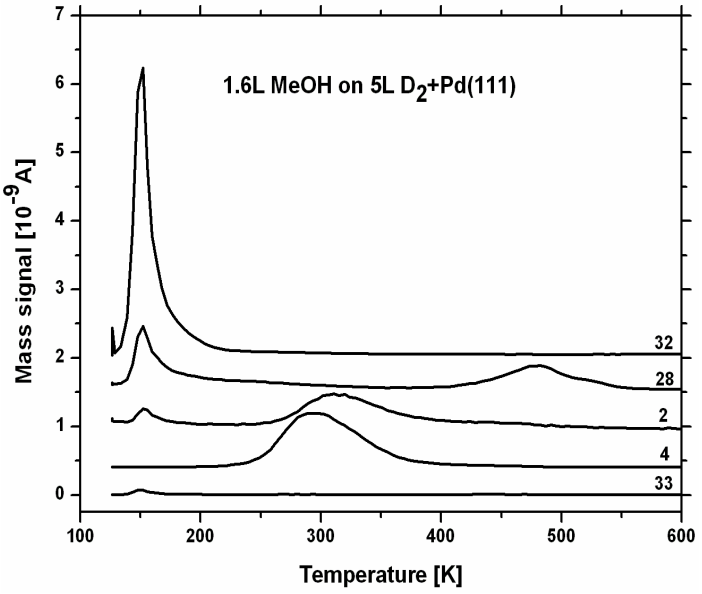

Fig.5.4. Thermal desorption spectra after dosing a deuterium pre-covered Pd(111) surface (5 L D_2) with 1.6 L methanol at 125 K. Heating rate: 2 K/s.

We verified that this deuterium exposure is sufficient to saturate the Pd(111) surface. It is interesting to note that in the literature, to the best of our knowledge, no quantitative data on the saturation coverage of hydrogen or deuterium on Pd(111) are available. This is probably due to the fact that the saturation coverage depends on the surface temperature during dosing and that hydrogen also can populate subsurface sites. Nevertheless, under the given experimental conditions (T_s = 130 K, p_{H2} = 10^{-8} Torr) a well defined saturation coverage can be obtained, which we assign to 1 monolayer (ML) [6,125].

Comparison of the desorption spectra in Fig. 5.3 and Fig. 5.4 reveals some interesting features. First of all the physisorption peak for methanol desorption around 160 K is much more pronounced on the deuterium pre-covered surface than on the initially clean Pd(111) surface. At the same time desorption from the chemisorbed layer is almost totally suppressed. The dissociation products CO and hydrogen are also significantly reduced. From our quantitative calculations we conclude that in this case only about 17±5 % of the adsorbed methanol has been dissociated. Obviously, the pre-adsorbed deuterium impedes the formation of a chemisorbed species, which would lead to a desorption peak around 195 K. Since this chemisorbed state can also be seen as a precursor for the subsequent dehydrogenation, it is clear that less H_2 and CO

desorption shows up in the case of deuterium pre-adsorption. We have also checked on possible reactions between the pre-adsorbed deuterium and the methanol (masses 33-36) but we did not find any deuterated methanol in the desorption spectrum. The signal for m=33 (CH_3OD) in Fig. 5.4 is about 1% of mass 32 and corresponds to the natural isotope ratio. The result of these investigations is that adsorbed deuterium (hydrogen) deactivates the palladium surface in such a way that at 140 K almost all methanol adsorbs in the physisorbed state, and hence also the dehydrogenation reaction is greatly reduced.

5.3.2 Adsorption of molecular deuterium on methanol covered Pd(111)

In Fig. 5.5 multiplexed desorption spectra are shown which were obtained after dosing a methanol covered Pd(111) surface (0.8 L methanol exposure at 125 K) with 5 L of D_2 at 125 K.

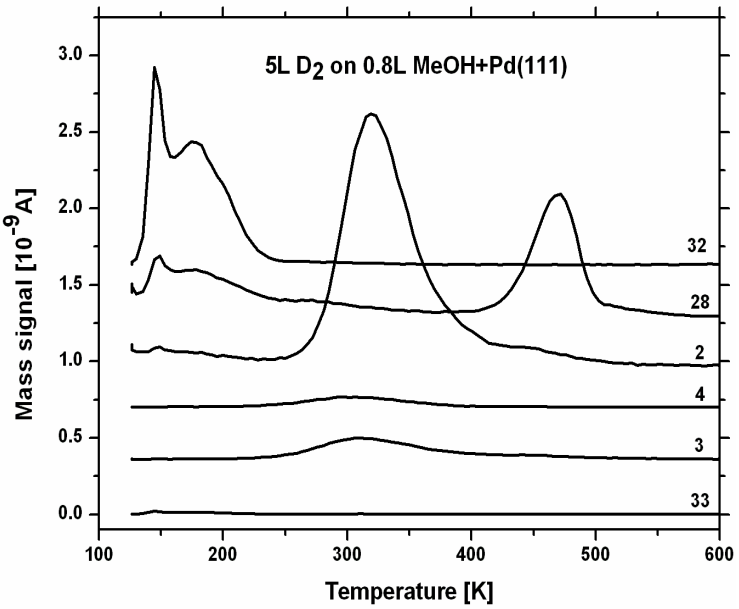

Fig.5.5. Thermal desorption spectra after dosing a methanol pre-covered Pd(111) surface (0.8 L MeOH) with 5 L molecular deuterium at 125 K. Heating rate: 2 K/s.

The fraction of methanol which dissociates into CO and hydrogen is nearly the same as for pure methanol adsorption (Fig. 5.3), but the desorption spectrum for molecular methanol has changed due to deuterium post-adsorption. As the methanol coverage in this case is somewhat smaller

than in Fig. 5.3 one would not expect any desorption from the multilayer state. However, post-adsorption of molecular deuterium apparently changes some of the chemisorbed methanol into physisorbed methanol. One can see from the signals m=3 and m=4 in Fig. 5.5 that some deuterium has been adsorbed on the methanol pre-covered surface. The dissociatively adsorbed deuterium atoms occupy surface sites. This may result in a weakening of the methanol-surface interaction and hence to a change of chemisorbed methanol to physisorbed methanol.

We have again checked for a possible mixing between deuterium and methanol, but could not find any deuterated methanol in the desorption spectrum within the detection limit. This is a strong indication that the chemisorbed methanol is a molecular state rather than a dissociated methoxy + H state, as proposed in some literature [113,131].

5.3.3 Adsorption and reaction of atomic deuterium with methanol covered Pd(111)

Dosing a methanol covered Pd(111) surface with atomic deuterium leads to significant changes in the primary adsorbate. Fig. 5.6 shows multiplexed desorption spectra obtained after exposing a methanol pre-covered surface (1.6 L) to 26 L of atomic deuterium, at a substrate temperature of 130 K. The most significant change as compared to Fig. 5.3 is observed in the methanol desorption peak. The double peak of the chemisorbed (195 K) and physisorbed (160 K) layer is replaced by a single peak around 180 K, with a small shoulder around 200 K.

The important observation is, however, that in the same temperature range additional desorption of the masses m=33 and m=34 can be clearly observed. Partial deuteration of the hydroxyl as well as the methyl group is apparently possible by impinging atomic deuterium. A second evident feature of Fig. 5.5 is the almost vanishing hydrogen peak. Although some of the hydrogen is contained in the HD peak, the total amount of desorbing hydrogen is significantly smaller than that in Fig. 6.3, whereas the CO signal is slightly increased. The most straightforward explanation for this observation is that some of the adsorbed hydrogen has been removed by impinging deuterium due to an Eley-Rideal reaction ($D_{imping} + H_{ads} \rightarrow HD_{gas}$). The existence of such a reaction has been proven for H/D on Ni(110) [135] and on other metal surfaces [136,137,138,139]. We will address this point in more detail below.

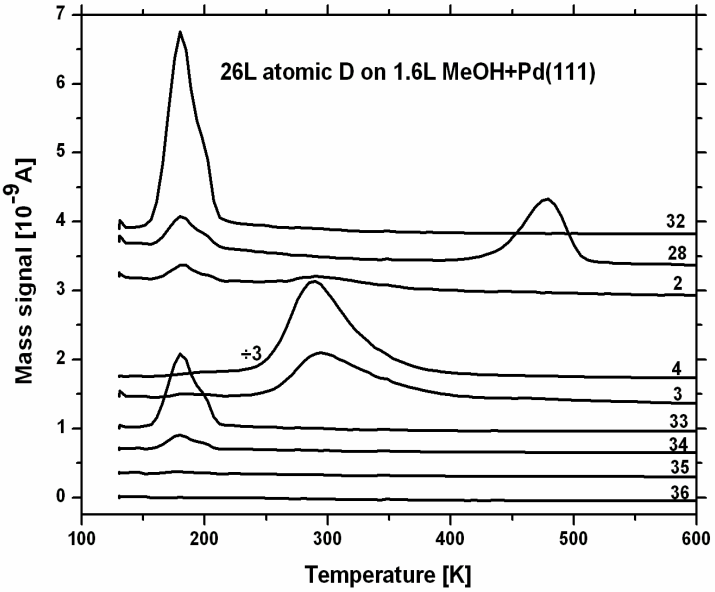

Fig.5.6. Thermal desorption spectra after dosing a methanol pre-covered Pd(111) surface (1.6 L MeOH) with 26 L atomic deuterium at 130 K. Note the different scale for m = 4.

A further increase of the atomic deuterium exposure leads to enhanced deuteration of the methanol molecules, as shown in Fig. 5.7 for the highest D exposure of 416 L used in this work. Most significant is the appearance of all types of deuterated methanol, from mass 32 (CH_3OH) through mass 36 (CD_3OD). In addition, the amount of CO increases by a factor of 4 compared to the non D-dosed methanol layer and also the total amount of desorbing hydrogen increases again. From these results we can draw the following qualitative conclusions: impinging deuterium atoms can exchange with hydrogen atoms of the methanol molecule, without breaking the molecule, as well as contribute to enhanced dehydrogenation of the methanol molecule. We conclude this from the similar shape of all methanol desorption peaks around 200 K, for m=32 through m=36, and from the increased CO and (H_2 + HD) signals with increasing D exposure.

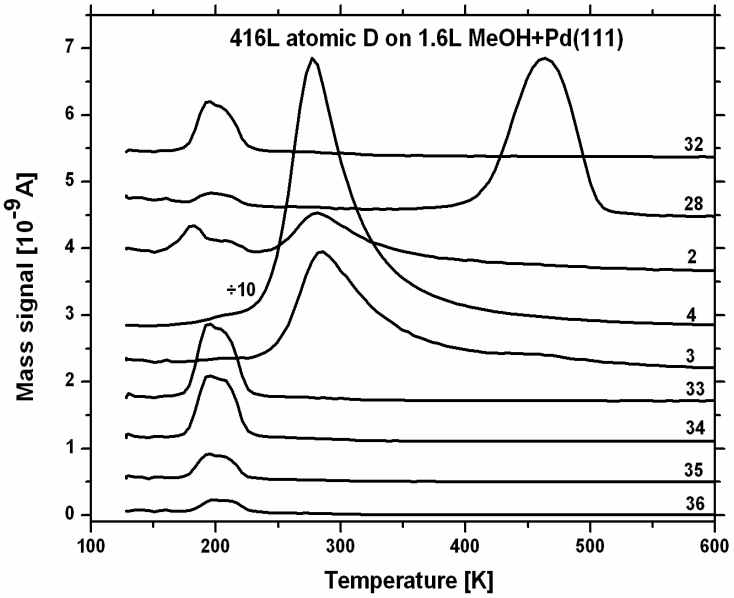

Fig.5.7. Thermal desorption spectra after dosing a methanol pre-covered Pd(111) surface (1.6 L MeOH) with 416 L atomic deuterium at 130 K. Heating rate: 2 K/s. Note the different scale for m = 4.

In Fig. 5.8 we present quantitative data for all relevant desorption products after dosing a methanol covered surface (exposure:1.6 L) as a function of the atomic deuterium exposure. The total amount of desorbing hydrogen has been obtained from the m = 2 and m = 3 signals, using the formula, I(hydrogen-total) = I(H_2) + 0.5·I(HD)/0.63. The relative correction factors *C* for the HD and D_2 sensitivities of our mass spectrometer, with respect to the hydrogen sensitivity, have been experimentally determined from saturation desorption spectra of pure hydrogen, pure deuterium and H/D mixtures on Pd(111): $C(H_2)$ = 1, C(HD) = 0.63, $C(D_2)$ = 0.27. The quantitative amount of the individual desorption products has been calculated by using a calibration procedure as described in detail elsewhere [6]. Furthermore, we have assumed that the mass spectrometer sensitivity is equal for all deuterated methanol species, CH_3OH through CD_3OD.

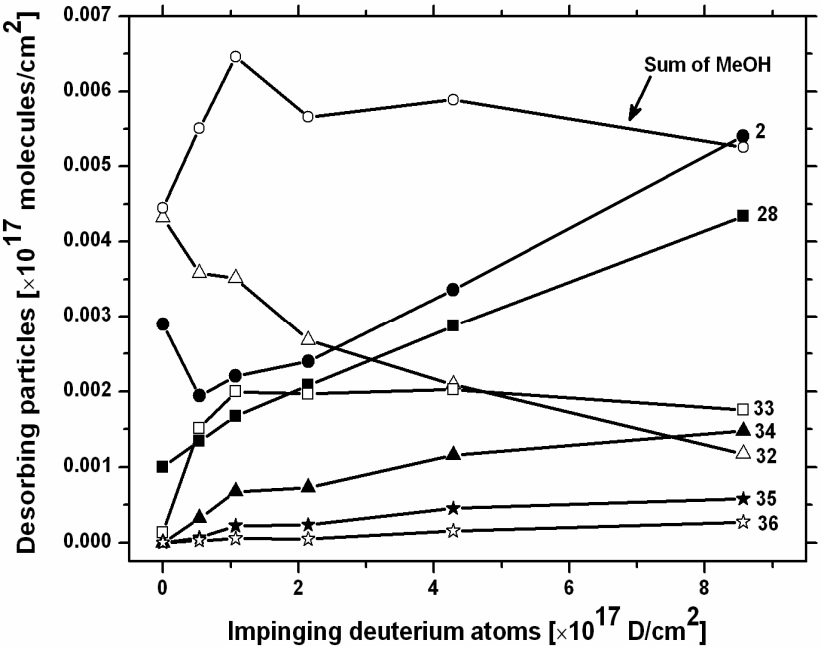

Fig.5.8. Number of desorbing particles of the individual reaction products after dosing a methanol pre-covered Pd(111) surface (1.6 L MeOH) to different amounts of atomic deuterium at 130 K. For details see text.

Several interesting findings can be deduced from Fig. 5.8. First of all, the amount of pure methanol (m = 32) decreases significantly with increasing D exposure, and consequently the amount of deuterated methanol increases. However, the probability to produce multiple deuterated methanol decreases rapidly from methanol-D1 (m = 33) to methanol-D4 (m = 36). From the initial increase of the amount of deuterated methanol with respect to the impinging D-atoms we obtain the following initial deuteration probabilities: 2.9×10^{-3} MeOH-D1/D-atom, 6.5×10^{-4} MeOH-D2/D-atom, 2.0×10^{-4} MeOH-D3/D-atom and 5×10^{-5} MeOH-D4/D-atom. Interestingly, the total amount of desorbed methanol molecules (sum of methanol-D0 through methanol-D4) as a function of D exposure shows a rather strange behaviour: It first increases and only later on it decreases again. This is most probably due to an experimental artefact: the cracking of the higher deuterated methanol molecules partially contributes to the lower masses and hence falsify the signal. Unfortunately, only for some of the deuterated methanol species the cracking patterns are available and therefore a quantitative correction is not possible. Furthermore, it is not clear if the mass spectrometer sensitivity for all deuterated methanol (D0-

D4) is indeed the same, as assumed in this work. Nevertheless, one can estimate that in this case more than 50% of the methanol undergoes dehydrogenation at the highest D exposure in Fig. 5.8.

With respect to the hydrogen evolution we see first a fast decrease and subsequently a continuous rise of the total amount of desorbing hydrogen. As already outlined above, we attribute the initial decrease to the abstraction of pre-adsorbed hydrogen atoms by an Eley-Rideal process. We have previously shown that prior to methanol adsorption at 130 K some co-adsorption of hydrogen always takes place [6]. This is also the reason why the ratio between desorbed H_2 molecules and CO molecules for pure methanol adsorption is 2.9 instead of 2.0, as one would expect (Fig. 5.8, zero D exposure). This pre-adsorbed hydrogen can apparently be effectively removed by D-atoms. The further increase of hydrogen, parallel to the increase of CO, is then attributed to the enhanced dissociation of methanol due to atomic deuterium impingement. The fact that after the induction period the H_2/CO ratio is always smaller than 2.0, throughout the whole D-exposure range, is an indication that hydrogen is also partially abstracted from the methanol molecules. From our data set we cannot unambiguously decide whether this abstraction takes place on adsorbed hydrogen, which has prior been split off the methanol molecule, or directly at the intact methanol molecule. A further question is how one should visualise the deuterium induced methanol dehydrogenation. Does it take place already at the low sample temperature of 130 K, or do the impinging D atoms lead to less stable methanol molecules, which then more easily dissociate during sample heating? For the pure methanol/Pd(111) system it is assumed that the partial dehydrogenation takes place in the same temperature range in which the desorption of the chemisorbed methanol takes place. We argue that the latter process is the more probable, because in case of the direct dehydrogenation at 130 K one would expect that these hydrogen atoms could be abstracted also with high efficiency and hence nearly no hydrogen (H_2, HD) should be visible in the desorption spectra at all.

The assumption that the methanol molecules are not directly dehydrogenated by the impinging D atoms is further corroborated by the very similar shape of the desorption spectra for all deuterated methanol species (see Fig. 5.7). Recombination of second or higher order would lead to significantly different desorption traces and can be ruled out. That means that the hydrogen within the methyl or hydroxyl group has to be directly replaced by D atoms, without involving the substrate.

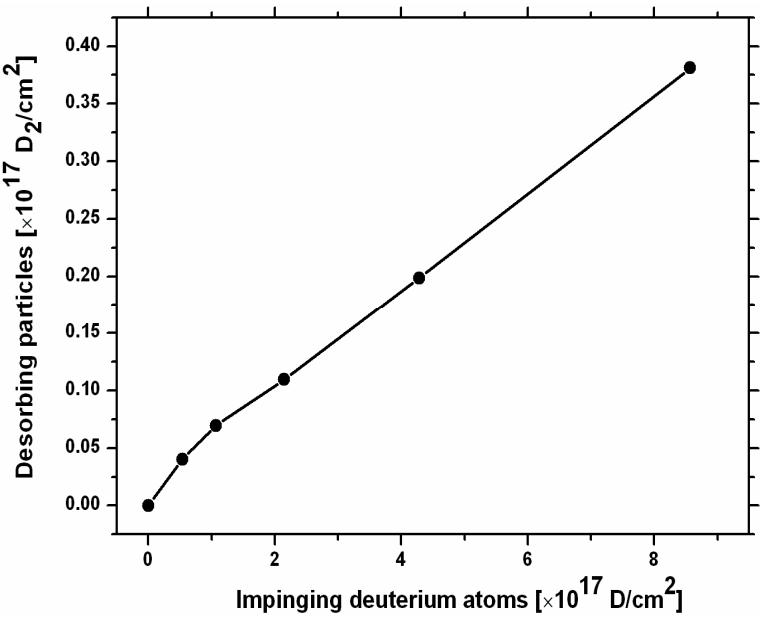

Fig.5.9. Number of desorbing deuterium molecules after dosing a methanol pre-covered Pd(111) surface (1.6 L MeOH) to different amounts of atomic deuterium at 130 K.

Finally we have to discuss the fate of the impinging deuterium atoms. We have seen that only some of the impinging deuterium shows up in form of deuterated methanol and of HD molecules. The overwhelming amount of deuterium desorbs in form of deuterium molecules. In Fig. 5.9 we show the relation between the number of impinging D atoms on the methanol covered Pd(111) surface and the desorbing D_2. We see that the deuterium atoms do not only adsorb on the palladium surface (which would yield a saturation coverage of about 1 monolayer (1 ML = 1.53×10^{15} atoms/cm^2)) but also absorb in the surface near region. The highest amount of desorbed deuterium in Fig. 5.9 corresponds to 25 ML and there is still no indication of saturation. The sticking coefficient (or in this case the uptake coefficient) is directly obtained from the slope of the curve in Fig. 5.9 yields. The initial uptake coefficient is 0.15, and the uptake coefficient levels off to a nearly constant value of 0.08 for higher deuterium exposure. It is often assumed that atomic deuterium (hydrogen) sticks with a probability of unity. This can only be true for the initial sticking on a clean surface, but even in this case it has been shown that the initial sticking coefficient might be smaller than unity [140]. On a surface already covered with deuterium (hydrogen) the uptake coefficient can be at most 0.5, due to the abstraction of already adsorbed species. The observed small initial sticking coefficient for D atoms of 0.15 is just due to the abstraction of pre-adsorbed hydrogen as described above. The value of 0.08 for higher D

exposure is basically governed by the activation barriers for surface penetration and bulk diffusion and will of course level off at still higher D exposure.

5.4. Summary and conclusions

A quantitative determination of the amount of desorbing reaction products based on in-line thermal desorption spectroscopy has been performed. Dosing a Pd(111) surface at 140 K to methanol up to saturation of the chemisorbed layer yields the desorption species of methanol, hydrogen and carbon monoxide. The total amount of adsorbed methanol has been determined to be 2.6×10^{14} MeOH/cm^2. Since water and some of the hydrogen stem from co-adsorption, which block adsorption sites for methanol, the measured methanol coverage has to be seen as a lower limit. While 62% of the adsorbed methanol desorb associatively, 38% of the adsorbed methanol dehydrogenate, resulting in desorption of hydrogen and carbon monoxide. No indication for C-O bond scission could be observed when methanol was adsorbed on the clean Pd(111) surface.

In addition to the quantitative study, the interaction of pre-adsorbed deuterium with impinging molecular and atomic deuterium on a methanol/Pd(111) has been investigated. While the pre-adsorbed deuterium reduces the probability to form chemisorbed methanol on the surface most of the methanol molecules are physisorbed on the surface. The amount of dehydrogenation during heating of the sample is also reduced compared with adsorption on the clean Pd(111) surface. Post-adsorption of molecular deuterium on the methanol covered surface does not significantly influence the dehydrogenation probability. However, there is again a trend to change chemisorbed methanol into physisorbed methanol. In both cases, for pre-adsorption and post-adsorption of deuterium, no indication of methanol deuteration could be found.

Considerable changes in the methanol layer are seen due to atomic deuterium exposure. All species of deuterated methanol, from CH_3OH to CD_3OD, can be observed in the TDS. Moreover, the dehydrogenation probability of methanol is increased. Another effect of atomic deuterium exposure is the removal of adsorbed hydrogen atoms by an Eley-Rideal mechanism. This is particularly effective for pre-adsorbed hydrogen from the residual gas, but to some extent also for the dehydrogenated hydrogen atoms. The impinging D atoms do not only react with the surface

species or adsorb on the surface, but they also penetrate the palladium surface, which leads to significant amounts of deuterium in the surface near bulk.

Chapter VI

6. Adsorption behaviour of nickel tetra-carbonyl on Cu(110)

Nickel tetra-carbonyl ($Ni(CO)_4$) is an organo-metallic complex which can easily be formed by CO on nickel surfaces at room temperature. On the other hand at somewhat elevated temperatures this compound can decompose again into nickel and CO. The synthesis and decomposition of this compound are described by the well known Mond process. Due to its easy preparation and decomposition it makes this volatile molecule highly toxic, because of the release of nickel in the body. On the other hand the special properties of nickel carbonyl are frequently exploited to deposit high purity nickel films on surfaces, in particular for the preparation of bimetallic surfaces and surface alloys.

6.1. Introduction

Nickel carbonyl may form at room temperature when CO gets in contact with nickel or nickel containing compounds such as stainless steel [141].Therefore nickel carbonyl is a common impurity in CO gas lines. $Ni(CO)_4$ can unintentionally be produced by storing CO in a stainless steel container or gas line. Even small amounts of nickel carbonyl in the CO atmosphere can be sufficient to contaminate surfaces by nickel and thus alter their adsorption and reaction properties [9]. Although this is a well known issue and precautions can be taken [142], we believe that in many cases unexpected and peculiar experimental results in the context of CO interaction with surfaces can be traced back to nickel carbonyl contaminations. For example, Enbæk et al. [143] have shown that the dissociation of CO on stepped nickel surfaces can be considerably increased by adding just minute amounts of nickel carbonyl to the gas phase. Given the important role CO is playing for many modern technologies, e.g. heterogeneous catalysis, plasma etching in

semiconductor industry, etc., the consequences of co-adsorption of nickel carbonyl during CO exposure should be considered.

6.2. Mass spectrum of $Ni(CO)_4$

The gas mixture of $CO+Ni(CO)_4$ was obtained after CO was stored in a stainless steel gas inlet system for about 3 month. However, in a second, similar gas inlet system, where we intentionally tried to obtain a $CO+Ni(CO)_4$ gas phase for comparison, no such gas mixture could be obtained. Thus, one has to conclude that the formation of nickel carbonyl has to be correlated with minute, non controllable catalyzing defects or impurities in the gas inlet system. In Fig. 6.1 the mass spectra of the isotropic gas phase, when introducing the gas from the clean CO gas line is shown.

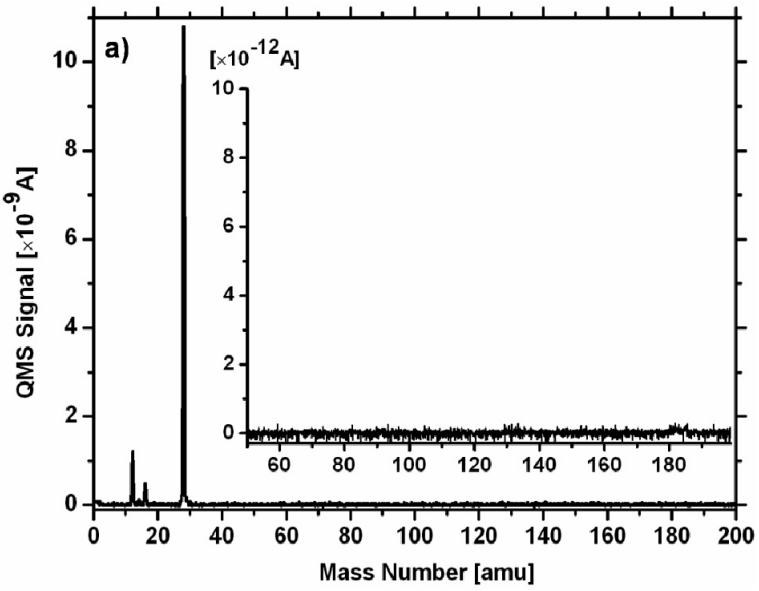

Fig.6.1. Mass spectrum of a clean CO gas phase at $4x10^{-8}$ Torr. The inserts show a three orders of magnitude higher magnification of the spectra.

In Fig. 6.2, the mass spectrum for the $CO + Ni(CO)_4$ mixture is presented. Only in the insert with a three orders of magnitude higher magnification the cracking pattern of nickel carbonyl can be observed in the latter case (Ni: 58 amu, NiCO: 86 amu, $Ni(CO)_2$: 114 amu, $Ni(CO)_3$: 142 amu, $Ni(CO)_4$: 170 amu; the signals at 60 amu and 88 amu stem from the Ni^{60} isotope).

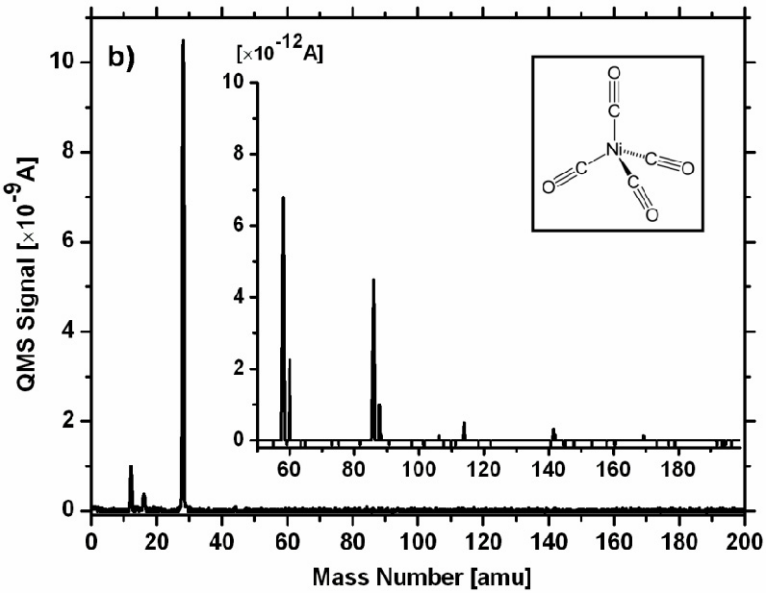

Fig.6.2. Mass spectrum of a CO + $Ni(CO)_4$ gas mixture as obtained in our particular case at a total pressure of $4x10^{-8}$ Torr. The inserts show a three orders of magnitude higher magnification of the spectra. The chemical structure of $Ni(CO)_4$ is also shown.

This gas mixture was used to investigate the adsorption of $Ni(CO)_4$ and co-adsorption of CO on the Cu(110) surface at low temperatures. From quantitative thermal desorption spectroscopy we were able to determine the relative effusion rate ratio of the CO/$Ni(CO)_4$ gas mixture to be about 1000:1. Gas dosing was performed by in-line dosing via a 1/8" stainless steel tube. The enhancement factor F_{CO} for CO dosing (ratio of the effective impingement rate between in-line dosing and off-line dosing) was experimentally determined for our setup to be about 5. All exposure values given in the text are effective values ($1L^* = F_{CO} \cdot 10^{-6}$ Torr·s) corresponding to the total pressure increase during dosing, which is mainly determined by the CO partial pressure.

6.3. Adsorption of CO+$Ni(CO)_4$ gas mixture at 110 K

As mentioned above, the CO/$Ni(CO)_4$ gas mixture consists of a high amount of CO. Therefore even small amounts of exposure quickly yields to a saturation layer of CO on the Cu(110) surface. CO saturation, at the adsorption temperature of 110 K, corresponds to 0.8 ML [144]. CO desorbs from Cu(110) around 210 K (α_1 peak) and exhibits a broad shoulder extending to about 150 K (α_2 peak) [145]. In our case these adsorption states are already saturated at an effective

exposure of about 2.5 L*. With increasing exposure a new, low temperature peak of m = 28 appears at ca. 140 K, designated as the γ_1 peak (Fig. 6.3a). This peak grows temporarily until a second peak of m = 28 appears at ca. 150 K, designated as the γ_2 peak (Fig. 6.3b). Interestingly, with further increase of exposure the γ_1 peak disappears again, while the γ_2 peak increases continually. This is a quite unexpected result and will be discussed in more detail below.

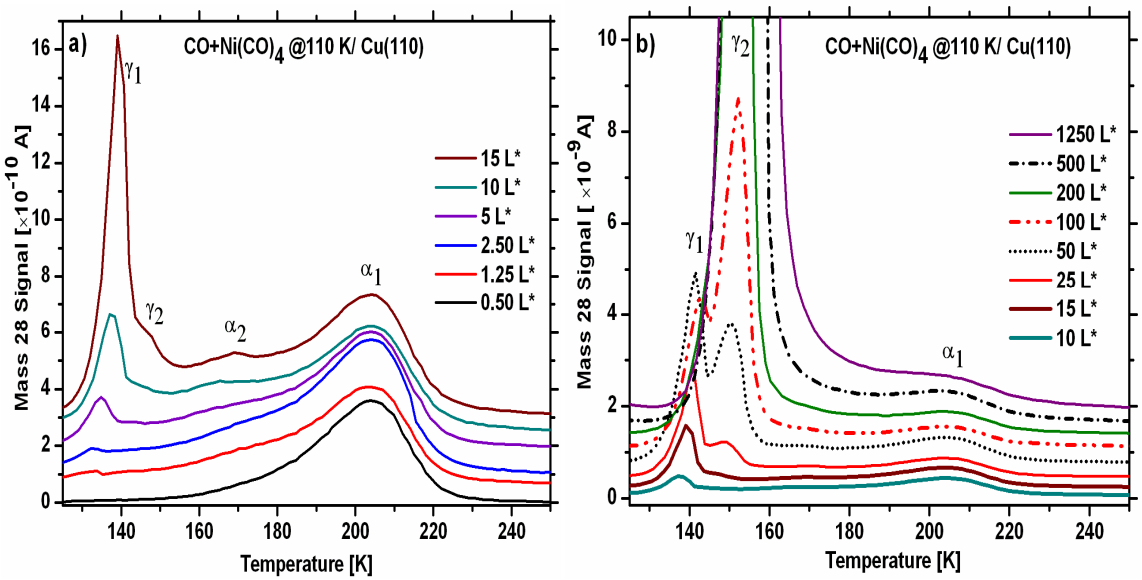

Fig.6.3a,b: Thermal desorption spectra (m = 28 amu) as a function of exposure to the CO + $Ni(CO)_4$ gas mixture. Adsorption temperature: 110 K, Heating rate: 2 K/s. The effective exposures via in-line dosing are given in L*, as described in the text.

First of all we could show that both peaks, γ_1 and γ_2, are actually due to $Ni(CO)_4$ desorption. Multiplexed desorption spectra for high exposure (Fig.6.4) exhibit all the masses corresponding to the cracking pattern of nickel carbonyl. When referencing to the CO signal (m=28) as 100 %, the following relative QMS signals for the other masses were obtained: m=58 (Ni): 13%, m=86 (NiCO): 12%, m=114 ($Ni(CO)_2$): 3.5%, m=142 ($Ni(CO)_3$): 2.5% and m=170 ($Ni(CO)_4$): 1.5%. In addition, signals corresponding to the Ni isotope Ni^{60} were observed in the mass spectrum. Actually, the intensities of the $Ni(CO)_x$ species with respect to the CO signal are significantly larger than those presented in the standard NIST spectrum [146], where the ratio of m=58/m=28 is less than 1%, and the higher masses are even less pronounced. We believe that this is due to the fact that nickel carbonyl readily cracks at any surface and it is therefore not possible to detect the

correct cracking pattern when measuring an isotropic gas of "nickel carbonyl". However, by directly detecting a flux of desorbing $Ni(CO)_4$ with an in-line mass spectrometer, as in our case, will yield the true cracking pattern. Of course, the electron energy for impact ionisation will also influence the cracking pattern. In our case the energy of the ionising electrons was 70 eV.

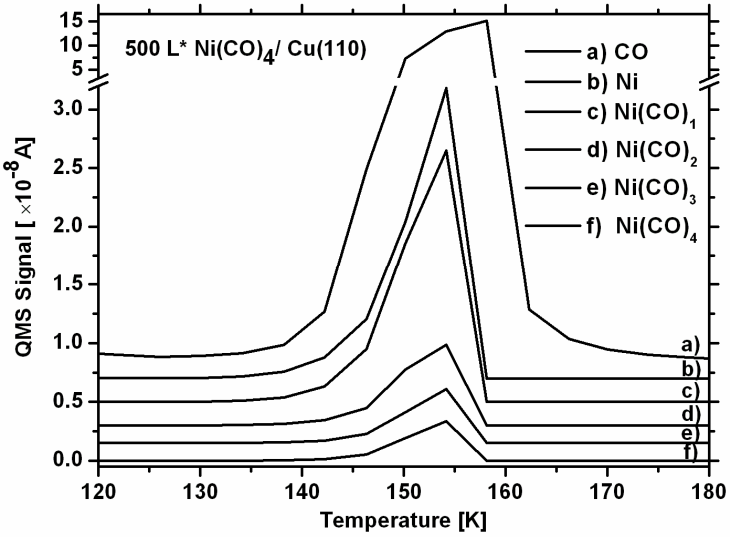

Fig.6.4. Multiplexed thermal desorption spectra of nickel carbonyl from Cu(110) after exposing the surface to 500 L* of the CO + $Ni(CO)_4$ gas mixture at 110 K.

Auger electron spectra for high exposure of the nickel carbonyl condensation on Cu(110) compared with the clean surface are presented in Fig.6.5. The copper signal at 920 eV disappears with the exposure of 500 L* $Ni(CO)_4$. Huge amounts of carbon (at 270 eV) and oxygen (at 510 eV) together with the nickel Auger peaks are clear evidence of $Ni(CO)_4$ condensation on Cu(110).

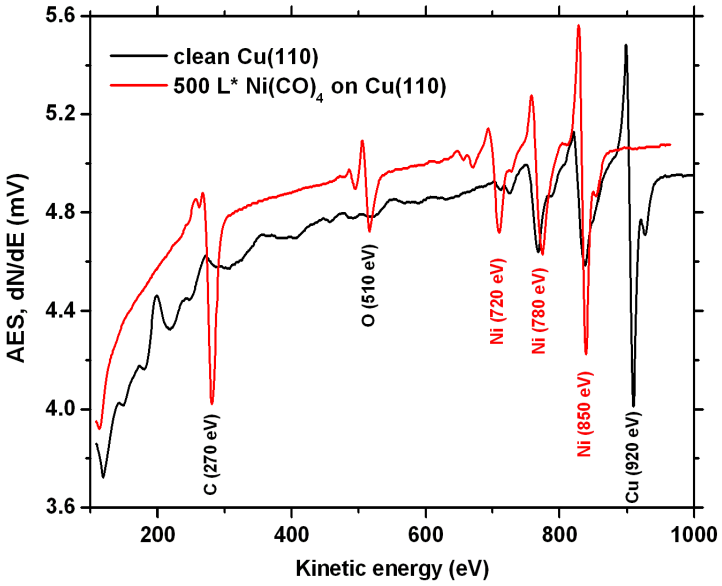

Fig.6.5. Auger electron spectra of clean Cu(110) and after exposure of 500 L* $Ni(CO)_4$ at 110 K on Cu(110).

6.4. Quantitative determination of condensed $Ni(CO)_4$

Having verified that the γ peaks stem from nickel carbonyl desorption, the question arises why first a more weakly bound desorption state appears, before it changes into a more strongly bound state. For a proper discussion of this issue a calibration of the carbonyl desorption spectra is necessary. This has been done by comparing the CO desorption spectrum of the saturated CO chemisorbed layer with the corresponding C-Auger signal and then searching for the m=28 desorption spectrum of the γ-peak which corresponds to a twice as large C-Auger signal. This was reached at an effective exposure of about 350 L* in Fig.6.6. The corresponding spectrum (by interpolating between the 200 L* and 500 L* in Fig. 6.3b) can be associated with the amount of nickel carbonyl molecules equivalent to ¼ CO molecules of the CO saturation layer (which corresponds to 0.8 ML = $8.7 \cdot 10^{14}$ CO/cm^2 [145]), neglecting the attenuation of the Auger signal in a first approximation. The result of this calculation is that only about $2 \cdot 10^{13}$ $Ni(CO)_4$/cm^2 contribute to the γ_1 peak. Taking into account the size of the nickel carbonyl molecule (6.7 Å in diameter) a dense packed monolayer would correspond to $2.2 \cdot 10^{14}$ $Ni(CO)_4$/cm^2.

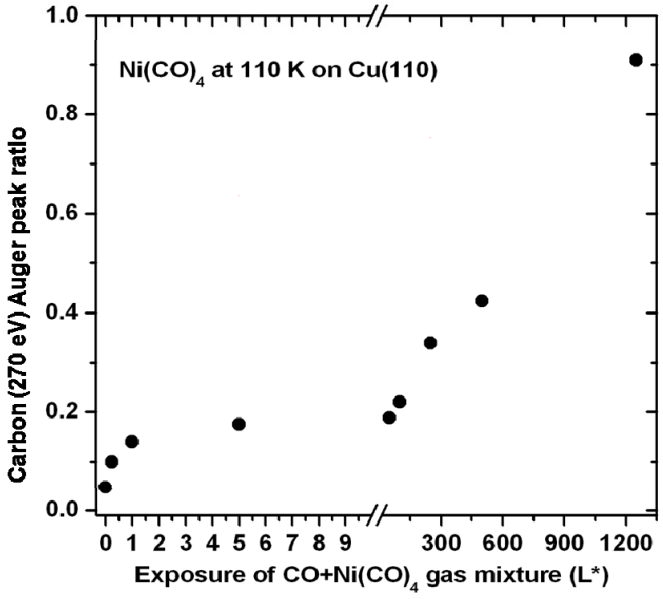

Fig.6.6. Auger peak height of carbon at 270 eV on Cu(110) after exposing the surface with the $CO + Ni(CO)_4$ gas mixture at 110 K.

Thus, the saturation of the γ_1 peak is only about 10% of a monolayer. With increasing coverage this state disappears and it is incorporated into the γ_2 state, which shows the typical features of a zero order desorption (common leading edge), i.e. desorption from a multilayer. A plausible explanation for this rather unusual desorption behaviour could be that for the adsorbed monomers (at low coverage) only 3 ligands of the $Ni(CO)_4$ molecule contribute to the bonding, whereas for higher coverage nucleation takes place and in the bulk phase all 4 CO ligands participate in the bonding. A similar desorption feature has been observed for large organic molecules (benzene on Ru(001) [147], HAT-CN on Au(111) [148], where also structural changes in the adsorbed layer have been attributed to the shift of the desorption peaks.

6.5. Determination of desorption energy and frequency factor

The desorption energy (heat of evaporation) of the $Ni(CO)_4$ bulk phase and the pre-exponential factor can be deduced from the leading edge of the multilayer desorption spectrum, according to the desorption rate equation for zero-order desorption [21]:

$$R_{des} = \Theta_0 \nu \cdot \exp\left(\frac{-E_{des}}{k_B T}\right) \tag{6.1}$$

Here Θ_0 is the (constant) number of molecules per surface unit area, ν is the frequency factor, E_{des} the desorption energy, k_B the Boltzmann factor and T the surface temperature. A plot of $ln(R_{des})$ vs. $1/T$ should yield a straight line and from the slope of this line the desorption energy can be calculated.

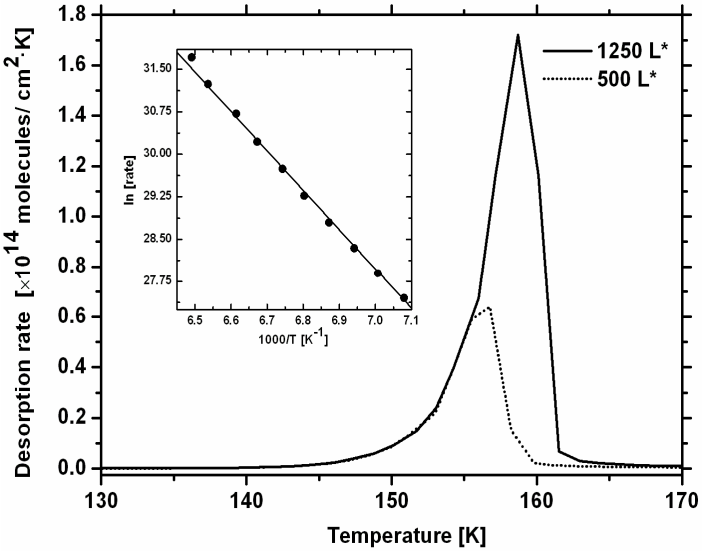

Fig.6.7. Quantitative multilayer desorption spectrum of $Ni(CO)_4$ from Cu(110) for two different exposures, demonstrating the zero-order desorption. The insert shows the plot of $ln(R_{des})$ vs. $1/T$, according to the Polanyi-Wigner equation for the determination of the desorption energy and the frequency factor.

From the plot as shown in Fig. 6.7 a desorption energy of 0.61±0.03 eV was obtained. This value is significantly larger than that found in the literature (0.31 eV [149]). We believe that this is due to the fact that Clausius-Clapeyron type measurements of the heat of evaporation, in which the vapour pressure of a material is determined as a function of the temperature, have to fail in this case because of the easy cracking of nickel carbonyl.

Interestingly, also the pre-exponential factor ($\Theta_0 \cdot \nu$), which can be deduced from the intercept of the regression line in Fig. 6.7 with the Y-axis, is extremely large. (We note that for this evaluation the desorption rate has to be known quantitatively. In our case we have achieved this

via Auger measurements, as described above). We obtained a value of $1.8 \cdot 10^{33}$ $cm^{-2}s^{-1}$. Taking into account the monolayer density of $2.2 \cdot 10^{14}$ $Ni(CO)_4/cm^2$ this yields a frequency factor $\nu = 8.2 \cdot 10^{18}$ s^{-1}. This value is considerably larger than the typically used values of about $1 \cdot 10^{13}$ s^{-1} for the desorption of small molecules.

According to classical transition state theory (TST) the desorption rate for a first order process, *i.e.*, for non-associative molecular desorption, can be described as follows [150]:

$$r_{des} = \kappa\Theta \frac{k_B T}{h} \frac{q^*}{q_{ads}} \exp\left(\frac{-E_{des}}{RT_s}\right) = \kappa\Theta \frac{k_B T}{h} \exp\left(\frac{\Delta S}{R}\right) \exp\left(\frac{-E_{des}}{RT_s}\right) \tag{6.2}$$

Where the κ is a transmission coefficient, which is usually taken as unity, q^* and q_{ads} are the partition functions of the molecules in the transition state and the adsorbed phase, respectively, ΔS the entropy change during desorption and h the Planck constant. (Note that the transition state for a desorption system with non-activated adsorption is equivalent to the final state, *i.e.*, the gas phase. Furthermore, the term q^* actually denotes the partition function for all modes in the activated complex without that of the reaction coordinate [151]). Thus, the desorption rate is a function of both E_{des} and ΔS, *i.e.*, the ratio of the molecular partition functions in the gaseous and adsorbed state. For a simple (mono-atomic) desorption system the entropy change can be neglected, and the pre-exponential factor reduces to $k_B T/h$, which is 1×10^{13} s^{-1} for T = 500 K. However, for large molecules significant changes of the partition functions of the adsorbed and the free gaseous state are expected due to the possible excitation of rotational and vibrational states. Such high pre-exponential factors (up to 10^{25} s^{-1}) were indeed observed for the desorption of large organic molecules [148,152,153,154]. Thus, the relatively high value of $\nu = 8.2 \cdot 10^{18}$ s^{-1} for nickel carbonyl desorption from the multilayer suggests that the adsorbed phase is rather immobile prior to desorption, due to the directional bonds in the tetrahedral coordination geometry of the bulk phase.

6.6. Influence of the surface temperature on the adsorption and decomposition of $Ni(CO)_4$

Finally, we would like to show the influence of the surface temperature on the adsorption and decomposition of nickel carbonyl on Cu(110). In Fig. 6.8 desorption spectra are shown for m=28 amu after exposure of 30 L* of the gas mixture at different surface temperatures. Apparently, adsorption of nickel carbonyl at a surface temperature above the desorption temperature of the carbonyl leads to a modification of the surface resulting in extra CO desorption peaks between 220 K and 380 K. We could show that these new CO desorption peaks are due to the desorption from Ni-Cu ensemble sites [9]. Nickel tetra-carbonyl can be used to deposit high purity nickel films on surfaces, in particular for the preparation of bimetallic surfaces and surface alloys. [9,155,156].

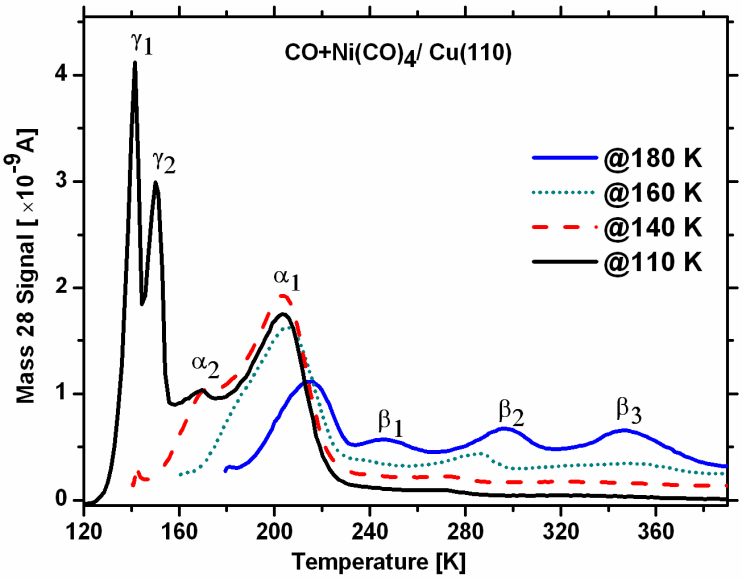

Fig.6.8. Desorption spectra (m = 28) after exposing the Cu(110) surface to 30 L* of the CO + $Ni(CO)_4$ gas mixture at different surface temperatures. The peaks γ_1 and γ_2 stem from nickel carbonyl desorption, α_1 and α_2 are due to CO desorption from clean copper sites, β_1, β_2 and β_3 result from CO desorption from Cu-Ni bimetallic adsorption sites.

6.7. Summary and conclusions

We have shown that nickel tetra-carbonyl ($Ni(CO)_4$) desorbs from a CO covered Cu(110) surface around 150 K, exhibiting a zero-order desorption reaction. The evaluation of the desorption spectra according to the Polanyi-Wigner equation yields a desorption energy of 0.61 eV, which is considerably larger than the literature value for the heat of evaporation of 0.31 eV. We believe that the heat of evaporation cannot easily be obtained from equilibrium measurements due to the high propensity for nickel carbonyl decomposition. The pre-exponential factor for nickel carbonyl desorption is $8.2 \cdot 10^{18}$ s^{-1}. This rather large value suggests, according to transition state theory, that the entropy change during desorption is rather large, or in other words, that the molecules are rather immobile prior to desorption. An interesting feature of nickel carbonyl desorption is that the first 10% of a monolayer exhibit a clearly distinct desorption peak (γ_1), which disappears with increasing coverage and becomes incorporated into the emerging main desorption peak (γ_2). This is attributed to the weaker bonding of the nickel carbonyl monomers to the CO covered copper surface (via three CO ligands) before the nucleation into bulk islands starts, where the molecules are coordinated via four ligands. Adsorption of nickel carbonyl at higher substrate temperature leads to decomposition of the molecules and to the formation of a bimetallic Ni-Cu(110) surface, on which new adsorption states for CO are created.

Chapter VII

7. Adsorption of CO on Ni/Cu(110) bimetallic surface prepared by $Ni(CO)_4$ dissociation and electron beam evaporation

A very attractive model system of bimetallic surfaces is the Ni/Cu system. These bulk metals have very similar geometric properties. They both crystallize in the face centered cubic (fcc) system and their lattice constants are 3.52 Å (Ni) and 3.61 Å (Cu), respectively. On the other hand their electronic and magnetic properties are very different. The non-magnetic noble metal copper has a filled d-band and therefore the electron density at the Fermi level is rather small. The magnetic transition metal nickel has a partially filled d-band, which leads to a high electron density at the Fermi level. This difference in the electronic structure is responsible for the higher chemical reactivity of Ni as compared to Cu, However, for the proper activity and selectivity of a particular catalyst often a very distinct surface reactivity is required. A too low reactivity may result in a poor turn over frequency, whereas a too high reactivity of the surface atoms can lead to permanent adsorption of some reaction partners and therefore to poisoning. This is exactly what makes the bimetallic surfaces so attractive, because one can expect to be able to tune the surface reactivity at will.

7.1. Introduction

Bimetallic surfaces play a decisive role in heterogeneous catalysis. Due to the particular arrangement of the different atoms at the surface, new reaction pathways can be opened and both the activity and selectivity of catalysts can be improved. Various concepts for the specific reaction properties of bimetallic surfaces have been discussed in the literature, amongst them the

most important are the (electronic) ligand effect and the (geometric) ensemble effect [157]. In recent years this subject has been addressed in several excellent review articles, e.g. by Campbell [158], Goodman [159], Rodriguez [160], Ponec [161] and Chen et al. [162], to name just a few. Very recently increased effort has been made to get an improved understanding of the properties of bimetallic surfaces by using theoretical approaches, mainly by using density functional theory (DFT) calculations [162, 163, 164, 165].

Cu-Ni bimetallic surfaces have attracted the interest of surface scientists starting in the 1950´s. One of the most important reason is that Ni and Cu have similar geometry but very different electronic properties. Both metals have fcc crystal structures with lattice constants of 3.52 Å (Ni) and 3.61 Å (Cu), respectively. The relatively small lattice mismatch of 2.4% allows pseudomorphic growth on top of each other [166]. On the other hand, their electronic properties are very different. Copper, being a coinage metal has a completely filled *3d*-band and therefore no *d*- states at the Fermi level; in conrtrast, nickel, being a transition metal with a partially filled *3d*-band, has a high density of states at the Fermi level. This difference in the electronic structure is responsible for the higher chemical reactivity of Ni as compared to Cu.

In this work we use carbon monoxide as a probe molecule to test the adsorption properties of a Ni/Cu(110) bimetallic surface. It is known that CO desorbs from a Cu(110) surface already at around 210 K [144,145], whereas CO is much more strongly adsorbed on Ni(110) and desorbs around 420 K [167, 168]. In an early experiment Yu, Ling and Spicer [169] made an attempt to study the CO interaction with the surface of a 10%Cu/90%Ni bulk alloy, where the surface composition was varied by heat treatments and sputtering. They came to the conclusion that the CO activation energy of desorption from a Ni site decreases linearly with increased Cu concentration on the surface, indicating that long range electronic effects (ligand effects) are dominating the CO interaction. A somewhat later performed theoretical study by Castellani [170], using a cluster approach and the extended Hückel method to calculate the electron energies, seemed to corroborate the experimental data. In the present work, however, we arrive at a quite different conclusion, namely that CO on a Ni/Cu(110) surface exhibits several very distinct desorption peaks, which indicates that local site effects (ensemble effects) play a major role for CO adsorption. This assumption is corroborated by density functional theory (DFT) calculations.

7.2. Preparation of the nickel-copper bimetallic surface

7.2.1 Nickel tetra-carbonyl ($Ni(CO)_4$)

For the preparation of the nickel-copper bimetallic surface we applied two different methods. In the first case a nickel covered Cu(110) surface could be prepared by dosing a gas mixture of CO and $Ni(CO)_4$ at the appropriate surface temperature (180 K). This mixture was unintentionally obtained when CO was filled into a stainless steel gas inlet system and after a residence time of about 3 month. A semi-quantitative calculation yielded a mixture ratio of $CO:Ni(CO)_4 \approx 1000:1$ for the gas effusing from the doser. The reason for the synthesis of this gas mixture in the gas line is not quite clear. It is probably related to some catalyzing defects or impurities in the gas inlet system. It is known that nickel carbonyl, which is highly toxic, can easily be formed by CO on nickel surfaces [171,172]. However, the storage of CO in another stainless steel gas line did not result in a detectable amount of nickel carbonyl after the same residence time. Nevertheless, we took advantage of this gas mixture to study the concomitant decomposition of nickel carbonyl and the adsorption of CO on the altered Cu(110) surface. This work should also demonstrate that small traces of $Ni(CO)_4$ in the CO gas phase can cause tremendous (usually unwanted) effects in CO adsorption and desorption studies.

7.2.2 Nickel evaporation

Alternatively, to check the validity of the above described preparation method, nickel was evaporated onto the Cu(110) surface by a commercial electron beam evaporator. The amount of evaporated nickel was measured with a quartz microbalance, which could instead be positioned in front of the evaporator. This allowed the quantitative determination of the nickel coverage and hence of the stoichiometry of the bimetallic surface. Combined with Auger electron spectroscopy also the influence of the surface temperature on the formation of the bimetallic layer could be studied. CO adsorption on the such prepared Ni/Cu(110) surface was then performed typically at 130 K.

7.3. Computational details

The aim of the calculations was to identify the various adsorption configurations of CO on the bimetallic surface which lead to the observed discrete desorption peaks. The calculations were performed with the Vienna ab-initio simulation package (VASP) [173]. Electronic exchange and correlation were described in the general gradient approximation (GGA), using the functional proposed by Perdew, Burke and Ernzerhof (PBE) [61]. The wave function is represented by a plane-wave basis set with an energy cut-off of 400 eV. The ion cores were represented by the projector augmented wave (PAW) method [174]. A Monkhorst-Pack mesh of 11 x 11 x 1 *k*-points was used for the (1x1) surface unit cell (5 x 5 x 1 *k*-points for the (2x2) unit cell), to achieve an accurate description of the density of states near the Fermi level.

The substrate was modeled by slabs typically consisting of 5 copper layers and one nickel layer with the appropriate coverage. The periodicity of the nickel over-layer and of the CO layer was modeled by a (2x2) unit cell with 1 - 4 atoms (molecules) in the basis. The slabs were separated by a 13 Å thick vacuum. The coordinates of the upper two copper layers and the nickel layer, as well as that of the CO molecules, were allowed to relax, while the remaining substrate layers were fixed at the bulk position. For our calculations we used an energy difference of $\Delta E = 0.5$ meV for the break conditions of the relaxation loop to determine the final positions of the CO molecules.

7.4. Adsorption of a CO + $Ni(CO)_4$ gas mixture on Cu(110)

In Fig. 7.1, a set of CO desorption spectra taken after in-line dosing a Cu(110) surface at 180 K with different exposure of a CO + $Ni(CO)_4$ gas mixture is shown. Exposures are given in Langmuir equivalents ($1L = 10^{-6}$ Torr·s) obtained from the isotropic CO pressure increase and by taking into account an experimentally determined enhancement factor of 5.0 for in-line dosing of CO. Small exposure values (up to about 2.5 L) lead to a rapidly increasing desorption peak at around 210 K, which is due to desorption of CO from the still nearly clean Cu(110) surface [144,145].

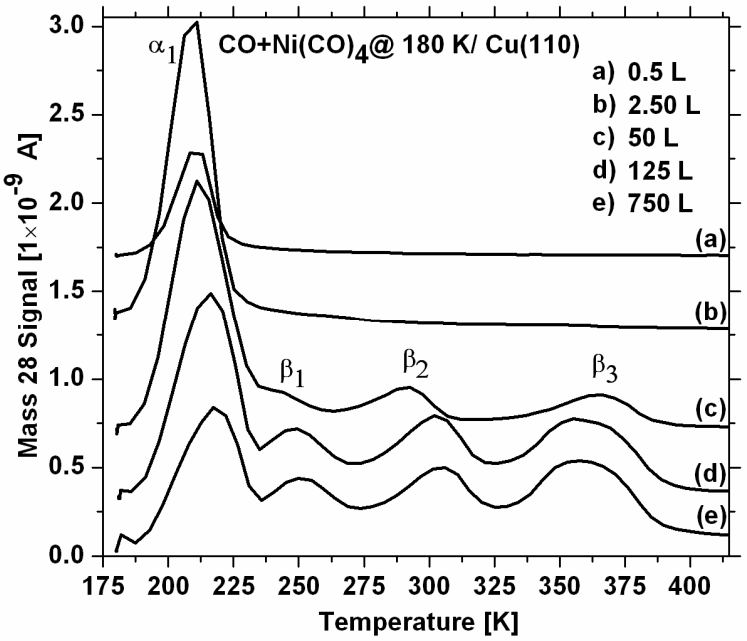

Fig.7.1. Set of CO desorption spectra after dosing the initially clean Cu(110) surface with various amounts of the CO + $Ni(CO)_4$ gas mixture at 180 K. Heating rate: 2 K/s.

With increasing exposure new desorption peaks start to emerge at around 250 K, 300 K and 360 K. These peaks do not show up when the sample is dosed with the same exposure of pure carbon monoxide. It is obvious that these new peaks have to be correlated with nickel on the surface, resulting from dissociation of nickel tetra carbonyl, as verified by Auger electron spectroscopy. While these new desorption peaks, labeled β_1 (250 K), β_2 (300 K) and β_3 (360 K), increase with increased dosing of the gas mixture, the intensity of the CO desorption peak around 210 K (α_1) goes through a maximum at about 2 L and decreases again for higher exposure. In addition to that the desorption peak maxima of the α_1 peak shift by about 10 K to higher temperature. The corresponding uptake curves for the individual desorption peaks are shown in Fig. 7.2. Above 300 L the β peaks saturate, indicating a saturation of the nickel coverage.

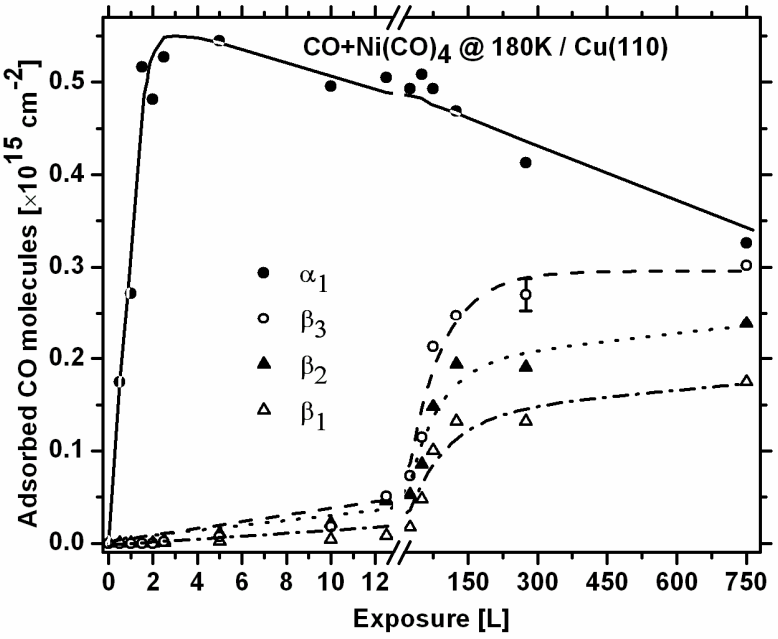

Fig.7.2. Uptake curves for CO when dosing the Cu(110) surface with the CO + $Ni(CO)_4$ gas mixture, as obtained from a series of TDS, including those in Fig. 7.1.

LEED patterns of a clean and a ½ monolayer Ni covered Cu(110) surface are shown in Fig.7.3a and 3b. From the observed (1x2) LEED pattern and by comparison with the CO desorption spectra after calibrated nickel evaporation (see below) we suppose that the maximum nickel coverage under these experimental conditions corresponds to about ½ monolayer.

Finally, we have exposed the Cu(110) surface to the gas mixture for extended time at 400 K. After a very high exposure (37000 L) and a subsequent heating to 500 K an Auger analysis showed a clean nickel spectrum, without any detectable Cu signal or signals from other impurities, like carbon. The corresponding LEED pattern showed a (1x1) structure (Fig.7.3c). This demonstrates that under these experimental conditions a thick epitaxial nickel film can be grown on the Cu(110) surface by decomposition of nickel carbonyl. The desorption spectrum of CO from this surface was equivalent to literature data for CO desorption from a Ni(110) surface [167, 168]. It is important to emphasize that such a thick nickel layer on Cu(110) remains stable over extended time even at the rather high sample temperature of 500 K. On the other hand, for small nickel coverages, as prepared at 180 K, some of the nickel atoms dissolved in the bulk during heating of the sample to 500 K.

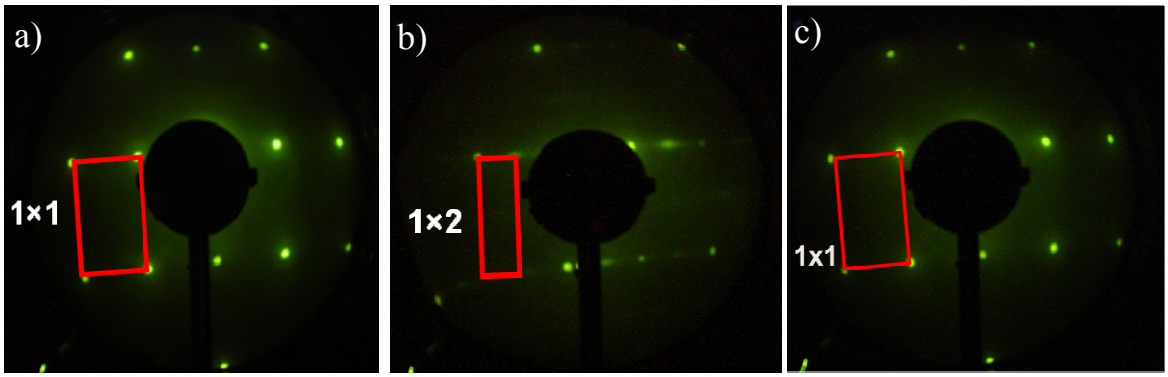

Fig.7.3. a) A (1x1) LEED pattern of the clean Cu(110) surface, b) A (1x2) LEED pattern of the Ni/Cu(110) surface, c) A (1x1) LEED pattern of Ni(110) (an epitaxially grown thick Ni film on Cu(110)). U_B=120 eV.

7.5. Adsorption of CO on a Ni/Cu(110) surface prepared by Ni evaporation

In order to double-check the above described desorption behavior of CO we have performed CO adsorption/desorption experiments on a nickel covered Cu(110) surface prepared by direct evaporation of nickel. The advantage of this procedure is that the amount of evaporated nickel can be determined quantitatively by a quartz microbalance. Furthermore, the sample temperature can be independently adjusted for nickel evaporation and CO adsorption, respectively. In Fig. 7.4 a series of CO saturation desorption spectra (CO exposure: 3 L) from a Cu(110) surface with increasing amounts of nickel is shown. Nickel was evaporated at 175 K and afterwards CO was exposed at 130 K. One can clearly see that on the nickel modified Cu(110) surface the same new adsorption sites β_1, β_2 and β_3 evolve as after decomposition of nickel carbonyl. The additional shoulder at around 175 K (α_2-peak) stems from CO adsorption on the clean Cu sites due to the lower adsorption temperature [145].

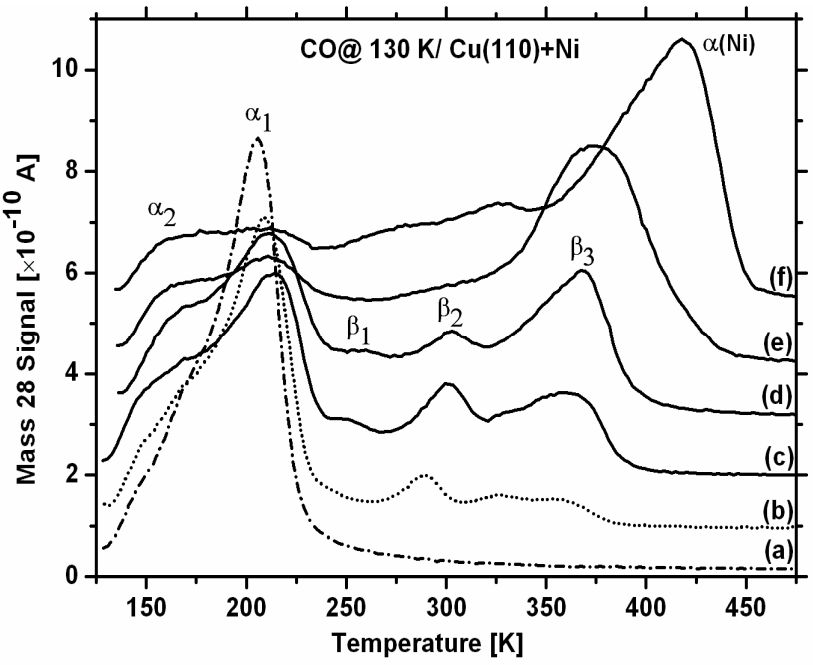

Fig.7.4. CO desorption spectra after dosing 3 L CO at 130 K on a Cu(110) surface, covered with various amounts of nickel. Nickel was evaporated onto the surface at 175 K. (a): clean surface, (b): 0.05 ML Ni, (c): 0.19 ML Ni, (d): 0.27 ML Ni, (e) 1.02 ML Ni, (f): 4.4 ML Ni.

Similarly as for the nickel carbonyl decomposition the CO peak from clean copper at 210 K (α_1-peak) decreases with increasing nickel coverage while the new desorption peaks start to increase. The only difference is that the β_1 peak, and to some extent also the β_2 peak, is not so well pronounced than in the case of carbonyl decomposition. The β_3 peak, which is located at around 360 K, also increases with increasing nickel coverage, but eventually starts to shift to higher temperature (at $\Theta_{Ni} > 1$ ML) with a final peak maximum at 420 K. This is close to the desorption temperature of CO from a pure nickel surface (designated as α(Ni) peak) [167,168]. For this high nickel coverage the original β peaks are rarely visible, indicating that these peaks are related to the bimetallic surface. It should be noted that after each desorption run the surface had to be prepared again, because some of the adsorbed nickel dissolves in the bulk during heating up to 500 K, similarly as in the case of nickel carbonyl decomposition.

If one compares the new adsorption peaks, they are more pronounced when Ni is produced on the surface by decomposition of $Ni(CO)_4$, than by physical vapor deposition of nickel. However, when Ni is evaporated onto a CO pre-covered Cu(110) surface or in a CO atmosphere, then the

desorption spectra are very similar to that obtained after nickel carbonyl decomposition. Furthermore, the desorption features depend on the surface temperature during Ni evaporation. This hints to a very delicate influence of the local atomic arrangement at the bimetallic surface on the adsorbate and to interplay between the CO adsorbate and the surface atoms. It is known that nickel atoms adsorbed on a copper surface are metastable at temperatures below 200 K [187]. With increasing temperature the atoms start to penetrate the surface and finally they become dissolved in the copper bulk. Unfortunately, this rearrangement of the nickel atoms might proceed in the same temperature range as CO desorption takes place.

One further interesting result of this work is that the desorption temperature of CO on the bimetallic Ni/Cu(110) surface does not change continuously with increasing nickel concentration in the coverage regime up to 1 ML Ni, by going from a clean Cu(110) surface (desorption peak temperature: 210 K) to a clean Ni(110) surface (desorption peak temperature: 420 K). Contrary, three distinct sharp desorption peaks additionally emerge at 250 K, 300 K and 360 K. This suggests that the CO adsorption energies are determined by short range geometrical arrangements rather than by long range electronic effects.

Further insight into the effect of adsorbed nickel on CO adsorption can be gained by preparing the nickel layer at different substrate temperatures. In Fig. 7.5 the change of the relative coverage corresponding to the individual desorption peaks, as a function of the preparation temperature, is compiled. In this case first always 0.2 ML of Ni were evaporated at different temperatures and subsequently 3 L of CO were dosed at 130 K. It is clear that those peaks which are correlated with the bimetallic surface (β_1-β_3) decrease with increasing preparation temperature, whereas the desorption peaks from the clean Cu surface (α_1, α_2) increase. This is due to the partial subsurface penetration and subsequent dissolution of nickel in the copper bulk at elevated temperature.

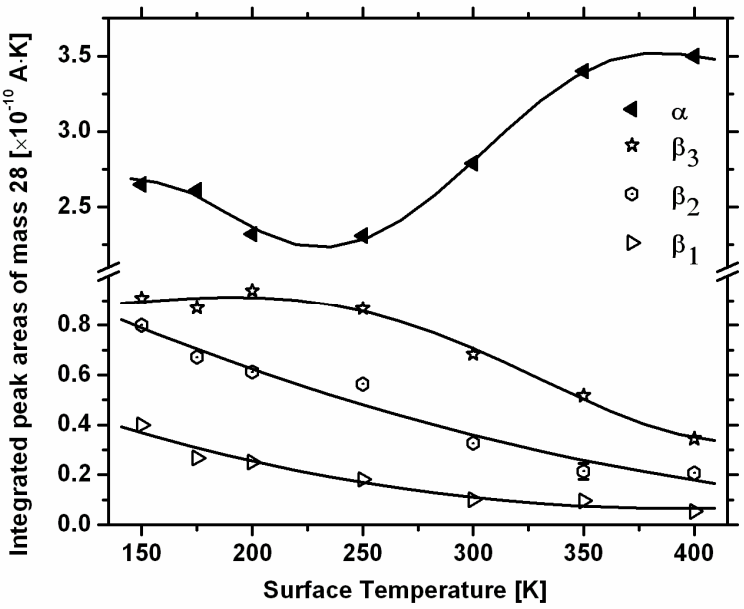

Fig.7.5. Change of the amount of adsorbed CO in the individual adsorption sites after preparing the Ni/Cu(110) bimetallic surface by evaporation of 0.2 ML nickel at different substrate temperatures. Subsequent CO exposure at 130 K is 3 L.

One additional experimental feature should be mentioned in this context. A comparison of the CO desorption spectra as obtained after decomposition of nickel carbonyl with that obtained after adsorption of CO on a Ni covered Cu(110) surface showed that the β peaks are always less pronounced in the latter case. However, if nickel was evaporated onto a CO pre-saturated Cu(110) surface or if nickel was evaporated in CO atmosphere ($1x10^{-8}$ Torr) then the desorption spectra were very similar to that obtained after nickel carbonyl decomposition.

Finally, in Fig. 7.6 saturation CO desorption spectra are compared as obtained from the clean Cu(110) surface (a), from the Ni/Cu(110) bimetallic surface as prepared by $Ni(CO)_4$ decomposition (b) and from a thick epitaxial Ni(110) film (c).

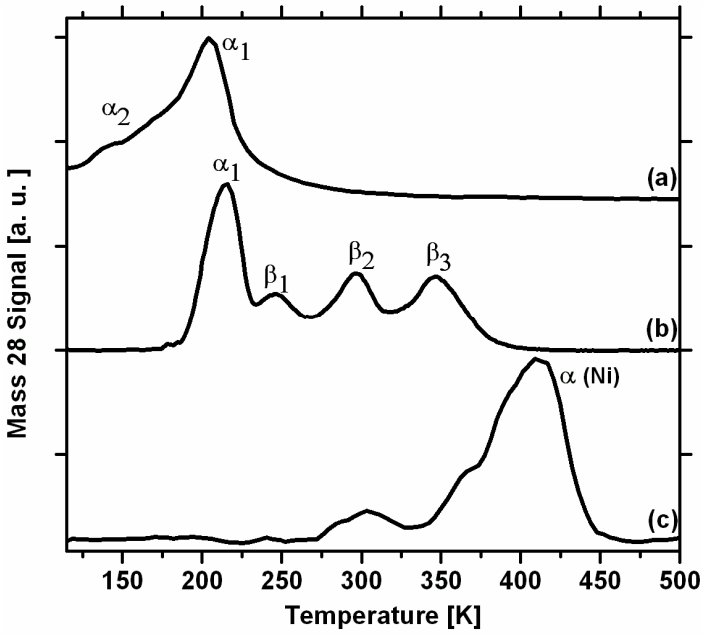

Fig.7.6. Compilation of saturation CO desorption spectra after dosing (a) 3 L of pure CO on (a) the clean Cu(110) surface (T_{ad} = 110 K), (b) 250 L of the CO+$Ni(CO)_4$ gas mixture on the Cu(110) surface (T_{ad} = 180 K) and (c) 3 L pure CO on the epitaxially grown Ni(110) surface (T_{ad} = 110 K).

This compilation shows impressively the potential of the bimetallic Ni-Cu surface to tailor the CO adsorption energy. However, rather than leading to a continuous shift of the adsorption energy for CO on the copper surface with increasing nickel concentration, three new discrete adsorption sites are generated. The origin of these peaks will be clarified by DFT calculations.

Experimentally the adsorption energies for CO on the clean Cu(110) and Ni(110) surface were calculated. CO desorbs from Cu(110) with a first order reaction kinetics at around 210 K when heated with 2K/s ($\Theta < 0.5$ ML). A desorption energy of 0.6 eV ± 10% and a pre-exponential factor ranging from $1x10^{13}$ s^{-1} to $1x10^{14}$ s^{-1} was reported in the literature [144,145,179]. For CO desorption from Ni(110), which takes place at around 420 K for low coverages and a heating rate of 2K/s, desorption energies between 1.2 eV [183] and 1.4 eV [167,183] were reported, with pre-exponential factors ranging from $1x10^{13}$ s^{-1} to $8x10^{15}$ s^{-1}. On the average, the correlation between the desorption peak maxima T_m and the desorption energies E_{des} can be quite well described by the Redhead formula for first order desorption [21]:

$$E_{des} \approx kT_m\left(\ln\left(\frac{\nu T_m}{\beta}\right) - 3.64\right) \tag{7.1}$$

We use this formula to determine the desorption energies for the individual desorption peaks from the peak maxima T_m observed in our studies: α_1 (Cu): 210 K, β_1: 250 K, β_2: 300 K, β_3: 360 K and α (Ni): 420 K, assuming a similar desorption kinetics for all desorption peaks. Thus, we take an average pre-exponential factor of $1x10^{14}$ s^{-1} for the calculations. The heating rate is β = 2 K/s. This yields:

E_{des} (α_1(Cu)) = 0.61 eV,

E_{des} (β_1) = 0.73 eV,

E_{des} (β_2) = 0.88 eV,

E_{des}(β_3) = 1.06 eV and

E_{des}(α(Ni)) = 1.24 eV

(An error of the pre-exponential factor by one order of magnitude effects the calculated desorption energy only by about 0.06 eV). These results will be compared with the theoretically calculated adsorption energies.

7.6 Results of the theoretical calculations

First of all we will give a summary of our calculations for CO adsorption on the clean Cu(110) and Ni(110) surface. For these systems comprehensive experimental data are available for comparison with the calculations. We would like to point out that we are well aware of the fact that DFT calculations generally yield too high adsorption energies for CO on metal surfaces, due to the underestimation of the HOMO-LUMO gap of the CO molecule [175]. For the (111) planes of fcc metals in some cases even the adsorption sites for CO cannot be calculated correctly [176]. However, for the Cu(110) plane these restrictions seem not to hold [177, 178]. As we will show below a quite good agreement between the calculations and the experimental data with respect to the adsorption configuration is obtained. Concerning the adsorption energies it should at least be possible to calculate the relative trends in the activity of bimetallic systems [165].

The adsorption energies for CO molecules are determined by using a (2x2) unit cell with n = 1 - 4 molecules in the basis, to simulate coverages of 0.25, 0.5, 0.75 and 1.0 monolayers (ML), respectively. The adsorption energy of the n^{th} molecule is determined by:

$$E_{ads}^{nth} = E^{nCO/Cu} - (E^{(n-1)CO/Cu} + E^{CO}) \quad (7.2)$$

Where $E^{nCO/Cu}$ is the total slab energy of the substrate with n adsorbed CO molecules, $E^{(n-1)CO/Cu}$ the corresponding total slab energy for (n-1) adsorbed CO molecules and E^{CO} the total energy of the free CO molecules. This energy has been calculated as E^{CO}=14.8 eV in our study. It should be noted that the adsorption energy is negative in case of stable adsorption. In this text, however, we use the expressions adsorption energy, desorption energy and binding energy of CO to the surface synonymously and use the absolute value of the calculated adsorption energy.

7.6.1 CO on clean Cu(110)

Experimentally it is well known that the maximum coverage of CO on Cu(110), at an adsorption temperature of 110 K, is 0.8 ML. 0.3 ML desorb at ca. 175 K and 0.5 ML at ca. 210 K [145]. For coverages $\Theta_{CO} \leq 0.5$ ML the adsorption energy was determined to be 0.6 eV ± 10% [144,179,180] and only weakly coverage dependent. The LEED pattern of the 0.5 ML covered surface exhibits a weak (2x1) superstructure [144,181]. This information was taken as a basis for the modeling.

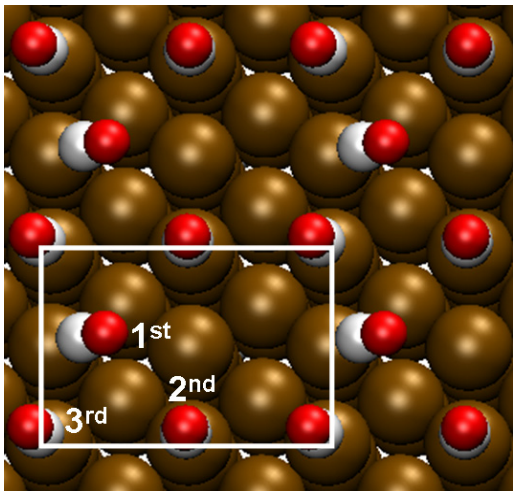

Fig.7.7. Relaxed CO molecule configuration on a Cu(110) surface for a coverage of 0.75 ML. A (2x2) surface unit cell was used for the calculations and the molecules in the basis of the unit cell are numbered according to their sequential removal.

Table 7.1: Tilt angles in x-direction and adsorption energies of CO on Cu(110) as a function of the coverage for given adsorption sites. Compare with Fig. 7.7.

Coverage (ML)	Tilt angle in x-direction (°) n^{th} molecule/ C-O/ Me-C			Adsorption energy (eV) /(n^{th} molecule)
0.75 (long bridge)	1^{st}	35	35	0.46 (1^{st})
	2^{nd}	0	0	
	3^{rd}	-7	-7	
0.75 (on-top)	1^{st}	0	0	0.20 (1^{st})
	2^{nd}	0	0	
	3^{rd}	0	0	
0.50	2^{nd}	0	0	0.82 (2^{nd})
	3^{rd}	0	0	
0.25	3^{rd}	0	0	0.94 (3^{rd})

The adsorption energies and adsorption configurations were calculated for different scenarios:

In the first scenario two CO molecules (2^{nd} and 3^{rd} molecule) in the surface unit cell were initially located on-top and another molecule (1^{st} molecule) at a long bridge site. (The molecules in the

surface unit cell are numbered according to their removal from the surface for the energy calculations). It should be noted that always several calculations were performed with different initial molecule configurations to test the reliability of the calculations for the relaxed final configuration.

In table 7.1 the final CO adsorption configuration (tilt angles between C-O and Me-C in x-direction) and the adsorption energies for three different coverage regimes are compiled. Tilting into y-direction is generally small. The molecule configuration for 0.75 ML CO is shown in Fig. 7.7. We estimate the numerical uncertainty of the calculated energy values to be about ±20 meV and the uncertainty of the calculated tilt angles to be about ± 3°, depending on the corrugation of the potential. It turns out that the 2nd and 3rd molecules in the surface unit cell remain located at the on-top position after relaxation. These molecules are nearly vertically oriented. (Calculated values of tilt angles below 3° have been considered as corresponding to vertical orientation). This result is in good agreement with photoelectron diffraction experiments [182] and with other DFT calculations [177,178]. The adsorption energy for the molecules with $\Theta \leq 0.5$ ML is about 0.9 eV. However, the 1st molecule in the unit cell (total coverage 0.75 ML) rearranges after relaxation and becomes strongly tilted. The binding energy for these molecules is 0.46 eV. It can be considered as being nearly vertically adsorbed with respect to the (111) facet of the (110) plane in a three fold hollow site, and therefore strongly tilted with respect to the surface normal. When the 1st CO molecule is initially positioned at an on-top site it remains at this site according to the DFT calculations, apparently due to a local potential minimum, but this configuration is energetically much less favorable (E_{ads} = 0.2 eV) (See table 7.1). We have also calculated the adsorption energies and configurations for the 2nd and 3rd CO molecule in short bridge positions and it turned out that the adsorption energies are nearly the same as for the on-top configuration (0.9 eV). This shows that only a very weak lateral corrugation of the adsorption well exists along the [1-10] direction and that therefore no pronounced superstructure of the CO overlayer forms on the surface. This also explains why the experimentally obtained LEED patterns of the (2x1) superstructure are generally very weak [144,179].

7.6.2 CO on clean Ni(110)

For CO on Ni(110) a saturation coverage of 1 ML at T_{ads} < 250 K has been determined experimentally [168]. The desorption energy remains nearly constant over the whole coverage range and the following values for the adsorption energy can be found in the literature: 1.4 eV [167], 1.2 eV [183] and 1.0 eV [168]. For coverages above 0.75 ML a tilting of the CO molecules by about 19° was determined by ESDIAD measurements [183]. For our calculations we used again a (2x2) unit cell with 1 - 4 CO molecules in the basis. The results are compiled in table 7.2a and table 7.2b for CO molecules located at on-top sites and short bridge sites, respectively. For both configurations we obtain tilt angles which are close to the experimentally obtained 19° for Θ > 0.5 ML. However, for the on-top configuration the adsorption energy for coverages Θ > 0.5 ML (E_{ads} ≈ 1.0 eV) is significantly different from that for Θ < 0.5 ML (E_{ads} ≈ 1.7 eV). On the other hand, when the molecules are located at short bridge sites the adsorption energies change only from 1.6 eV at Θ = 1.0 ML to 1.8 eV at Θ = 0.25 ML.

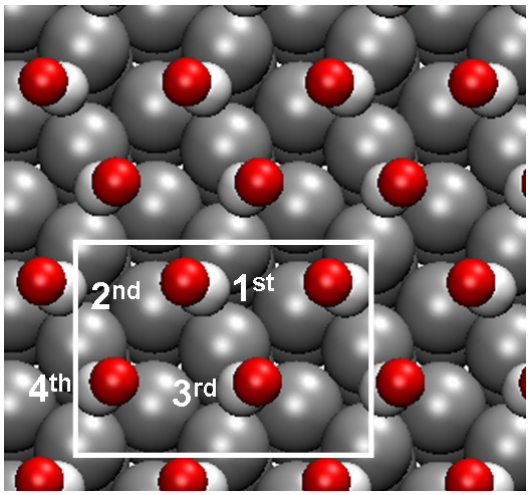

Fig.7.8. Relaxed CO molecule configuration on a Ni(110) surface for a coverage of 1.0 ML. A (2x2) surface unit cell was used for the calculations and the molecules in the basis of the unit cell are numbered according to their sequential removal.

Table 7.2. (a) Tilt angles and adsorption energies of CO on Ni(110) for molecules in on-top position. (b) Tilt angles and adsorption energies of CO for molecules in short-bridge position. Compare with Fig. 7.8.

	Coverage (ML)	Tilt angle in x-direction (º) n^{th} molecule/ C-O/ Me-C			Adsorption energy (eV) /(n^{th} molecule)
(a)	1	1^{st}	-16	-19	1.02 (1^{st})
		2^{nd}	-16	-19	
		3^{rd}	16	19	
		4^{th}	16	19	
	0.75	2^{nd}	-15	-17	1.07 (2^{nd})
		3^{rd}	-6	-6	
		4^{th}	18	17	
	0.50	3^{rd}	0	0	1.68 (3^{rd})
		4^{th}	0	0	
	0.25	4^{th}	0	0	1.70 (4^{th})
(b)	1	1^{st}	-20	-20	1.61 (1^{st})
		2^{nd}	-20	-20	
		3^{rd}	20	20	
		4^{th}	20	20	
	0.75	2^{nd}	-15	-16	1.59 (2^{nd})
		3^{rd}	-5	-5	
		4^{th}	17	18	
	0.50	3^{rd}	0	0	1.77 (3^{rd})
		4^{th}	0	0	
	0.25	4^{th}	0	0	1.83 (4^{th})

This is in good agreement with the experimentally obtained small coverage dependence of the adsorption energy. Thus we conclude that the short bridge configuration is the correct one, at least for high CO coverages, as shown in Fig. 7.8. This agrees very well to existing ESDIAD [183] and EELS measurements [184].

7.6.3 CO on bimetallic Ni/Cu(110) surfaces

As already mentioned before, about ½ ML Ni prepared with $Ni(CO)_4$ in Cu(110) is consistent with the observed LEED pattern of a (1x2) superstructure. By direct nickel evaporation one can of course adjust any coverage and in addition also vary the surface temperature. But also in this case the new desorption peaks $\beta_1 - \beta_3$ are most pronounced at a nickel coverage of about 0.5 ML. Thus we have focused our calculations mainly on the bimetallic Ni/Cu(110) surface containing 0.5 ML nickel. Furthermore, we know that the Ni atoms not necessarily remain adsorbed on the surface, but that with increasing surface temperature the Ni atoms start to move into surface and subsurface sites of the copper substrate. This has also been demonstrated by using other experimental techniques, like HREELS (high resolution electron energy loss spectroscopy) [185,186], and theoretically by the first-principles Greens`s function technique [187]. The kinetics of subsurface penetration and finally the dissolution into the bulk, however, depends not only on the temperature but also on the amount of nickel and on the amount of CO adsorbed on the surface, as will be outlined in the discussion.

Our own DFT calculations also yield an increase of the (negative) total energy of the Ni/Cu(110) system when moving the Ni atoms from the adsorbed sites into the in-surface sites (surface alloy) and further into the subsurface sites. However, when CO molecules were adsorbed on the Ni covered Cu(110) surface, the Ni atoms tend to remain at the surface (see below).

We have therefore performed our calculations of CO adsorption on the Ni-Cu bimetallic surfaces for different scenarios: i) ½ ML Ni *adsorbed* on the Cu(110) surface in four fold hollow sites in a (1x2) superstructure, ii) A 1:1 Ni-Cu *surface alloy* with alternating rows of Ni and Cu in [1-10] direction, iii) ½ ML *subsurface* Ni in four-fold hollow sites in a (1x2) superstructure configuration, iv) ½ ML Ni forming a *mixture of adsorbed and in-surface sites* along the [1-10] direction, v) ½ ML Ni forming a *mixture of in-surface and sub-surface sites* along the [1-10] direction. It turns out that only for the latter case, a mixture of in-surface and sub-surface nickel on Cu(110), the calculated values for the adsorption energies can be best reconciled with the experimental data.

i.) CO on ½ ML Ni adsorbed on Cu(110) in a (1x2) superstructure

Again we have used a (2x2) supercell with 1 - 4 CO molecules in the basis and have started with various initial CO configurations to find the most favorable final constellation of the molecules after relaxation. The values for the adsorption energies and the tilt angles are compiled in table 7.3 and the ball models for the arrangement of the CO molecules on the bimetallic surface for different coverages are depicted in Fig. 7.9 a-d. For all scenarios the common feature is that the CO molecules are always attracted to the Ni atoms. In the case of 1 ML coverage half of the molecules are located in Ni short bridge positions and they are slightly tilted (3^{rd}, 4^{th} molecule).

Table 7.3. Tilt angles and adsorption energies of CO on a Ni/Cu(110) bimetallic surface (1/2 ML Ni adsorbed on Cu(110)) as a function of CO coverage. Compare with Fig. 7. 9.

Coverage (ML)	Tilt angle in x-direction (º) n^{th} molecule/ C-O/ Me-C			Adsorption energy (eV) /(n^{th} molecule)
1	1^{st}	-48	-12	0.50 (1^{st})
	2^{nd}	46	10	
	3^{rd}	17	7	
	4^{th}	21	-10	
0.75	2^{nd}	42	-9	0.84 (2^{nd})
	3^{rd}	-39	-44	
	4^{th}	-12	-10	
0.50	3^{rd}	-26	-25	1.94 (3^{rd})
	4^{th}	26	25	
0.25	4^{th}	0	0	2.21 (4^{th})

The second half (1^{st}, 2^{nd} molecule) are located in three-fold hollow sites of the (111) facets of the (110) surface and these molecules are strongly tilted (Fig. 7. 9a). It is remarkable that due to the strong interaction with the CO molecules the Ni atoms are laterally displaced and they form a zig-zag row along the [1-10] direction. The alternating displacement is +0.25 Å and -0.30 Å, respectively. The removal of one CO molecule from the unit cell (1^{st} CO), which costs an energy of 0.5 eV, leads to a further striking redistribution of the remaining CO molecules (3/4 ML total coverage). A quite symmetric situation is established where every second short bridge site is occupied by nearly vertical CO molecules and in between two CO molecules occupy three-fold

hollow sites of the (111) facets and are therefore strongly tilted (Fig. 7. 9b). The lateral displacement of the Ni atoms is lifted.

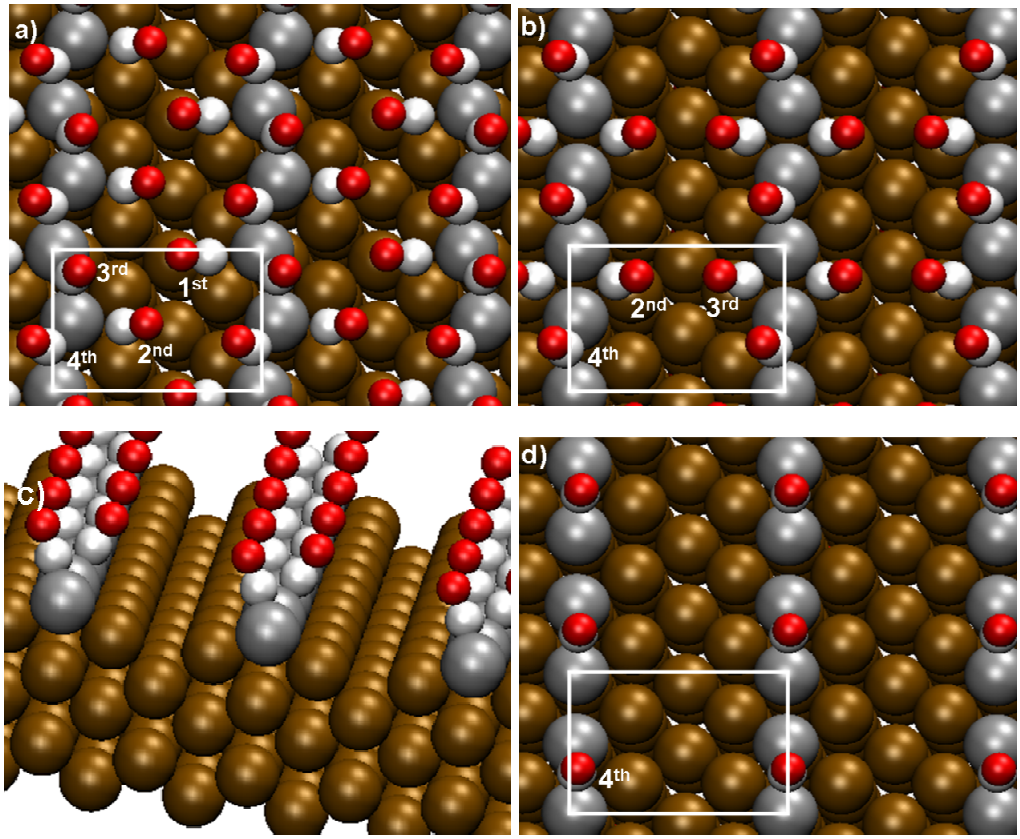

Fig.7. 9 a-d: Relaxed CO molecule configuration on a Ni/Cu(110) bimetallic surface with ½ ML nickel adsorbed in a (1x2) superstructure. (a) 1.0 ML CO, (b) 0.75 ML CO, (c) 0.5 ML CO, (d) 0.25 ML CO.

The desorption energy for the next (2^{nd}) CO molecule is 0.84 eV and the configuration of the remaining CO molecules changes again (1/2 ML total coverage). The CO molecules are now arranged in short bridge sites of the Ni rows alternately tilted by about 26°. Fig. 7. 9c shows a side view of this configuration. This situation is similar to the 1 ML coverage on the clean Ni(110) surface. Removing the next CO molecule from the unit cell (3^{rd} CO molecule), which costs an energy of 1.94 eV, leads to a situation where on every second short-bridge site of the Ni rows a CO molecule is adsorbed in a vertical arrangement (1/4 ML coverage, Fig. 7.9d). The desorption energy for these last molecules is 2.21 eV.

ii.) CO on a 1:1 Ni/Cu surface alloy

The adsorption behavior of CO on the Ni-Cu surface alloy clearly differs from the ad-atom case. The adsorption configurations for various CO coverages are shown in Fig. 7.10a-d.

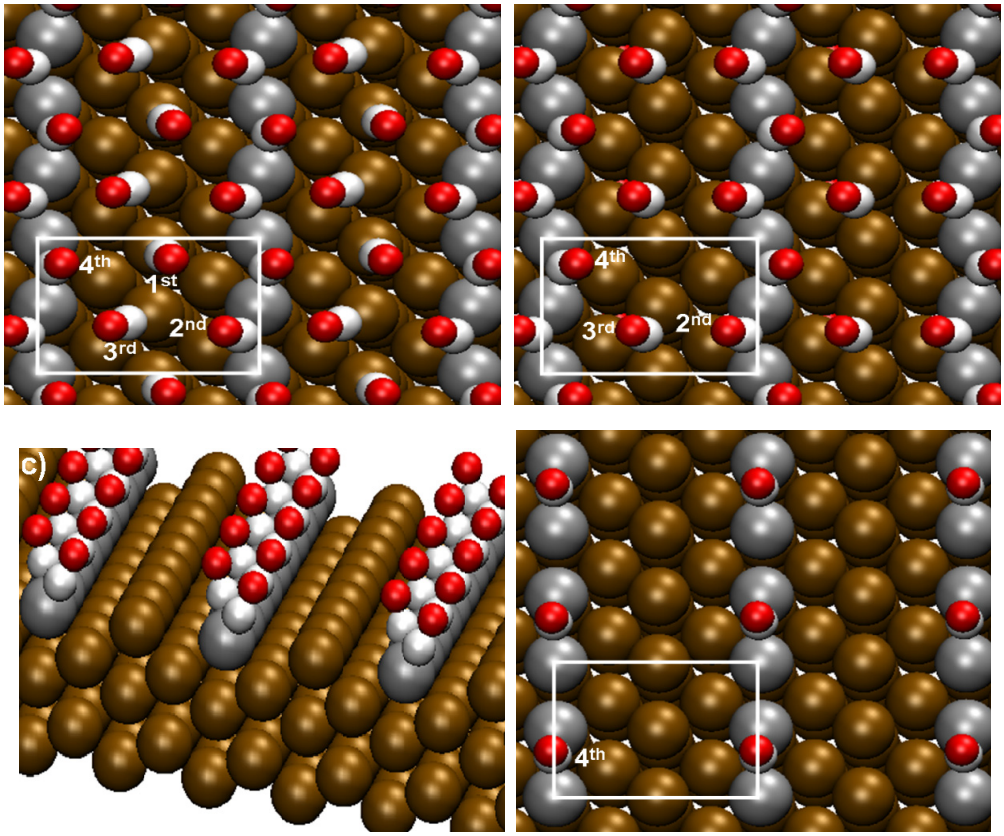

Fig. 7.10 a-d. Relaxed CO molecule configuration on a 1:1 Ni/Cu surface alloy (a) 1.0 ML CO, (b) 0.75 ML CO, (c) 0.5 ML CO, (d) 0.25 ML CO.

The tilt angles and adsorption energies are compiled in table 7.4. In case of the 1 ML coverage less CO molecules can be adapted at the Ni rows. Half of the CO molecules are bonded to Ni atoms at short bridge sites and they are alternately tilted. The other half of the molecules occupy on-top Cu sites and they are also tilted (Fig. 7.10a).

Table 7.4. Tilt angles and adsorption energies of CO on a 1:1 Ni/Cu(110) surface alloy as a function of CO coverage. Compare with Fig. 7.10.

Coverage (ML)	Tilt angle in x-direction (º) n^{th} molecule/ C-O/ Me-C			Adsorption energy (eV) /(n^{th} molecule)
1	1^{st}	19	16	0.38 (1^{st})
	2^{nd}	-18	-22	
	3^{rd}	-23	-18	
	4^{th}	20	19	
0.75	2^{nd}	23	25	0.82 (2^{nd})
	3^{rd}	-25	-19	
	4^{th}	-7	-12	
0.50	3^{rd}	-21	-20	1.73 (3^{rd})
	4^{th}	20	20	
0.25	4^{th}	0	0	2.14 (4^{th})

The latter molecules are much weaker bound and can be removed first. After removal of the 1^{st} molecule (adsorption energy 0.38 eV) the molecules bound to the Ni atoms are only little effected. However, the on-top copper bound CO molecules shift to short bridge positions. The removal of these (2^{nd}) molecules costs 0.82 eV. For desorption of the remaining, nickel bonded, molecules a much higher energy is needed. The adsorption energy of the 3^{rd} CO molecule is 1.73 eV and of the 4^{th} molecule it is 2.14 eV.

iii.) CO adsorption on ½ ML Ni in subsurface sites of Cu(110)

First we have checked the most favorable adsorption sites for CO on the subsurface Ni atoms by using a (1x1) unit cell. It turned out that the on-top site is favored (E_{ads} = -0.67 eV) versus the short bridge site (E_{ads} = -0.55 eV). This has been taken into account for the following calculations where again a (2x2) unit cell with 1 - 4 CO molecules was used. The results are compiled in table 7.5 and Figs. 7.11 a-d. We start for the 1 ML situation with an initial configuration of CO molecules located on each Ni atom in the four fold hollow sites and with CO molecules located at the adjacent Cu rows either in short bridge or on-top sites.

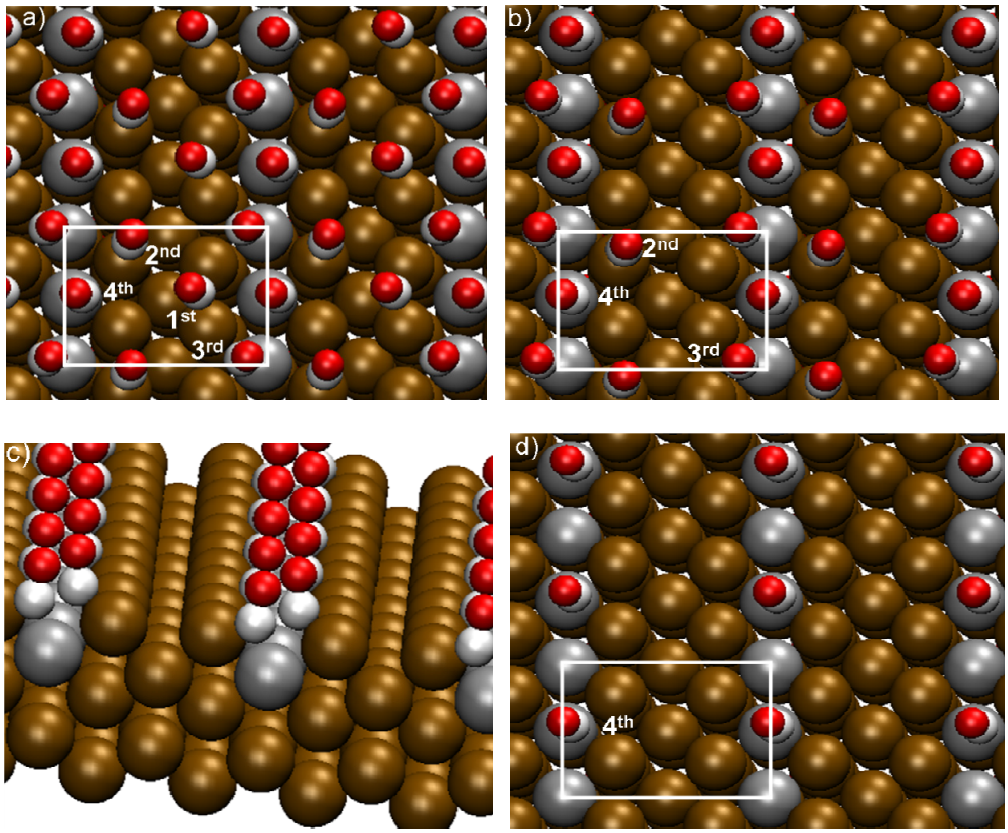

Fig. 7.11 a-d. Relaxed CO molecule configuration on a Ni/Cu(110) bimetallic surface with ½ ML nickel in subsurface sites, forming a (1x2) superstructure. (a) 1 ML CO, (b) 0.75 ML CO, (c) 0.5 ML CO, (d) 0.25 ML CO.

It turns out that all the molecules become slightly tilted but no significant rearrangement of the molecules takes place after relaxation (Fig. 7.11a). It is worth mentioning that in this case also a non-negligible tilting in the y direction (along the [1-10] direction) shows up. Removing successively the CO molecules, first from the Cu sites and subsequently from the Ni sites, yields adsorption energies of about 0.5 eV for the first two molecules, 0.72 eV for the 3rd and 1.11 eV for the 4th molecule. In all cases, but in particular for the ½ ML situation, a rather unusual tilting of the CO molecules in x-direction can be observed, where the C atoms tend to move closer to the three fold hollow sites of the (111) facets of the bimetallic (110) surface. This is shown in a side view in Fig. 7.11c.

Table 7.5. Tilt angles and adsorption energies of CO on Cu(110) with ½ ML Ni in subsurface sites, as a function of coverage. Compare with Fig. 7.11.

Coverage (ML)	Tilt angle in x-direction (º) n^{th} molecule/ C-O/ Me-C			Adsorption energy (eV) /(n^{th} molecule)
1	1^{st} 2^{nd} 3^{rd} 4^{th}	-10 10 13 -8	-11 16 -20 19	0.50 (1^{st})
0.75	2^{nd} 3^{rd} 4^{th}	10 0 -11	12 -22 13	0.52 (2^{nd})
0.50	3^{rd} 4^{th}	6 -6	-22 22	0.72 (3^{rd})
0.25	4^{th}	-8	10	1.11 (4^{th})

iv.) A mixture of ¼ ML adsorbed and ¼ ML in-surface Ni atoms on Cu(110)

The previous calculations have shown that no good agreement can be obtained between the calculated adsorption energies and the experimentally obtained desorption peaks. Therefore we have extended our calculations by taking into account a mixture of different nickel sites on the Cu(110) surface. A quite obvious arrangement would be that every second Ni atom from an adsorbed Ni row moves into an in-surface site. The relaxed configurations of CO adsorption sites for coverages ranging from 0.25 ML to 1 ML on such a bimetallic surface are shown in Fig. 7.12 and the tilt angles and adsorption energies are compiled in table 7.6. Again, for coverages $\leq$ 0.5 ML the adsorption energies are about 1.9 eV, which is too large to explain the β peaks.

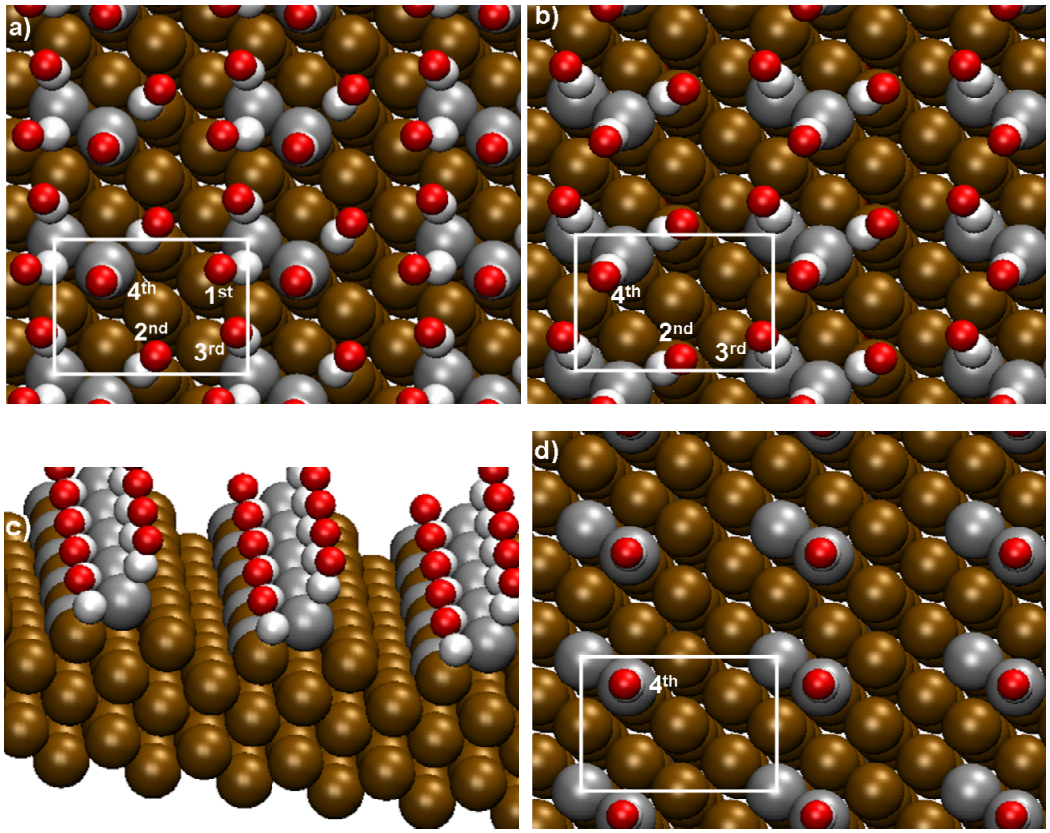

Fig. 7.12 a-d. Relaxed CO molecule configuration on a Ni/Cu(110) bimetallic surface with ¼ ML adsorbed nickel and ¼ ML nickel in surface sites. (a) 1 ML CO, (b) 0.75 ML CO, (c) 0.5 ML CO, (d) 0.25 ML CO.

Table 7.6. Tilt angles and adsorption energies of CO on a Ni/Cu(110) bimetallic surface (1/4 ML Ni adsorbed and ¼ ML Ni in surface sites on Cu(110)) as a function of CO coverage. Compare with Fig. 7.12.

Coverage (ML)	Tilt angle in x-direction (º) n^{th} molecule/ C-O/ Me-C			Adsorption energy (eV) /(n^{th} molecule)
1	1^{st}	-42	-6	0.34 (1^{st})
	2^{nd}	35	-5	
	3^{rd}	-9	0	
	4^{th}	0	14	
0.75	2^{nd}	40	-6	0.94 (2^{nd})
	3^{rd}	-15	5	
	4^{th}	0	-11	
0.50	3^{rd}	-28	8	1.88 (3^{rd})
	4^{th}	5	17	
0.25	4^{th}	4	6	1.964th)

v.) A mixture of ¼ ML in-surface and ¼ ML sub-surface Ni atoms on Cu(110)

Equivalent calculations have been carried out for a bimetallic surface consisting of ¼ ML of Ni atoms in surface sites and ¼ ML of Ni atoms in adjacent subsurface sites. The results are compiled in Fig.7.13 and table 7.7. At a CO coverage of 1 ML, half of the CO molecules in the surface unit cell are adsorbed next to in-surface Ni atoms (4^{th} and 3^{rd} CO) with alternate tilting, ¼ are adsorbed on-top of the subsurface nickel (2^{nd} CO) and ¼ occupy on-top sites of Cu (1^{st} CO). The adsorption energy of the latter is only 0.45 eV. The removal of the weakly bound CO molecules does not influence the molecule configuration of the 3^{rd} and 4^{th} CO, but the 2^{nd} CO becomes slightly displaced.

Table 7.7. Tilt angles and adsorption energies of CO on a Ni/Cu(110) bimetallic surface (1/4 ML Ni in surface sites and ¼ ML in sub-surface sites on Cu(110)) as a function of CO coverage. Compare with Fig.7.13.

Coverage (ML)	Tilt angle in x-direction (º) n^{th} molecule/ C-O/ Me-C			Adsorption energy (eV) /(n^{th} molecule)
1	1^{st}	0	-7	0.45 (1^{st})
	2^{nd}	0	11	
	3^{rd}	15	14	
	4^{th}	-14	-18	
0.75	2^{nd}	0	17	0.93 (2^{nd})
	3^{rd}	19	20	
	4^{th}	-18	-16	
0.50	3^{rd}	22	20	1.10 (3^{rd})
	4^{th}	-23	-22	
0.25	4^{th}	-5	-5	1.65 (4^{th})

The removal of this molecule costs an energy of 0.93 eV. Finally, for the removal of the 3^{rd} CO molecule an energy of 1.1 eV, and for the 4^{th} CO an energy of 1.65 eV is needed. Apparently, these desorption energies coincide best with the experimentally obtained values for the β_1-β_3 peaks. Again, we would like to emphasize that for this particular Ni configuration quite significant tilting of the CO molecules in the y direction takes place.

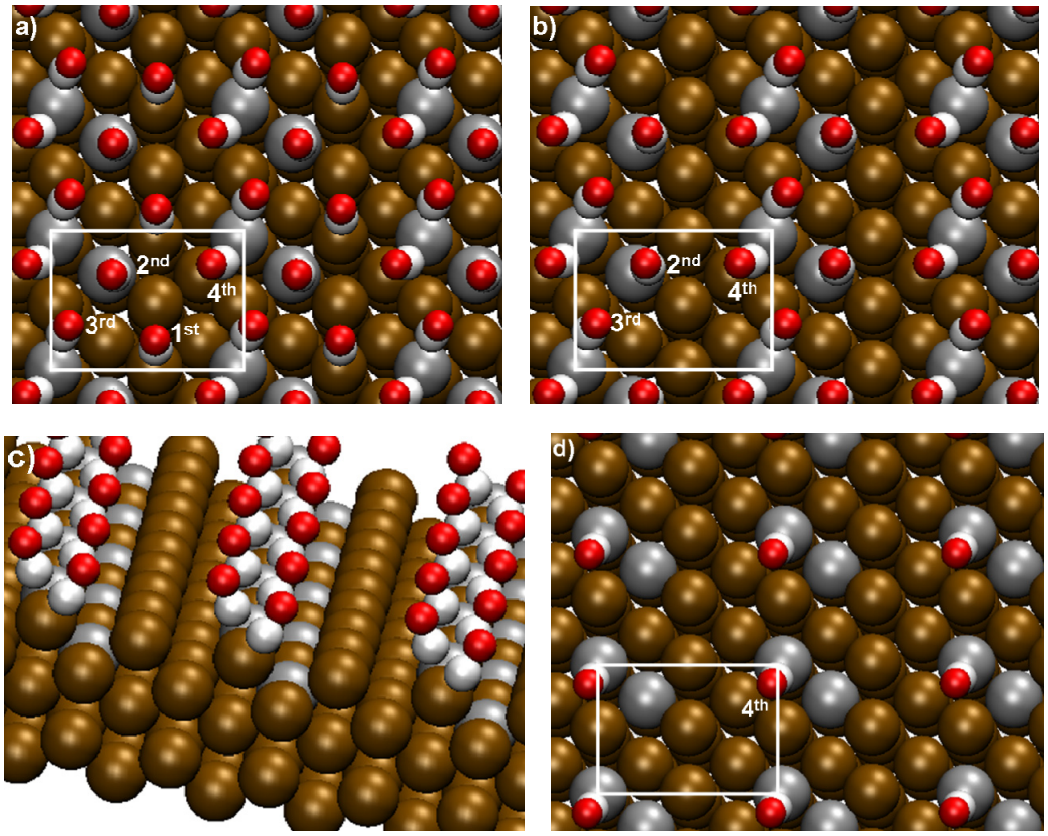

Fig. 7.13 a-d. Relaxed CO molecule configuration on a Ni/Cu(110) bimetallic surface with ¼ ML nickel in surface sites and ¼ ML in sub-surface sites. (a) 1 ML CO, (b) 0.75 ML CO, (c) 0.5 ML CO, (d) 0.25 ML CO.

7.6.4 Total energies of CO/Ni/Cu(110) systems

In Fig. 7.14 the total energies of a 5 layer copper slab with a (2x2) unit cell, including 2 Ni atoms in various positions and different amounts of adsorbed CO are compiled. From the total slab energies, one can determine the thermodynamically stable phases of the CO/Ni/Cu(110) systems. The arrangements of the Ni atoms correspond to the scenarios as depicted in Figs.7.9 – 13: (ad+ad): Both Ni atoms are adsorbed, (ad+sa): 1 Ni atom adsorbed, 1 Ni atom forming a surface alloy, (sa+sa): both Ni atoms are in in-surface sites, (sa+ss): 1 Ni atom in surface site, 1 Ni atom in sub-surface site, (ss+ss): Both Ni atoms are located in subsurface sites. (ss+ss1) and (ss1+ss1): Ni atoms located in deeper layers.

The plotted energies correspond to $E_{tot} = E_{slab} - xE_{Cu}^{bulk}$, where x is the number of Cu atoms from the bulk reservoir that replace Ni atoms from the substrate layers that are put at adsorption sites. Thus the energies of the scenarios with a different number of Cu atoms per unit cell are comparable. For the first scenario 2 Cu atoms and for the second scenario 1 Cu atom had to be removed from the bulk, respectively. Furthermore, 1-4 CO molecules were placed on the bimetallic surface as shown in Figs.7.9-13.

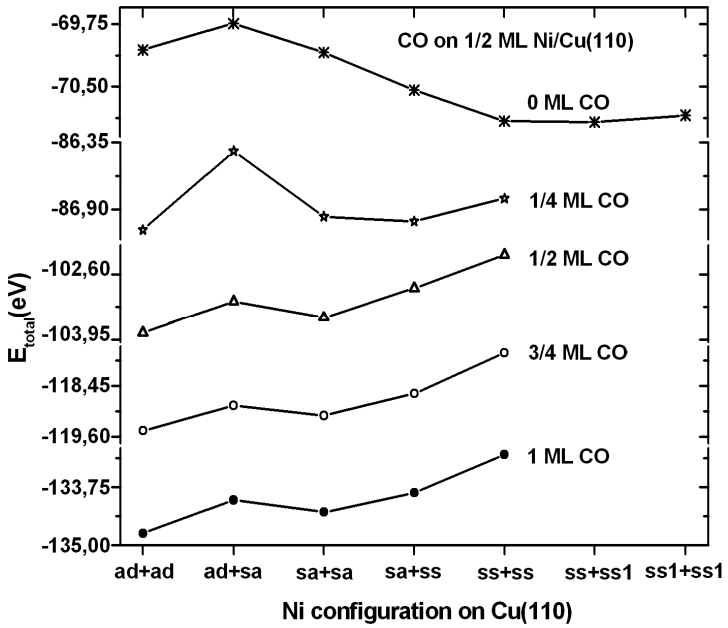

Fig. 7.14. Total energies of five-layer copper slabs with (2x2) unit cells, including 2 Ni atoms in various positions and different amounts of adsorbed CO. The arrangements of the nickel atoms correspond to the scenarios as depicted in Figs. 9–13. It is evident that without CO (upper curve) the Ni atoms tend to go into subsurface layers, whereas with adsorbed CO (lower curves) the Ni atoms tend to stay on the surface. For details see the text.

The calculations show that on the clean bimetallic surface the Ni atoms tend to move into subsurface states where a local energy minimum exists. However, when CO molecules are adsorbed on the surface the Ni atoms tend to be rather stabilized at the surface. This is exactly what we have also observed experimentally. One could now argue that the individual β desorption peaks are actually the result of the complex interplay between the Ni stabilization by CO and the Ni dissolution after partial CO desorption. Although we cannot fully exclude this scenario, the experimental data, however, indicate that in the temperature range between 200 K

and 500 K the arrangement of the Ni atoms in the surface unit cell is not changed considerably. This has been checked by various temperature dependent Ni preparations at the copper surface and the corresponding influence on the CO desorption. In particular, this can be inferred from the simultaneous increase of the β desorption peaks as a function of $Ni(CO)_4$ decomposition (Fig. 7.2), as well as from the common decrease of these peaks as a function the Ni preparation temperature (Fig. 7.4). This indicates that islands of the particular bimetallic surface exists which grow during Ni decomposition or evaporation and shrink during sample heating, respectively. The CO desorption spectra are then a mixture of desorption from these bimetallic islands with a largely stable Ni/Cu arrangement and the clean parts of the surface.

7.7 Compilation of experimental and theoretical results

A comparison of the calculated and experimentally obtained desorption energies in table 7.8a for the clean surfaces yields that the calculated values are by a factor of about 1.4±0.1 too large. We use this factor to determine the expected calculated values for the β_1- β_3 peaks from the desorption energy as obtained from the Redhead formula (Eq.7.1)and obtain E_{des}^{calc} (β_1) = 1.0±0.1 eV, E_{des}^{calc} (β_2) = 1.2±0.1 eV and E_{des}^{calc} (β_3) = 1.5±0.1 eV.

Let us next analyze the calculated adsorption energies obtained for CO on the various bimetallic surfaces. In principle, determining the most likely scenario underlying the TD spectra would require the evaluation of the barriers for possible exchange processes in the substrate and an adequate modeling of these processes within a kinetic treatment. Such an extensive modeling is beyond the scope of the present study.

Table 7.8.a. A comparison of the adsorption energies between theory and experiment.

Surface/CO(ML)	E_{ads} (eV) Experiment	E_{ads} (eV) Theory	
Cu(110)/0.5	0.61	0.9	**E_{cal}/E_{exp}≈1.4±0.1**
Ni(110)/ 0.5	1.24	1.8	

Table 7.8.b. A comparison of the adsorption energies between theory and experiment.

States/Adsorption Energies	*Experimental (eV)*	*Experimental × 1.4 ≈ Expected (eV)*	*Theoretical (eV)*
β_1	*0.73*	*1.0±0.1*	*0.93*
β_2	*0.88*	*1.2±0.1*	*1.10*
β_3	*1.06*	*1.5±0.1*	*1.65*

Instead, we sketch the most likely processes based on the energetics of the structure and the comparison of the corresponding calculated CO adsorption energies with the observed desorption peaks. In case of nickel *adsorbed* on Cu(110), for a half monolayer coverage in form of a (1x2) superstructure as well as for a full nickel monolayer (calculations not shown), the highest adsorption energy for CO (Θ = 0.25 ML) is 2.2 eV. This is even larger than the calculated value for CO adsorption on the pure Ni(110) sample (1.8 eV). At first glance this seems to be a surprising result. However, it has been shown recently that the deposition of a more reactive metal (e.g. Ni) onto a less reactive metal substrate (e.g. Cu) makes the overlayer even more reactive with respect to CO adsorption [163]. This is explained by the weaker coupling of the reactive overlayer to the inert substrate, resulting in a stronger bonding to the adsorbate. Thus, the calculated desorption energies for the β_1-β_3 states can not be correlated with CO bonding to *adsorbed* nickel on the Cu(110) surface.

The calculated adsorption energies for CO on a 1:1 Ni-Cu *surface alloy* are similar to that on the nickel adsorbed layer. Again, the adsorption energies of 1.73 eV (0.5 ML) and 2.07 eV (0.25 ML) are too high to explain the β-peaks. On the other hand, the calculation for CO adsorption on a subsurface Ni layer (1/2 ML in (1x2) configuration) yields too small values for the adsorption energies. In this case for the most strongly bound CO molecules (0.25 ML) an adsorption energy of just 1.0 eV is calculated (see table V).

Reasonable adsorption energies could only be obtained from DFT calculations by assuming a mixture of adsorbed, in-surface and subsurface Ni atoms. In particular the arrangement of ¼ ML Ni in surface sites and ¼ ML in subsurface sites, as shown in Fig. 7.13, yields a set of adsorption energies which are close to the expected ones, as summarized in table 7.8b. The smallest

adsorption energy of 0.46 eV for the 1st molecule in the surface unit cell, which occupies an on-top Cu site, is similar to that of the long bridge adsorbed CO on a clean Cu(10) surface (c.f. table 7.1). This adsorption energy can be correlated with the α_2-peak (175 K) in the desorption spectrum (Fig. 7.4). It also explains why this peak does not decrease very much with increasing Ni coverage on the surface.

The adsorption energy for the 2nd CO molecule in the surface unit cell (on-top adsorption at subsurface nickel) is 0.93 eV. This peak can be correlated with the β_1 desorption peak, with an expected desorption energy of 1.0±0.1 eV. The calculated adsorption energies for the further CO molecules in the surface unit cell are 1.1 eV for the 3rd and 1.65 eV for the 4th CO molecule, respectively. They can be correlated quite well with the β_2 peak (expected value: 1.2±0.1 eV) and the β_3 peak (expected value: 1.5±0.1 eV). It seems that only these special dimers, consisting of adjacent in-surface and subsurface nickel atoms, yield adsorption energies which can be reconciled with the experimental results. These final results are summarized in Fig. 7.15, where a typical CO desorption spectrum is shown and the calculated arrangement of the CO molecules on this special bimetallic surface. In addition, the experimental desorption energies of β_1- β_3 and the corresponding calculated adsorption energies are inserted. Please note that in this case the calculated values have been divided by the above described factor of 1.4, to account for the known overestimation of the CO adsorption energies in DFT calculations.

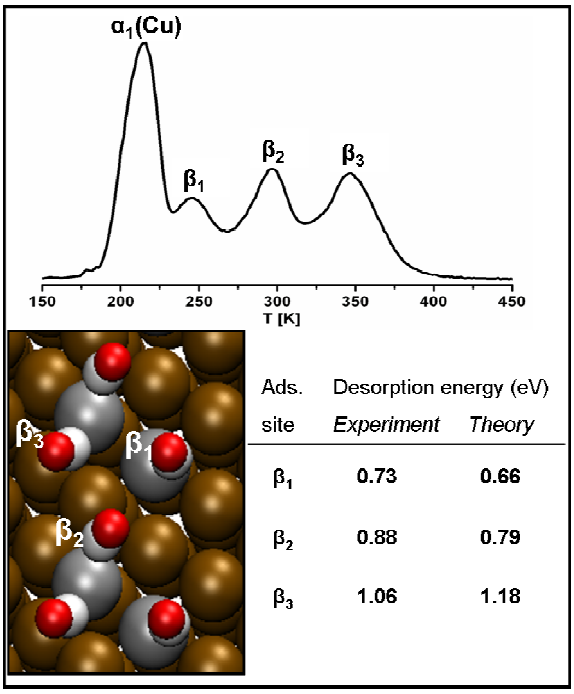

Fig.7.15. Compilation of the experimental CO desorption peaks and the associated adsorption sites on the Ni-Cu(110) bimetallic surface, as obtained by DFT calculations. The experimental and the theoretical values for the CO desorption energies of the β-states are also inserted. Note that the theoretical values are those from Table 7.7, divided by the factor of 1.4, due to the overestimation of the CO binding energy, as described in the text.

Calculations for increased nickel coverage (not shown), in adsorbed, in-surface and/or sub-surface sites always lead to increased adsorption energies for small CO coverage. This is in accord with the experimental data for CO adsorption on the bimetallic surface with increased nickel coverage, which shows a continuous shift of the β_3 state into the α(Ni) state (Fig.7.4). However, we never observed a CO desorption peak temperature on the bimetallic surface which was larger than that on the clean Ni surface. This implies that at temperatures above 400 K no stable thin nickel layer ($\Theta \leq 1$ ML) can be preserved on the Cu(110) surface. On the other hand, thicker nickel films ($\Theta > 4$ ML) remain adsorbed at least during short heating up to 500 K (above the CO desorption temperature on clean nickel).

7.8 Summary and conclusions

The adsorption behavior of CO on the bimetallic Ni/Cu(110) surface has been studied experimentally by thermal desorption spectroscopy, including Auger electron spectroscopy and low energy electron diffraction, and theoretically by DFT calculations. The bimetallic surface was produced either by evaporation of nickel or by decomposition of $Ni(CO)_4$ on Cu(110). With both methods similar bimetallic surfaces could be obtained. Adsorption of CO on such a bimetallic surface yields three new adsorption states with adsorption energies between that on clean Cu(110) and clean Ni(110). The desorption peak maxima for CO on clean Cu(110) are located at 210 K and on clean Ni(110) at 420 K. The new desorption peaks from the bimetallic surface, labeled as β_1-β_3 , can be observed at 250 K, 300 K and 360 K, respectively. These new states are most pronounced when ½ monolayer of nickel is present on the Cu(110) surface. This result shows that CO adsorption is determined by local (geometric) effects rather the by long range (electronic) effects.

A great number of DFT calculations, using the VASP code, were performed to identify the most probable Ni/Cu atomic arrangement at the bimetallic surface to reconcile with the experimental results. It turned out that CO adsorption on nickel dimers consisting of in-surface and adjacent sub-surface atoms give the best agreement with the observed experimental data. These results should contribute to a better understanding of tailoring catalytic processes with the help of bimetallic catalysts. Both the reactivity and selectivity of a catalyst can be influenced in this way because generally a specific arrangement of the surface atoms (ensemble) is needed to run a catalytic reaction, and appropriate adsorption energies for the reactants have to be available.

Chapter VIII

8. Interaction of atomic H and CO with Cu(110) and bimetallic Ni/Cu(110)

Investigation of the adsorption and coadsorption of hydrogen and carbon monoxide on metal surfaces is of great interest, because both molecules play a fundamental role in hydrocarbon synthesis. The coadsorption of two gases has been frequently investigated on transition metals both experimentally and theoretically. The general conclusion is that carbon monoxide displaces preadsorbed hydrogen from the metal surface and blocks further hydrogen adsorption. However, no studies on the co-adsorption of H and CO on copper surfaces, in particular on Cu(110), are available due to the fact that the sticking probability for molecular hydrogen at room temperature is exceedingly small. Results on the adsorption/desorption behavior of hydrogen and the mutual interaction between adsorbed hydrogen and CO on the Ni/Cu(110) bimetallic surface are presented in this chapter.

8.1. Introduction

The study of the interaction of CO and hydrogen with the transition metal surfaces is of great interest since both gases play a fundamental role in technologically important catalytic reactions such as the hydrogenation of carbon monoxide. No studies on the co-adsorption of H and CO on copper surfaces, in particular on Cu(110), are available due to the fact that the sticking probability for molecular hydrogen at room temperature is exceedingly small. However, atomic hydrogen [140,188,189,190] or translationally hot molecular hydrogen [93] can adsorb on copper with sufficiently high sticking probability. Since copper is used as a highly specific catalyst for the formation of formaldehyde [191] and for the synthesis of methanol [192,193] it is of importance to understand the basic processes of the involved species on such a surface. In addition to that the tailoring of the turn over frequency and selectivity of catalysts by surface

alloying is of great relevance. Therefore, the reaction properties of bimetallic surfaces have been the object of increased interest [162,163].

Recently we published a combined experimental and theoretical study on the carbon monoxide adsorption on a Ni/Cu(110) bimetallic surface [9]. Three new adsorption states of CO have been observed with desorption energies between that of CO on clean Cu(110) and on clean Ni(110). Since for the proper activity and selectivity of a particular catalyst often very distinct adsorption energies are required, bimetallic surfaces can be used to tailor the catalytic properties. Therefore this work focuses on the adsorption/desorption behavior of hydrogen and the mutual interaction between adsorbed hydrogen and CO on the Ni/Cu(110) bimetallic surface.

One of the motivations for this work was to search for the occurrence of possible intermediates, like COH and HCO, which could be expected in case of atomic H interaction with CO [194]. Actually, such intermediates have been frequently discussed in the context of methanation reactions [195,196]. Unfortunately, no such reaction products could be observed. However, some interesting features of atomic hydrogen interaction with the clean and nickel modified Cu(110) surface could be discovered, in particular an H induced surface roughening and a quite unusual site blocking for CO adsorption sites by atomic H.

8.2. Atomic hydrogen and hot molecular hydrogen

Most experiments on this study were performed using atomic hydrogen and hot molecular hydrogen. Therefore, we will first explain how atomic and hot molecular are obtained. Atomic hydrogen was supplied to the sample via a doser of the Bertel type [132]. This doser consists of an electron beam heated tungsten tube which yields nearly 100% of hydrogen in atomic form at a temperature of about 1950 K [133]. Molecular hydrogen at room temperature was dosed with the same doser without heating the device. When heating the tungsten tube to 1250 K hot molecular hydrogen can be produced which possesses enough translational energy to yield a reasonable sticking coefficient on Cu(110) [93]. At this temperature no significant amount of atomic hydrogen can be found in the gas beam [133]. For some experiments a tube temperature of 1450 K was chosen which yields a mixture of hot molecular and atomic hydrogen.

For the in-line dosing of H_2 an enhancement factor F=5 was experimentally determined, as compared to isotropic dosing. The enhancement factor was measured by comparing the H_2 uptake of in-line dosing and off-line dosing of a Pd(111) surface. The effective exposure due to in-line dosing is characterized by Langmuir* (L*). 1 L* is equivalent to the exposure of 5 L [1 L=1x10^{-6} Torr·s] as obtained from the isotropic pressure increase and the exposure time. For atomic hydrogen dosing it was found that the angular distribution of the effusing hydrogen atoms from the tungsten capillary was the same as for effusing molecules [133]. Therefore we can also use L* to characterize the number of impinged hydrogen atoms ($1H_2$ = 2H). It turned out that the Cu(110) surface was to some extent roughened after atomic hydrogen dosing. To obtain an atomically flat surface it was necessary to anneal the sample at 900 K for at least 10 minutes.

8.3. Adsorption of atomic and hot molecular hydrogen on Cu(110)

The adsorption probability of molecular hydrogen at room temperature on copper surfaces is exceedingly small, due to a rather high activation barrier for dissociative adsorption. Based on molecular beam experiments by Anger at al. [93] an activation barrier for dissociative adsorption of hydrogen molecules in the vibrational ground state of 0.66 eV was calculated by Jian-Jun et al. [197]. However, with hot molecular hydrogen [93] or with atomic hydrogen [189,190] a saturation coverage of about 0.5 ML H on Cu(110) can be obtained rather easily. One difference between the use of hot molecular and atomic hydrogen is that in the latter case subsurface adsorption states can be populated too. In Fig. 8.1 a set of thermal desorption spectra of hydrogen after in-line dosing with atomic hydrogen is presented. The spectra are similar to that published in the literature, showing the desorption peak for recombination of surface hydrogen (α-peak) and the subsurface peak, denoted γ. However, the desorption peak temperature of the α peak (275 K) is significantly smaller than that published in the literature (320 K [189,190]), where also atomic H exposure was applied. A careful check of the temperature measurement, by comparing with the peak maximum of CO from the same surface and the desorption peaks of H_2 and CO from an epitaxial Ni(110) layer on the same Cu(110) surface (vide infra) confirmed that the temperature measurement was correct.

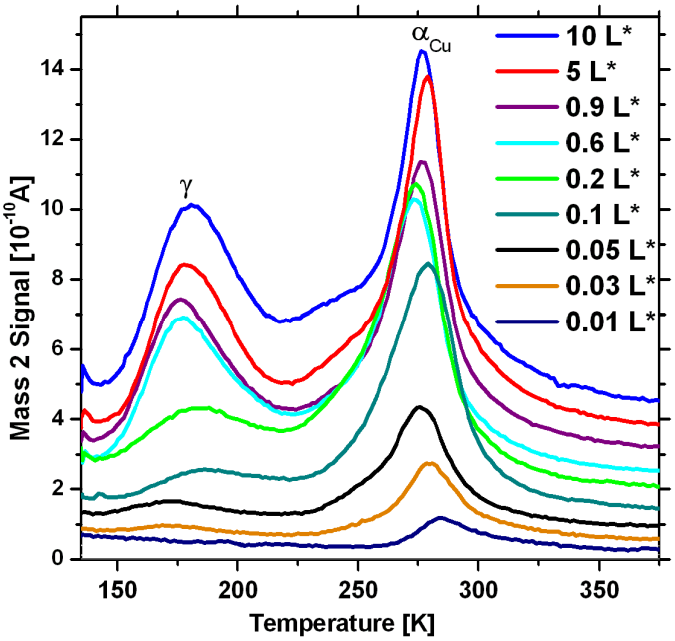

Fig. 8.1. A set of hydrogen desorption spectra after dosing a clean Cu(110) surface with increasing amounts of atomic H at 130 K. Heating rate: 2 K/s. The exposure due to direct dosing of H is given in L*. 1 L* equals 5 L of isotropic impingement.

Thus we came to the conclusion that prolonged atomic hydrogen exposure leads to a roughening of the surface on the atomic scale, which influenced the desorption peak temperature. Such a roughening was also reported, by applying high-resolution energy loss spectroscopy (HREELS), for the interaction of H with other metal surfaces, e.g. H/Rh(100) [198], H/Cu(100) [188]. Short heating of the sample to 800 K (as done for the TDS series shown in Fig. 8.1) is apparently not sufficient to level the surface, but an increase of the annealing temperature just to 900 K leads to a smoothing of the surface, as evidenced by a significant change of the desorption temperature of the α peak. This is verified in Fig. 8.2. The desorption peaks of traces (a) and (b) stem from hot molecular exposure of 1 L* and 10 L*, respectively, after the surface was sputter cleaned and annealed for 10 min at 900 K. In this case the peak maxima are around 310 K.

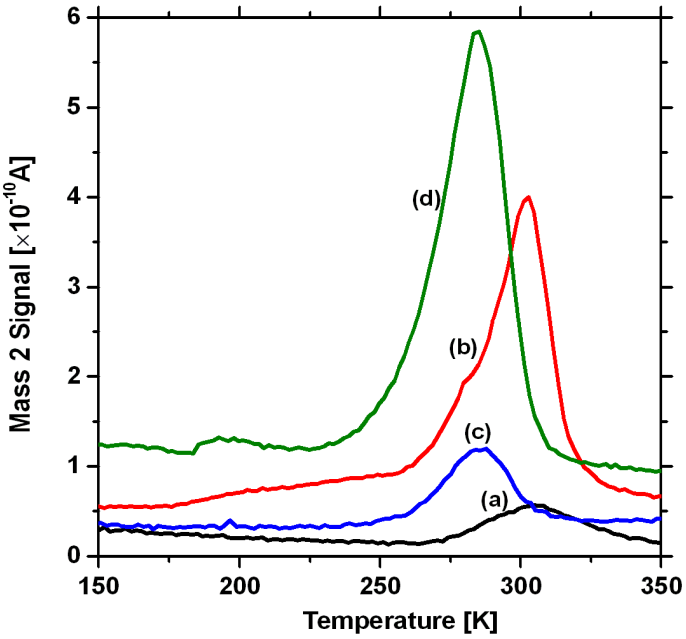

Fig. 8.2. Hydrogen desorption spectra after exposing the Cu(110) surface at 130 K to hot molecular hydrogen (doser temperature 1250 K) after different surface preparation: Exposure to 1 L* (a) and 10 L* (b) after cleaning by Ar^+ sputtering at 300 K and annealing at 900 K for 10 min (flat surface). Exposure to 1 L* (c) and 10 L* (d) after roughening the surface by 150 L* H, short Ar^+ sputtering and short heating to 800 K.

The peaks of traces (c) and (d) result from the same H exposures as in (a) and (b), respectively, but before that the sample was extensively exposed to atomic hydrogen (150 L*), briefly flashed to get rid of the hydrogen, sputtered by Ar^+ to remove residual C and again briefly flashed to 800 K. In this case the peak maxima are at around 280 K, as already observed in Fig. 8.1. In all cases the cleanliness of the surface was checked by AES. Completely the same difference in the desorption peak maxima could be observed for hydrogen desorption between a well annealed and a purely Ar* sputter roughened Cu(110) surface.

A comparison with the literature shows that the peak maximum of 310 K agrees quite well with hydrogen desorption after dosing with translationally hot molecular hydrogen [93]. One explanation for the discrepancy with the literature could be that in the mentioned work [189,190] always high annealing temperatures and rather small H exposures were used, which maintained a smooth surface. It is well known that the activation barriers for dissociative adsorption, and hence also for recombinative desorption, are decreased at rough surfaces [199]. Thus the difference in

the desorption peak temperatures reflects just the difference in the mean activation barriers between the flat and the rough Cu(110) surface. A rough estimate of the change of the activation barrier for hydrogen desorption, according to the Redhead formula [21], results in a decrease of this barrier of about 0.1 eV, by going from a flat to a rough Cu(110) surface.

One can only speculate as to the origin of the surface roughening due to the impingement of atomic hydrogen. Due to the small mass and low kinetic energy of thermalized H the removal of copper atoms by momentum transfer is of course impossible. Also the removal of Cu in form of CuH following an Eley-Rideal reaction process [200] seems to be highly unlikely. However, it is known that the formation and subsequent decomposition of metal hydrides can lead to a destruction of the crystal lattice [201,202].

A further manifestation of the different effect of H atoms and hot H_2 molecules on adsorption on Cu(110) is presented in Fig. 8.3, where a doser temperature of 1450 K was chosen, which yields a mixture of hot molecular and atomic hydrogen. Spectrum (a) shows the desorption peaks following 10 L* exposure, after the surface was Ar^+ sputter cleaned and annealed at 800 K. The double peak indicates desorption from “rough” and “smooth” areas of the Cu(110) surface. No significant subsurface hydrogen is observed. Spectrum (b) was obtained for the same exposure at 1450 K, but prior to that the surface was extensively exposed to H (100 L*) and then flashed to 800 K. Now only desorption from the rough surface is observed. In addition to that quite some subsurface absorption does already exist. This shows that the activation barrier for subsurface penetration is also influenced by the local atomic arrangement on the surface. For comparison spectrum (c) shows again the desorption peaks after adsorption of pure H as obtained at 1950 K doser temperature. In this case 1 L* is already enough to nearly saturate the surface peak and to produce significant amounts of subsurface hydrogen.

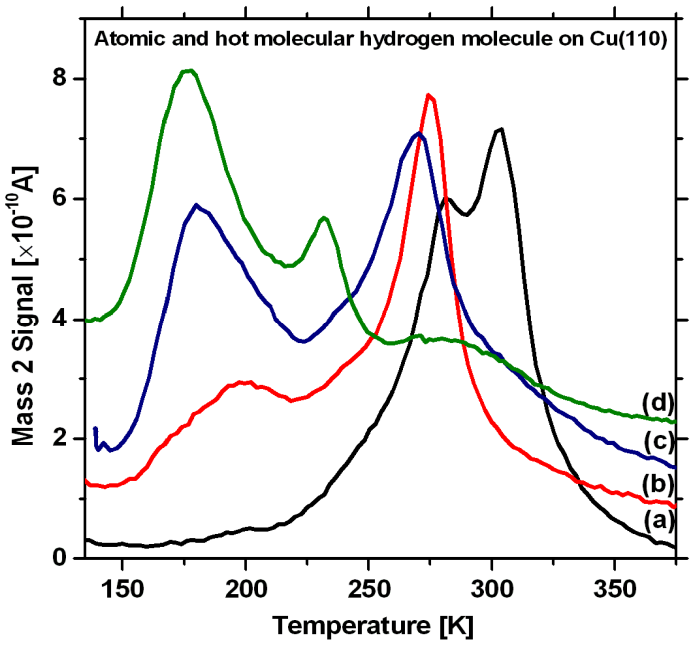

Fig.8.3. Hydrogen desorption spectra after exposing the individually prepared Cu(110) surface to a mixture of hot molecular and atomic hydrogen, obtained at 1450 K doser temperature. (a) Exposure of 10 L* after Ar^+ sputtering and heating to 800 K for 10 min. (b) Exposure of 10 L* after 100 L* surface roughening and short sputtering and flashing to 800 K. (c) For comparison exposure of 1 L* atomic hydrogen (obtained at 1950 K) exposed to the surface as in (b). (d) Exposure to 1 L* atomic hydrogen after prolonged H dosing (100 L*) and short heating to 400 K (C-contaminated surface).

Spectrum (d) finally shows the hydrogen desorption behavior from a carbon contaminated Cu(110) surface. This surface was obtained after prolonged dosing to atomic hydrogen (100 L*), without subsequent cleaning by Ar^+ sputtering. This leads inevitably to quite some carbon contamination. Spectrum (d) was then obtained after flashing the sample to 800 K and an anew H exposure of 1 L*. It shows that the surface adsorption states are virtually completely blocked, whereas the amount of subsurface absorption was actually increased. In fact, the total amount of hydrogen uptake was nearly unchanged. This demonstrates that the sticking coefficient for atomic hydrogen on clean and C-contaminated Cu(110) is nearly the same, the hydrogen atoms just occupy preferentially the subsurface absorption sites because no surface adsorption sites are available.

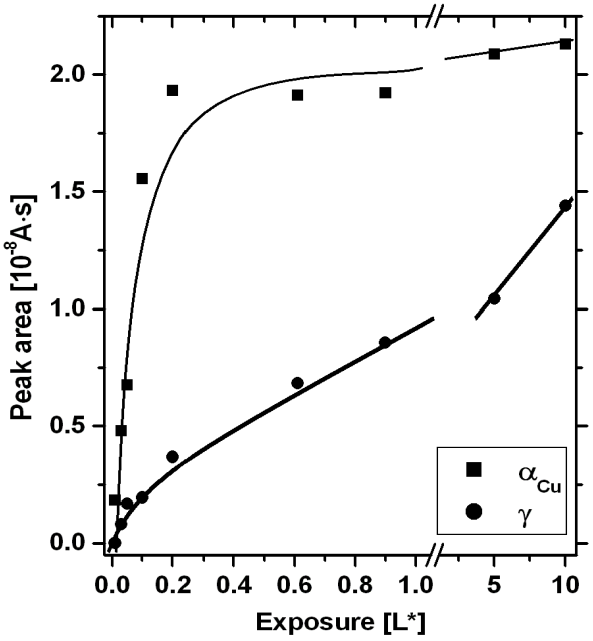

Fig.8.4. Uptake curves for hydrogen surface adsorption (α_{Cu}) and subsurface adsorption (γ) when dosing the Cu(110) surface with atomic hydrogen, as obtained from the TDS of Fig. 8.1.

The hydrogen uptake for the individual desorption states versus atomic H exposure on a clean but roughened Cu(110) surface, as obtained from Fig. 8.1, is shown in Fig. 8.4. At around 0.2 L* of atomic hydrogen the associative desorption peak from surface sites saturates already, whereas the subsurface peak still increases continuously. From the initial slope of the uptake curve the initial sticking coefficient can be calculated. Taking a hydrogen saturation of 0.5 ML ($N_{ads.}$=5.45×10^{14} atoms/cm^2) for the surface state and an intercept of the initial slope with the saturation level at around 0.1 L*, the initial sticking coefficient of hydrogen can be calculated to s_0 = 0.38. (Slope crossing with saturation level at 0.1 L*, corresponding to 0.5 L, impingement rate per 1 L = 2.9×10^{15} H-atoms/cm^2). For comparison, a value of s_0 = 0.18 was determined by Sandl et al. [189].

Considering the possibly higher roughness of our Cu(110) surface this difference in the sticking coefficient is plausible. It is a general rule that the sticking coefficient for *dissociative* adsorption increases with increasing roughness on the atomic scale, due to a decrease of the activation barriers for dissociation [199]. Actually, a similar structure dependence has not yet been confirmed for *atomic* hydrogen adsorption on a quantitative level. However, since the excitation

of phonons will be one major contribution for energy dissipation of the impinging H atoms [203], the specific arrangements of the surface atoms might play an important role for energy accommodation. One has to consider that a significant amount of translational energy has to be released because the incoming atoms are accelerated in front of the surface by a potential of about 2.7 eV (2.25 eV due to ½ dissociation energy of H_2 plus 0.5 eV of adsorption energy per H-atom), in addition to their initial translational energy ($E_{tr} = 2kT$) of about 0.3 eV, according to a doser temperature of 1950 K. But, as pointed out in the literature [204,205], a major contribution to the energy dissipation stems from normal to parallel momentum transfer. It can be supposed that this momentum transfer is more efficient on a rough surface than on a flat surface.

From Fig. 8.4 also the coefficient for subsurface uptake can be deduced. Apart from an initially faster increase of the subsurface uptake, probably due to the faster uptake at some defect sites, the nearly linear increase of subsurface uptake in the used exposure range can be described by an uptake coefficient of 1.3×10^{-2}.

8.4. Coadsorption of atomic H and CO on Cu(110)

One of the aims of this work was to gain insight into possible reactions between adsorbed CO and impinging atomic hydrogen to obtain hydrocarbons or oxo-compounds. However, no indications were found for any reaction products neither during H adsorption at low temperature (130 K) nor during subsequent heating in thermal desorption. Nevertheless, some interesting co-adsorption behavior of CO and H could be observed. In this experiment a CO saturated Cu(110) surface (0.75 ML as obtained after 5 L CO exposure) was exposed to increasing amounts of atomic hydrogen at 130 K. Subsequently, the desorption spectra of CO and H_2 were recorded, as plotted in Fig. 8.5 and Fig. 8.6, respectively.

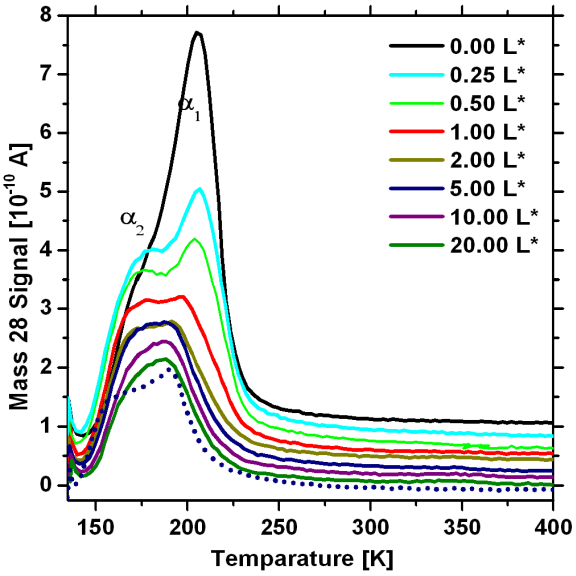

Fig. 8.5. CO desorption spectra after 0.75 ML CO pre-coverage on Cu(110) at 130 K and subsequent exposure to various amounts of atomic H. The heating rate was 2 K/s. The bottom curve (dotted line) shows for comparison the TDS after saturating the surface with H and post-exposure of 5L CO.

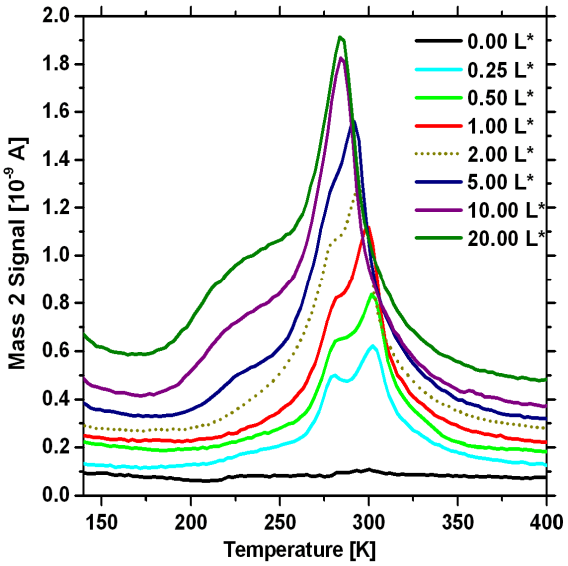

Fig. 8.6. H_2 desorption spectra after 0.75 ML CO pre-coverage on Cu(110) at 130 K and subsequent exposure to various amounts of atomic H. The heating rate was 2 K/s.

The CO desorption spectra show a quite interesting behavior. Without H post-adsorption the CO spectrum exhibits two desorption peaks, α_1 at 210 K and α_2 at 170 K, respectively, in agreement with the literature [144,145]. The α_1 peak, which contains 0.5 ML, corresponds to CO molecules adsorbed in on-top position, forming a (2x1) superstructure [206]. The α_2 peak was attributed to CO molecules adsorbed in the pseudo threefold hollow sites of the (111) facets of Cu(110) [9] (see Fig. 8.7a), which are therefore strongly tilted. With increasing H post-adsorption the α_1 peak decreases very quickly whereas the α_2 peak is virtually not influenced.

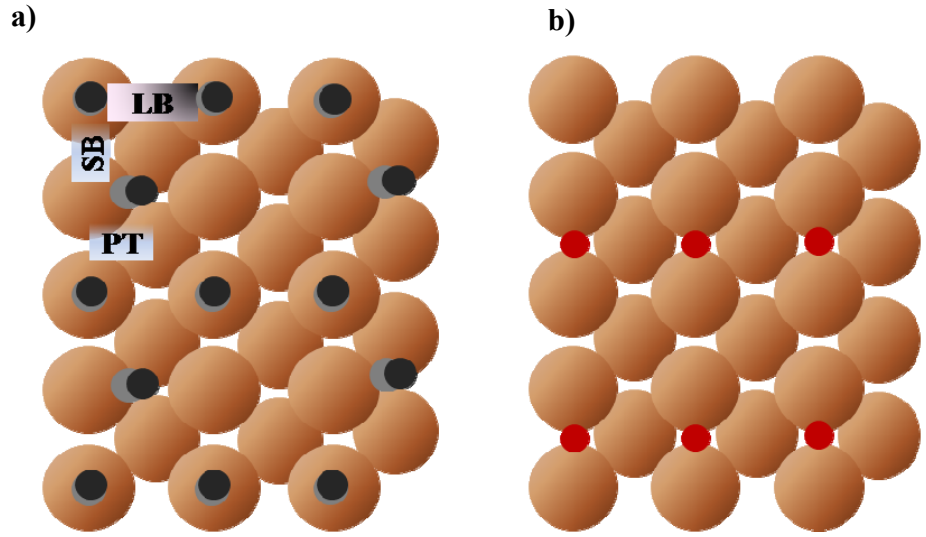

Fig.8.7. a) Arrangement of CO molecules on Cu(110) for a coverage of 0.75 ML [9], b) Arrangement of H atoms on Cu(110) for 0.5 ML [207,208].

An initial "removal coefficient" of 0.06 CO(α_1)/H can be deduced from Fig. 8.5, by comparing the CO desorption traces for 0 L* and 0.25 L* H post-adsorption. This is a quite surprising result, because one would expect that the more weakly bound CO (α_2 state) is removed first. This is even more surprising because it is known that the adsorbed H atoms occupy preferentially the region between the short bridge sites and the pseudo threefold hollow sites of the (111) facets [207,208], as sketched in Fig. 8.7b

There is also the question as to the specific process which leads to the removal of the CO molecules by impinging hydrogen. One could speculate about an Eley-Rideal reaction process [200] in which a formyl radical (HCO) or even formaldehyde (H_2CO) is formed, which could immediately desorb from the surface. Actually, no such species was observed in the mass spectrum during H dosing, although it could be possible that the sensitivity of the spectrometer is just too low to detect such a small amount in the isotropic gas phase. Also during heating of the sample after co-adsorption no desorbing hydrocarbons could be detected. That such a direct abstraction process can be excluded is also suggested by the complementary experiment, where first the Cu(110) surface was saturated with hydrogen and then 5 L CO was dosed (bottom curve in Fig. 8.5). In this case the CO desorption spectrum is nearly the same as that when a CO pre-covered surface is exposed to 20 L* of atomic hydrogen. This shows that the removal of CO by impinging H is not a reaction process, but it is just the result of a competition of adsorption sites.

In Fig. 8.6 the hydrogen desorption spectra after the co-adsorption experiments are compiled. The double peaks for the α state are not specific for the co-adsorption experiment, they are just due to the desorption from smooth and rough areas of the surface, as already discussed before and shown in Fig. 8.3 (curve a). Thus, the surface recombination of H is essentially not influenced by the pre-adsorbed CO, as one would expect because the CO is already gone at the H_2 desorption temperature. However, the desorption kinetics of subsurface hydrogen is significantly changed. A comparison with Fig. 8.1 shows that the γ state of hydrogen desorption at around 180 K is totally suppressed. Hydrogen desorption (probably again from subsurface hydrogen) starts just above 200 K, after the desorption of CO (α_2 state) has ceased. The CO molecules adsorbed in the pseudo threefold hollow sites apparently block the recombination of subsurface hydrogen.

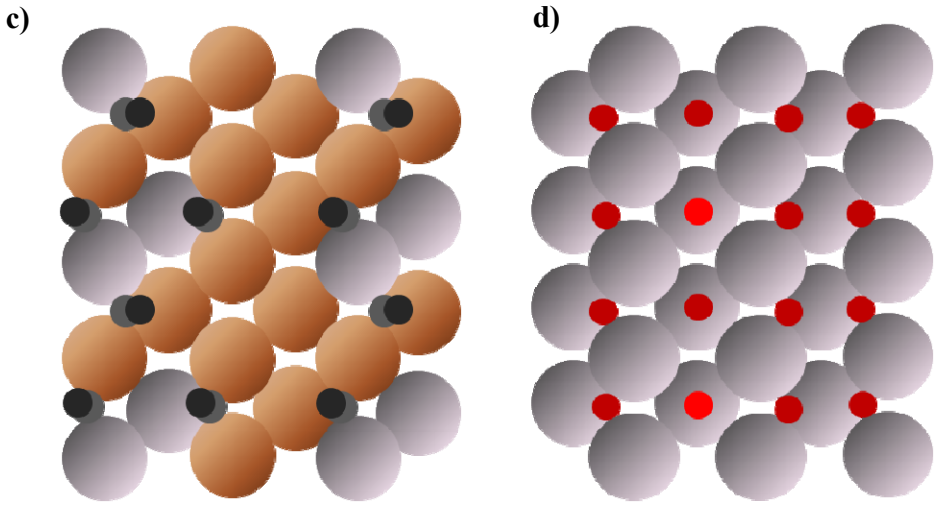

Fig. 8.7. c) Arrangement of 0.75 ML CO on the 0.5 ML Ni/Cu(110) surface [9], d) Arrangement of 1.5 ML H atoms on Ni(110) resulting in a (1x2) reconstruction [214].

The evolution of the CO and H coverage following H exposure of a CO saturated surface, as obtained from Fig. 8.5 and Fig. 8.6, is summarized in Fig. 8.8. The absolute values of the coverage in monolayers was obtained from a de-convolution of the spectra and using the literature values for the saturation values of 0.5 ML for the $\alpha_1(CO)$ peak [144] and 0.5 ML for the $\alpha(H_2)$ peak [93]. When ignoring the subsurface contribution, which is seen as a shoulder around 230 K (Fig. 8.6), the sum of CO and H coverage remains nearly constant throughout the hydrogen exposure. This means that 1 CO molecule, namely the on top adsorbed CO, is

effectively replaced by 1 H atom, which is most probably adsorbed in short bridge and/or pseudo threefold hollow sites.

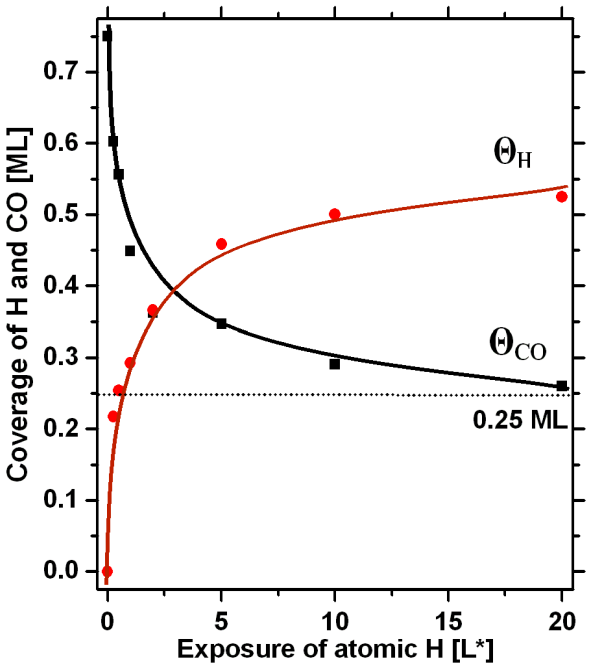

Fig.8.8. Total coverage of hydrogen and carbon monoxide versus exposure of atomic hydrogen on the 0.75 ML carbon monoxide pre-covered Cu(110) surface, as obtained from TDS in Fig. 8.5 and Fig. 8.6.

8.5. Adsorption of atomic H on the Ni/Cu(110) bimetallic surface

A partially nickel covered Cu(110) surface was prepared by direct evaporation of nickel. The amount of evaporated nickel was determined quantitatively by a quartz microbalance. A series of hydrogen saturation desorption spectra (atomic H exposure: 10 L*) from a Cu(110) surface with increasing amounts of nickel is shown in Fig. 8.9. Nickel was evaporated at 175 K and afterward atomic H was exposed at 130 K. Note that a surface temperature of 175 K was chosen for the Ni preparation because nickel starts to dissolve in Cu (110) at higher temperatures [9]. Actually, after thermal desorption indeed most of the nickel was dissolved. Therefore a new nickel layer had to be prepared for each desorption experiment. As a consequence of this, bimetallic Ni-Cu substrates will unfortunately not be suitable for real catalytic applications.

One can clearly see that on the $\Theta < 0.15$ ML nickel modified Cu(110) surface only the copper related hydrogen desorption peaks around 175 K and 280 K are found in the spectrum (curve a, b, c in Fig. 8.9). However, the α-peak decreased considerably with increasing nickel coverage, whereas the total amount of hydrogen remained nearly constant, due to increased hydrogen desorption between 200 K and 250 K. No desorption feature around 330 K was observed, which would indicate desorption from nickel sites. Only for increased nickel coverage ($\Theta > 0.2$ ML) a nickel related desorption of hydrogen starts to appear. At a nickel coverage of 0.5 ML, where LEED shows a (1x2) superstructure, both a copper (270 K) and a nickel (330 K) derived desorption peak can be observed.

With increasing nickel coverage, at around 1 ML of nickel (curve e: 0.85 ML), only a broad featureless desorption spectrum, ranging from 160 K – 370 K, exists. For a significantly higher Ni coverage (curve f: 3.5 ML), however, the desorption spectrum resembles the hydrogen desorption from a pure Ni(110) surface very well [209]. Indeed, the LEED pattern of the substrate shows now a sharp (1x1) structure and the Auger analysis confirms already a pure nickel surface. Thus it can be concluded that nickel forms a perfect epitaxial film on Cu(110). By attributing the saturation of the surface desorption peak for hydrogen on Cu(110) to 0.5 ML, the saturation of hydrogen on the Ni(110) surface (curve f) corresponds to 1.39 ± 0.14 ML. This is in good agreement with the literature value of 1.45 ± 0.15 ML for H_2 on Ni(110) [210]. It is known that at H-saturation on Ni(110) a (1x2) LEED structure exists, which is due to a surface reconstruction. From quantitative LEED [211,212], helium scattering [213] and recent DFT calculations [214] it was concluded that on this pairing row reconstructed surface the hydrogen atoms occupy fourfold hollow sites and pseudo threefold sites, leading to a (1x2)-3H structure, equivalent to a surface coverage of 1.5 ML (Fig.8.7d).

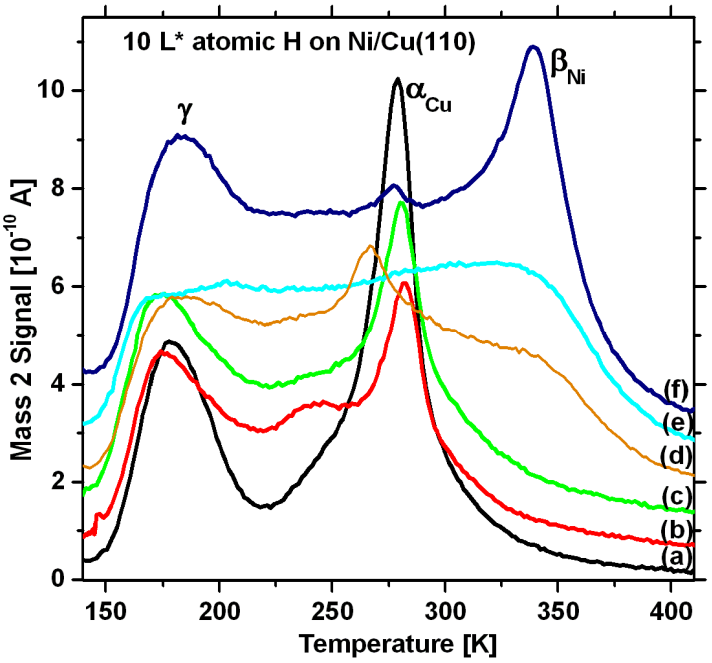

Fig.8.9. Hydrogen desorption spectra from the bimetallic Ni/Cu(110) surface, with varying Ni coverage, prepared at 175 K. 10 L* H exposure at 130 K. (a) 0 ML Ni, (b) 0.08 ML Ni, (c) 0.15 ML Ni, (d) 0.50 ML Ni, (e) 0.85 ML Ni and (f) 3.50 ML Ni surfaces. The heating rate was 2 K/s.

How can the experimental results for hydrogen adsorption on the Ni/Cu(110) surface be interpreted? The fact that at low Ni coverage (<0.15 ML) no Ni derived *surface* hydrogen desorption peaks can be observed, which would have to be correlated with pseudo threefold Ni sites, suggests that in this case the Ni atoms occupy subsurface sites only. From recent DFT calculations of CO adsorption on a 0.5 Ni containing Cu(110) surface it was concluded [9] that 0.25 ML of Ni occupy surface sites and 0.25 ML subsurface sites. One can assume that at a Ni coverage of 0.25 ML mainly the subsurface sites will be occupied. This would be in accord with the missing Ni derived surface desorption peak. However, above 0.5 ML already surface areas should exist containing some Ni trimers, consisting of two in-surface and 1 sub-surface Ni atom, which would lead to the hydrogen desorption around 340 K. On the other hand the influence of the subsurface Ni atoms is sufficient to suppress the desorption from clean Cu areas and to generate new desorption peaks which are similar to subsurface desorption. It is of course not straightforward to correlate adsorption states with the desorption peaks because the desorption rate limiting factor is the activation barrier for recombination. It is actually this new, Ni induced

multidimensional potential energy surface (PES) for recombination of H atoms which would lead to the observed desorption spectrum. Only a full molecular dynamics calculation on the ab-initio determined PES would allow to simulate the desorption behavior.

Nevertheless, at a Ni coverage around 0.5 ML, hydrogen desorption from both, Ni (at 350 K) and Cu sites (at 270 K), can be observed. Due to the fact that the Ni derived peak is rather broad and the Cu derived peak is superimposed on a large background, one could argue that the surface alloy is not very well ordered. On the other hand, on a comparable surface alloy, clearly three new, distinct CO desorption peaks were observed [9] which were attributed to special Ni/Cu atom arrangements, indicating a very local effect being responsible for the desorption energy. Apparently, the corrugation of the PES which governs the recombinative desorption of hydrogen is more smeared out, leading to the nearly structureless desorption between 0.5 ML and 1 ML Ni on the Cu(110) surface. Only at higher Ni coverage, when a nearly perfect Ni(110) overlayer is formed, the desorption peaks become again more pronounced. However, the subsurface peak from the Ni(110) surface is not as sharp as for a perfect singly crystal surface. It was shown in the literature that this peak at around 200 K (called α peak in the literature) depends critically on the perfectness of the surface [211,212].

8.6. Co-adsorption of atomic H and CO on Ni/Cu(110)

The coadsorption of two gases is widely investigated on transition metals and bimetallic surfaces both experimentally [215,216,217,218,219,220] and theoretically [221,222,223]. The general conclusion is that carbon monoxide displaces with the preadsorbed hydrogen from the metal surface and blocks further hydrogen adsorption. Finally we have investigated the co-adsorption of CO and hydrogen on the Ni/Cu(110) bimetallic surface. The result is shown in Fig. 8.10. First 5 L CO were adsorbed on the clean Cu(110) surface at 175 K, which leads to saturation with CO, and then 0.5 ML Ni were evaporated onto this surface. We have shown recently [9] that under these conditions the new CO adsorption sites (β_1- β_3) on the bimetallic surface are best pronounced, as can be observed in the dashed desorption curve in Fig. 8.10. The reason for that is that on a CO covered surface the nickel atoms do not so easily dissolve in the bulk, but they are stabilized by CO in the surface near region. When such a prepared surface is exposed to atomic hydrogen for 5 L* at 130 K, H_2 and CO desorb in a way as shown in Fig. 8.10. The influence of

atomic hydrogen dosing on the CO adsorption state α_1 is similar to that on the clean Cu(110) surface. It is strongly suppressed, whereas the low temperature α_2 state is hardly influenced. (Unfortunately, the CO desorption spectrum from Ni/Cu(110) for comparison (dotted curve) was obtained after adsorption at 175 K. Therefore the low temperature desorption peak α_2 does not appear in this case). The desorption peaks β_1- β_3 are also somewhat decreased due to H exposure, but they remain still well pronounced. This tells us that the CO molecules adsorbed on the Ni/Cu sites (see Fig. 8.7c) are more stable against replacement by H than CO adsorbed on-top of the Cu sites.

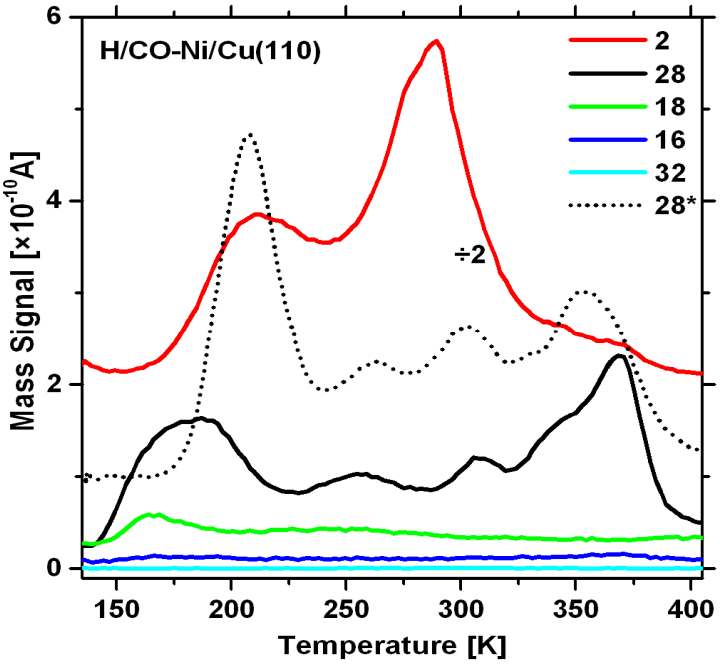

Fig.8.10. Multiplexed desorption spectra (m=2: H_2; m=16: methane, m=18: water, m=28: CO, m=32: methanol) after sequenced exposure of a 0.5 ML Ni covered Cu(110) surface to 5 L CO and 5 L* H. The dotted curve (m=28) shows for comparison the desorption after pure CO exposure of the 0.5 ML Ni/Cu(110) surface.

Associative desorption of H_2 from surface sites (280 K) is not much influenced by adsorbed CO. The recombination of subsurface hydrogen takes place at a slightly higher temperature (210 K) than on the clean Cu(110), but still at a lower temperature than on the CO saturated Cu(110) surface. The small peak at 350 K stems from recombination at Ni sites. The difference of the CO+H co-adsorption between the Cu(110) and Ni/Cu(110) surface is that in the former case

hydrogen desorption starts only after CO has already desorbed, whereas in the latter case both, CO and H_2 desorb concomitantly in the same temperature range. Therefore one could suspect that some reaction between these two adsorbed species could take place. However, no such reaction products could be observed, e.g. water (m=18), methane (m=16) or methanol (m=32), as shown in Fig. 8.10. This just tells us that even on the bimetallic surface no dissociation of CO takes place.

8.7. Summary and conclusions

The exposure of atomic hydrogen to Cu(110) and to the bimetallic Ni/Cu(110) surface leads not only to fast adsorption into surface sites and subsurface sites, but also to some roughening of the surface, which results in a decrease of the desorption temperature for surface recombination from 310 K to 280 K. This is equivalent to a decrease of the activation barrier for recombinative desorption by about 0.1 eV. Hot molecular hydrogen, which also sticks with reasonable probability, does not go subsurface on Cu(110) and does not lead to significant surface roughening. Exposure of a CO saturated Cu(110) surface to atomic hydrogen induces a displacement of the on-top adsorbed CO (α_1 state), whereas the less strongly bound α_2 state is not influenced. CO adsorption on the 0.5 ML Ni/Cu(110) bimetallic surface leads to three new, distinct adsorption states, with adsorption energies between that on clean Cu(110) and clean Ni(110), demonstrating the rather local character of the CO bonding. On the other hand, recombinative desorption of hydrogen takes place either at Cu or Ni sites, but the broadening of the desorption spectra indicates that the influence of surface alloying is rather a long range effect in this case. Unfortunately, no specific intermediates and reaction products between the adsorbed CO and the impinging or adsorbed atomic hydrogen could be observed, neither for the clean Cu(110) nor for the Ni/Cu(110) bimetallic surface.

Chapter IX

9. Summary

In this thesis the adsorption- and desorption kinetics of different molecules, namely hydrogen (H_2), carbon monoxide (CO) and methanol (CH_3OH) on Cu(110), Cu(110)-oxygen stripe phase, Pd(111) and on the Ni/Cu(110) bimetallic surface have been investigated using several surface science techniques. In addition to that, theoretical (DFT) calculations were performed to support the experimental results. In the following the most important results are summarized.

Methanol on Cu(110) and Cu(110)-(2x1)O

The interaction of methanol with the Cu-CuO stripe surfaces was investigated by several surface science techniques, namely thermal desorption spectroscopy (TDS), reflection absorption infrared spectroscopy (RAIRS) and reflectance difference spectroscopy (RDS). Although the main interest concerned the 0.25 ML oxygen stripe phase on Cu(110), we also performed a series of experiments on clean and fully oxygen covered Cu(110) surfaces. TDS revealed that recombinative desorption of methanol and water takes place already at temperature between 200 K and 300 K. Angular resolved thermal desorption spectroscopy of these reaction species shows a cosine angular desorption distribution. At temperature around 350 K again methanol and in addition formaldehyde and hydrogen desorb, which exhibit a strongly forward focused angular distribution. This indicates a quite complicated desorption process, involving high activation barriers for the C-H bond breaking, as suggested by recent theoretical calculations. At 450 K finally CO_2 desorbs. For the Cu-CuO stripe phase the angular distribution of the reaction products at 350 K is clearly anisotropic. The desorption distribution along the stripes shows a forward focused distribution, whereas the distribution normal to the stripes shows a bimodal shape, indicating inclined desorption at the border lines between the Cu and CuO stripes. Exposure of a high amount of methanol (50 L) on clean Cu(110) yields to a very similar TDS as on the oxygen stripe phase surface, due to the coadsorption of water. This has also been confirmed by RAIRS measurements. Temperature programmed RAIRS experiments showed in addition, that the

formation of carbon dioxide occurred via a previously unknown formaldehyde and OH intermediate on the surface. The initial sticking coefficient of methanol has been determined for the clean, partially and fully oxygen covered Cu(110) surface by RDS and TDS. On the clean and on the fully oxygen saturated surface the initial sticking coefficient of methanol is very low, but on the Cu-CuO stripe phase it is close to unity. In addition, on the well ordered Cu-CuO stripe phase, the sticking coefficient of methanol is smaller at 270 K than at 200 K, in contrast to clean Cu(110) surface. This situation can be best explained by a precursor assisted adsorption kinetics. The RMS displacement of methanol in the precursor state, which depends on the activation barrier for diffusion, increases with increasing surface temperature, whereas the life time in the precursor, which depends on the desorption energy, decreases.

Methanol on Pd(111): A quantitative determination of the reaction species and co-adsorption with deuterium

TDS has been used to determine the quantitative amounts of the desorbing reaction products, which are in this case methanol, hydrogen and carbon monoxide. The saturation coverage of chemisorbed methanol has been determined to be 2.6×10^{14} MeOH/cm^2. However, co-adsorption of water and/or hydrogen from the residual gas can block the adsorption sites for methanol, therefore, the measured methanol coverage has to be seen as a lower limit. While 62% of the adsorbed methanol desorbs associatively, 38% dehydrogenate into hydrogen and carbon monoxide. However, no evidence of C-O bond scission could be seen on the clean Pd(111) surface. Furthermore, the interaction of pre-adsorbed deuterium and of impinging molecular and atomic deuterium with the methanol/Pd(111) system has been quantitatively studied. Since pre-adsorbed deuterium reduces the probability to form chemisorbed methanol on the surface most of the methanol molecules are physisorbed on the surface. The amount of dehydrogenation during heating of the sample is also reduced compared with the adsorption on the clean Pd(111) surface. Post-adsorption of molecular deuterium on the methanol covered surface does not significantly influence the dehydrogenation probability. However, there is again a trend to change chemisorbed methanol into physisorbed methanol. In both cases, for pre-adsorption and post-adsorption of molecular deuterium, no indication of methanol deuteration could be found. On the other hand considerable changes in the methanol layer are seen due to atomic deuterium

exposure. All species of deuterated methanol, from CH_3OD to CD_3OD, can be observed in the TDS. Moreover, the dehydrogenation probability of methanol is increased. Another effect of atomic deuterium exposure is the removal of adsorbed hydrogen atoms by an Eley-Rideal mechanism. This is particularly effective for pre-adsorbed hydrogen from the residual gas, but to some extent also for the dehydrogenated hydrogen atoms

Nickel carbonyl adsorption on Cu(110)

Dosing nickel carbonyl ($Ni(CO)_4$) to Cu(110) at 110 K leads to physisorption. The molecules desorb again from the surface at around 150 K, exhibiting a zero-order desorption reaction. In this case the surface is actually always saturated with a monolayer of CO, because nickel carbonyl can only be dosed as a mixture of CO and $Ni(CO)_4$. The evaluation of the desorption spectra according to the Polanyi-Wigner equation yields a desorption energy of 0.61 eV. The pre-exponential factor for nickel carbonyl desorption is $8.2 \cdot 10^{18}$ s^{-1}. This rather large value suggests, according to transition state theory, that the entropy change during desorption is rather large, or in other words, that the molecules are rather immobile prior to desorption. An interesting feature of nickel carbonyl desorption is that the first 10% of a monolayer exhibit a clearly distinct desorption peak (γ_1), which disappears with increasing coverage and becomes incorporated into the emerging main desorption peak (γ_2). This is attributed to the weaker bonding of the nickel carbonyl monomers to the CO covered copper surface (via three CO ligands) before the nucleation into bulk islands starts, where the molecules are coordinated via four ligands. Adsorption of nickel carbonyl at temperatures above 180 K leads to decomposition of the molecules and to the formation of a CO covered bimetallic Ni-Cu(110) surface. High exposure of nickel carbonyl at temperatures at around 300 K finally leads to an epitaxial thick film of nickel on Cu(110).

Carbon monoxide on the bimetallic Ni/Cu(110) surface

The adsorption behavior of CO on the bimetallic Ni/Cu(110) surface has been studied experimentally by thermal desorption spectroscopy, including Auger electron spectroscopy and low energy electron diffraction, and theoretically by DFT calculations. The bimetallic surface

was produced either by evaporation of nickel or by decomposition of $Ni(CO)_4$ on Cu(110). With both methods similar bimetallic surfaces could be obtained. Adsorption of CO on such a bimetallic surface yields three new adsorption states with adsorption energies between that on clean Cu(110) and clean Ni(110). The desorption peak maxima for CO on clean Cu(110) are located at 210 K and on clean Ni(110) at 420 K. The new desorption peaks from the bimetallic surface, labeled as β_1-β_3, can be observed at 250 K, 300 K and 360 K, respectively. These new states are most pronounced when ½ monolayer of nickel is present on the Cu(110) surface. This result shows that CO adsorption is determined by local (geometric) effects rather the by long range (electronic) effects.

A great number of DFT calculations, using the VASP code, were performed to identify the most probable Ni/Cu atomic arrangement at the bimetallic surface to reconcile with the experimental results. It turned out that CO adsorption on nickel dimers consisting of in-surface and adjacent sub-surface atoms give the best agreement with the observed experimental data.

These results should contribute to a better understanding of tailoring catalytic processes with the help of bimetallic catalysts. Both the reactivity and selectivity of a catalyst can be influenced in this way because generally a specific arrangement of the surface atoms (ensemble) is needed to run a catalytic reaction, and appropriate adsorption energies for the reactants have to be available.

Interaction of atomic H and CO on Ni/Cu(110)

The exposure of atomic hydrogen to Cu(110) and to the bimetallic Ni/Cu(110) surface leads to fast adsorption into surface sites and subsurface sites. Unfortunately, atomic exposure also leads to some roughening of the surface, which results in a decrease of the desorption temperature for surface recombination from 310 K (at the smooth surface) to 280 K (at the rough surface). This is equivalent to a decrease of the activation barrier for recombinative desorption by about 0.1 eV. Hot molecular hydrogen, which also sticks with reasonable probability, does not go subsurface on Cu(110) and does not lead to significant surface roughening. Exposure of a CO saturated Cu(110) surface to atomic hydrogen induces a displacement of the on-top adsorbed CO (α_1 state), whereas the less strongly bound α_2 state is not influenced. On the other hand, recombinative desorption of hydrogen takes place either at Cu or Ni sites, but the broadening of the desorption spectra

indicates that the influence of surface alloying is rather a long range effect in this case. Unfortunately, no specific intermediates and reaction products between the adsorbed CO and the impinging or adsorbed atomic hydrogen could be observed, neither for the clean Cu(110) nor for the Ni/Cu(110) bimetallic surface.

List of publications and conference contributions

Publications in science citation index (SCI):

1. **Demirci E**., Winkler A.
   Interaction of atomic H and CO with Cu(110) and bimetallic Ni/Cu(110).
   SURFACE SCIENCE, Volume 604, Issues 5-6, 608-615 (2010)

2. Sun L.D., **Demirci E**., Balderas-Navarro R.E.,Winkler A., Hohage M., Zeppenfeld P.
   Optical characterization of methanol adsorption on the bare and oxygen precovered Cu(110) surface.
   SURFACE SCIENCE, Volume 604, Issues 9-10, 824-828 (2010)

3. **Demirci E**., Carbogno C., Gross A.,Winkler A.
   Adsorption of CO on Ni/Cu(110) bimetallic surfaces.
   PHYSICAL REVIEW B, 80, S. 085421-1 - 085421-13 (2009)

4. **Demirci E**., Winkler A.
   Condensation and desorption of nickel-tetracarbonyl on Cu(110).
   SURFACE SCIENCE, Volume 603, Issue 20, 3068-3071 (2009)

5. Singnurkar P., Bako I., Koch H. P., **Demirci E.**, Winkler A. and Schennach R.
   DFT and RAIRS investigations of methanol on Cu(110) and on oxygen modified Cu(110).
   JOURNAL OF PHYSICAL CHEMISRTY C 112 (36) 14034 (2008)

6. **Demirci E**., Winkler A.
   Quantitative determination of the reaction products by thermal desorption spectroscopy: The system methanol/Pd(111).
   JOURNAL OF VACUUM SCIENCE AND TECHNOLOGY A (JVSTA) 26, 1, S. 78 - 82 (2008)

7. **Demirci E**., Winkler A.
   Reaction of molecular and atomic deuterium with methanol on Pd(111).
   THE JOURNAL OF CHEMICAL PHYSICS (JCP) 128, 5, S. 084703-1 - 084703-7 (2008)

8. **Demirci E**., Stettner J., Kratzer M., Schennach R., Winkler A.
   Methanol adsorption on Cu(110) and the angular distribution of the reaction products.
   THE JOURNAL OF CHEMICAL PHYSICS (JCP) 126, S. 164710 (2007)

Proceedings:

1. **Demirci E**., Carbogno C., Groß A.,Winkler A.
   CO adsorption states on the bimetallic Ni/Cu(110) surface.
   SYMPOSIUM ON SURFACE SCIENCE (3S`09), Switzerland (2009)

2. **Demirci, E**.; Winkler, A.
   Adsorption and reaction of methanol on Pd(111) and Cu(110).
   SYMPOSIUM ON SURFACE SCIENCE (3S´08), Austria (2008)
3. **Demirci E**., Carbogno C., Groß A.,Winkler A.
   Reaction properties of Ni-Cu surface alloys.
   International Conference on Nanomaterials and Nanosystems **(**Nanomats 2009), August 10-13, 2009 Istanbul, Turkey

Conference contributions (Talks and poster presentations):

1. **Demirci E**., Carbogno C., Groß A.,Winkler A.
   Tailoring the adsorption states of CO on Ni/Cu(110) bimetallic surfaces.
   13th European Conference on Applications of Surface and Interface Analysis (ECASIA´09), October 18-23, 2009/Antalya-Turkey -***(Talk, Demirci)***

2. **Demirci, E**.; Carbogno, C.; Groß, A.; Winkler, A.:
   Co-adsorption of atomic H and CO on Ni/Cu(110) bimetallic surfaces.

59**.** Jahrestagung der Österreichischen Physikalischen Gesellschaft and Swiss Physical Society, 708, 02.-04.September 2009; Innsbruck, Austria-***(Talk, Demirci)***

3. **Demirci E**., Carbogno C., Groß A.,Winkler A.
   Reaction properties of Ni-Cu surface alloys.
   NanoMats2009, August 10-13, 2009 Istanbul, Turkey-***(Talk, Demirci)***

4. **Demirci E**., Carbogno C., Groß A.,Winkler A.
   Tailoring the adsorption energy of CO on Cu(110) by Ni deposition: Experiment and theory.
   8th INTERNATIONAL WORKSHOP 'Nanoscience on Surfaces' NSOS; May 10-12, 2009, Seggauberg, Austria-***(Talk, Demirci)***

5. **Demirci E**., Carbogno C., Groß A.,Winkler A.
   CO adsorption states on the Ni-Cu surface alloy.
   56th IUVSTA NFN WORKSHOP ON TEMPLATE MEDIATED GROWTH OF NANOSTRUCTURES; 3rd-6th November 2008 Stadtschlaining, Austria-***(Talk, Demirci)***

6. **Demirci, E**.; Carbogno, C.; Groß, A.; Winkler, A.:
   Adsorption states of CO on Ni/Cu(110) bimetallic surface studied by LEED, TDS and DFT.
   58**.** Jahrestagung der Österreichischen Physikalischen Gesellschaft, 137, 22.-26.September 2008; Leoben, Austria-***(Poster)***

7. **Demirci, E**.; Winkler, A.:
   Adsorption and reaction of methanol on Pd(111) and Cu(110).
   Symposium on Surface Science ; 2008 St. Christoph am Arlberg, Austria-***(Talk, Winkler)***

8. **Demirci, E**.; Winkler, A.
   New adsorption states of carbon monoxide on Cu(110)+Ni.
   72nd Annual meeting and DPG spring meeting O 62.8 p 636 Berlin, 2008, Germany-***(Talk, Demirci)***

9. **Demirci, E**.; Winkler, A.
Unusual adsorption/desorption kinetics of CO on Cu(110)
6th Internatiol Workshop 'Nanoscience on Surfaces' NSOS, December 12-15, 2007 Linz, Austria-***(Talk, Demirci)***

10. Sun, L.; **Demirci, E**.; Balderas Navarro, R.; Winkler, A.; Hohage, M.; Zeppenfeld, P.:
*Methanol oxidation on the Cu-CuO stripe phase: a RDS study***.**
6th International Workshop 'Nanoscience on Surfaces' NSOS, December 12-15, 2007 Linz, Austria-***(Talk, Sun)***

11. **Demirci, E**.; Schennach, R.; Winkler, A.
Influence of CO on the adsorption and reaction of methanol on Pd(111).
Jahrestagung der Österreichischen Physikalischen Gesellschaft, Krems ; 57 (2007), S. 71 - 71 -***(Talk, Demirci)***

12. **Demirci, E**.; Stettner, J.; Kratzer, M.; Schennach, R.; Winkler, A.:
Methanol adsorption on Cu(110) and the angular distribution of the reaction products.
Bunsentagung 2007, Graz/Austria-***(Poster)***

13. Singnurkar, P.; **Demirci, E**.; Winkler, A.; Bako, I.; Schennach, R.:
RAIRS and DFT investigation of methanol on Cu(110) and on the Cu – O stripe phase.
International Vacuum Congress ; 17 (2007), S. SSP1-165 - SSP1-165, Stockholm/Sweden-***(Talk, Schennach)***

14. Schennach, R.; **Demirci, E**.; Singnurkar, P.; Winkler, A.:
RAIRS of Methanol Reactions on Cu(110) surfaces.
Europacat 8 (2007), S. P3-14 - P3-14, European Congress on Catalysis, Turku/Finland-***(Talk, Schennach)***

15. Singnurkar, P.; **Demirci, E**.; Winkler, A.; Bako, I.; Schennach, R.: *Reaction of methanol on Cu(110) and on the Cu-O stripe phase.*
Österreichische Chemietage, Klagenfurt ; 12 (2007), S. 16 – 16-***(Talk, Schennach)***

16. **Demirci, E**.; Winkler, A.:
Interaction of methanol with the Cu-CuO stripe phase.
Jahrestagung der Österreichischen Physikalischen Gesellschaft ; 2006-***(Poster)***

17. Sun, L.; **Demirci, E**.; Balderas Navarro, R.; Winkler, A.; Hohage, M.; Zeppenfeld, P.:
Methanol adsorption on Cu(110) and the Cu(110)(2x1) stripe phase studied by reflectance difference spectroscopy.
Jahrestagung der Österreichischen Physikalischen Gesellschaft ; 2006-***(Talk, Sun)***

18. **Demirci, E**.; Winkler, A.:
Interaction of methanol with the Cu-O stripe phase.
4th NSOS Workshop 'Nanoscience on Surfaces', May 29th-31st, 2006 Burgenland, Austria-***(Talk, Winkler)***

Bibliography

[1] J. R. Jennings, *Catalytic Ammonia synthesis*, Plenum Press, New York (1991)

[2] H. Schulz, *Short history and present trends of Fischer-Tropsch synthesis*, Applied Catalysis A: General, 186 (1-2), 3 (1999)

[3] E. Demirci, J. Stettner, M. Kratzer, R. Schennach and A. Winkler. J. Chem. Phys. 126, 164710 (2007)

[4] P. Singnurkar, I. Bako, H. P. Koch, E. Demirci, A. Winkler, and R. Schennach, J. Phys. Chem. C 112, 14034 (2008)

[5] L. D. Sun, E. Demirci, R.E. Balderas-Navarro, A. Winkler, M. Hohage and P. Zeppenfeld, Surface Science, accepted (2010)

[6] E. Demirci and A. Winkler, J. Vac. Sci. Technol. A 26 (1) 78-82 (2008)

[7] E. Demirci and A. Winkler, J. Chem. Phys.128, 084703 (2008)

[8] E. Demirci, A. Winkler, Surface Science 603, 20, 3068-3071 (2009)

[9] E. Demirci, C. Carbogno, A. Gross, A. Winkler, Phys. Rev. B, 80, 085421 (2009)

[10] E. Demirci, A. Winkler, Surface Science 604, 608-615 (2010)

[11] R. I. Masel, *Principles of Adsorption and Reaction on Solid Surfaces*, John Wiley & Sons, Inc. (1996)

[12] H. Ibach, *Physics of Surfaces and Interfaces*, Springer Verlag, (2006)

[13] P. Monk, *Physical Chemistry*, Wiley (2004)

[14] M. C. Desjonquères, and D. Spanjaard, *Concepts in Surface Physics*, Springer (1993)

[15] D. P. Woodruff, The *Chemical Physics of Solid Surfaces*, Vol.11 (2003)

[16] A. W. Adamson, *Physical Chemistry of Surfaces*, 5th Ed., John Wiley & Sons. (1990)

[17] F. C. Tompkins, *Chemisorption of Gases on Metals*, Acad. Press (1978)

[18] K. Oura, V.G. Lifshits, A. A. Saranin, A.V. Zotov, and M. Katayama, *Surface Science, An Introduction*, Springer Verlag (2003)

[19] D. D. Eley and E.K.Rideal, Nature 146, 401 (1940)

[20] G. Eilmsteiner, W. Walkner and A. Winkler, Surface Science 352, 263-267 (1996)

[21] P. A. Redhead, Vacuum 12, 203 (1962)

[22] W. van Willigen, Phys. Letters A 28, 80 (1968)

[23] K. D. Rendulic and A. Winkler, Surface Science 299/300 261-276 (1994)

[24] F. Settle, *Handbooks of Inst. Tech. for Chem. Analysis*, Texas Univ. (2003)

[25] C. C. Chang, *Auger Electron Spectroscopy. Surface Science*, 25(1), 53 (1971)

[26] K. W. Kolasinski, *Surface Science*, Wiley, Second Edition (2007)

[27] H. Bubert, H. Jenett, *Surface and Thin Film Analysis*, Wiley (2003)

[28] A. Zangwill, *Physics at Surfaces*, Cambridge University Press (1988)

[29] S. Schroeder and M. Gottfried, *Lecture notes, Temperature-Programmed Desorption (TPD)*, FU Berlin (2002)

[30] http://www.omicron.de/products/mbe_deposition/e_beam_evaporators/

[31] http://en.wikipedia.org/wiki/Nickel_tetracarbonyl

[32] N. G. Yaroslavsky and A.N. Terenin, Dokl Akad Nauk SSSR, 66, 885 (1949)

[33] E Gilli, MSc. thesis TU Graz (2009)

[34] H. P. Koch PhD thesis, TU Graz (2009)

[35] P. Hofmann, K.C. Rose, V. Fernandez, A.M. Bradshaw and W. Richter, Phys. Rev. Lett. 75, 2039 (1995)

[36] L.D. Sun, M. Hohage, P. Zeppenfeld, R.E. Balderas-Navarro and K. Hingerl, Phys. Rev. Lett. 90, 106104 (2003)

[37] L. D Sun, M. Hohage, P. Zeppenfeld, and R. E. Balderas-Navarro, phys. stat. sol. (c) 0, No. 8, 3022–3026 (2003)

[38] D.E. Aspnes, J. Vac. Sci. Technol. B 3, 1498 (1985)

[39] L. D. Sun, PhD thesis, Johannes Kepler Universität Linz (2002)

[40] K. Kern, H. Niehus, A. Schatz, P. Zeppenfeld, J. Goerge and G. Comsa, Phys. Rev. Lett. 67, 855 (1991)

[41] P. Hohenberg and W. Kohn, Phys. Rev., 136, B864 (1964)

[42] L. H. Thomas, Proc. Cambridge Philos. Soc.,23:542–548 (1927)

[43] E. Fermi, Z. Phys., 48, 73 (1928)

[44] E. H. Lieb, Rev. Mod. Phys., 53, 603–641 (1981)

[45] W. Kohn and L. J. Sham, Phys. Rev., 140, A1133 (1965)

[46] W. Kohn, Rev. Mod. Phys. 71, 1267 (1999)

[47] R. Dreizler and A. Gross, *Density Functional Theory: An Approach to the Quantum Many-Body Problem*, Springer, Berlin (1990)

[48] M. Lischka, TU-München (2003)

[49] S. Sakong, TU-München (2005)

[50] J. W. Rayleigh, Phil. Trans., 161, 77 (1870)

[51] W. Ritz, J. reine angew. Math., 135, 1–61 (1908)

[52] G. B. Arfken and H. J. Weber, *Mathematical Methods for Physicists* Academic Press, San Diego, 4th edition (1995)

[53] D. D. Johnson, Phys. Rev. B, 38 (18), 12807–12813, (1988)

[54] J. F. Janak, Phys. Rev. B, 18,7165 (1978)

[55] D. M. Ceperley and B. J. Alder, Phys. Rev. Lett., 45:566 (1980)

[56] M. C. Payne, M. P. Teter, D. C. Allan, T. A. Arias, and J. D. Joannopoulos, Rev. Mod. Phys., 64, 1045 (1992)

[57] J. Perdew, Phys. Rev. Lett. 55, 1665 (1985)

[58] A. Groß, *Theoretical Surface Science: A Microscopic Perspective* (Springer, Berlin, [2002)

[59] C. Lee,W. Yang, and R. Parr, Phys. Rev. B 37, 785 (1988)

[60] J. Perdew, J. Chevary, S. Vosko, K. Jackson, M. Pederson, D. Singh, and C. Fiolhais, Phys. Rev. B 46, 6671 (1992)

[61] J. Perdew, K. Burke, and M. Ernzerhof, Phys. Rev. Lett. 77, 3865 (1996)

[62] Y.Wang and J. P. Perdew, Phys. Rev. B 43, 891 (1991)

[63] M. Methfessel and A. Paxton, Phys. Rev. B 40, 3616 (1989)

[64] P. Blöchl, O. Jepsen, and O. Andersen, Phys. Rev. B 49, 16223 (1994)

[65] M. Payne, M. Teter, D. Allan, T. Arias, and J. D. Joannopoulos, Rev. Mod. Phys. 64, 1047 (1992)

[66] P. Pulay, Chem. Phys. Lett. 73, 393 (1980)

[67] G. Kresse and J. Hafner, J. Phys. Condens. Matter 6, 8245 (1994)

[68] G. Kresse and J. Furthmüller, Comput. Mater. Sci. 6, 15 (1996)

[69] P. Teter, M. Payne, and D. Allan, Phys. Rev. B 40, 12255 (1989)

[70] D. Bylander, L. Kleinman, and S. Lee, Phys. Rev. B 42, 1394 (1990)

[71] A. Wood and D. Zunger, J. Phys. A Math, Gen. 18, 1343 (1985)

[72] R. Feynman, Phys. Rev. 56, 340 (1939)

[73] N. Troullier and J. L. Martins, Phys. Rev. B, 43:1993 (1991)

[74] A. M. Rappe, K. M. Rabe, E. Kaxiras and J. D. Joannopoulos, Phys. Rev. B, 4,1227 (1990)

[75] A. Pasquarello, K. Laasonen, R. Car, C. Lee, and D. Vanderbilt, Phys. Rev. B 69, 1982 (1992)
[76] K. Laasonen, A. Pasquarello, R. Car, C. Lee, and D. Vanderbilt, Phys. Rev. B 47, 10142 (1993)
[77] J. Furthmüller, P. Käckell, F. Bechstedt, and G. Kresse, Phys. Rev. B 61, 4576 (2000)
[78] M. Fuchs, M. Bockstedte, E. Pehlke, and M. Scheffler, Phys. Rev. B 57, 2134 (1998)
[79] G. Brivio and M. Trioni, Rev. Mod. Phys. 71, 231 (1999)
[80] R. Smoluchowski, Phys. Rev., 60, 661–674 (1941)
[81] A. Gross, Lecture notes in Theoretical Surface Science (2008)
[82] M. Bowker, Top. Catal. 3, 461 (1996).
[83] J. Yoshihara and C. T. Campbell, J. Catal. 161, 776 (1996)
[84] I. E. Wachs and R. J. Madix, J. Catal. 53, 208 (1978)
[85] M. Bowker and R. J. Madix, Surf. Sci. 95, 190 (1980)
[86] S. M. Francis, F. M. Leibsle, S. Haq, N. Xiang, and M. Bowker, Surf. Sci. 315, 284 (1994)
[87] C. Ammon, A. Bayer, G. Held, B. Richter, T. Schmidt, and H. P. Steinrück, Surf. Sci. 507–510, 845 (2002).
[88] D. J. Coulman, J. Wintterlin, R. J. Behm, and G. Ertl, Phys. Rev. Lett. 64, 1761 (1990).
[89] F. Jensen, F. Besenbacher, E. Laegsgaard, and I. Steensgaard, Phys. Rev.B 41, 10233 (1990)
[90] K. Kern, H. Niehus, A. Schatz, P. Zeppenfeld, J. George, and G. Comsa, Phys. Rev. Lett. 67, 855 (1991).
[91] P. Zeppenfeld, V. Diercks, C. Tölkes, R. David, and M. A. Krzyzowski, Appl. Surf. Sci. 130–132, 484 (1998)
[92] B. A. Sexton, A. E. Hughes, and N. R. Avery, Surf. Sci. 155, 366 (1985)
[93] G. Anger, A. Winkler, and K. D. Rendulic, Surface Sci. 220, 1 (1989)
[94] K. Christmann, Surf. Sci. Rep. 9, 1 (1988)
[95] P. J. Estrup, E. F. Greene, M. J. Cardillo, and J. C. Tully, J. Phys. Chem. 90, 4099 (1986)
[96] G. R. Darling and S. Holloway, Rep. Prog. Phys. 58, 1595 (1995)
[97] A. Groß, Surface Science 363, 1 (1996)
[98] J. P. Camplin and E. M. McCash, Surf. Sci. 360, 229 (1996)
[99] K. Mudalige and M. Trenary, J. Phys. Chem. B 105, 3823 (2001)
[100] K. Mudalige and M. Trenary, Surf. Sci. 504, 208 (2002)

[101] G. Krenn, H. P. Koch and R. Schennach, Vacuum 80, 40 (2005)

[102] H. P. Koch, G. Krenn, I. Bako and R. Schennach, J. Chem. Phys. 122, 244720 (2005)

[103] D.S. Martin, A. Maunder and P. Weightman, Phys. Rev. B 63, p. 155403 (2001)

[104] L.D. Sun, M. Hohage, P. Zeppenfeld and R.E. Balderas-Navarro, *Surf. Sci.* 589, p. 153 (2005)

[105] M. Hohage, L.D. Sun, and P. Zeppenfeld, Appl. Phys. A 80, 1005 (2005)

[106] S. Sakong and A. Gross, J. Catal. 231, 420 (2005)

[107] F.M. Leibsle, S.M. Francis, R. Davis, N. Xiang and M Bowker, Phys. Rev. Lett. 72, 2569 (1994)

[108] S.L. Silva, R.M. Lemor and F.M. Leibsle, Surf. Sci. 421, 135 (1999)

[109] P. Stoltze, J. Phys., Condens. Matter 6, 9496 (1994)

[110] O. Rodriguez de la Fuente, M. Borasio, P. Galletto, G. Rupprechter and H. J. Freund Surf. Sci. 566-568 740 (2004)

[111] R.Schennach, A. Eichler and K. D. Rendulic J. Phys. Chem. B, 107 2552 (2003)

[112] C. Zhang J. and P. J. Hu Chem. Phys., 115 (15) 7182 (2001)

[113] J. J.Chen, Z. C.Jiang, Y. Zhou, B. R. Chakraborty and N. Winograd, Surf. Sci., 328 248 (1995)

[114]M. Rebholz and N. J. Kruse Chem. Phys., 95 (10) 7745 (1991)

[115] J. J. Chen and N. J. Winograd, Am. Chem. Soc., 114, 2722 (1992)

[116] X. Guo, L. Hanley and Jr. J. T. Yates, J. Am. Chem. Soc., 111 3155 (1989)

[117] R. J. Levis, J. Zhicheng and N. J. Winograd, Am. Chem. Soc. 111 4605 (1989)

[118] A. Winkler, J. Vac. Sci. Technol. A 5, 2430 (1987)

[119] R.L. Summers, NASA TN D-5285

[120] G. Comsa and R. David, Surf. Sci. Rep. 5, 145 (1985)

[121] G.R. Darling and S. Holloway, Rep. Prog. Phys. 58, 1595 (1995)

[122] X. Guo and J.T. Yates, Jr., J. Chem. Phys. 90, 6761 (1989)

[123] B. Klötzer, W. Unterberger, and K. Hayek, Surf. Sci. 532-535, 142 (2003)

[124] H.P. Steinrück, A. Winkler, and K.D. Rendulic, J. Phys. C 17, L311 (1984)

[125] G. Pauer and A. Winkler, J. Chem. Phys. 120, 3864 (2004)

[126] M. Kratzer, J. Stettner, and A. Winkler, Surf. Sci. 601, 3456 (2007)

[127] J.L. Davis and M.A. Barteau, Surf. Sci. 187, 387 (1987)

[128] J. A. Gates and L. L. Kesmodel, J. Catalysis 83, 437 (1983)
[129] J.L. Davis and M. A. Barteau, Surf. Sci. 197, 123 (1988)
[130] C.J. Zhang and P. Hu, J. Chem. Phys. 115, 7182 (2001)
[131] K. Christmann and J.E. Demuth, J. Chem. Phys. 76, 6308 (1982)
[132] U. Bischler and E. Bertel, J. Vac. Sci. Technol. A11, 458 (1993)
[133] C. Eibl, G. Lackner, and A. Winkler, J. Vac. Sci. Technol. A16, 2979 (1998)
[134] C. Resch, H.F. Berger, K.D. Rendulic, and E. Bertel, Surf. Sci. 316, L1105 (1994)
[135] G. Eilmsteiner, W. Walkner, and A. Winkler, Surf. Sci. 352-354, 263 (1996)
[136] C.T. Rettner, Phys. Rev. Lett. 69, 383 (1992)
[137] S. Wehner and J. Küppers, J. Chem. Phys. 108, 3353 (1998)
[138] T. Kammler and J. Küppers, J. Chem. Phys. 111, 8115 (1999)
[139] J. Boh, G. Eilmsteiner, K.D. Rendulic, and A. Winkler, Surf. Sci. 395, 98 (1998)
[140] A. Winkler, Appl. Phys. A 67, 637 (1998)
[141] L. Mond, C. Langer, F. Quincke, J. Chem. Soc. 57 749 (1890)
[142] C. Wyse, J. Vininski, T. Watanabe, Solid State Technol. 45 (7), 125 (2002)
[143] J. Engbæk, O. Lytken, J.H. Nielsen, I. Chorkendorff, Surf. Sci. 602, 733 (2008)
[144] C. Harendt, J. Goschnick, W. Hirschwald, Surface Sci. 152/153, 453 (1985)
[145] M. Christiansen, E.V. Thomsen, J. Onsgaard, Surface Sci. 261, 179 (1992)
[146] NIST Chemistry WebBook: http://webbook.nist.gov/chemistry
[147] P. Jakob, D. Menzel, Surface Sci. 220, 70 (1989)
[148] P. Frank, N. Koch, M. Koini, R. Rieger, K. Müllen, R. Resel, A. Winkler, Chem. Phys. Lett. 473, 321 (2007)
[149] K.A. Walsh, Energy Citation Database, DOE, 4339736 (1953)
[150] K.J. Laidler, *Chemical Kinetics*, Harper Collins, New York (1987)
[151] P.W. Atkins, *Physical Chemistry,* Oxford University Press (1986)
[152] K.R. Paserba and A.J. Gellman, Phys. Rev. Lett. 86, 4338 (2001)
[153] S. Müllegger and A. Winkler, Surf. Sci. 600, 1290 (2006)
[154] S.L. Tait, Z. Dohnalek, C.T. Campbell, and B.D. Kay, J. Chem. Phys. 122, 164708 (2005)
[155] C.M.A.M. Mesters, A.F.H-Wielers, O.L.G. Gijzeman, J.W. Geus, G.A. Bootsma, Surf. Sci. 115, 237 (1982)
[156] C.M.A.M. Mesters, G. Wermer, O.L.G. Gijzeman, J.W. Geus, Surf. Sci. 135, 396 (1983)

[157] W. H. M. Sachtler, Faraday Disc. Chem. Soc. 72, 7 (1981)
[158] C. T. Campbell, Ann. Rev. Phys. Chem. 41, 775 (1990)
[159] D. W. Goodman, Surf. Sci. 299/300, 837 (1994)
[160] J. A. Rodriguez, Surf. Sci. Rep. 24, 223 (1996)
[161] V. Ponec, Appl. Catal. A: General 222, 31 (2001)
[162] J. G. Chen, C. A. Menning, and M. B. Zellner, Surf. Sci. Rep. 63, 201 (2008)
[163] A. Groß, Topics Catal. 37, 29 (2006)
[164] S. Sakong, C. Mosch, and A. Groß, Phys. Chem. Chem. Phys. 9, 2216 (2007)
[165] A. Groß, J. Phys: Condens. Matt. 21, 084205 (2009)
[166] G. Held, Applied Physics A 76, 689-700 (2003)
[167] J. L. Falconer and R. J. Madix, Surf. Sci. 48, 393 (1975)
[168] R. J. Behm, G. Ertl, and V. Penka, Surf. Sci. 160, 387 (1985)
[169] K. Y. Yu, D. T. Ling, and W. E. Spicer, Solid State Comm. 20, 751 (1976)
[170] N. J. Castellani, Int. J. Quant. Chem. 41, 599 (1992)
[171] D. Shriver, P. Atkins, and C. Lanford, *Inorganic Chemistry,* W.H. Freeman & Co (1990)
[172] K. Lascelles and L.V. Renny, Surf. Sci. 125, L67 (1983)
[173] G. Kresse and J. Furthmüller, Phys. Rev. B 54, 11169 (1996)
[174] G. Kresse and D. Joubert, Phys. Rev. B 59, 1758 (1999)
[175] G. Kresse, A. Gil and P. Sautet, Phys. Rev. B 68, 073401 (2003)
[176] P. J. Feibelmann, B. Hammer, J. K. Norskov, F. Wagner, M. Scheffler, R. Stumpf, R. Watwe, and J. Dumesic, J. Phys. Chem. B 105, 4018 (2001)
[177] F. Mehmood, A. Kara, T. S. Rahman, and K. P. Bohnen, Phys. Rev.B 74, 155439 (2006)
[178] S.Y. Liem and J. H. R. Clarke, J. Chem. Phys. 121, 4339 (2004)
[179] J. Ahner, D. Mocuta, R. D. Ramsier, J. T. Yates, Jr., J. Chem. Phys. 105, 6553 (1996)
[180] S. Vollmer, G. Witte, and C. Wöll, Catal. Lett. 77, 97 (2001)
[181] K. Horn, M. Hussain, and J. Pritchard, Surf. Sci. 63, 244 (1977)
[182] P. Hofmann, K.-M. Schindler, S. Bao, V. Fritzsche, A. M. Bradshaw and D. P. Woodruff, Surf. Sci. 337, 169 (1995)
[183] M. D. Alvey, M. J. Dresser, and J. T. Yates, Jr., Surf. Sci. 165, 447 (1986)
[184] B. A. Gurney and W. Ho, J. Vac. Sci. Technol. A 3, 1541 (1985)
[185] S. Yang, M. Yu, G. Meigs, X. H. Feng, and E. Garfunkel, Surf. Sci. 205, L777 (1988)

[186] Y. Tzeng, H. Wu, K. Shiang, T. Tsong, Phys. Rev. B 48, 5549 (1993)
[187] L. V. Pourovskii, N. V. Skorodumova, Yu. Kh. Vekilov, B. Johansson, I. A. Abrikosov, Surf. Sci. 439, 111 (1999)
[188] I. Chorkendorff and P.B. Rasmussen, Surf. Sci. 248, 35 (1991)
[189] P. Sandl, U. Bischler, E. Bertel, Surf. Sci. 291, 29 (1993)
[190] M. Rohwerder, C. Benndorf, Surf. Sci. 307-309, 789 (1994)
[191] I.E. Wachs, R.J. Madix, J. Catal. 53, 208 (1978)
[192] J. Yoshihara, C.T. Campbell, J. Catal. 161, 776 (1996)
[193] J. Nerlov, I. Chorkendorff, J.Catal. 181, 271 (1999)
[194] W.J. Mitchell, J. Xie, T.A. Jachimowski, W.H. Weinberg, J. Am. Chem. Soc. 117 2606, (1995)
[195] M.P. Andersson, F. Abild-Pedersen, I.N. Remediakis, T. Bligaard, G. Jones, J. Engbæk, O. Lytken, S. Horch, J.H. Nielsen, J. Sehested, J.R. Rostrup-Nielsen, J.K. Nørskov, I. Chorkendorff, J. Catal. 255, 6, (2008)
[196] S. Shetty, A.P.J. Jansen, R.A. Van Santen, J. Am. Chem. Soc. 131, 12874 (2009)
[197] X. Jian-Jun, J. Ping, Z. Kai-Ming, Acta Physica Sinica 4, 691 (1995)
[198] G. Pauer, A. Eichler, M. Sock, M.G. Ramsey, F. Netzer, A. Winkler, J. Chem. Phys. 119, 5253 (2003)
[199] K.D. Rendulic, A. Winkler, Intern. J. Mod Phys. B3, 941 (1989)
[200] D.D. Eley, E.K. Rideal, Nature 146, 401 (1946)
[201] V.N. Verbetsky, S.V. Mitrokhin, in *Hydrogen in Metals II*, F.A Lewis and A. Aladjem, Ed., Solid State Phenomena, 73-75, 503 (2000)
[202] N.P. Fitzsimonis, W. Jones, P.J. Harley, Catal. Lett. 15, 83 (1992)
[203] F.O. Goodman, Progr. Surf. Sci. 5 261 (1975)
[204] U. Bischler, P. Sandl, E. Bertel, T. Brunner, W. Brenig, Phys. Rev. Lett. 70, 3603 (1993)
[205] S. Caratzoulas, B. Jackson, M. Persson, J. Chem. Phys. 107, 6420 (1997)
[206] P. Hofmann, K.M. Schindler, S. Bao, V. Fritzsche, A.M. Bradshaw, D.P. Woodruff, Surf. Sci. 337, 169 (1995)
[207] C.S. Bae, D.L. Freeman, J.D. Doll, G. Kresse, J. Hafner, J. Chem. Phys. 113, 6926 (2000)
[208] N. Ozawa, T. Roman, H. Nakanishi, W.A. Dino, H. Kasai, Phys. Rev. B. 75, 115421 (2007)

[209] A. Winkler, K.D. Rendulic, Surf. Sci. 118, 19 (1982)

[210] H.P. Steinrück, M. Luger, A. Winkler, K.D. Rendulic, Phys. Rev. B 32, 5032 (1985)

[211] K. Christmann, F. Chehab, V. Penka, G. Ertl, Surf. Sci. 152/153, 356 (1985)

[212] T.E. Jackman, K. Griffiths, W.N. Unertl, J.A. Davies, K.H. Gurtler, D.A. Harrington, P.R. Norton, Surf. Sci. 179, 297 (1987)

[213] G. Parschau, B. Burg, K.H. Rieder, Surf. Sci. 293, L830 (1993)

[214] G. Kresse, J. Hafner, Surf. Sci. 459, 287 (2000)

[215] D.E. Ibbotson, T.S. Wittrig, W.H. Weinberg, Surf. Sci. 97, 297 (1980)

[216] G. Rangelov, U. Bischler, N. Memmel, E. Bertel, V. Dose, M. Pabst, N. Rösch, Surf. Sci. 273, 61 (1992)

[217] J. Lauterbach, M. Schick, W.H. Weinberg, J. Vac. Sci. Technol. A14, 1511 (1996)

[218] S. Haq, J.G. Love, D.A. King, Surf. Sci. 275, 170 (1992)

[219] C. Becker, U. Schröder, G.R. Castro, U. Schneider, H. Busse, R. Linke, K. Wandelt, Surf. Sci. 307-309 412 (1994)

[220] M. Morkel, G. Rupprechter, H.J. Freund, J. Chem. Phys. 119, 10853 (2003)

[221] M. Lischka, C. Mosch, A. Gross, Surf. Sci. 570, 227 (2004)

[222] L. Xu, H.Y. Xiao, X.T. Zu, Chem. Phys. 323, 334 (2006)

[223] P. van Heiden, E. van Steen, J. Phys. Chem. C 112, 16505 (2008)